Aachener Verfahrenstechnik Series
AVT.CVT – Chemical Process Engineering
Volume 34 (2023)

Denis Mathias Wypysek

Visualization of Complex Flow Phenomena in Multichannel Membrane Modules

DOI: 10.18154/RWTH-2022-11651

Visualization of Complex Flow Phenomena in Multichannel Membrane Modules

Visualisierung komplexer Strömungsphänomene in Mehrkanalmembranmodulen

Von der Fakultät für Maschinenwesen
der Rheinisch-Westfälischen Technischen Hochschule Aachen
zur Erlangung des akademischen Grades eines Doktors der
Ingenieurwissenschaften genehmigte Dissertation

vorgelegt von

Denis Mathias Wypysek

Berichter:
Univ.-Prof. Dr.-Ing. Matthias Wessling
Prof. Dr.ir. Walter G. J. Van der Meer

Tag der mündlichen Prüfung: 06.07.2022

Diese Dissertation ist auf den Internetseiten der Universitätsbibliothek online verfügbar.

Parts of this dissertation have been published. Reproduced with permission from:

Denis Wypysek, Matthias Wessling
MRI in membrane filtration processes in *Magnetic Resonance Microscopy: Instrumentation and Applications in Engineering, Life Science and Energy Research*
John Wiley & Sons, Ltd, 2022. ISBN: 978-3-527-82725-1

Denis Wypysek, Deniz Rall, Martin Wiese, Tobias Neef, Geert-Henk Koops, Matthias Wessling,
Shell and lumen side flow and pressure communication during permeation and filtration in a multibore polymer membrane module
Journal of Membrane Science 584, 2019, 254-267.
DOI: 10.1016/j.memsci.2019.04.070

Denis Wypysek, Deniz Rall, Tobias Neef, Alex Jarauta, Marc Secanell, Matthias Wessling,
How does porosity heterogeneity affect the transport properties of multibore filtration membranes?
Journal of Membrane Science 636, 2021, 119520.
DOI: 10.1016/j.memsci.2021.119520

Denis Wypysek, Anna Maria Kalde, Florian Pradellok, Matthias Wessling,
In-situ investigation of wetting patterns in polymeric multibore membranes via magnetic resonance imaging
Journal of Membrane Science 622, 2021, 119026.
DOI: 10.1016/j.memsci.2020.119026

Titel: Visualization of Complex Flow Phenomena in Multichannel Membrane Modules

Autor: Denis Mathias Wypysek

Reihe: Aachener Verfahrenstechnik Series
AVT.CVT - Chemical Process Engineering
Volume: 34 (2023)

Herausgeber: Aachener Verfahrenstechnik
Forckenbeckstraße 51
52074 Aachen
Tel.: +49 (0)241 8095470
Fax.: +49 (0)241 8092252
E-Mail: secretary.cvt@avt.rwth-aachen.de
http://www.avt.rwth-aachen.de/AVT

Volltext verfügbar: 10.18154/RWTH-2022-11651

Acknowledgement

Es ist an der Zeit Danke zu sagen. Danke, für 4 Jahre voller Wissenschaft, Hürden und Lichtblicke. Danke, für erlebnisreiche Reisen, Events und Konferenzen. Danke, für tolle Kollegen und spannende Diskussionen. Und Danke, dass aus diesen Kollegen Freunde geworden sind.

Zunächst einmal möchte ich meinem Doktorvater Prof. Matthias Wessling danken, dass er mir alle Freiräume zum Forschen gelassen hat und mir an den wichtigen Abzweigungen während meiner Promotionszeit einen wegweisenden Schubs gegeben hat. Also, I want to thank Prof. Walter Van der Meer for being my second examiner and for the nice atmosphere during the exam.

Ohne die Hilfe vieler, ist so eine Promotion gar nicht möglich. Deswegen ein großer Dank an die IT, wenn es mal Computerprobleme gab; Karin, für viele Mikroskopieaufnahmen; der Werkstatt, für diverse Basteleien und vor allem Susi, die bei allen organisatorischen Fragen immer mit Rat und Tat zu Seite stand. Geert-Henk Koops gilt ein Dank als guter Diskussionspartner und unserer Quelle für die hier untersuchten Membranen.

Jeden einzelnen Kollegen zu nennen, mit dem ich diesen Weg gehen durfte, würde hier einfach den Rahmen sprengen. Einige würde ich trotzdem gerne hervorheben. Danke an Martin Wiese, bei dem ich jede meiner studentischen Arbeiten schreiben durfte, von dem ich viel gelernt habe und der mich gut an das Thema meiner Dissertation mit der Übergabe des Tomographen herangeführt hat. Danke an Deniz Rall und Korcan Percin, die mich im ersten Jahr als Bürokollegen begleitet haben und mir bei meinen anfänglichen Problemen geholfen haben. Danke an Felix Stockmeier: mit dir wurde jeder Freitag im Büro ein musikalisches Fest! Danke an die beiden MuCo-Gruppen (zunächst mit Johannes Lohaus, Morten Logemann, Robert Keller und Felix Stockmeier; dann mit Lucas Stüwe, Niklas Köller, Matthias Geiger, Berinike Bräsel, Florian Wiesner), die sich jedes Problemchen angehört und es wegdiskutiert haben. Danke an Maik Tepper, als guter Diskussionspartner und vor allem für das schöne Foto der Membran, das ich zum Ende der Schreibphase noch benötigt habe. Und nicht zu vergessen: ein Riesendank an die KaffeeBabos Kristina Baitalow, Anna Kalde und Felix Stockmeier - mit euch vergingen die 4 Jahre wie im Flug.

Ich hatte zwar nie viele Studenten, aber ohne euch wäre meine Dissertation einfach nicht das geworden, was sie nun ist - fertig! Ich bedanke mich bei Peter Schrader, Hannah Buchholz, Tobias Neef, Lorenz Aldefeld und Florian Pradellok.

Ohne meine Familie und meine Freunde hätte ich diesen langen Weg von meiner Schulzeit bis zur Promotion nicht geschafft. Danke, dass ihr immer an meiner Seite seid und mich unterstützt habt und unterstützen werdet.

Und zu guter Letzt: Sarah und Mila! Sarah, was du alles geleistet hast, damit ich zu diesem Abschluss komme, ist nicht selbstverständlich. Deine ständige Bereitschaft mir den Weg zu ebnen und Zeit zu schenken waren und sind der Wahnsinn. Danke! Mila, auch wenn Corona eine doofe Zeit war, habe ich die Zeit zuhause während des Schreibens meiner Dissertation genossen: ich konnte dich beinahe uneingeschränkt in deinem ersten Jahr aufwachsen sehen. In schweren Zeiten hast du mir dann doch immer mal wieder ein Lächeln aufs Gesicht gezaubert!

Danke!

Contents

Abstract

Water poverty is one of the most critical problems affecting the world's society of the 21st century. Therefore, the development and optimization of sustainable water purification technologies is an essential research objective. A growing field of interest in achieving current and future challenges regarding water purification is membrane technology.

Recently, multibore geometries for hollow fiber membranes have promised to overcome many drawbacks of the single bore geometry, thus finding their way into many applications such as drinking water production and seawater desalination. In the past, several studies have focused on optimizing their geometry and material, and investigated flow distribution inside them. However, their related permeation properties, such as fundamental understanding of internal pathways and their hydrodynamic operation conditions in modules, are still unknown.

This study aims to tackle these challenges by deepening the understanding of multibore membrane filtration and hydrodynamic effects in membrane modules. To achieve these goals, the interconnection of magnetic resonance imaging measurements and computational fluid dynamics simulations allows investigating multichannel membrane modules at different orders of magnitude: from a highly-packed membrane module consisting of several multichannel membranes; to a single membrane with and without a module as a housing; toward a closer look into the dynamic wetting behavior of the porous structure of each membrane.

This thesis revealed that small deviations from the ideal membrane position inside a membrane module highly influence its flow field and filtration behavior. A bent multichannel membrane introduces secondary flows on the shell side, leading to drag forces inside each lumen channel which influence particle fouling behavior. Also, a simulation model with heterogeneously distributed material properties was set up to model a multichannel membrane correctly and, thus, internal flux pathways. This model unraveled an unequal flow distribution over the lumen's circumference, with higher velocities closer to the membrane's outer skin. Moreover, the investigation of highly-packed membrane modules showed evolving jet streams on the shell side, which disturb the equal flow distribution in all lumen channels. Finally, wetting experiments of highly-packed modules revealed the need for a wetting time of over six hours when wetting membranes that are not pre-wetted.

This study shows that the combination of magnetic resonance imaging and computational fluid dynamics is a powerful tool to unravel the hydrodynamic behavior of multichannel membranes and modules in full detail. Such information on membrane filtration behavior allows optimizing membranes and membrane modules to create a highly efficient and sustainable process for water purification.

Zusammenfassung

Wasserknappheit ist eines der größten Probleme des 21. Jahrhunderts. Daher ist die Entwicklung und Optimierung nachhaltiger Wasseraufbereitungstechnologien ein wesentlicher Schritt, um dieses Problem zu lösen. Ein immer wichtig werdender Bereich für die Bewältigung aktueller und zukünftiger Herausforderungen in der Wasseraufbereitung ist die Membrantechnologie.

In jüngster Zeit haben Mehrkanalmembran-Geometrien viele Nachteile der Hohlfaserstruktur überwunden und damit ihren Weg in viele Anwendungen wie die Trinkwassergewinnung gefunden. Studien in der Vergangenheit haben die Optimierung der Membrangeometrie und des -materials, sowie die Strömungsverteilung in ihnen untersucht. Die damit zusammenhängenden Permeationseigenschaften, wie z. B. das grundlegende Verständnis der internen Flusswege und die hydrodynamischen Eigenschaften in den Modulen, blieben jedoch unbekannt.

Ziel der vorliegenden Arbeit ist es, diese unerschlossenen Phänomene durch die Vertiefung des Verständnisses der Mehrkanal-Membranfiltration zu erklären. Dafür werden Mehrkanal-Membranmodule in verschiedenen Größenordnungen mit Hilfe von Magnetresonanztomographie und numerischen Strömungssimulationen untersucht: von einem dichtgepackten Membranmodul, das aus mehreren Mehrkanal-Membranen besteht, über eine einzelne Membran mit und ohne Modul als Gehäuse, bis hin zu einem detaillierten Blick auf das dynamische Benetzungsverhalten der porösen Struktur jeder Membran.

Es wird gezeigt, dass kleine Positionsabweichungen von der idealen Membranposition das Strömungsfeld und Filtrationsverhalten stark beeinflussen. So führt eine Biegung in der Mehrkanalmembran zu Sekundärströmungen auf der Mantelseite, die das Foulingverhalten von Partikeln negativ beeinflussen. Simulationen von Membranen mit heterogen verteilten Materialeigenschaften liefern mit den experimentellen Messungen vergleichbare Strömungswege. Dieses Modell enthüllt eine ungleiche Strömungsverteilung über den Lumenumfang. Darüber hinaus zeigt die Untersuchung von dichtgepackten Membranmodulen, dass sich auf der Mantelseite Jetströme entwickeln, die die Strömungsverteilung in allen Lumenkanälen beeinflusst. Zuletzt ergeben Benetzungsexperimente an dichtgepackten Modulen, dass eine Benetzungszeit von über sechs Stunden erforderlich ist, um alle Membranen vollständig zu benetzen, wenn die Membranen nicht vorbenetzt werden.

Diese Arbeit verdeutlicht, dass die Kombination von Magnetresonanztomographie und rechnergestützter Fluiddynamik ein leistungsstarkes Werkzeug darstellt, um das hydrodynamische Verhalten in Mehrkanalmembranen und -modulen in allen Einzelheiten zu entschlüsseln und hilft diese zu optimieren, um ein hocheffizientes und nachhaltiges Verfahren zur Wasseraufbereitung zu entwickeln.

1 Introduction

Without water, we cannot survive. A human being has to consume around 3.2 liters of water a day to stay healthy [Inst2005]. Overall, we use more than 120 liters of water daily, including washing clothes, cooking, and using bathroom facilities [UNIC2018]. However, access to clean water is not granted to billions of people [UNIC2021]. Especially in high water-stressed countries, water reserves are little. Thus, water poverty is one of the most important problems affecting the world's society of the 21st century [Bigg2015; Park2017]. That is why the United Nations declared the 'ensure[d] access to water and sanitation for all' as one of their 17 Sustainable Development Goals [Unit2021].

The availability of clean water benefits the health of people and the economy [Geis2010]. Even though about two-thirds of the Earth's surface is covered with water, 97 % of the available water resources on our 'Blue Planet' are saltwater in the oceans. Therefore, developing and optimizing sustainable water purification technologies, such as desalination processes, is an essential research objective to provide fresh water [Diop2002; Shan2008]. One possible solution for desalinating water is membrane filtration [Geis2010].

A growing field of interest to achieve the current and future challenges regarding water purification is membrane technology with a wide variety of tasks ranging from medical applications such as dialysis, blood oxygenators or controlled drug delivery to fuel cells, water purification, and other industrial applications [Li2008; Bake2012; Scot2013]. To be more precise on membrane processes, in desalination plants, e.g., the combination of ultrafiltration with reverse osmosis is commonly used [Muld2000; Geis2010; Sing2015; Werb2016].

Ultrafiltration is a key technology for pre-treatment in water purification or desalination plants [Shan2008; Geis2010; Sing2015; Werb2016]. Thereby, a typical geometry of membranes is hollow fiber membranes. These membranes can be described as thin tubes made of polymers or ceramics [Bake2012]. Polymeric hollow fiber membranes have been widely used in membrane processes due to their high surface area, excellent flexibility and simple module fabrication [Drio2007; Peng2012]. However, the single bore geometry of hollow fiber membranes leads to increasing concerns about manufactured modules' long-term stability and potting durability [Wang2014b].

Recently, multibore geometries for hollow fiber membranes have promised to overcome the drawbacks of the single bore geometry. They have been realized as polymeric membranes made of polyethersulfone (PES) [Gill2005; Bu-R2007; Spru2013; Wang2014b; Luel2018] and polyvinylidene fluoride (PVDF) [Teoh2011; Wang2012; Wang2013; Wang2014a; Lu2016; Back2019] with high water permeability and high pH tolerances, and as ceramic membranes that are used for harsher environments [Zhu2015a; Zhu2015b; Zhu2017; Chi2017; Atec2019]. Figure 1.1 shows an example of a polymeric PES multibore membrane.

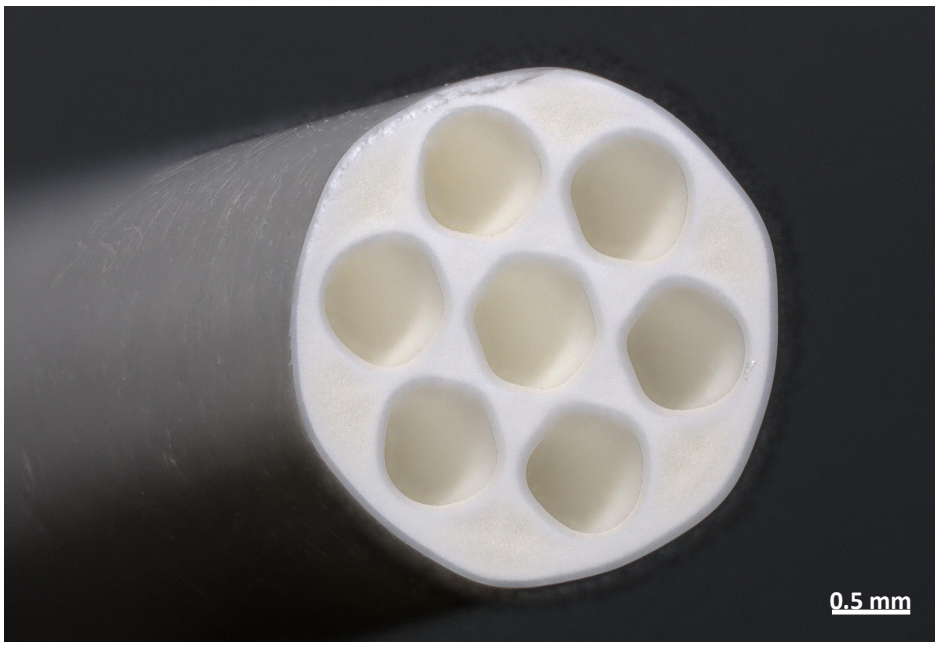

Figure 1.1: Image of a SevenBore multibore membrane from SUEZ Water Technologies & Solutions.

Multibore membranes contain various lumen channels combined in one porous structure resulting in significant robustness improvement [Gill2005; Heij2012; Wang2014b; Wan2017]. Due to their superior tensile properties, multibore membranes have found their way into many applications such as drinking water production and seawater desalination [Gill2005; Bu-R2007; Heij2012], as well as wastewater and surface water filtration (direct contact membrane distillation [Teoh2011; Wang2012; Wang2014b] and vacuum membrane distillation [Wang2013; Wang2014a; Lu2016]).

This wide variety of applications led to several studies regarding optimized geometry [Teoh2011; Peng2011; Heij2012; Bony2012; Wang2014b; Luel2018; Luel2018], membrane material [Luo2014; Luo2015; Lu2016], experimental flow distribution studies [Heib2003; Gill2005; Bu-R2007; Teoh2011; Heij2012; Wan2017; Zhu2017; Zhu2017; Le H2018; Wypy2019; Schu2019; Simk2020], and simulated flow distribution investigations based on computational fluid dynamics (CFD) [Kagr2001; Fred2018; Wypy2019]. However, multibore membranes possess micro- and macro-voids and porosity gradients. Also, multiple channels that influence each other are incorporated in one porous monolithic structure. Consequently, quantifying their porous structures, their related permeation properties such as fundamental understanding of internal pathways, and their hydrodynamic operation conditions in modules is challenging [Zhu2017; Wypy2019; Schu2019].

An innovative approach to extending the measurement capability for evaluating porous multibore membranes is combining magnetic resonance imaging (MRI) with computational fluid dynamics simulations. MRI and flow-MRI are experimental, noninvasive tools to monitor fluid velocities and particle depositions online and in-situ (see Chapter 3: Literature Review). By combining experimental imaging techniques and numerical simulations, the occurring phenomena inside membrane modules can be understood entirely to create the most efficient process for water purification and contribute to the solution of providing unlimited access to clean water some time hopefully.

1.1 Open research questions and thesis goals

Even though polymeric multichannel membranes were the focus of many research studies, the findings in the publications mentioned above raise several research questions and provoke to keep investigating these kinds of membranes.

- First, regarding the **flow distribution inside multibore membrane modules**: Do axial and radial flow distribution exist in such modules, and what are their particular characteristics? How do minor geometric deviations from the ideal membrane position influence the hydrodynamic conditions inside the lumen and outside of multibore membranes? Does such uneven flow distribution affect the membranes' filtration performance?

- Backwashing is a crucial step in each membrane filtration process. Yet, little is known about the **backwashing efficiency in multibore membrane modules**. Does the backwashing flow reach every lumen channel, even in the case of heterogeneous fouling? And what is the case for **modules containing more than one multibore membrane**? Again, does the fluid reach every membrane and even every lumen channel?

- For all membrane filtration modules in general: what is the **role of the permeate outlet position**? Do hydrodynamic conditions change after the location of the outlet?

- Lastly, technical membranes are usually pre-wetted with a pore stabilizer during delivery and before use and must be pre-treated before reaching a steady state. How does displacement of this **initial wetting of multibore membranes** progress during the first phase of permeation until the porous structure of the membranes is thoroughly wetted? Can these wetting times be decreased for starting the filtration task in steady-state quicker?

All these questions lead to the following scope of this thesis.

1.2 Scope of the thesis

This thesis intends to answer the raised questions by deepening the understanding of multibore membrane filtration and hydrodynamic effects in membrane modules. This aim is achieved by looking at multibore membrane modules at different orders of magnitude, as shown in Figure 1.2. In detail, the thesis is structured as follows:

- In **Chapter 2: Fundamentals, Methodology, and Materials**, a brief introduction of membranes and membrane processes is given, including performance-decreasing phenomena and countermeasures. Additionally, the theoretical background on NMR and MRI is summarized, and the experimental methods used in this thesis are explained.
- **Chapter 3: Literature Review** gives a comprehensive overview of the milestones in NMR history and the successful utilization of MRI and velocimetry in membrane filtration processes in the past decades.
- **Chapter 4: Single Multibore Membrane Module Performance** focuses on the module design using CFD simulations. It answers the questions on the influence of small geometric deviations from the ideal membrane position on the hydrodynamic conditions inside a membrane module with one multibore membrane.
- Multibore membranes possess a separation layer inside each lumen channel, a porous support structure, and a layer on the outer membrane wall. These layers have different properties and must be considered when simulating multibore membranes. Therefore, in **Chapter 5: Single Multibore Membrane with Porosity Gradients**, simulations of a single multibore membrane with gradients in porosity and permeability are conducted, revealing the flow distribution in the membrane structure and each channel's contribution to the overall filtration performance.
- After the hydrodynamic behavior of a single membrane is understood, in **Chapter 6: Hydrodynamics in Multi-Multibore Membrane**

Modules, the influence of the membrane module's packing density on the flow field is investigated. Thereby, a closer look is taken at forward permeation and backwashing phenomena in multibore membrane modules and the influence of the permeate outlet position.

- All results above were obtained after the membranes reached a steady state. However, membranes in the delivery state are filled with a pre-wetting agent that first has to be removed. In **Chapter 7: Initial Wetting Patterns in Multibore Membrane Modules**, this early-stage removal of various pre-wetting agents in multibore membrane modules with different packing densities is analyzed.
- Finally, in **Chapter 8: Conclusion and Future Perspectives**, a brief evaluation of the thesis at hand is given.

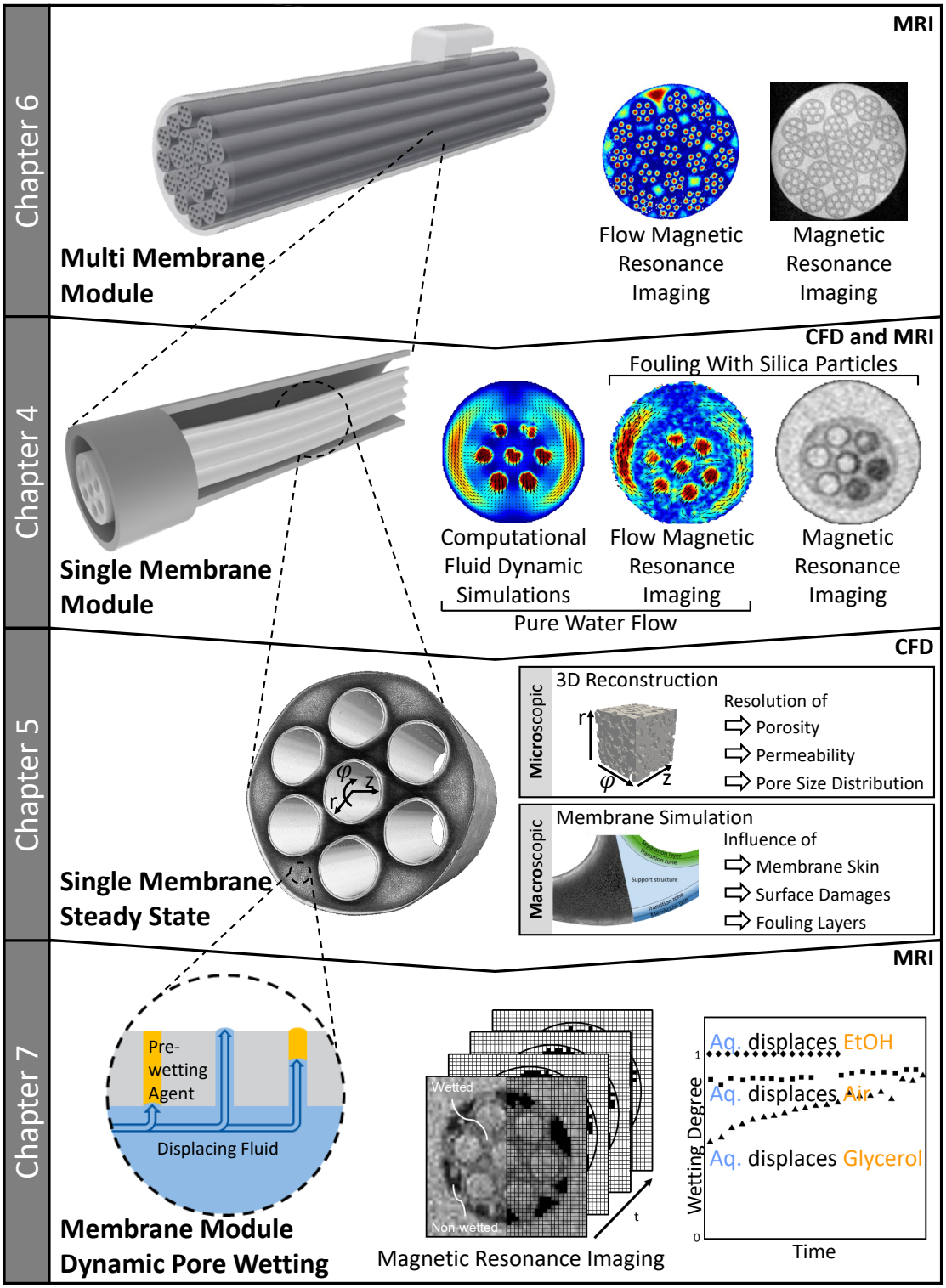

Figure 1.2: Multibore membrane module evaluation at different orders of magnitude.

1.3 Publication information

This thesis' content and results originate from research conducted under the affiliations and positions of the author as a research fellow (Wissenschaftlicher Mitarbeiter) at DWI - Leibniz Institute for Interactive Materials e.V., and as a Ph.D. candidate (Promotionsstudent) at RWTH Aachen University. Both positions are associated with the Chair for Chemical Process Engineering (Prof. Dr.-Ing. Matthias Wessling), AVT.CVT, RWTH Aachen University. The author and his co-authors have previously published or will publish parts of the content presented in this thesis. Text passages and illustrations throughout this thesis are taken from published material under copyright regulations. The results are published under the author's ORCID ID 0000-0001-6571-9102. Relevant publications are mentioned at the beginning of the respective chapters. This thesis also contains data developed and presented in student theses. In particular, the following publications and theses shall be considered:

Published

- [Wypy2019] Wypysek, D., Rall, D., Wiese, M., Neef, T., Koops, G.-H., & Wessling, M., "Shell and lumen side flow and pressure communication during permeation and filtration in a multibore polymer membrane module", *Journal of Membrane Science* 584 (2019) 254-267. DOI: 10.1016/j.memsci.2019.04.070
- [Wypy2021a] Wypysek, D., Kalde, A.M., Pradellok, F., & Wessling, M., "In-situ investigation of wetting patterns in polymeric multibore membranes via magnetic resonance imaging", *Journal of Membrane Science* 622 (2021) 119026. DOI: 10.1016/j.memsci.2020.119026
- [Wypy2021b] Wypysek, D., Rall, D., Neef, T., Jarauta, A., Secanell, M., & Wessling, M., "How does porosity heterogeneity affect the transport properties of multibore filtration membranes?", *Journal of Membrane Science* 636 (2021) 119520. DOI: 10.1016/j.memsci.2021.119520

- Wypysek, D. & Wessling, M., "MRI in membrane filtration processes" in "Magnetic Resonance Microscopy: Instrumentation and Applications in Engineering, Life Science and Energy Research", *John Wiley & Sons, Ltd* (2022). ISBN: 978-3-527-82725-1

In preparation for publication

- Wypysek, D., Wennemaring, S., & Wessling, M., "Flow, Fouling, and Backwashing in Highly-Packed Multibore Membrane Modules", *Journal of Membrane Science* (2022).

Student theses

- Schrader P., "Hydrodynamics, Fouling and Backwashing Behavior in Multi-Heptabore Membrane Modules using Magnetic Resonance Imaging [Bachelor thesis]", *RWTH Aachen University* (2018).
- Neef, T., "Non-idealities in membrane modules - MRI aided CFD study [Bachelor thesis]", *RWTH Aachen University* (2018).
- Neef, T., "Shell and lumen side flow and pressure communication of porous membrane structures [Master thesis]", *RWTH Aachen University* (2019).
- Pradellok, F., "Wetting Behaviour in Heptabore-Membranes via MRI [Master thesis]", *RWTH Aachen University* (2020).

1

2

Fundamentals, Methodology, and Materials

Parts of this chapter have been published as:
Denis Wypysek, Matthias Wessling, "MRI in membrane filtration processes" in "Magnetic Resonance Microscopy: Instrumentation and Applications in Engineering, Life Science and Energy Research", *John Wiley & Sons, Ltd* (2022). ISBN: 978-3-527-82725-1

2.1 Introduction to membranes and membrane processes

Membranes Membranes have emerged as a key technology for molecular separations. They act as a semipermeable or permeable barrier between two phases and are impermeable for at least one component. Membranes can be classified based on their fabrication and material, such as synthetic (under those liquid, solid, organic, inorganic, and others) or biological membranes. Depending on the application, some kinds of membranes are more advantageous than others. In the case of water treatment, e.g., solid synthetic membranes dominate the market as they are, for example, easier to fabricate in a vast amount. These membranes may differ in their inner structure and can be porous, dense, or a dense-porous composite depending on the substances that are to be separated. [Bake2012]

Another possibility to classify membranes is their geometry used in modules for filtration processes. Two main membrane geometries are distinguished: flat sheet membranes and hollow fiber or tubular membranes. Flat

sheet membranes are comparable to a flat and thin permeable, semipermeable, or dense surface. In contrast to flat sheet membranes, hollow fiber membranes have a tubular shape. Further development of hollow fiber membranes has resulted in multibore membranes. In these, one support structure contains several lumen channels. [Bake2012]

Membrane module and membrane processes While membrane materials are improving, the housing and thus the hydrodynamic conditions inside membrane modules are emerging as a bottleneck. Figure 2.1 (a) depicts a schematic drawing of a membrane separation unit. In membrane

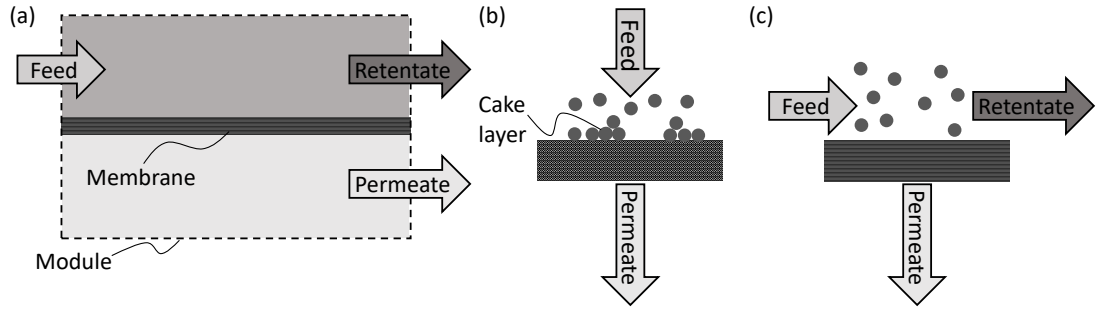

Figure 2.1: (a) Scheme of a basic membrane module, including membrane, feed inlet, permeate outlet, and retentate outlet. (b) Dead-end arrangement. (c) Cross-flow flow arrangement.

processes, the membrane module combines the membrane and the housing with all connections for inlet and outlet streams. The inlet or feed stream is the educt that the process shall treat. The membrane, which acts as a barrier, separates the feed into two fractions: the permeate passes the membrane and the retentate is held back. The product of a membrane process can either be the retentate or the permeate. Hence, processes where only the permeate is required can be conducted without a retentate volume flow. This flow arrangement is called dead-end and is visualized in Figure 2.1 (b). If permeate and retentate outlets are open, the flow arrangement is called cross-flow (Figure 2.1 (c)). [Bake2012]

Inside membrane modules, the necessary driving force for the process can be applied in different ways. In general, these driving forces are either a gradient of pressure (e.g. reverse osmosis, micro-/ultrafiltration), concen-

tration (e.g. dialysis), temperature (e.g. membrane distillation), or electrical potential (e.g. electrodialysis). The performance of membrane processes is determined by the transport phenomena inside and around the membrane. One important parameter is the membrane flux. The flux is defined as the permeate flow rate per membrane unit area. It can be calculated for each feed component individually or the entire mixture. The flux decreases with increasing transport resistances and decreasing driving forces. Equation 2.1 states this general relationship. [Bake2012]

$$\text{Flux} = \frac{\text{Driving Force}}{\text{Transport Resistance}}. \tag{2.1}$$

The reciprocal value of the membrane transport resistance is defined as the membrane's permeability. For water and wastewater treatment applications, pressure-driven filtration processes dominate the market. The driving force for pressure-driven processes is the pressure difference between the feed/retentate side and the permeate side, the so-called transmembrane pressure (TMP). It can be calculated from the pressures p of feed, retentate, and permeate using Equation 2.2:

$$\Delta p = \text{TMP} = \frac{p_{\text{Feed}} + p_{\text{Retentate}}}{2} - p_{\text{Permeate}}. \tag{2.2}$$

Pressure-driven filtration processes can be further classified depending on the separated particle sizes and applied pressure gradients.

Performance-decreasing phenomena in membrane processes and countermeasures All membrane processes suffer from a decrease in performance (namely the flux) during operation. Besides the unavoidable resistance of the membrane itself and pressure losses on the feed and the permeate side, as well as in the porous structure, several resistances decrease the performance of a membrane filtration over time, namely (a) concentration polarization on the feed and permeate side, (b) fouling, scaling and pore blocking, and (c) temperature polarization on the feed and permeate side. According to Song [Song1998] the total resistance can be

calculated using the resistance-in-series model, Equation 2.3:

$$R_{\text{Total}} = R_{\text{Membrane}} + R_{\text{Adsorption}} + R_{\text{Pore}} + R_{\text{Layer}}, \tag{2.3}$$

where R_{Pore} is the resistance of blocked pores and R_{Layer} the resistance of fouling and/or scaling layers (e.g. Figure 2.1 (b)). In pressure-driven membrane processes, concentration polarization and layer formation are the main reasons for a decline in performance [Çulf2011].

Figure 2.2 (a) illustrates the phenomenon of concentration polarization. Due to the semipermeable character of the membrane, one substance passes through the membrane preferentially. Therefore, the concentration of the separated substance increases above the bulk concentration at the membrane, causing a concentration gradient. The concentration gradient results in a diffusive back-flow from the membrane toward the bulk phase. Since the diffusive flow away from the membrane is significantly slower than the opposing convective flow, the separated substance accumulates at the membrane surface. The increased chemical potential counteracts the pressure difference. The result is a lower permeate flux with a decreasing purity [Scot2013]. Concentration polarization is the main reason for a buildup of fouling or scaling layers. While fouling describes a layer of undesirably accumulated retained particles in and at the membrane, scaling describes the formation of a crystalline layer on the membrane surface. [Bake2012]

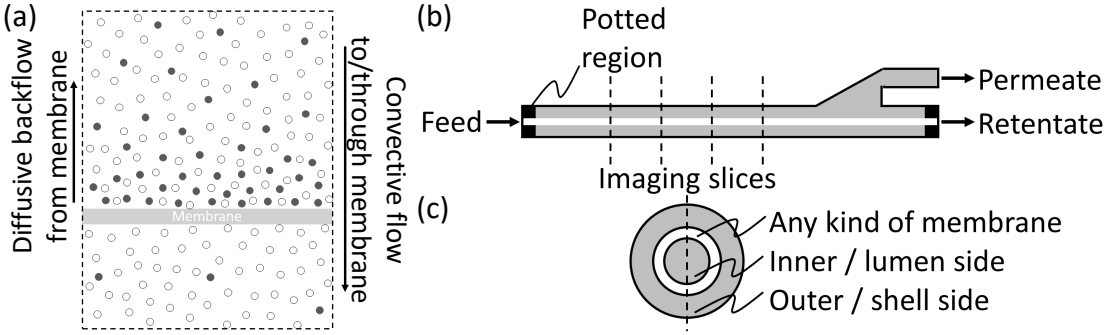

Figure 2.2: (a) Illustration of concentration polarization. (b) Membrane module side view. (c) Cross-sectional view of an arbitrary membrane module in cross-flow, inside-out mode.

To increase the process performance, concentration polarization has to be reduced [Bake2012]. The reduction of concentration polarization and fouling can be achieved by changing the hydrodynamic conditions inside the membrane module. One measure is the use of cross-flow filtration instead of dead-end filtration, as shown in Figures 2.1 (b) and (c) [Bake2012]. Other measures focus on increasing the vorticity within a membrane module, such as the generation of secondary flows, vibrating or rotating membranes that induce higher shear rates, inserts like spacers, or geometrical changes inside the membrane to distract the flow [Jaff2012]. These measures are often accompanied by a higher energy demand due to more pumping capacity required, which shows that a compromise between higher energy consumption and better process performance has to be found. Another aspect of this trade-off is the need for cleaning or replacing the membrane if the cake layer becomes too thick, and a critical TMP is reached. In industrial applications, membranes are cleaned by permeate backwashing. This means the flow over the membrane is reversed by increasing the pressure on the permeate side, and the cake layer is released from the membrane. Subsequent washing in cross-flow mode removes the loosened particles from the membrane module. [Bake2012]

2.2 Nuclear magnetic resonance and magnetic resonance imaging

The overall performance of membrane processes is easily monitored by measuring volume flows or pressures of feed, retentate, and permeate streams. These parameters do not leave much room for improvement. However, to understand the phenomena occurring during filtration, it is necessary to reveal the hydrodynamics inside the membrane module. A powerful technique for visualizing internal structures and flow dynamics noninvasively and in-situ during operation is Magnetic resonance imaging (MRI). MRI utilizes the phenomenon of nuclear magnetic resonance (NMR) and enables, e.g., the observation of flow profiles and polarization layers [Yao1995a], the observation of layer built-up and particle deposition [Wypy2019], or the analysis of systems that prevent concentration polarization and fouling [Wies2019]. When all these phenomena mentioned above are entirely understood, membrane processes, especially membrane modules, can be improved to counteract fluid resistances efficiently. These parameters obtained from experimental data also help to develop, validate, or improve numerical models.

This section gives a brief overview of NMR and MRI, explaining the elementary physics of nuclei and spins, followed by an overview on the correlation of spins and magnetism, spin precession, and the stimulation and relaxation of spins. At last, the fundamental building blocks of MRI are explained, and the methodology of flow imaging is elucidated.

2.2.1 Basics of nuclear magnetic resonance

Elementary physics of nuclei and spins

Atoms consist of a nucleus of protons and neutrons with surrounding electrons. Whereas important physical properties of an atomic nucleus like mass, electric charge, and magnetism are easy to catch, the (nuclear) spin is an unfamiliar measure. However, it represents the most important property in NMR. [Levi2009]

In quantum mechanics, a spin can be considered a rotation of the nucleus around its center of gravity. Analogue to a rotating object the spin results in a total rotational angular momentum L_{tot} which is expressed by Equation 2.4 [Binn2013]:

$$L_{tot} = [J(J+1)]^{1/2} \cdot \hbar \tag{2.4}$$

Here, J is a set of stable rotation states with integer values (J = 0,1,2...) that leads to only discrete values of the total angular momentum, and $\hbar$ is Planck's constant. The resulting rotational energy of a rigid molecule is defined by Equation 2.5 [Levi2009]:

$$E_J = BJ(J+1), \tag{2.5}$$

where parameter B is known as the molecule's rotational constant, with increasing values for decreasing molecule weights. Although the spin is a form of angular momentum, it is not generated by a rotation of the particle. Still, it can be understood as an intrinsic property of the particle itself. Nevertheless, Equations 2.4 and 2.5 stay valid for the determination of the angular momentum and rotational energy of a spin. To differentiate between spin angular momentum and rotational angular momentum, the spin number I is used instead of J.

Each elementary particle possesses a particular value for the spin number I, which is independent of external influences [Levi2009]. One relevant difference to the parameter J is that I can also take on half-integer values. Except for the ^{1}H-nucleus, every nucleus consists of more than one elementary particle. Therefore, the total spin angular momentum S_{tot} needs to be calculated, which is expressed by Equation 2.6, where I_3 describes the overall spin number. I_3 can be derived from the combination rule 2.7 with

the individual spin numbers I_1 and I_2.

$$S_{tot} = [I_3(I_3+1)]^{1/2} \cdot \hbar \tag{2.6}$$

$$I_3 = \begin{cases} |I_1 - I_2| \\ |I_1 - I_2| + 1 \\ \vdots \\ |I_1 + I_2| \end{cases} \tag{2.7}$$

The principles in this section focus on the ^{1}H nucleus as it is contained in all organic matter, has the highest natural abundance and has the largest gyromagnetic ratio γ. The spin numbers I_1 and I_2 for hydrogen reduces to $-\frac{1}{2}$ and $\frac{1}{2}$, and thus, to 2 possible (energy) states.

Nuclei and magnetism

^{1}H possesses a spin as the number of elementary particles in its nuclei is uneven. A simple model of a magnet can be taken into account to describe the magnetic characteristics of a spin. Analogously to conventional magnets, spins have a north and a south pole and posses a certain direction as shown in Figure 2.3 [Siem2003]. ´

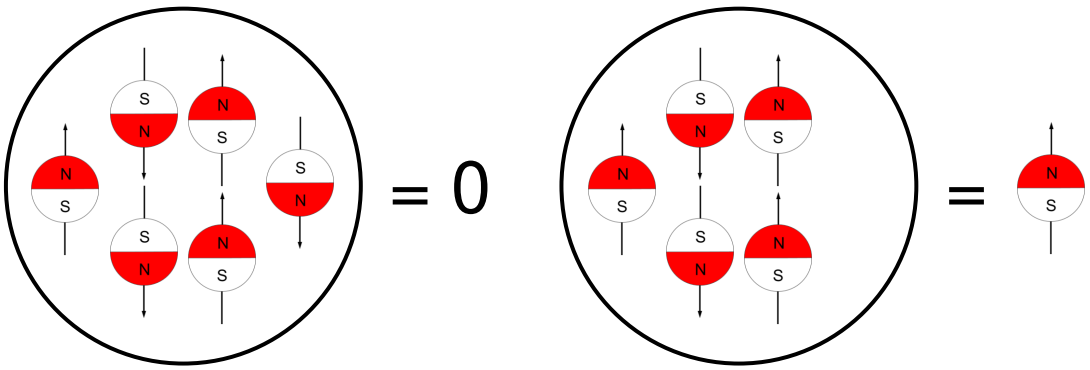

Figure 2.3: Schematic illustration of spins with its north pole N, south pole S, and its direction. Addition of spins inside a nucleus according to [Siem2003].

The effect of spins in different directions adds up like vectors in mathematics. An important rule in quantum mechanics prescribes that two identical particles inside one nucleus cannot be in the same state; their

orientations have to be antiparallel. Therefore, nuclei with even numbers of elementary particles cannot possess spins since the vectors add up to zero. This rule is known as the Pauli principle and is graphically explained in Figure 2.3. [Stap2006; Levi2009]

If the necessary condition for spin possessing nuclei is fulfilled, the vectors of all nuclei inside one spatial element add up in the same manner as spins inside one single nucleus. Spin vectors inside a volume element are completely disorientated when no magnetic field is applied to them. Therefore, their overall effect adds up to zero, and the ensemble seems non-magnetic. By applying an external magnetic field, the spins inside the volume element orientate themselves on the magnetic field lines. Thereby, the spin-directions are either parallel or antiparallel to the magnetic field lines, as shown in Figure 2.4.

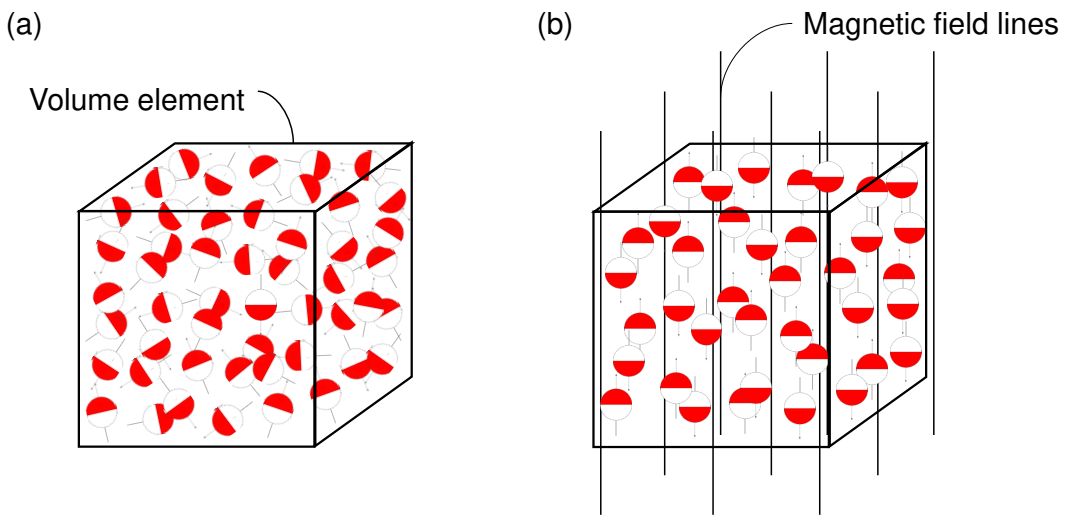

Figure 2.4: Spins inside a volume element: (a) without a magnetic field (b) with a magnetic field adapted from [Siem2003].

The quantity of parallel and antiparallel spins is not equal. If so, the spins would add up to zero, and the matter inside the volume element would be non-magnetic. In reality, a small surplus of parallel aligned spins exists. These parallel spins populate a lower energy level which is thermodynamic more favorable. The ratio of lower-energy-level and higher-energy-level

spins can be described by the Boltzmann distribution in Equation 2.8,

$$\frac{n_{-1/2}}{n_{+1/2}} = exp(-\frac{\gamma B_0 \hbar}{k_B T}), \tag{2.8}$$

with B_0 as the magnetic field strength, k_B as the Boltzmann coefficient, and T_0 as the temperature. The Boltzmann distributions show that more protons populate the lower energy level with a decreasing temperature or increasing magnetic field strength. Also, the higher the magnetic field strength, the higher the magnetic energy E_{mag} stated in Equation 2.9,

$$E_{mag} = \gamma B_0 \hbar, \tag{2.9}$$

which leads to a larger gap between high and low energy levels. The above-mentioned higher amount of parallel spins result in a slight magnetization of the considered volume element [Hore2015]. The magnetization points in the direction of the magnetic field (longitudinal magnetization) and describes the strength of the obtained NMR signal. The relation between the equilibrium magnetization M_0 and the magnetic field strength B_0 is described by the Curie law [Nish1996; Stap2006] in Equation 2.10:

$$M_0 = N\frac{\gamma^2 \hbar^2 I(I+1)}{3k_B T} B_0 \tag{2.10}$$

with N as the number of nuclei per volume element.

Spin precession

The direction of the spin angular momentum can be defined as spin polarization axis. As soon as a magnetic field is applied, the spin polarization axis of individual nuclei starts to precess around the vector of the magnetic field strength as illustrated in Figure 2.5. Thereby, the angle between the spin polarization axis and magnetic field strength stays constant and depends on initial spin polarization. The frequency ω_0 of the described pre-

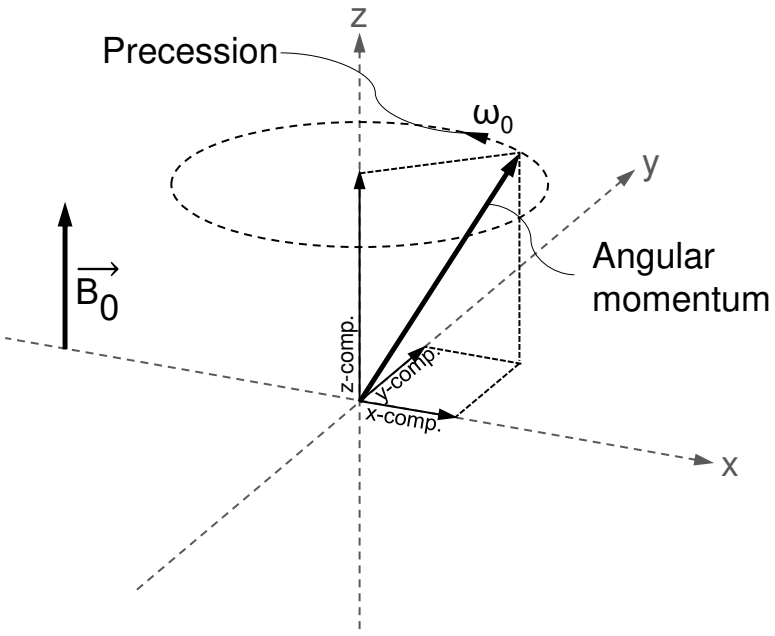

Figure 2.5: Larmor precession of the spin polarization axis adapted from [Dale2015].

cession is known as Larmor frequency. It can be expressed by the product of the gyromagnetic ratio γ and the magnetic field strength $\vec{B}_0$ as shown in the Larmor equation (Equation 2.11).

$$\omega_0 = \gamma \vec{B}_0 \tag{2.11}$$

A negative Larmor frequency accounts for a clockwise precession around the magnetic field lines [Levi2009; Dale2015; McRo2017].

Stimulation and relaxation of spins

By applying a magnetic field $\vec{B}_0$ to an ensemble of spins, they orientate along the magnetic field lines. Thereby, the magnetic moment $\mu = \gamma S_{tot}$ of the nuclei is built up. In the absence of the exciting magnetic field, the overall magnetic moment approximates to zero due to overlapping effects of individual magnetic moments of the nuclei. This approximation to a total magnetic moment of zero is known as T_1- and T_2-relaxation. [Stap2006] Here, T_1- and T_2-relaxation describe different directions of relaxation in a Cartesian coordinate system. With the direction of the magnetic field de-

fined as z-axis (see Figure 2.5), T_1-relaxation, or longitudinal relaxation, describes the orientation of spins in z-direction (see Figure 2.6 (a)). With a magnetic field acting on the spins, the spins start to move around the magnetic field lines with Larmor precession. Two equilibrium states can be observed concerning the magnetization of a sample - after turning on and after turning off the magnetic field. The magnetization after the magnetic field was turned on or off is calculated with Equation 2.12 or 2.13, respectively. [Levi2009; Hore2015].

$$M_z(t) = M_0 \cdot \Big(1 - exp\Big(-\frac{t - t_{on}}{T_1}\Big)\Big) \tag{2.12}$$

$$M_z(t) = M_0 \cdot exp\Big(-\frac{t - t_{off}}{T_1}\Big) \tag{2.13}$$

In Equations 2.12 and 2.13, $M_z(t)$ is the magnetization in z-direction at time t. The differences of time express the duration of a switched on or switched off magnetic field.

The relaxation behavior for the magnetization perpendicular (in x-y-plane) to the magnetic field, so-called transversal magnetization, is known as T_2-relaxation (see Figures 2.6 (c) and (d)). Due to the rotational movement of the Larmor precession, the magnetization in the x-y-plane shows an oscillating behavior. Equations 2.14 and 2.15 are used to calculate the magnetization along the x- and y-axis, respectively. [Levi2009; McRo2017]

$$M_x(t) = -M_0 cos(\omega_0 t) \cdot exp\Big(-\frac{t}{T_2}\Big) \tag{2.14}$$

$$M_y(t) = M_0 sin(\omega_0 t) \cdot exp\Big(-\frac{t}{T_2}\Big) \tag{2.15}$$

Since all spins initially point almost in the same direction, a strong magnetization is present. This magnetization decreases with time caused by the spins distributing isotropically within the x-y-plane (see Figures 2.6 (c) and (d)).

Coils detect the magnetic field created by the magnetization of the sample. An oscillating voltage is induced in the receiver coil caused by the precession of the spins in the transversal plane. The resulting current is called free-induction decay (FID) or NMR-signal. Measured signals are

proportional to the oscillating magnetization described in Equations 2.14 and 2.15. By Fourier transformation, an NMR spectrum is generated from the NMR signal. [Levi2009]

2.2.2 Magnetic resonance imaging

To generate an image via MRI, several different pulse sequences can be used. A pulse sequence fulfills the task to rotate the magnetization of a sample to different positions to create a measurable FID [Horo2012]. An often used pulse sequence is the spin-echo sequence described in the first part of this section. In addition, the importance of magnetic field gradients for MRI is explained. Subsequently, phase encoding, frequency encoding, and slice selection are presented, which can be seen as the building blocks of MRI. Lastly, the methodology of velocity encoding is elucidated.

Spin-echo sequence

The spin-echo sequence rotates the magnetization of the sample into different positions. To achieve a rotation of the magnetization, radiofrequency pulses (rf pulses) are used. These pulses represent the magnetic field that rotates the spins out of their equilibrium orientation in a constant magnetic field. Figure 2.6 illustrates magnetization vectors at five different stages during the spin-echo sequence.

Inside the coordinate systems, the vectors rotate with the Larmor frequency ω_0 around the z-axis. The system is initially in an equilibrium state with the magnetic field parallel to the z-axis (Figure 2.6 (a)). A $90°$ pulse flips the overall magnetization vector by $90°$ into the x-y-plane (Figure 2.6 (b)). Dephasing caused by small differences in rotation velocity of spins leads to a decay in the NMR signal. A following $180°$ pulse rotates each magnetization vector by $180°$. Immediately after the $180°$ pulse, individual spins are not in phase (Figure 2.6 (c)). However, since faster rotating spins catch up with slower ones, the spins rephase (Figure 2.6 (d)). Finally, a spin-echo is generated due to complete recovery of the net magnetization in the x-y-plane

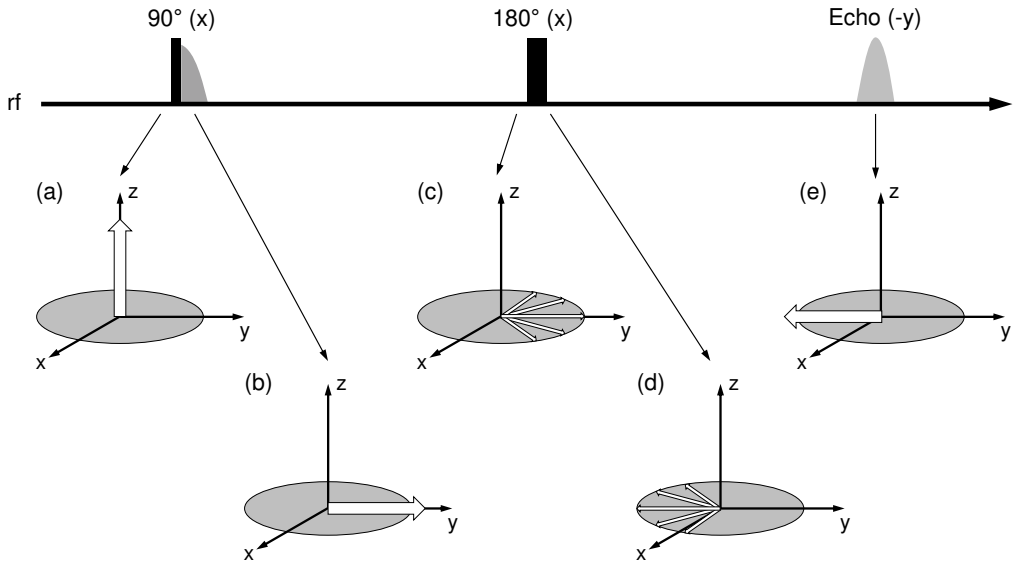

Figure 2.6: Illustration of the spin-echo sequence according to [Stap2006]. Top: FID (grey) responds to 90° pulse and 180° pulse (black), (a) to (e): Magnetization vectors at five stages during spin-echo sequence.

(Figure 2.6 (e)). The regenerated net magnetization is converted to an NMR signal by the receiver coils of the NMR system. [Stap2006; Levi2009]

Magnetic field gradients and signal equation

As already shown by Equation 2.11 the Larmor frequency is proportional to the magnetic field strength. Therefore, applied spatial gradients of the magnetic field strength result in different frequencies throughout the sample. The phenomenon of changing frequency depending on the magnetic field is a major principle of MRI. As a result, Equation 2.11 has to be modified to consider the gradient of a magnetic field. The modified correlation of the Larmor equation can be taken from Equation 2.16. [Stap2006]

$$\omega(\vec{r}) = \gamma|\vec{B}(\vec{r})| = \gamma(|\vec{B}_0| + \vec{g} \cdot \vec{r}) \tag{2.16}$$

In Equation 2.16, the vector $\vec{g}$ accounts for the gradient vector that displays the proportionality of the resonance frequency and the position vector $\vec{r}$. Consequently, with this modification, a spin-density distribution $\rho(r)$ can correlate the amount of spins to their spatial position. The shape of the

investigated object is then Fourier transformed from the reciprocal-space (k-space) to the direct-space (r-space) using the density distribution. When the reference value for an average field ($\omega_0 = \gamma|B_0|$) is taken into account, the frequency difference to a position $\vec{r} = 0$ can be calculated according to Equation 2.17.

$$\omega(\vec{r}) - \omega_0 = \gamma\vec{g} \cdot \vec{r} \tag{2.17}$$

In NMR, the gradient $\vec{g}$ is applied only over a certain time interval δ. When the gradient is switched off, the difference in frequencies leads to an accumulated phase shift. The resulting phase shift ϕ of spins at position $\vec{r}$ is defined by Equation 2.18 [Levi2009].

$$\phi(\vec{r}) = \gamma\vec{g} \cdot \vec{r}\delta \tag{2.18}$$

As the signal created by the precessing magnetization is a complex number, the phase shift created by this gradient pulse leads to the NMR signal. By multiplying the undisturbed NMR signal with the phase factor $exp[i\phi(\vec{r})]$, the NMR signal is determined. Examining the phase factor reveals that it is a complex number of the form $e^{i\phi}$ in which ϕ is the phase shift from Equation 2.18. To calculate the total signal S arising from all individual spins over the sample with a spin density distribution $\rho(\vec{r})$, all phase factors have to be integrated over the entire volume (see Equation 2.19) [Stap2006],

$$\begin{aligned} S(\vec{k}) &= \int \rho(\vec{r}) exp[i\phi(\vec{r})] d\vec{r} \\ &= \int \rho(\vec{r}) exp[i\gamma\vec{g} \cdot \vec{r}\delta] d\vec{r} \\ &= \int \rho(\vec{r}) exp(i2\pi\vec{k} \cdot \vec{r}) d\vec{r}, \end{aligned} \tag{2.19}$$

where the variable $k = \frac{1}{2\pi}\gamma\vec{g}\delta$ is introduced in order to generate a Fourier conjugate variable to $\vec{r}$. An inverse Fourier transformation is applied to Equation 2.19 what leads to the correlation shown in Equation 2.20 for $\rho(\vec{r})$,

to shape the measured object. [Stap2006]

$$\rho(\vec{r}) = \int S(\vec{k}) \cdot exp[-i2\pi\vec{k} \cdot \vec{r}]d\vec{k} \tag{2.20}$$

Solving Equation 2.20 using the Fast Fourier Transformation (FFT) finally leads to the object's shape.

Phase and frequency encoding, slice selection

A single **phase encoding (PE)** gradient generates an image in one spatial direction. Therefore, at least two gradients in different directions are necessary to obtain an image of the investigated sample (use of Equation 2.20 for two dimensions). In MRI, the spatial information about the spin density distribution, and thus the corresponding signal $S(\vec{k})$, is stored in a k-space. The information from the k-space is then Fourier transformed into the r-space, which represents the generated image. [Dale2015] For each coordinate, a range of different values for k_i between $-k_{i,max}$ and $+k_{i,max}$ are measured in n equidistant steps (see Equation 2.21). Thereby, the highest signal is usually measured in the middle at k_0. Following this heuristic along with different coordinates, a k-space develops.

For a known size of an object, the choice of a maximum gradient strength $\vec{g}_{max}$ and duration δ can be optimized. Inside the r-space, the imaged area depicted by a set of gradients is called field of view (FoV). The gradients which account for the two dimensions of the FoV are the read gradient and the phase gradient. The FoV can be determined with Equation 2.21. Practically speaking, if the FoV is adjusted too small and spins are outside the measured area, the imaged object is not displayed correctly, and aliasing (backfolding) of the border areas happens.

$$FoV = \frac{n-1}{2}\frac{2\pi}{\gamma\vec{g}_{max}\delta} \tag{2.21}$$

Significant advantages of PE are the robustness of the method and the signal generation in a homogeneous magnetic field. Therefore, the signal contains a complete set of information for each voxel. This means that be-

sides the spin density and its position, also the chemical composition in the respective voxel can be analyzed, showing the great potential in chemical engineering. [Glad1999; Glad2003; Brit2017; Glad2017] However, the major disadvantage is the extreme measuring times. Since each voxel has to be measured separately, e.g., MRI of an 3D object sampled into 64^3 pixels can take up to three days [Stap2006].

Frequency encoding (FE) is an efficient tool for the reduction of measurement time. During frequency encoding and in contrast to PE, the signal is generated with an active field gradient. The active field gradient is referred to as read gradient and Equations 2.18, 2.19, and 2.20 are still valid. In Figure 2.7, the difference of PE (a) and FE (b) becomes clear. In phase encoding, the time interval δ stays constant, and the gradient strength is controlled. Contrary to PE, the gradient strength stays constant in frequency encoding, and the gradient application time t varies.

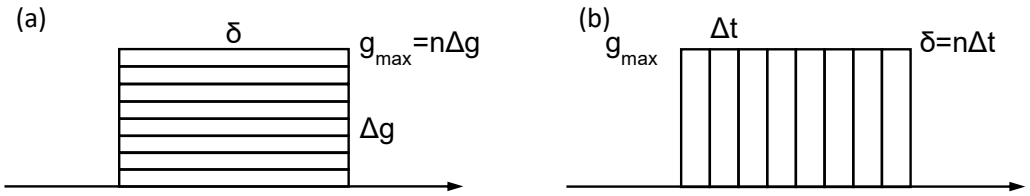

Figure 2.7: Demonstration of the difference of: (a) phase encoding (b) and frequency encoding according to [Stap2006].

With this approach, a signal acquisition of several milliseconds can be achieved. However, one disadvantage is the loss of information, e.g., chemical composition.

To generate an image, the signal intensities of volume elements (voxels) are determined. As PE and FE account for two measured dimensions, integration of the spins in the third dimension leads to averaging effects. To overcome this problem, a **slice selection** gradient is applied. Thereby, the signal is averaged over a set thickness of the third dimension. In contrast to the read and phase gradients, it is possible to set a spatial measurement range. The slice thickness is implemented by changing the frequency of the rf pulse. This can be realized because of the local position dependency in the Larmor frequency due to the magnetic field gradient $\vec{g}$ in Equation 2.16.

An alternative approach to changing the slice thickness is varying the gradient strength. While a steep gradient generates a thin slice thickness, a shallower gradient accounts for a thicker slice. [Stap2006]

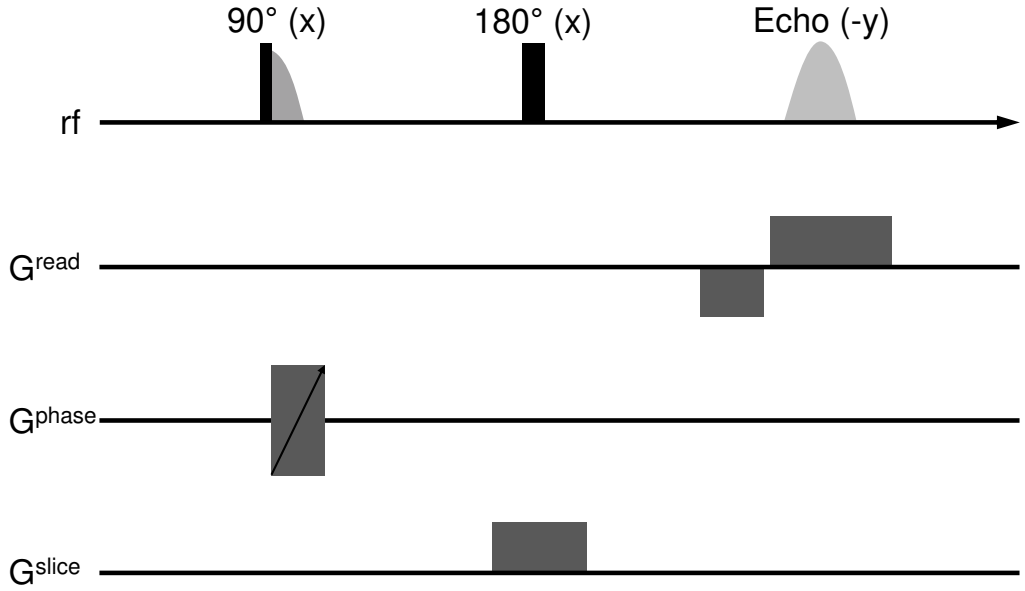

Figure 2.8: Graphic example of a three-dimensional pulse sequence with phase encoding, frequency encoding and slice selection in three orthogonal directions.

Figure 2.8 depicts a typical imaging sequence in MRI. The pulse sequence is constructed from the three building blocks of MRI. It consists of a phase encoding gradient, a frequency encoding gradient and the slice selection gradient. All three gradients are applied orthogonal to each other. An important detail of the read gradient is that it is preceded by a negative value. This negative value is necessary for the complete mapping of the k-space. In the case of a read gradient starting at zero, the gradient would only be applied to positive values of k. In this case, not the complete k-space would be monitored. [Stap2006]

Velocity encoding

Measuring flow velocities inside opaque systems is the main interest in membrane science when using MRI. For this purpose, velocity encoding gradients are introduced that encode a phase proportional to the spin displacement [Mark2005]. Therefore, the phase shift in Equation 2.18 is sup-

plemented with a time-dependent Larmor frequency $\vec{\omega}(t)$ and position of the spins $\vec{r}(t)$:

$$\Phi(\vec{r}, t) = \int_0^t \vec{\omega}(t) \cdot \vec{r}(t) dt = \int_0^t \gamma \vec{g}(t) \cdot \vec{r}(t) dt \tag{2.22}$$

Applying a Taylor series to the position of a spin ($\vec{r}(t) = \vec{r_0} + \vec{v_0}t + \frac{1}{2}\vec{a_0}t^2 + ...$) leads to

$$\begin{aligned}
\Phi(\vec{r}, t) &= \gamma \int_0^t \vec{g}(t)[\vec{r_0} + \vec{v_0}t + \frac{1}{2}\vec{a_0}t^2 + ...]dt && (2.23)\\
&= \gamma \left(\vec{r_0} \int_0^t \vec{g}(t)dt + \vec{v_0} \int_0^t \vec{g}(t)tdt + \frac{1}{2}\vec{a_0} \int_0^t \vec{g}(t)t^2 dt + ... \right) && (2.24)\\
&= \gamma \left(\vec{r_0}\vec{m_0} + \vec{v_0}\vec{m_1} + \frac{1}{2}\vec{a_0}\vec{m_2} \right) && (2.25)
\end{aligned}$$

as terms of higher order can be neglected in MRI. In Equation 2.25, $\vec{m_0}$, $\vec{m_1}$, and $\vec{m_2}$ are known as the zeroth, first, and second moment, respectively, and are crucial parameters for designing pulse sequences. For velocity encoding, while the zeroth moment encodes the spin density position, the first moment encodes the velocity distribution and the second moment encodes the acceleration of spins. To investigate flow fields, position and velocity have to be encoded simultaneously. In analogy with Equation 2.18, a phase shift resulting from bipolar velocity gradients determines the average velocity $\vec{v}$ of each pixel with Δ as the encoding time, and $\vec{q}$ (equal to $\vec{k}$ and $-\vec{k}$) as the wave vector:

$$\Phi(\vec{v}) = 2\pi \vec{q} \cdot \vec{v} \cdot \Delta \tag{2.26}$$

In practice, to avoid an extra contribution of the phase shift, two images, one with and one without velocity encoding gradient, are acquired and subtracted from each other to gain velocity fields.

Comparing with the FoV in Equation 2.21, the maximum flow velocity has to stay within the bounds of 2π within the field of flow (FoF), otherwise

aliasing effects occur. The FoF can be calculated with Equation 2.27:

$$\mathrm{FoF} = \frac{n-1}{n}\frac{2\pi}{\gamma g_{max}\delta\Delta} \tag{2.27}$$

2.2.3 Magnetic resonance imaging in this thesis and data processing

MRI is a noninvasive tool to visualize and evaluate the hydrodynamic conditions inside the investigated membrane modules. All MRI measurements in this thesis are carried out on a Magritek low-field NMR tomography system combined with a KEA^2 low-frequency spectrometer. The tomograph operates with a field strength of 0.56 T at a Larmor frequency of 23.8 MHz. Within the 60 mm inner diameter imaging probe, the membrane modules are placed horizontally. Measurements in the tomograph are carried out in the x-y-plane, being the cross section of the membrane modules. To control the hardware, Magritek's software Prospa is used. Since MRI parameters depend on the experimental procedure and the membrane module, measurement settings are listed in the methods part in the corresponding chapters. For each setting, preliminary tube flow measurements validated the set parameters. All obtained images have a signal-to-noise ratio (SNR) of larger than ten and are post-processed using self-written Matlab scripts to derive corresponding images of the axial and radial velocities.

Signal acquisition is realized by the 2D spin-echo pulse sequence with velocity encoding shown in Figure 2.9 and adapted from previous studies [Perl2015; Luel2018; Wies2018a; Wies2018b; Wies2019].

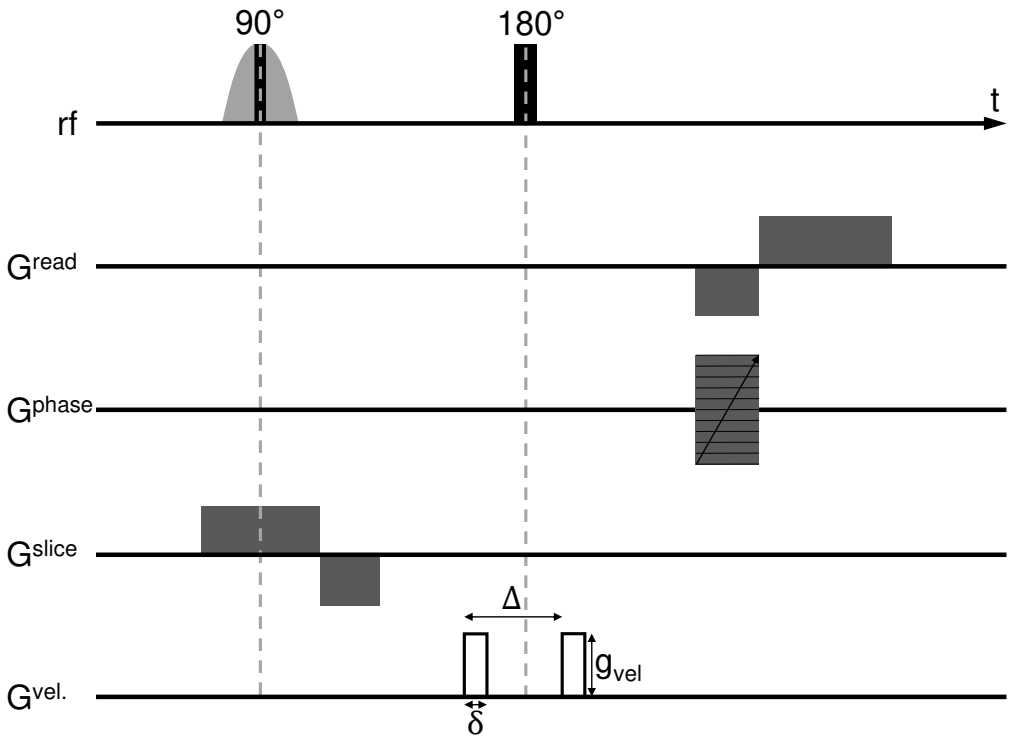

Figure 2.9: Spin-echo pulse sequence used in this thesis.

2.3 Computational fluid dynamics

Computational fluid dynamics is a powerful tool to predict hydrodynamic behavior. In this thesis, CFD simulations are used to understand fluid flows in multibore membranes and membrane modules and are compared to flow-MRI measurements. In the following, the underlying governing equations are explained.

2.3.1 Governing equations

The mass balance equation for steady-state, incompressible, single-phase fluid flow equals Equation 2.28

$$\rho \boldsymbol{\nabla} \cdot \mathbf{u} = 0 \tag{2.28}$$

where ρ is the density, and $\mathbf{u}$ is the velocity. [Batc2010]

The momentum balance equation for steady-state, incompressible, single-phase fluid flow equals Equation 2.29, with the momentum density $\rho\mathbf{u}$ and the velocity $\mathbf{u}$. The momentum balance equation for fluids is also known as the Navier-Stokes equation. [Batc2010]

$$[\boldsymbol{\nabla} \cdot \rho \mathbf{u}\,\mathbf{u}] = \boldsymbol{\nabla} \cdot \underbrace{[-p\hat{\mathbf{I}} + \hat{\boldsymbol{\sigma}}]}_{\boldsymbol{\Pi}} + \rho \mathbf{f} \tag{2.29}$$

The term $[\boldsymbol{\nabla}\cdot\rho\mathbf{u}\mathbf{u}]$ represents inertial forces and disappears for creeping flow (Re$\ll$1). Without considering gravity, the external force vector $\rho\mathbf{f}$ equals the structure resistance $\frac{\mu}{\kappa}\mathbf{u}$ for laminar flow in porous media (with the dynamic viscosity μ and the intrinsic permeability κ). The tensor $\boldsymbol{\Pi}$ is the stress tensor, which is composed of the hydrostatic pressure $p\hat{\mathbf{I}}$ and the viscous tensor $\hat{\boldsymbol{\sigma}}$. For Stokes flow, the viscous tensor can be written as

$$\hat{\boldsymbol{\sigma}} = 2\mu \boldsymbol{\nabla}_s \mathbf{u} \quad \text{with} \quad \boldsymbol{\nabla}_s \mathbf{u} = \frac{1}{2}(\boldsymbol{\nabla}\mathbf{u} + \boldsymbol{\nabla}\mathbf{u}^T) \tag{2.30}$$

Simplifying Equation 2.29 leads to the Brinkman equation (Equation 2.31).

$$-2\mu\nabla\cdot\nabla_{\mathbf{s}}\mathbf{u}-\frac{\mu}{\kappa}\mathbf{u}+\nabla p=\mathbf{0} \tag{2.31}$$

The first term is neglectable for slow velocities $\mathbf{u}$ (creeping flow), and the Brinkman equation simplifies into Darcy's law in Equation 2.32.

$$\mathbf{u}=-\frac{\kappa}{\mu}\nabla p \tag{2.32}$$

2.3.2 Simulation parameters

Detailed information on the mesh, boundary conditions, and other simulation parameters can be found in the methods part in *Chapter 4: Single Multibore Membrane Module Performance* and *Chapter 5: Single Multibore Membrane with Porosity Gradients* for each simulation study, respectively. In addition, the individual meshes are optimized for each geometry as part of a mesh independence study.

2.4 Multibore membranes

All membranes investigated in this thesis are commercially available PES inside-out ultrafiltration SevenBore™ membranes supplied by SUEZ Water Technologies & Solutions [SUEZ] with a nominal pore size of approx. 40 nm. The membrane cross section contains a central bore, surrounded by six symmetrically arranged bores close to the outer fiber diameter, which is approx. 3.9 ± 0.1 mm, depending on the batch. Each bore has a diameter of about 0.9 mm. To reveal the membrane pore structure, field emission scanning electron microscope (FeSEM) images of the membrane's cross section are taken by a Hitachi High-Technologies Corporation Model S-4800, Japan. To maintain the pore structure, the membrane is broken in liquid nitrogen. The cross section of the membrane is displayed at different magnifications in Figure 2.10 and depicts the unique pore structure of the investigated membrane fibers. Less porous layers can be seen on the inner lumen wall and the membrane's outer skin. As these membranes are inside-out filtration membranes, the inner layer contributes to particular matter separation. Bigger pores can be found especially between the outer lumen channels and provide mechanical stability of the fiber.

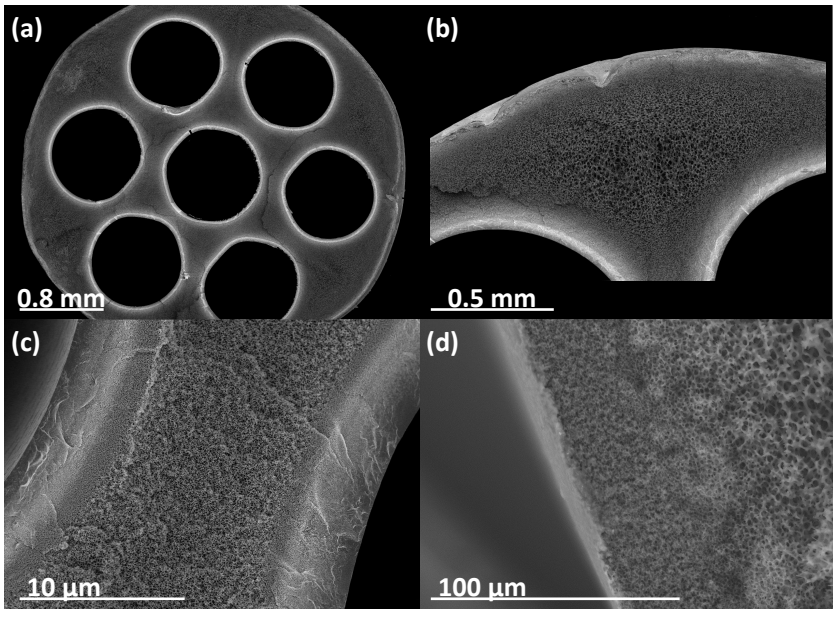

Figure 2.10: (a) and (b): FeSEM images at different magnification of a SevenBore™ fiber supplied by SUEZ. The background of the FeSEM images is adapted for better visibility. (c) Separation layer. (d) Outer membrane skin.

3

Literature Review

Parts of this chapter have been published as:
Denis Wypysek, Matthias Wessling, "MRI in membrane filtration processes" in "Magnetic Resonance Microscopy: Instrumentation and Applications in Engineering, Life Science and Energy Research", *John Wiley & Sons, Ltd* (2022). ISBN: 978-3-527-82725-1

3.1 Magnetic resonance imaging in membrane filtration processes

Magnetic resonance imaging (MRI) is a noninvasive tool with the ability for in-situ measurements of structure and flow in opaque and nontransparent systems and is nowadays indispensable. It all started in the late 1930s when Rabi et al. [Rabi1938] demonstrated that molecules sent through a magnetic field emit radio waves at a specific frequency. Eight years later, Bloch et al. [Bloc1946a; Bloc1946b] and Purcell et al. [Purc1946] were the first to succeed in detecting nuclear resonance signals in solids and liquids, which was awarded the Nobel Prize in Physics in 1952. Suryan [Sury1951] reported flow measurements by NMR in 1951, where he uses the fact that the NMR signal changes when saturated spins are replaced due to flow. However, all developed techniques suffered from long measurement times and a bad resolution until Ernst et al. [Erns1966], in 1966, further developed NMR tomography. The breakthrough of Pulse Fourier Transform (PFT) spectroscopy earned R. R. Ernst a Nobel Prize in Chemistry in 1991. It took seven more years when in 1973, Mansfield et al. [Mans1973b; Mans1973a] introduced a new and faster method to localize the NMR signal on a slide-

by-slide basis using pulsed sequences, followed by the first MR image from Lauterbur [Laut1973]. He used multiple measured NMR signals to conduct a 2D image. For this achievement, Mansfield and Lauterbur were awarded the Nobel Prize in Physiology and Medicine in 2003. Later, in a series of four publications in 1982, Wüthrich et al. [Wüth1982; Wagn1982; Bill1982; Wide1982] enhanced 2D and multidimensional NMR techniques to outline a framework for protein structure determination, which led to the Nobel Prize in Chemistry in 2002.

The amount of Nobel Prizes for the investigation and improvement of different NMR techniques show the importance and strength of its measurement methods. From this time on, NMR measurements and MR imaging spread in all kinds of different directions. All the works mentioned above contributed decisively to the development of modern MRI and paved the way not only in diagnostics and therapy in medicine but also in other scientific fields, such as chemical engineering [Glad1999; Glad2003; Glad2017] and especially membrane filtration science [Chen2004a; Chen2004b; Li2017]. This chapter summarizes the milestones in NMR history and elucidates the importance of MRI in membrane filtration processes. All discussed achievements are listed chronologically in Figures 3.1 to 3.2. In contrast to the arrangement of the publications in the mentioned figures, this chapter presents them thematically sorted.

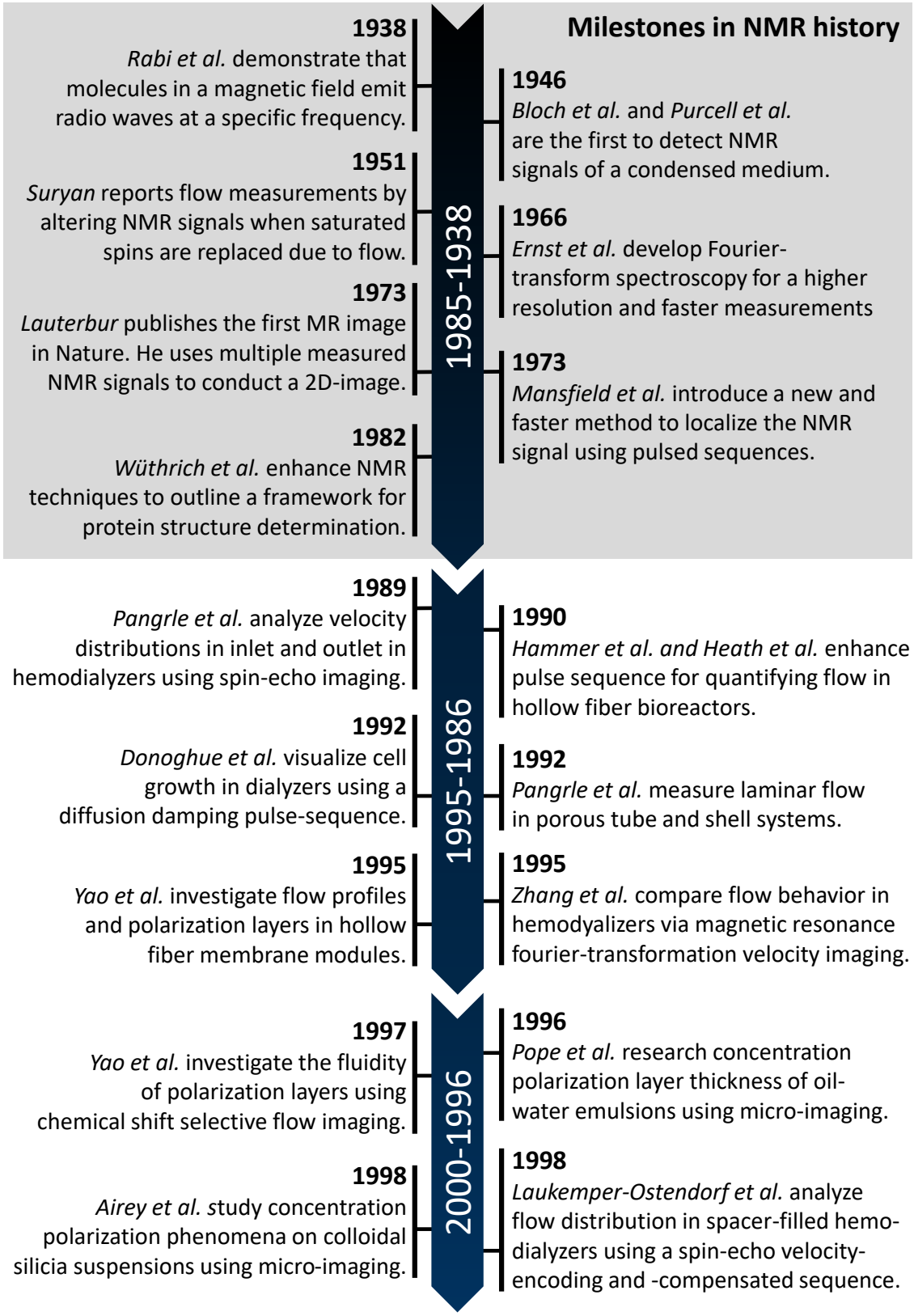

Figure 3.1: Publications dealing with MRI in membrane filtration processes from 1938 to 2000. Milestones in NMR history are marked in gray.

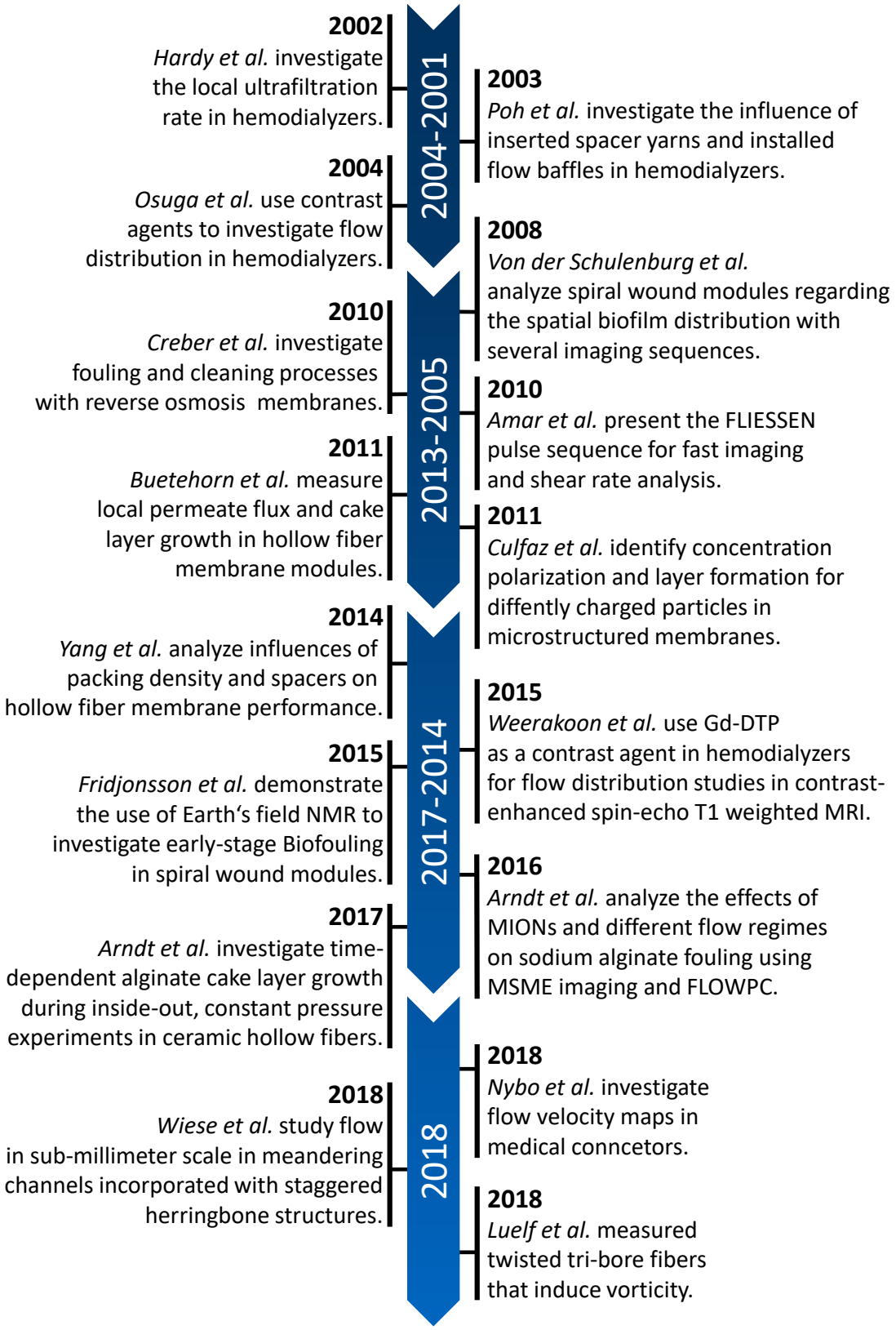

Figure 3.2: Publications dealing with MRI in membrane filtration processes from 2001 to 2018.

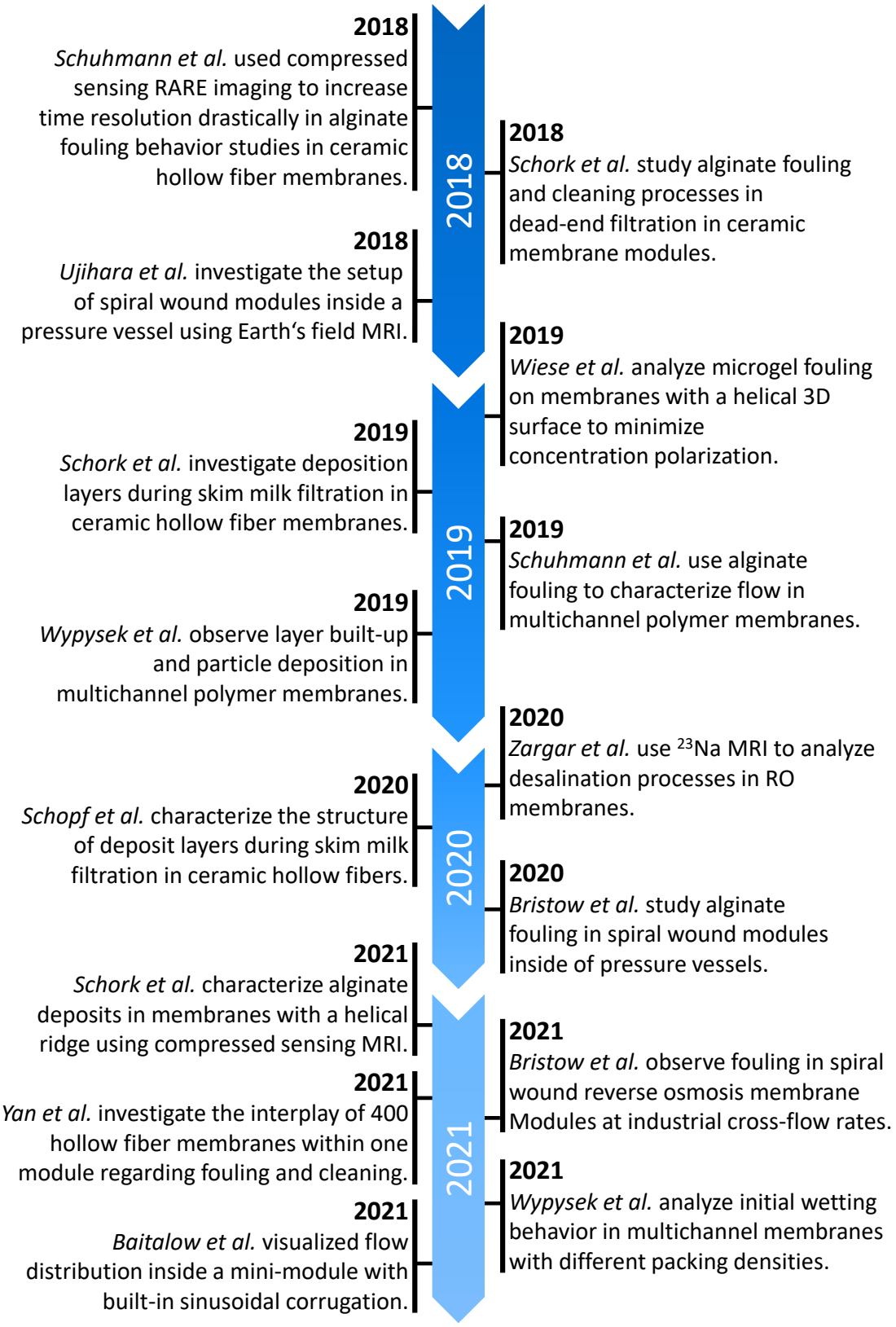

Figure 3.3: Publications dealing with MRI in membrane filtration processes from 2018 to 2021.

3.1.1 Flow investigation and oil and silica fouling analysis in polymeric hollow fiber modules

Beginning in the early 1990s, two of the first studies to successfully combine MRI and membranes was performed by Hammer et al. [Hamm1990] and Heath et al. [Heat1990]. They further develop two-dimensional Fourier transform imaging sequences for quantifying flow in hollow fiber bioreactors and analyzed multiple fibers in a membrane module and saw channeling effects on the shell side of the membrane. Prangle et al. [Pang1992] followed by measuring and analyzing laminar flow in porous tube and shell systems.

To characterize concentration polarization and deposit layers and, thus, draw conclusions about inhibiting factors during filtration, ^{1}H NMR micro-imaging was used later in the 1990s by the working group around Yao, Pope, and Fane [Yao1995a; Yao1995b; Yao1997; Pope1996; Aire1998].

Yao et al. [Yao1995a] observed flow profiles and polarization layers in hollow fiber membrane modules containing five or 15 membranes sealed into a glass tube. As expected, parabolic flow profiles developed in each lumen channel showing good agreement of set volume flow rates and those obtained from MRI measurements. The denser-packed membrane module showed channeling on the shell side and, thus, an uneven flow distribution which can lead to performance and efficiency losses. Figure 3.4 shows chemical shift selective images of the filtration of the oil-water emulsion in a module containing five fibers. Yao et al. [Yao1995a] showed that it is possible to visualize only the oil phase (Figures 3.4 (a) to (c)) or the water phase (Figure 3.4 (d)), respectively. A layer of oil surrounded each membrane from the outside, which thicknesses were pressure dependent. Additionally, the authors recognized high swelling of the membranes during filtration experiments with the oil-water emulsion. Pope et al. [Pope1996] and Airey et al. [Aire1998] continued the work of Yao et al. [Yao1995a]. While Pope et al. investigated fouling layer thicknesses of oil-water emulsions, Airey et al. studied colloidal silica suspensions; both investigated a tubular polypropylene membrane with a bigger diameter using chemical shift selective micro-imaging. Pope et al. [Pope1996] saw an increase in oil

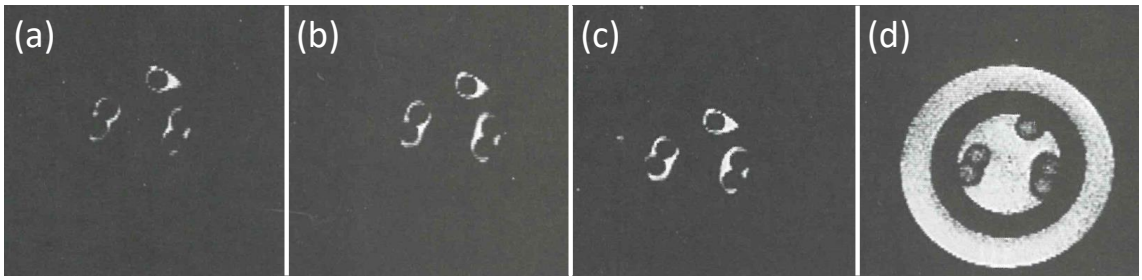

Figure 3.4: Chemical shift images of the oil polarization layer dependence on feed pressure and flow rate. Oil images obtained for (a) 2.9 kPa or 1.38 mL min^{-1}, (b) 4.5 kPa or 2.10 mL min^{-1}, (c) 7.6 kPa or 3.75 mL min^{-1}, respectively. (d) Water image corresponding to the intermediate pressure head value. Slice thickness 1 mm. Adapted from Yao (1995) [Yao1995a] with permission of Elsevier.

concentration polarization layer thickness on the inside of the membrane with increasing filtration time and, thus, a decreasing permeate flux. Moreover, a lower signal intensity within the membrane suggested oil droplets enter the membrane and cause internal fouling. The authors calculated the oil polarization layer thickness over time based on a pixel-by-pixel analysis of the obtained MR images. The averaged thickness increased exponentially during filtration and reached steady-state after three hours of filtration. Additionally, fitting the measured polarization layer thicknesses with a mass transfer-polarization model led to a good agreement between observed flux and flux predicted by Brownian diffusion. Thus, Brownian diffusion was found to be the prevailing back-transport mechanism in this filtration setup.

Airey et al. [Aire1998] investigated the formation and dissipation of concentration polarization phenomena of colloidal silica suspensions. The authors found linearly decreasing T_1- and T_2-relaxation times with an increase in silica suspension concentration. Thus, it is possible to measure silica concentrations online and in-situ in MR images using a suitable calibration curve. Figure 3.5 shows cross-sectional intensity images of the membrane module before (Figure 3.5 (a) and after (Figure 3.5 (b)) flow of the silica suspension was turned on. A highlighted circle on the membrane's inner side can clearly be seen in Figure 3.5 (b). Additionally, the peaks in the signal intensity profile close to the membrane wall in Figure 3.5 (d) confirm the possibility of visualizing silica polarization layers. These peaks are not visible in the intensity profile before the silica suspension filtration in

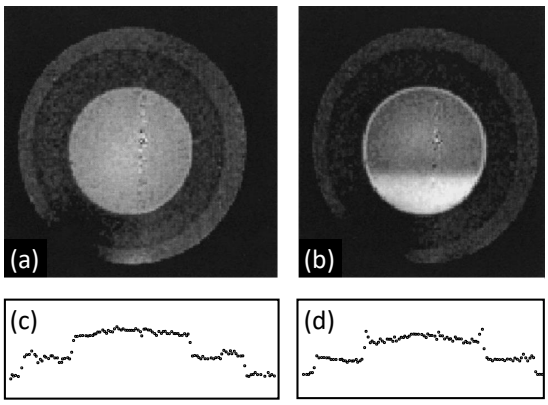

Figure 3.5: 2D cross-sectional T_1-weighted ^{1}H spin density images obtained from the tubular membrane module approx. MR images (a) before and (b) after flow of colloidal silica feed suspension was turned on. Profiles of the signal intensity along a horizontal line through the centers (c) before and (d) after filtration of the silica suspension. Adapted from Airey (1998) [Aire1998] with permission of Elsevier.

Figure 3.5 (c). In this study, the thickness of silica polarization layers was highly non-uniform. A thick deposition layer of silica particles on the bottom side of the membrane (bright shade, Figure 3.5 (b)) gives a hint that gravitational forces influenced the fouling process under these conditions.

Based on the previous studies, Airey et al. [Aire1998] and Yao et al. [Yao1995b; Yao1997] investigated the fluidity of polarization layers. While Airey et al. analyzed colloidal silica particles, Yao et al. looked further into oil-water emulsions. Airey et al. [Aire1998] saw a discontinuity in the velocity profiles between the feed and silica layer. There was a significant axial flow inside the particle layer up to half of the layer thickness. Contrary, Yao et al. [Yao1995b; Yao1997] recognized a rather stationary polarization layer within the measurement error. This shows that the fluidity of polarization layers is highly dependent on the composition of the foulant.

In contrast to the studies mentioned above, Buetehorn et al. [Buet2011] applied MRI to visualize and measure the distribution of local permeate flux and local silica cake layer growth in a hollow fiber membrane module in outside-in mode that was placed vertically in an MRI system. Thus, the effect of gravitational forces influencing the filtration process was negligible in this study. The authors found a position-dependent behavior of the permeate (lumen-sided) velocity: the further away from the position of the module's outlet, the lower the measured velocities. Additionally, an increase in average permeate flux caused the maximum velocity to increase linearly. This linearity showed that the lumen-sided pressure loss is lower than the pressure loss through the porous structure. They found a faster

cake layer growth at the beginning of the filtration that slowed down with increasing filtration time, caused by varying transmembrane pressures (TMP) over time. The TMP grows exponentially with increasing cake layer thickness. Buetehorn et al. [Buet2011] also investigated cake growth for different positions in the membrane module. They found thicker cake layers at the outlet position during the entire filtration time than at positions further away from the outlet. It seems that the cake growth started next to the outlet position (active permeate extraction point) and continued growing away from that point. After fouling of the membrane, the authors successfully applied a shell-sided air bubbling to remove the cake layer and restore the membrane's performance.

Çulfaz et al. [Çulf2011] used the same experimental setup and MRI pulse sequences as Buetehorn et al. [Buet2011] to investigate the influence of differently charged particles on the deposition behavior on self-made hollow fiber membranes of two shapes, round and structured [Çulf2010]. The membranes were operated in constant flux filtration and backwashing experiments. MR images of the fouling behavior over filtered permeate volume of round and structured hollow fiber membranes can be seen in Figure 3.6. With increasing filtered permeate volume, the resistances for both round and structured fiber increased as well. However, the increase in resistance for the structured fiber was greater than that of the round fiber for all fluxes and particle concentrations measured. In the case of the Bindzil filtration, a continuous, homogeneously distributed cake layer with the same thickness for the round and the structured membrane grows on the outer surface. In the Ludox filtration case, the cake layer grows symmetrically on the round fiber, while on the structured fiber, the grooves are filled first, and the fins are hardly covered with particles. The authors explained the different deposition behavior by unequal particle concentrations in the cake layer resulting from differences in back diffusion. While Bindzil particles formed a smaller but highly concentrated cake layer, Ludox particles formed a larger and looser cake layer. Due to the high resistance in the Bindzil cake layer, the permeation started to self-regulate earlier and caused a homogeneous cake layer thickness. However, the Ludox parti-

cles were trapped at the bottom of the grooves due to the low resistance of the cake layer, causing a delayed self-regulation permeation and a reduced back diffusion.

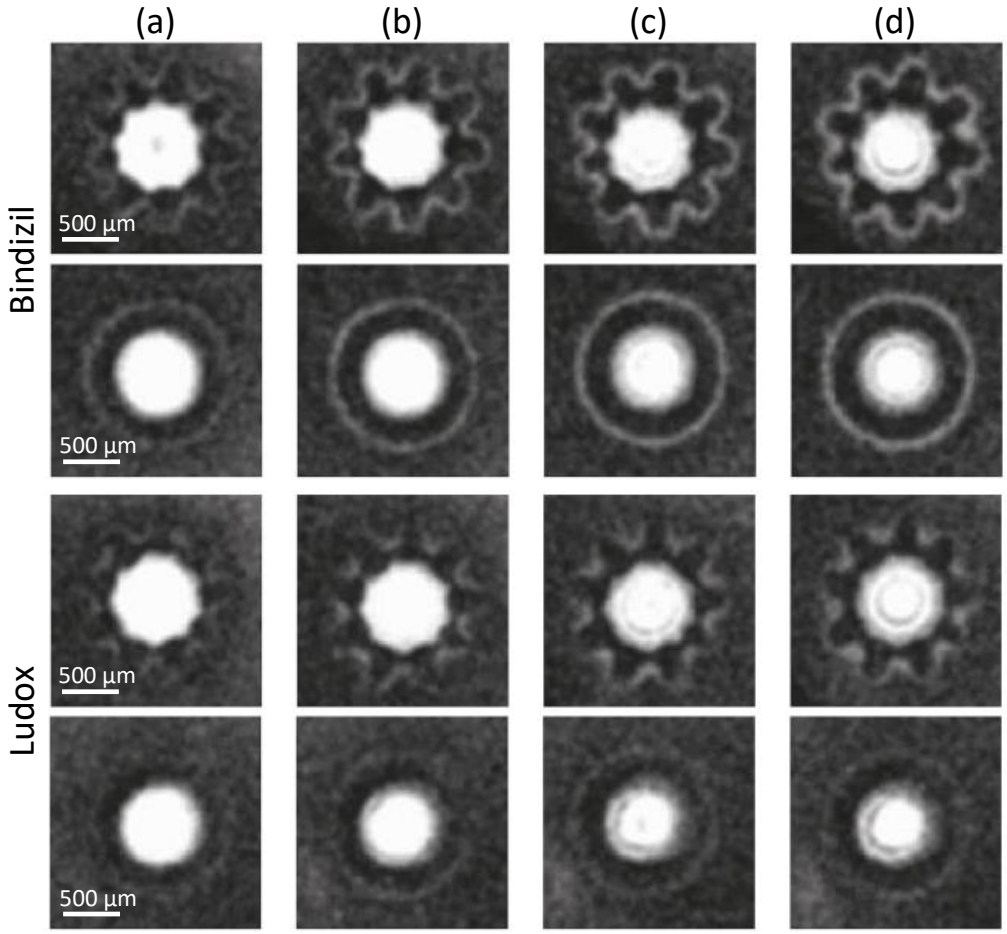

Figure 3.6: Particle deposition on structured and round fibers at 70 LMH with 0.1 wt% Ludox and Bindzil sols. Images are from filtered permeate feed V_f = 0.01 (a), 0.02 (b), 0.04 (c), and 0.06 m^3/m^2 (d). Adapted with permission from Çulfaz [Çulf2011]. Copyright (2011) American Chemical Society.

All above-mentioned phenomena occurred in a membrane module containing one multibore membrane or in a membrane module with low packing density. For understanding underlying hydrodynamic effects, the investigation of one multibore membrane is a suitable approach. However, industrially relevant membrane modules consist of several hundred membranes. Yan et al. [Yan2021] monitored highly-packed ultrafiltration membrane modules consisting of 400 hollow fiber membranes and analyzed velocity fields and fouling inside individual fibers using benchtop MRI. Figure 3.7 shows

the UF module's velocity maps (a) before and (b) after fouling with an alginate solution and (c) after cleaning with an acetic acid solution.

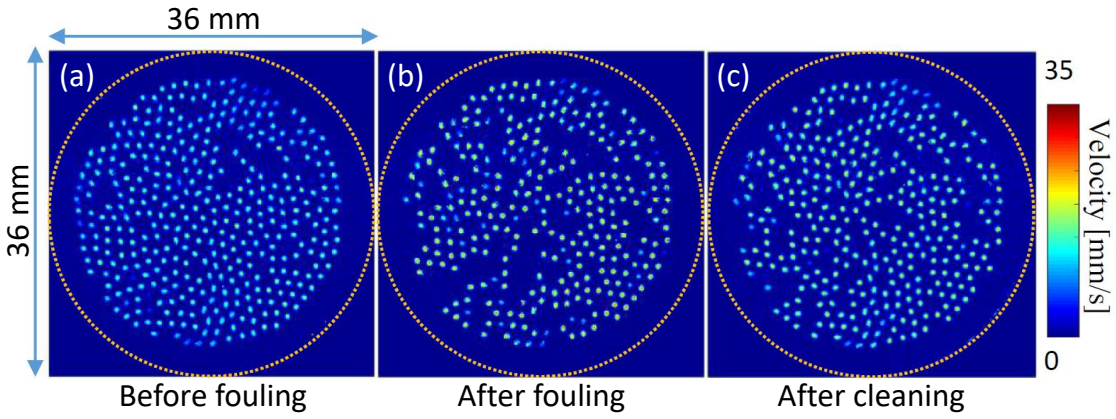

Figure 3.7: MRI velocity images of a UF module (a) before fouling, (b) after fouling, and (c) after cleaning with a acetic acid solution. Adapted from Yan (2021) [Yan2021] with permission of Elsevier.

MRI measurements revealed that even before the filtration of alginate, only 91 % of the fibers participated in pure water filtration. Also, that the membrane module cannot be recovered after chemical cleaning. The number of active fibers decreased to 73 % after fouling and increased to 79 % after cleaning. The irreversible membrane blockage is favored by poor accessibility resulting from channeling and by-passing effects of the single hollow fiber membranes.

This section summarized how MRI measurements were implemented in the field of membrane filtration processes and revealed its possibilities. The information gained from these measurements, like cake and polarization layer thicknesses, flow distributions, swelling of membranes, and the behavior of different foulants, leads to a better understanding of simple membrane processes and underlying physical phenomena and helps to optimize them in the future in terms of process conditions and materials used.

3.1.2 Flow investigation and sodium alginate fouling analysis in ceramic hollow fiber modules

This section condenses methods and possibilities for using MRI with regard to other types of membranes and foulants than in the previous section, which again leads to a better understanding of filtration processes and elucidates the behavior of fouling layers: dense, compressible gel layers and reversible, loose, and fluffy layers. The working group around Arndt et al. [Arnd2016; Arnd2017], Schork et al. [Scho2018], and Schuhmann et al. [Schu2018] investigated filtration processes of sodium alginate in vertically placed ceramic hollow fiber modules. In all the studies, similar membranes made of Al_2O_3 were used. A sodium alginate solution was used as a model foulant. To investigate the influence of gel layer buildup, $CaCl_2$ was added to the fouling solution; the solution without $CaCl_2$ resembled a concentration polarization layer structure. Additionally, magnetic iron oxide nanocrystallites (MIONs) were added to the feed to increase the contrast in the MR images. In one of their latest studies, the groups around Schork et al. [Scho2019] and Schopf et al. [Scho2020] investigated deposition layers during skim milk filtration.

Arndt et al. [Arnd2016] performed inside-out dead-end and cross-flow experiments to analyze the effects of the contrast agent and different flow regimes. The images before and after filtration without the addition of MIONs resemble each other. In contrast, the addition of MIONs makes it possible to distinguish between alginate layer and bulk solution, as MION particles accumulated at the surface of the gel layer. Thus, it was possible to conclude layer thicknesses and the composition of the layer. The authors claimed that in the presence of Ca^{2+}, the layer was dense enough and formed a gel layer that hindered particles from penetrating the layer. These findings are in agreement with filtration data linked to the cake-filtration model. In-situ flow measurements during cross-flow mode showed a significant difference in flow profiles. The flow velocities in a membrane fouled with calcium ions increased since a dense layer was built on the membrane's inner surface (approx. $0\,\mathrm{mm\,s^{-1}}$ gel layer velocity) leading to a

decreased inner diameter of the membrane. This behavior was not visible for the membrane fouled without calcium ions, which performed like a new membrane. [Arnd2016]

The subsequent study of Arndt et al. [Arnd2017] focused on time-dependent cake layer growth during inside-out, constant-pressure experiments. Flow during dead-end filtration and cake layer thicknesses during cross-flow filtration were measured. To achieve industrial relevant cross-flow velocities, the authors utilized MRI outflow effects to increase the contrast and visualize cake formation. The results showed an increase in cake layer thickness for both solutions, in the presence and the absence of Ca^{2+} ions during filtration. Yet, the increase was significantly higher for the filtration without Ca^{2+}. However, in the absence of calcium ions, the fouling layer formed a loose and fluffy structure increasing the permeation flux. Investigating the fouling mechanisms revealed a dense gel layer formation for filtration in the presence of Ca^{2+}, whereas in the case without Ca^{2+}, a deviation from a linear trend was observed indicating other influencing factors such as pore blocking and adsorption phenomena. These fouling mechanisms also influenced the flow profiles inside the membrane, shown in Figure 3.8. With increasing filtration time, the maximum velocity decreases

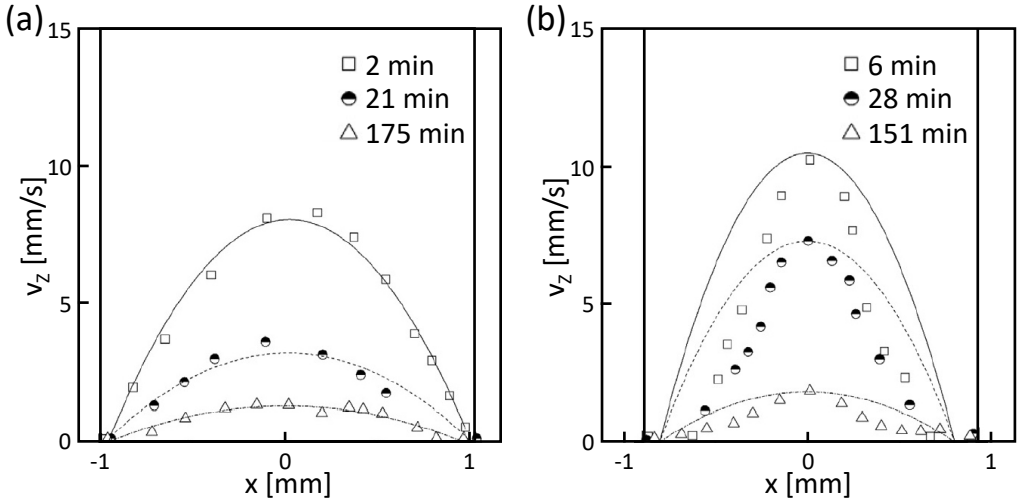

Figure 3.8: Dead-end filtration (a) with Ca^{2+} and (b) without Ca^{2+}. Data points were obtained from MRI measurements. Lines visualize the velocity profiles according to the Hagen-Poiseuille equation. Adapted from Arndt (2017) [Arnd2017] with permission of Elsevier.

for both cases. In the case of filtration with Ca^{2+} (Figure 3.8 (a)), the flow profiles develop as laminar (tubular) flow and meet the predicted profiles (lines). The channel's width seems to decrease over time, which accounts for a relatively stable layer with velocities close to zero. In the case of filtration without Ca^{2+} (Figure 3.8 (b)), the velocity profiles deviate from the ones calculated for simple laminar flow, and a stagnant region next to the membrane wall is observable. These phenomena support the interpretation of a fluffy and more loose structure. In cross-flow experiments, the high velocities (and, thus, shear rates) are the reason for thinner cake layers. The authors saw only little fouling in the absence of Ca^{2+}, which again indicates the development of a fluffy, unstable concentration polarization layer rather than a dense gel layer.

In a next step, Schork et al. [Scho2018] looked at dead-end fouling processes and subsequent backwashing and flushing steps to regenerate the membrane. Figure 3.9 shows MR images with (Feed A) and without (Feed B) Ca^{2+} for the different process steps. Figures 3.9 (a_1) and (b_1)

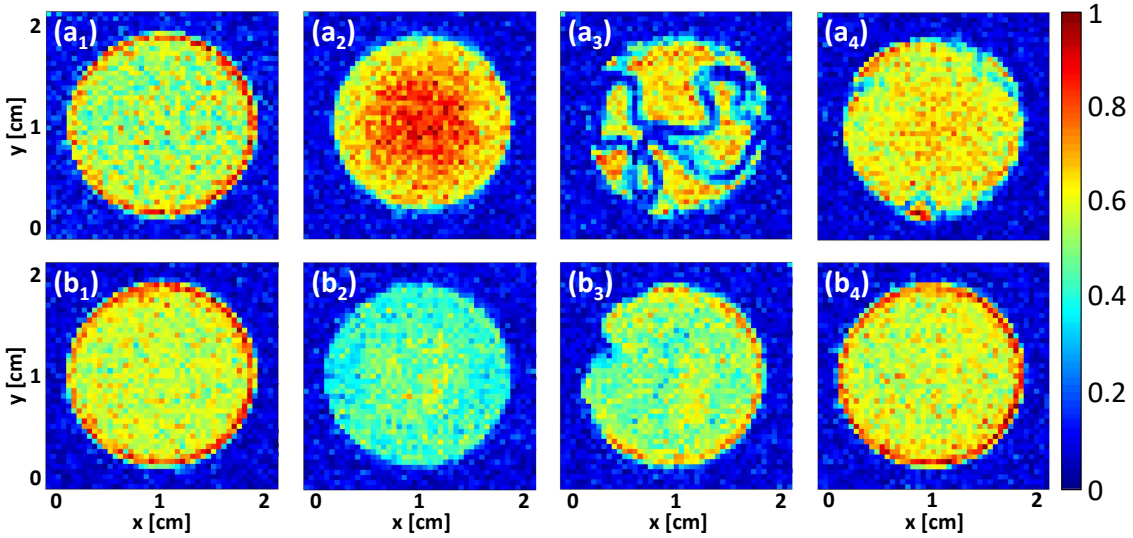

Figure 3.9: MRI images at different filtration steps of Feed A (with Ca^{2+}) and Feed B (without Ca^{2+}) for the first four process steps. (a_1/b_1) before filtration, (a_2/b_2) after 20 min dead-end filtration, (a_3/b_3) after backwashing, (a_4/b_4) after flushing. Adapted from Schork (2018) [Scho2018] with permission of Elsevier.

show the reference state before the filtration. In the presence of Ca^{2+}, a compact and round fouling layer built up, whereas, in the absence of cal-

cium ions, a loose and fluffy structure developed (Figures 3.9 (a_2) and (b_2)). After applying the backwashing flux (Figures 3.9 (a_3) and (b_3)), the difference in cake layer composition became clear. Figure 3.9 (a_3) reveals a gel-like layer in the presence of calcium ions that still sticks partly to the membrane surface. This layer was removed during the flushing step. However, incomplete backwashing was visible over two subsequent filtration cycles. Contrarily, the loose concentration polarization layer that built up in the absence of Ca^{2+} ions could be removed (Figure 3.9 (b_3)) and flushed away (Figure 3.9 (b_4)) entirely after the first cycle so that the membrane was regenerated completely. However, after two subsequent filtration and backwashing cycles, the layer could not be removed anymore. In conclusion, for the chosen imaging slice and the applied conditions, the regeneration of the membrane filtered without calcium ions was more successful.

Schuhmann et al. [Schu2018] extended the earlier work on alginate fouling behavior characterization by increasing the time resolution drastically. During in-situ dead-end inside-out filtration experiments, the same behavior for filtration experiments with and without calcium ions was observed. Cake layer growth in the lumen was analyzed quantitatively, exploring the membrane's symmetry. Modeling the intensity of these measurements led to similar observations of different fouling mechanisms as in the studies before: a gel-like, compressible layer was obtained for the filtration with Ca^{2+} and a reversible, fluffy, loose concentration polarization layer for the filtration without Ca^{2+}. The authors also observed fouling along the membrane's length. Gel layer formation experiments revealed a small increase in time and position toward the permeate outlet. This increase was also visible for concentration polarization measurements. However, the increase was much more pronounced, and the layer thickness at the position closest to the outlet is approx. eleven times higher than that of the gel layer.

3.1.3 Flow investigation and sodium alginate and silica fouling analysis in polymeric multibore membrane modules

The techniques mentioned above are also adaptable for polymeric multibore membranes. Multibore membranes consist of several lumen channels embedded in one porous support structure. Due to their special geometry, these membranes behave differently compared to hollow fiber membranes. MRI makes it possible to analyze flow distributions inside such membranes and helps to understand flow phenomena online and in-situ. Schuhmann et al. [Schu2019] and Wypysek et al. [Wypy2019] analyzed flow distribution and fouling behavior in a membrane system containing one multibore membrane with seven lumen channels.

Schuhmann et al. [Schu2019] performed inside-out dead-end measurements using pure water and an alginate solution as a model foulant. Figure 3.10 illustrates cross-sectional MR intensity images obtained during filtration without (top row) and with (bottom row) calcium ions in the feed solution. A concentration polarization layer developed during filtration without calcium ions, increasing with filtration duration, which can be seen by the decreasing signal intensity in the whole lumen channels' cross section. At the end of filtration, the deposit was located in the entire lumen area. The central channel seemed less fouled compared to the outer channels. One explanation for this finding is the higher mass transfer resistance due to the longer pathway of the middle lumen channel towards the shell side. A dense gel layer was formed during the filtration in the presence of calcium ions with increasing thickness over filtration time (decreasing signal at inner lumen wall). However, the layer stays stable and does not cover the whole lumen cross section. With this filtration mechanism, no significant difference in fouling in the different channels is observable. However, for both filtration solutions, the highest velocities and volume flows were measured for the center bore, showing that the velocity distribution between the different bores is uneven. Besides the uneven flow distribution, the authors saw regions with hardly any NMR signal marked by the dark blue spots in the

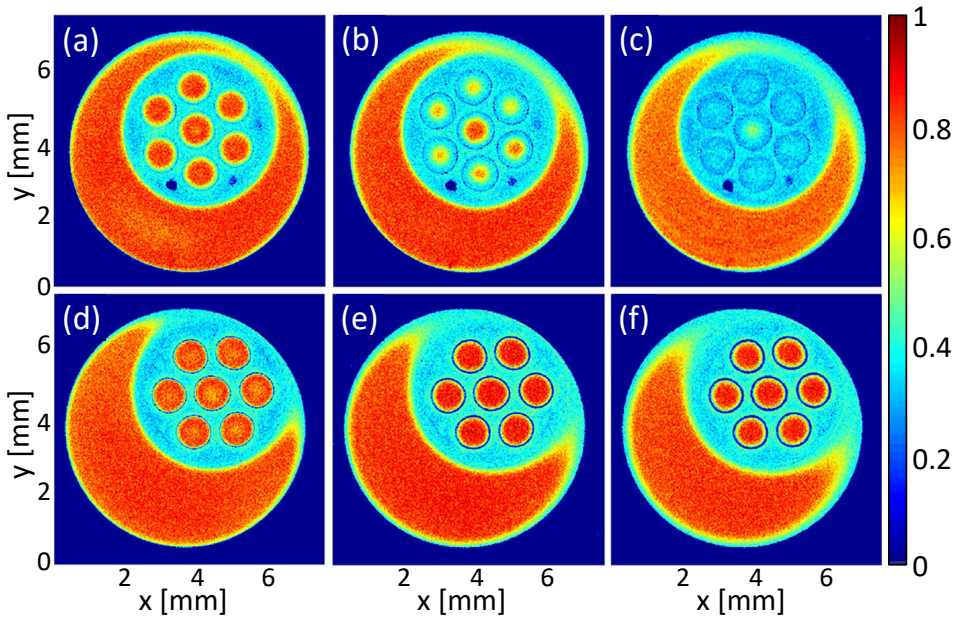

Figure 3.10: MRIs (intensity images) of an aqueous solution of sodium alginate without Ca^{2+} (a) after 2 min 25 s, (b) after 29 min 26 s, (c) after 43 min 35 s and with Ca^{2+} (d) after 4 min 44 s, (e) after 24 min 45 s, and (f) after 51 min 39 s filtration time. Adapted from Schuhmann (2019) [Schu2019] with permission of Elsevier.

porous structure between the outer lumen channels (see Figures 3.10 (a) to (c)), which may arise from not fully wetted membranes prior to the filtration process. Especially micro- and ultrafiltration membranes are impregnated with a pore-stabilizing agent, which is located in the membrane's porous structure after their production. This agent has to be removed before the filtration task to assure a maximal performance of the membrane.

Wypysek et al. [Wypy2019] investigated multibore membranes with pure water and a colloidal silica suspension as a model foulant. Figures 3.11 (a.i) to (c.i) show MR images of fouling with silica particles and two subsequent backwashing steps with corresponding velocity measurements in Figures 3.11 (a.ii) to (c.ii). After fouling experiments in dead-end mode, MR images show blocked bores on the bottom of the membrane indicated by dark regions (channel 3, 4, and 5). Channel one, two, and six seem to be free at all at the measured position. However, taking the velocity images into account, no fluid flow could be detected in channel two. This hints at a blockade at a position closer to the inlet. In contrast, channel one shows the

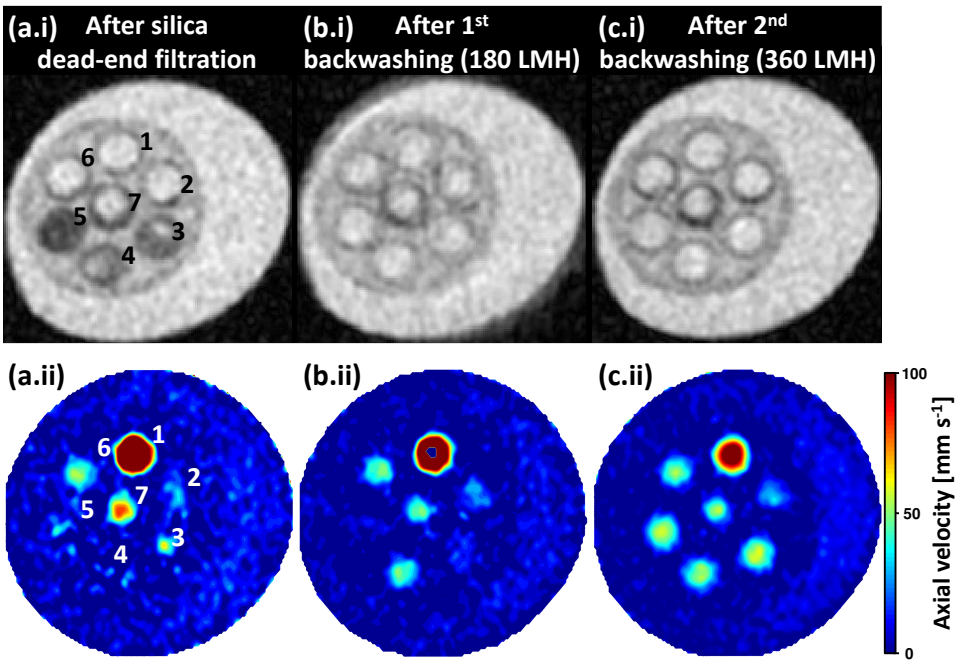

Figure 3.11: (.i): Images showing the deposition of silica particles after filtration and after two subsequent backwashing steps. (.ii): MRI velocimetry after silica dead-end filtration and after two subsequent backwashing steps.

highest velocities of more than 100 mm s^{-1} in the measured cross section, while channel six shows medium velocities of about 50 mm s^{-1}. This heterogeneous fouling behavior negatively influences filtration performance. After one backwashing step, the MR image shows a nearly fully recovered membrane. Yet, velocity images again show that some channels are still blocked. Even the second backwashing step with a higher backwashing flux could not restore the conditions of a new membrane. In other experiments, fouling in cross-flow mode showed particle deposition on the top right corner in each channel with increasing thickness during filtration. The reason for this is the position of the permeate outlet that leads to higher drag forces within this region. This study emphasized that only the combination of MR images and velocity maps fully reveals the hydrodynamic properties in such kinds of membranes.

Some of these phenomena can be explained by the pure water, inside-out dead-end permeation measurements depicted in Figure 3.12 (a) for the axial and (b) for the radial velocity distribution. The highest shell side axial velocities are located in the middle at the largest distance between

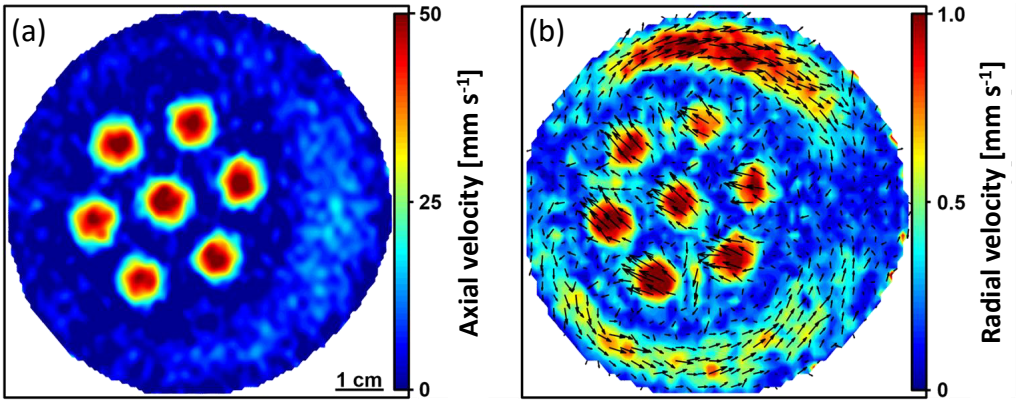

Figure 3.12: MRI of pure water dead-end permeation. (a) Axial and (b) radial flow patterns. Development of secondary radial flows on the shell side and directed flow in the lumen channels.

the whole membrane and the shell wall. A parabolic flow profile develops in every lumen channel. However, the total maximum velocities differs for different channels. Thus, the channels are not contributing equally to the filtration process.

Looking at the radial velocities, a secondary flow field develops on the shell side directed towards the largest distance between membrane and shell wall. Also, velocities in all lumen channels point in one direction. These velocities introduce drag forces and may influence the deposition of particles. Inside the porous membrane structure, the highest velocities are between two lumen channels, being the path of least resistance.

Backwashing with pure water shows that the flow preferentially enters the membrane from the bottom side and then reaches every lumen channel. However, the flow distribution is uneven between different lumen channels, which can influence the backwashing efficiency.

3.1.4 Measures preventing concentration polarization and fouling

The studies above explained and visualized challenges in operating membrane filtration processes like fouling and concentration polarization in several material systems. This section deals with modules and membrane geometries to tackle these problems. An enhancement in filtration perfor-

mance is typically measured by an increase in flux. Often, the reasons for the enhanced flux cannot be clarified entirely. Online and in-situ measurements via MRI can reveal hidden phenomena.

Wiese et al. [Wies2018a] studied flow at the sub-millimeter scale in a 3D-printed, meandering channel reactor with incorporated staggered herringbone structure (herringbone: height 2 mm, width 0.75 mm). For shear rate analysis, a three-dimensional expansion of the FLIESSEN [Amar2010] pulse sequence was used. Figure 3.13 shows different MR imaging slices of the herringbone structure for velocity and shear rate distributions and comparisons to CFD simulations. Figure 3.13 (a.i) reveals that a wave-like

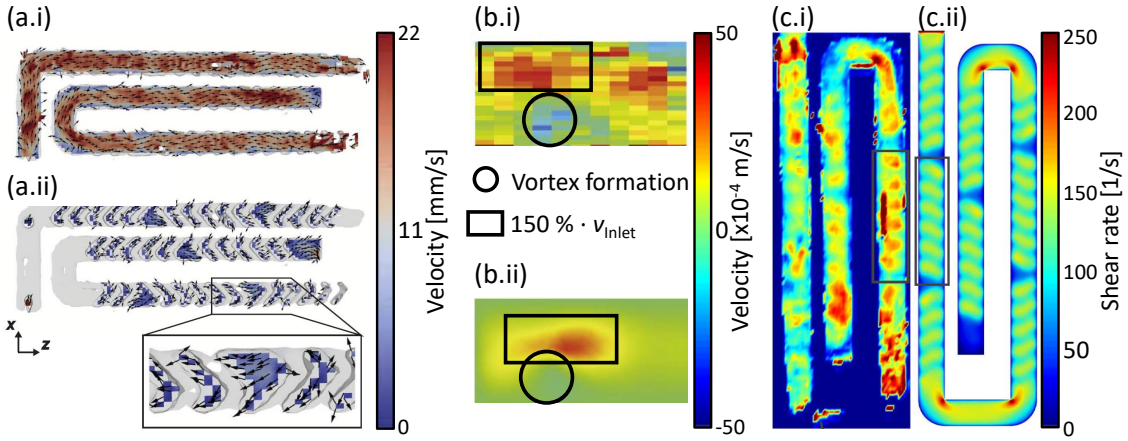

Figure 3.13: (a) Measured 2D velocity maps above (a.i) and within (a.ii) the herringbone structure. (b.i) Measured and (b.ii) simulated 2D velocity maps in height direction for the cross-sectional view. (c.i) Analytically derived and (c.ii) simulated shear stress patterns alter depending on tip orientation. Adapted from Wiese (2018) [Wies2018a] with permission of Elsevier.

velocity profile developed above the herringbone structure that changed periodically due to the height differences in this structure. This variation of higher and lower velocity magnitudes enhances mixing effects. The velocity distribution within the grooves of the structure (Figure 3.13 (a.ii)) was rather chaotic, as described by Stroock et al. [Stro2002]. Especially, velocities perpendicular to the main fluid flow emerged, which favor mixing in the fluid channel and, thus, reduce polarization effects. These transversal velocities, which were caused by small, local pressure differences, can be seen in Figure 3.13 (b.i). Here, upward and downward velocities were plotted

from which a vortex buildup can be recognized. The vortex center is at the position where negative velocities meet positive velocities. Figure 3.13 (c.i) shows measured shear stress patterns. These patterns occurred above the herringbone grooves and the channel surface and depended on the herringbone tip orientation. The alternating patterns enhanced mixing in the channel and, thus, increased the overall mass exchange. The obtained MRI results are in good agreement with an accompanying CFD study (Figure 3.13 (b.ii) and Figure 3.13 (c.ii)) [Wies2018a].

Luelf et al. [Luel2018] fabricated twisted tri-bore fibers to introduce vorticity during filtration processes and with that decrease concentration polarization and fouling. Figure 3.14 (a) depicts axial, and Figures 3.14 (b) and (c) radial velocity components measured by MRI.

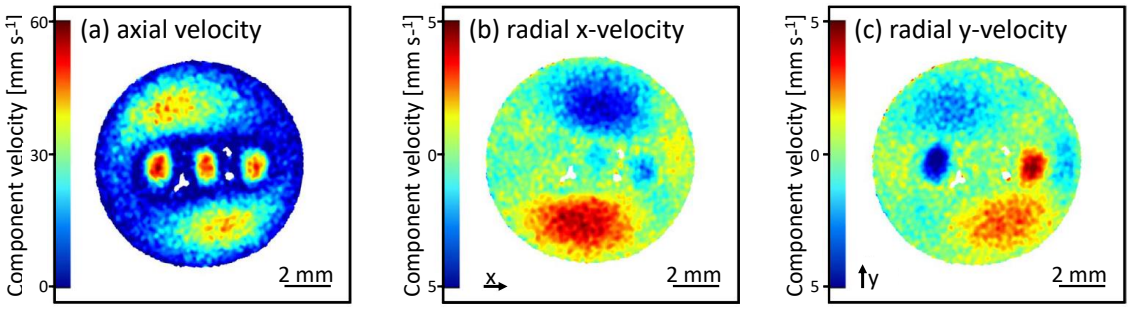

Figure 3.14: Cross-sectional view of the polymeric helical tri-bore hollow fiber resulting from flow-MRI. (a) Axial velocities. Radial velocities in (b) x- and (c) y-direction. Adapted from Luelf (2018) [Luel2018] with permission of Elsevier.

The membrane itself is visible in the axial velocity image (Figure 3.14 (a)). Parabolic flow profiles were visible inside the lumen channels and the shell side. Transversal velocities can be seen in Figures 3.14 (b) and (c). Due to the twisted geometry, regions with a counter-movement of high radial flow in the shell and on the lumen side occurred. These phenomena cause mixing and, thus, enhance mass transfer during filtration.

Wiese et al. [Wies2019] also investigated a membrane that introduces secondary flows. In contrast to the previously mentioned study, this study investigated a straight, tubular membrane with a double-helical structure on the inside and compared it to a membrane without the internal helical structure. MRI data of cross-flow inside-out filtration experiments were a basis

to explain classical filtration data. A microgel solution was used as a model foulant for soft colloids. Fouling of these colloids followed the 'gel model' and suggested an approx. 50 % higher mass transfer coefficient and a twice as high steady-state flux for the membrane with helical structure than for the membrane with a regular surface due to the mixing effect caused by the Helix. These mixing effects in the Helix membrane are shown in Figures 3.15 (a.i) (longitudinal slice) and (a.ii) (cross section). Velocities to-

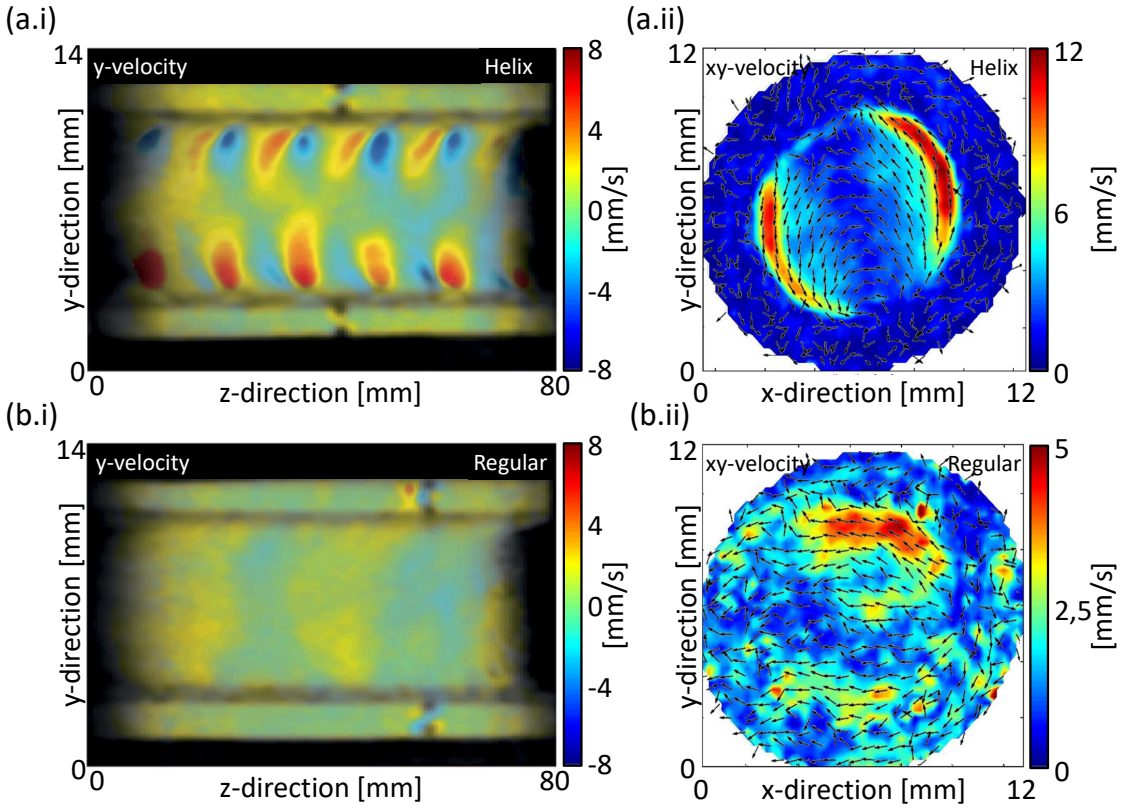

Figure 3.15: Flow-MRI of the *y*-velocity in a (a.i) Helix and (b.i) Regular membrane module at Re = 1000. Enhanced back transport of fluid from the membrane toward the bulk phase. (a.ii) and (b.ii): Vortex formation in dependence on a double Helix showing the huge impact of a 0.5 mm thick Helix surface patterning. Vortices turn along with the double Helix favoring mixing. Adapted from Wiese (2019) [Wies2019] with permission of Elsevier.

ward and away from the membrane can be seen that were up to eight times higher in the Helix membrane than in the Regular membrane. Particles that flow toward the membrane are redirected into the bulk phase again and, thus, fouling is reduced. An additional swirling flow can be seen in cross section measurements (Figures 3.15 (a.ii)), which changes in dependence

on the Helix position and enhances mixing. This swirling flow diminishes along the axial position with increasing distance from the inlet. In comparison, no mixing was visible for the Regular membrane. Evaluated flow-MRI measurements during microgel fouling at Re = 1000 at three positions indicate more severe fouling in the second part of the Regular membrane. In contrast, no significant flux penalty for the Helix membrane was observed. It is worth mentioning that in classical filtration experiments, both membranes performed similarly at low Reynolds numbers. However, flow-MRI measurements showed a huge difference in fouling behavior, emphasizing that only the combination of classical filtration and MRI experiments completely unravels all phenomena.

Schork et al. [Scho2021] analyzed the same Helix membrane in alginate cross-flow filtration measurements and found an increasing fouling layer with increasing filtration time. A gel layer formed on the inside of the membrane in the presence of $CaCl_2$ that formed a highly irregular structure in the bulk phase after a backwashing flux was applied. As the gel layer was still attached to the inner membrane wall at some positions, the reversibility of the filtration process was not given in the studied operating conditions.

Membrane modules in industrial processes are equipped with more than one membrane. Hence, another option to increase shear rates and vorticity is to alter the membrane's outer geometry in highly packed modules. For a membrane distillation process, Yang et al. [Yang2014] analyzed four kinds of membrane modules: a randomly packed module with straight hollow fibers, a module with straight hollow fiber membranes knitted into a spacer structure, a module with curly-fiber membranes, and a module with half curly fibers and half straight fibers. The flow in the curly membrane modules and the spacer knitted resulted in higher transverse velocities, better mixing, and filtration performance than in the randomly-packed one.

3.1.5 Analysis of medical products

While studies in the previous sections dealt with self-made modules and the analysis of fundamental fouling and hydrodynamic phenomena, this section

summarizes studies with commercially available products. Even commercially available products sometimes suffer from bad flow distributions and consequently a reduced filtration performance. MRI can help to find weaknesses and, thus, help optimize membrane modules.

Hemodialysis - Flow distribution in hemodialyzers MRI can be used in different medical applications. One big field of application is the analysis of hemodialyzers. Hemodialyzers are membrane modules consisting of up to several thousand polymeric hollow fiber membranes for the removal of toxins from the human blood. Typically, they are operated in counter-current cross-flow mode with blood inside the membranes and a dialysate solution on the shell side. The higher the uniformity of fluid distribution on the lumen and shell side, the better the removal of toxins and the better the prediction of dialysis processes.

Pangrle et al. [Pang1989] analyzed a Fresenius F80 dialyzer module in 'closed-shell' mode for different Reynolds numbers using MRI to obtain velocity distributions for the inlet and outlet sections at which the membranes are potted into the housing. The authors found a maldistribution throughout the module, which hinders toxin removal. At the inlet, the fluid flowed through the center part, whereas at the outlet, the flow moved to the outer membranes with only little flow through the central membranes. Donoghue et al. [Dono1992] used the same dialyzer to visualize cell growth inside such a module successfully.

Zhang et al. [Zhan1995] improved the previously mentioned measurements by imaging flow distributions in the shell and lumen side simultaneously. They compared three dialyzers with different packing densities with each other (CA170, Baxter; CT190, Baxter; and F60A, Fresenius). The flow distribution in all three dialyzers was relatively uniform inside the lumen channels in the whole cross section. In contrast, the flow distribution on the shell side was not uniform and skewed to higher flow rates. The authors reported no clear trend regarding the different packing densities of the dialyzers.

Laukemper-Ostendorf et al. [Lauk1998] analyzed two model dialyzers - one with and one without textile fibers as spacer yarns in between the hollow fiber membranes. Figure 3.16 depicts the flow distributions on the shell and lumen sides in these dialyzers. Due to the different packing densities, the shell-sided flow in the module with textile fibers (bottom) was much more homogeneously distributed (left) and narrowed (right) than in the module without spacers (top). Also, the authors found that due to swelling of the membranes in the potted area, the membranes' inner diameter decreased. Thus, the lumen velocity increased, influencing the filtration behavior.

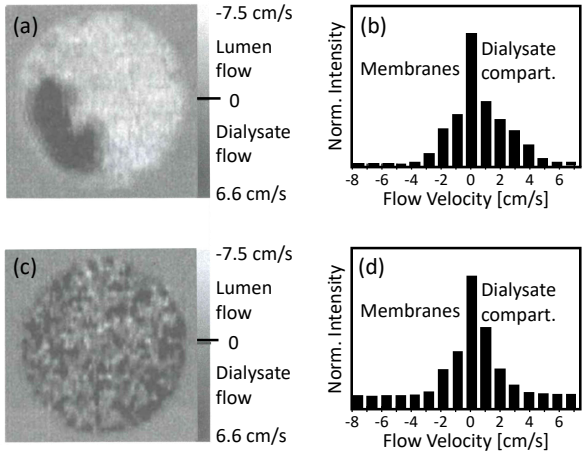

Figure 3.16: Velocity-weighted spin-density images measured on the model (a) without and (b) with textile fibers. The images were taken from the middle section of the model hemodialyzers. (b) and (d) are corresponding flow-velocity distributions. Adapted from Laukemper-Ostendorf (1998) [Lauk1998] with permission of Elsevier.

Hardy et al. [Hard2002] investigated a whole hemodialyzer system (SYNTRA 160, Baxter) with counter-current flow in the lumen and shell sides to analyze the aforementioned back-filtration processes. They succeeded in measuring the local ultrafiltration rate in hemodialyzers. The authors estimated a uniformly decreasing ultrafiltration rate in accordance with the TMP decreasing along the dialyzer. As the manufacturer only gives an average value for the whole module, this technique helps optimize dialyzers and dialysis processes.

Poh et al. further analyzed these findings by investigating the influence of inserted spacer yarns [Poh2003b] and installed flow baffles [Poh2003a] on shell-sided flow. In agreement with previous findings, the flow distribution was not uniform on the shell side, and channeling occurred in the peripheral region. However, spacer yarns between the membranes increased the

uniform distribution on the shell side of the studied dialyzers. Additionally, due to higher packing densities, the maximum velocities were higher, and, thus, the removal of toxins was better. All analyzed baffles failed to provide homogeneous flow conditions throughout the cross section.

Osuga et al. followed the approach of using contrast agents like Gd-DTPA [Osug2004a] or heavy water [Osug2004b] to investigate the flow distribution on the shell side of hemodialyzers. Figure 3.17 shows MR images of consecutive injection levels of a Gd-DTPA solution (black) into a dialyzer filled with a dialysate solution (white). The lumen channels were closed so

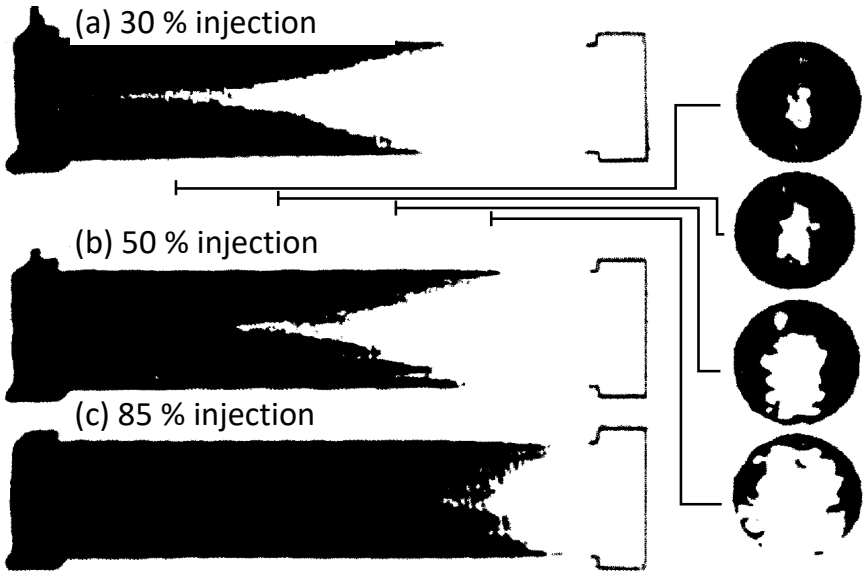

Figure 3.17: MRIs of central vertical section of the dialyzer after commencing the injection of the Gd-DTPA solution. Injection levels of (a) 30 %, (b) 50 %, and (c) 85 % taken after 6.0, 10.0, and 16.0 s. Black region: Gd-DTPA solution, white region: saline. Adapted from Osuga (2004) [Osug2004a] with permission of Elsevier.

that only flow through the shell side was possible. Fluid motion was faster at the peripheral area and decreased in velocity toward the center of the module, symmetrically in the cross section with small non-uniformities and channeling between the fibers. Subsequent flushing with dialysate solution revealed that the Gd-DTPA-tracer was still present inside the hollow fibers, although the inlet and outlet channels were closed. This back-filtration in real dialysis treatments can force toxins to enter the bloodstream again, which should be prevented. The authors obtained similar effects for ex-

periments with heavy water [Osug2004b], which acts as a contrast agent. However, they reported sedimentation of the heavy water as it flowed beneath the present dialysate solution due to higher density.

Weerakoon et al. [Weer2015; Weer2016] also used Gd-DTPA as a contrast agent to analyze the blood compartment of hemodialyzers. The authors stated a relatively uniform flow distribution over the cross section of the measured dialyzers close to the blood inlet and a more heterogeneous one close to the blood outlet. Additionally, they found a decrease in signal intensity toward the outlet, indicating the enrichment of substances from the inside toward the outside of the fibers.

Hemodialysis - Flow distribution in endotoxin adsorbers During dialysis treatment, the use of sterile filters with the ability to adsorb endotoxins has emerged in the last years. On the one hand, these filters pretreat the water used for dialysis. On the other hand, they reduce the amount of endotoxins, which increases the survival rate during dialysis treatment. Wiese et al. [Wies2018b] investigated such a dead-end filter in an MRI study, performing pure water filtration experiments and fouling measurements with colloidal silica particles. Figure 3.18 shows pure water flow measurements of the cross sections close to the inlet (Figure 3.18 (a.i)), next to the permeate outlet (Figure 3.18 (a.ii)), and a slice in perpendicular orientation (Figure 3.18 (b)). The three flow baffles in Figures 3.18 (a.i) and (a.ii) (white

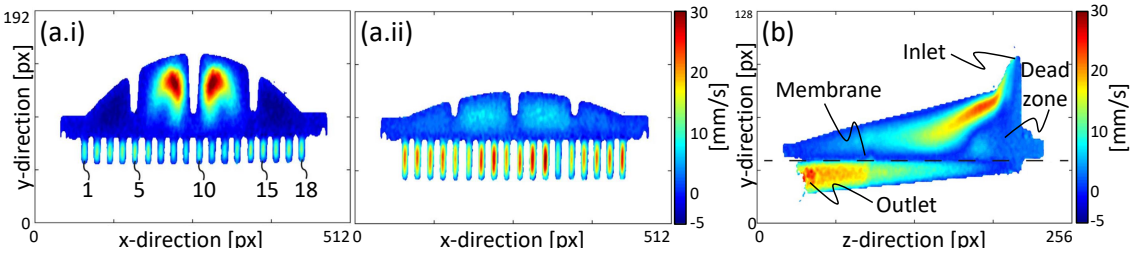

Figure 3.18: Cross-sectional view of the z-velocity in the membrane filter (a.i) at the inlet, and (a.ii) close to the outlet. (b) Longitudinal view of the total velocity. Adapted from Wiese (2018) [Wies2018b] with permission of Elsevier.

area in the top part) that strengthen the housing of the membrane module impact the inflow negatively. The main fluid flow was located in the mid-

dle two sections, whereas a back-flow develops in the two outer sections. This maldistribution affected the flow in the 18 permeate channels below the membrane (different maximum flow velocities in the channels). Additionally, this maldistribution led to a dead zone forming in the first part of the module (Figure 3.18 (b)), and thus to a loss of effective filtration area and a reduction in filtration performance. Figure 3.19 shows the deposition

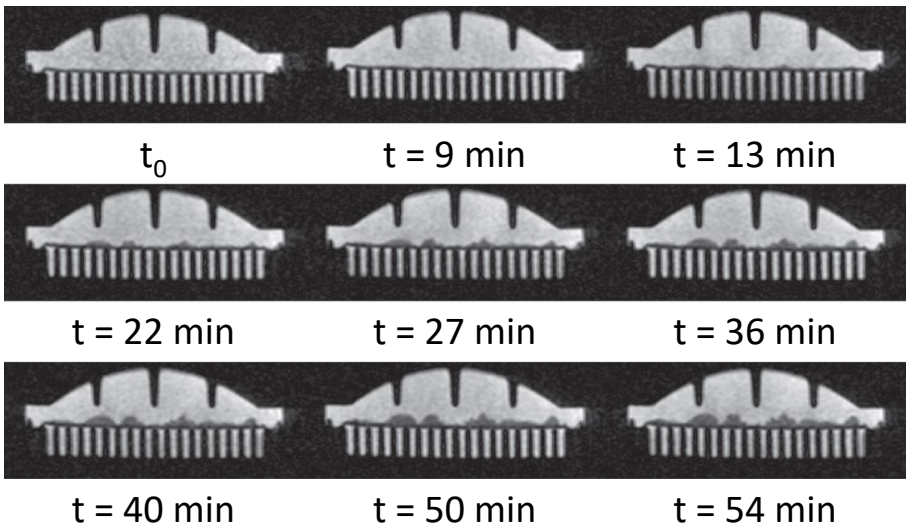

Figure 3.19: Temporal evolution of cake layer formation on the membrane surface. MRI shows the cross-sectional plane in the center of the membrane module. Largest silica particle depositions seem to develop below the left and right baffles. Adapted from Wiese (2018) [Wies2018b] with permission of Elsevier.

of silica particles on the membrane surface during filtration. The amount of deposited particles on the membrane increased with increasing filtration time, with stronger accumulations in the membrane center and below the baffles. The deposition was not homogeneous over the whole membrane area. A buildup of valleys and hills occurred caused by the maldistribution of flow. Subsequent flow measurements showed a decreased permeation and filtration performance. The only active permeate channels remaining were the two outer ones.

Purification processes - Mixing in a mini ultrafiltration device To enhance the purification process of fermentation broths in, for example, the medical industry Baitalow et al. [Bait2021] developed a mini-module with

an embedded spacer structure in the feed channel to increase mixing effects, and, thus, decrease concentration polarization and fouling. MR images of pure water cross-flow experiments were taken to evaluate the final product design: a module with sinusoidal corrugations on the feed side. Figure 3.20 (a) reveals the inner structure of the membrane module, and Figure 3.20 (b) shows the in-plane velocity distribution with its magnification in Figures 3.20 (c.i) and (c.ii). High velocities are present in the corrugations. These velocities were altering throughout the cross section. Thus, these corrugations could be linked to a local velocity increase in radial direction. Additionally, the magnification reveals vortex formation. This mixed flow favors filtration behavior as concentration polarization effects are decreased.

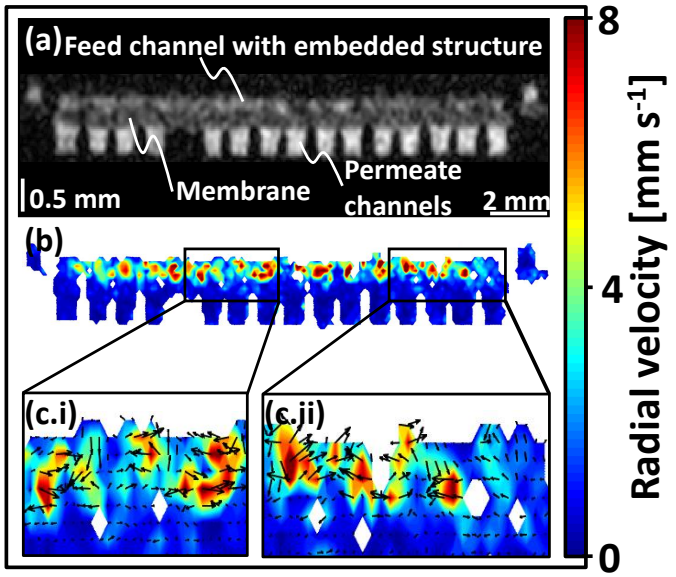

Figure 3.20: (Flow-)MRI on ambr crossflow module (a) reveals the inner structure of the module, (b) shows high radial velocities, and (c.i) and (c.ii) vortex formation in the sinusoidal structured feed channel. Adapted from Baitalow (2021) [Bait2021] with permission of Elsevier.

Connectors - Flow distribution in medical connectors All the above-mentioned medical devices have to be connected to a flow setup. For this purpose, several medical needleless connectors are available. Nybo et al. [Nybo2018] investigated flow velocity maps inside six different types of medical connectors. Every design has a unique flow distribution and complex flow paths, with secondary flows developing throughout the connector. This study demonstrates the strength of MRI that provides basic data for further bacteria or colloid transport investigations. With this experimental

data set, such connectors can be optimized, and CFD simulations can be validated.

3.1.6 Analysis of forward and reverse osmosis modules

Desalination in membrane filtration is an essential process for drinking water production. Two example processes are the so-called forward and reverse osmosis. In these processes, spiral-wound modules are often used in which a grid structure serves as a spacer between two membrane layers [Bake2012]. Besides other membrane processes, forward and reverse osmosis suffer from fouling and scaling, especially biofouling. Several research groups have focused on the investigation of biofouling using ^{1}H NMR [Graf2008; Creb2010; Frid2015; Ujih2018; Bris2020]. Recently, ^{23}Na NMR was presented as a method for analyzing desalination processes [Zarg2020].

Von der Schulenburg et al. [Graf2008] were the first to analyze spiral-wound modules regarding the spatial biofilm distribution, the velocity field inside the module, and the distributions of molecular displacement of tracers in a lab cell, as well as in an industrial membrane module. They found a decreasing active membrane surface area after biofouling and that it occurred at spacer junctions (for comparison, see Figure 3.21). Little biofouling was enough to cause stagnant zones and a profoundly changing flow field in experiments in a flow cell with spacer structures.

Creber et al. [Creb2010] used the same flow cell to investigate fouling and cleaning processes in spiral-wound membrane modules. Figure 3.21 shows similar results as seen by von der Schulenburg et al. [Graf2008]: even a little fouling had a large impact on the active surface area and the flow field. Cleaning the membrane with a sodium dodecyl sulfate and sodium hydroxide mixture showed a broadening effect of existing flow channels. It was not possible to remove the biofilm completely. However, cleaning at an early stage of biofouling seemed more efficient than cleaning a fouling layer that had aged longer.

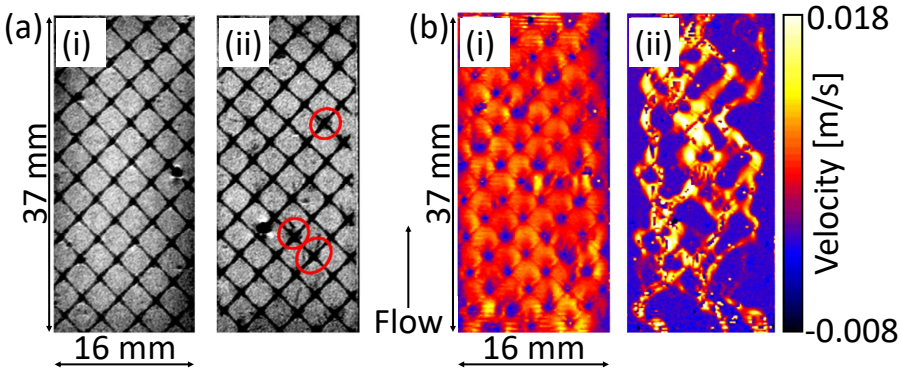

Figure 3.21: The grid structure serves as a spacer between two membrane layers. (a) MRI structural images of (i) an unfouled and (ii) a fouled flow cell. (b) MRI velocity images of (i) an unfouled and (ii) a fouled flow cell. Adapted from Creber (2010) [Creb2010] with permission of Elsevier.

Fridjonsson et al. [Frid2015] presented an approach to investigate this kind of early-stage biofouling and additionally evaluated cleaning efficiencies. The authors used Earth's field NMR methods to detect biofouling in commercial spiral-wound modules. With the NMR signal increasing under operational conditions, detecting early-stage biofouling at any position of the spiral-wound module was possible. This direct measurement technique could also be applied during cleaning processes to reduce the amount of chemicals used in industrial applications.

The setup of spiral-wound modules inside a pressure vessel was investigated by Ujihara et al. [Ujih2018]. The authors succeeded in imaging the inside of a spiral-wound reverse osmosis module in a pressure vessel during operation. Moreover, the authors enhanced the contrast between flowing and stagnant water and could also locate the foulant using an Earth's field tomograph. This technique is much cheaper in operating and investment costs than high-field systems. Although high-field MRI resolution is higher, low-field imaging was sufficient to visualize the desired phenomena.

Bristow et al. [Bris2020] used a high-field tomography system to look at fouling at different positions in a spiral-wound module inside a pressure vessel during filtration with a sodium alginate solution in two different concentrations. Directly at the module inlet, the highest heterogeneities and channeling could be observed. The authors found a highly variable velocity distribution after fouling experiments with the low concentrated solution at

the inlet. In contrast, only small changes in the middle and at the end of the module occurred. Furthermore, after filtration with the highly concentrated solution, the flow was bypassed the membrane module, thus reducing the module's filtration performance significantly as the fouling was irreversible.

Zargar et al. [Zarg2020] proposed another approach to analyze the performance of reverse osmosis processes. They did not investigate fouling in membrane modules but rather the saline feed solution. In their proof of concept study, the authors used ^{23}Na nuclear MRI to measure the sodium ion concentration inside the membrane and close to its surface. They succeeded in measuring the concentration polarization during desalination that decreases the filtration performance. This is the next step to better predict desalination processes, carry out simulations, or optimize them.

Bristow et al. [Bris2021] improved earlier studies by first measurements of spiral-wound membrane modules at industrially relevant cross-flow rates. For their quantification, they used the phenomenon of increasing NMR signal with increasing sodium alginate fouling. They found higher fouling located next to the membrane spacer sheet nodes, decreasing membrane performance. Also, local flow channeling resulting from foulant accumulation could be found, leading to a strongly altered flow field inside the membrane module.

4

Single Multibore Membrane Module Performance

Parts of this chapter have been published as:

Denis Wypysek, Deniz Rall, Martin Wiese, Tobias Neef, Geert-Henk Koops, Matthias Wessling, "Shell and lumen side flow and pressure communication during permeation and filtration in a multibore polymer membrane module", *Journal of Membrane Science* 584 (2019) 254-267. DOI: 10.1016/j.memsci.2019.04.070

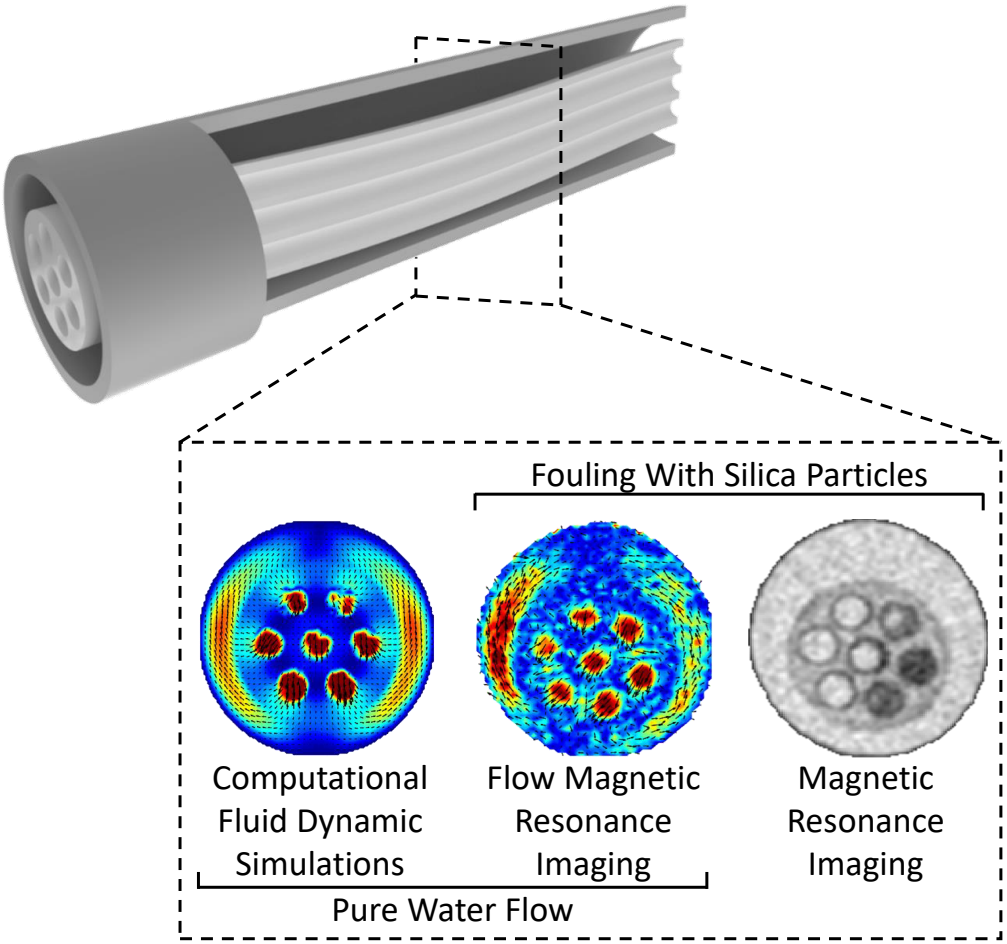

4.1 Introduction

As mentioned in *Chapter 3: Literature Review*, Schuhmann et al. [Schu2019] and Wypysek et al. [Wypy2019] analyzed the hydrodynamics in multibore membrane modules using magnetic resonance imaging. However, unexpected flow phenomena occurred, and some open questions remain, such as the influence of small geometric deviations from the ideal concentric membrane position on the lumen- and shell-sided flow conditions. Schuhmann et al. hypothesized that the location of the membrane in the module might influence the velocity field. The authors also provided some first insights through inside-out dead-end filtration and constant feed pressure at a single position only.

An innovative approach to extending the measurement capability for multibore membranes by MRI is validations by computational fluid dynamics (CFD) simulations [Luel2018]. So far, Kagramanov et al. and Frederic et al. simulated fluid flow in ceramic multibore membranes with homogeneous pore size distributions [Kagr2001; Fred2018]. The majority of studies focused on optimizing the membrane itself. However, shell-sided hydrodynamic effects in hollow fiber membrane modules have an equally pronounced impact on the membrane's performance. The tangential inlet and outlet flow influence the flow field inside membrane modules as validated by CFD simulations and particle image velocimetry (PIV) [Zhan2018].

In this chapter, the hydrodynamic effects inside a custom-made multibore membrane module are investigated inspired by the work of Hawthrone in 1951 [Hawt1951] on secondary flow within curved geometries. The positioning of the membrane inside the module affects the shell and lumen side flow and pressure communication during membrane operation. A comprehensive CFD study fully unravels the pathways of flow during filtration seen in the MRI measurements in Figure 4.8 and is used to interpret the complex velocity fields. The richness of information of the flow is visualized in multiple cross-sectional planes in vector plots for radial velocities and velocity magnitude plots for axial velocities.

4.2 Materials and Methods

4.2.1 Membrane

The used multibore membranes are polymeric PES SevenBore™fibers from SUEZ and are presented in detail in *Chapter 2.4: Multibore membranes*. Table 4.1 lists measured and calculated membrane specific input parameters for the simulation.

Table 4.1: Measured and calculated physical properties of the polymeric PES SevenBore™ fibers from SUEZ [SUEZ].

	Unit	Value	
Bore diameter	[mm]	0.9	measured
Outer diameter	[mm]	4	measured
Porosity	[–]	0.82	calculated
Intrinsic permeability	[m^2]	$1.14 \cdot 10^{-15}$	calculated
Pure water permeance	[LMH bar^{-1}]	1000	measured

The membrane's volume porosity is averaged over multiple FeSEM images. The software ImageJ is used to determine the porosity by the area fraction measurement. Other techniques to measure surface and overall porosity, as well as pore size, can be obtained from Lu et al. [Lu2018]. Pure water flux measurements evaluate the permeance for the membrane module arrangement. Subsequently, the intrinsic permeability is calculated using Darcy's law in Equation 4.1 based on pure water flow experiments

$$Q = \frac{kA\Delta P}{\eta L} \tag{4.1}$$

with Q as the total discharge, A as the cross-sectional area of flow, ΔP as the pressure drop, η as the fluid viscosity, L as the length, and k as the parameter for intrinsic permeability.

4.2.2 Computational fluid dynamics simulation

CFD simulations of the multibore membranes are performed using COMSOL Multiphysics® [COMS2021]. The numerical Finite Element Method (FEM) simulations solve the Navier-Stokes equations. All performed CFD studies use the *Free and Porous Media Flow* physics interface that combines the Laminar Flow interface and the Brinkman equation interface. The open spaces of the flow channels (lumen and shell) are modeled as *free water flow*, and the membrane is considered as a homogeneous porous medium.

Boundaries of the simulation domains are shown in Figure 4.1 and are defined according to a 2-end module arrangement. The flow scheme is dead-end inside-out. Inlet boundaries are set as standard inflow velocity. The outlet boundary is a pressure outlet with suppressed backflow set to ambient pressure. The simulation utilizes water for which the material properties are taken from the COMSOL library. The membrane is configured as porous media with user-defined porosity and intrinsic permeability. The material's density and dynamic viscosity correlate to the temperature of 293.15 K. Other physical properties of the membrane can be seen in Table 4.1. The respective mesh is optimized for each geometry study. All simulations are implemented as a time-independent study. The parallel sparse direct solver MUMPS is used as a solver for the stationary fluid dynamic simulation.

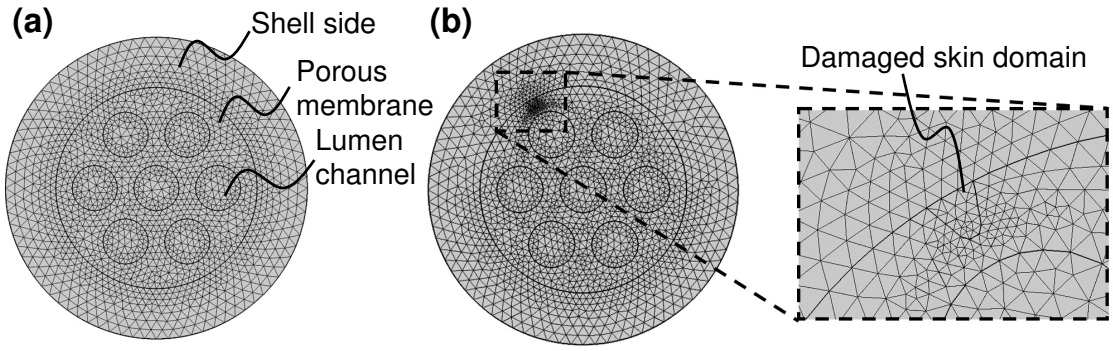

Figure 4.1: (a) Meshed simulation domain with lumen channels, the shell side, and the porous membrane. (b) Simulation domain for the membrane's damaged outer skin.

By solving the Navier-Stokes equation by FEM, all information about the velocities of all spatial directions of a Cartesian coordinate system is retrievable for each node of the meshed grid. However, for comparability with the flow-MRI, the displayed infinitesimal 2D CFD slice plots are averaged over the same slice thickness of 10 mm as in the 2D flow-MRI. This procedure is performed as described by Luelf et al. [Luel2018] and Wiese et al. [Wies2018a]. The axial velocity magnitudes are averaged as $|u_{\text{axial}}| = \sqrt{u_z^2}$ and the radial velocity magnitudes as $|u_{\text{radial}}| = \sqrt{u_x^2 + u_y^2}$, respectively. Arrows in the figures depict the direction of flow. The displayed slices A-A, B-B, and C-C depict flow fields 20 mm behind the inlet boundary, 50 mm and 80 mm, respectively.

4.3 Results and discussion

Throughout this chapter, pure water velocity fields are investigated by different geometrical modifications such as an eccentric membrane position (see Section 4.3.2), a sagging membrane (see Section 4.3.3), a damaged membrane skin (see Section 4.3.4), and altered module flow fields (see Section 4.3.5). All investigated membrane module geometries are compared to the ideal reference geometry stated in Section 4.3.1. All presented figures display the axial ((a.i) to (c.i)) and radial ((a.ii) to (c.ii)) velocity components as well as the pressure distribution ((a.iii) to (c.iii)) during inside-out permeation at the beginning (A-A), the center (B-B), and the end (C-C) of the module.

4.3.1 CFD velocimetry - ideal membrane position

First, the results of the reference module are presented in Figure 4.2 to evaluate the different non-ideal membrane positions. The membrane is positioned in the center of the module. Pure water flow enters the multibore membrane equally distributed in the seven bore channels and permeates in a dead-end arrangement through the porous structure to the shell side.

Due to a dead-end inside-out flow arrangement, the axial velocity magnitude in the seven bore channels decreases in axial direction. In contrast, the axial velocity in the shell side increases with the flow through the module to maintain the mass balance. In the bore and shell channel, the flow profiles show a laminar parabolic flow formation and is equally distributed. The shown velocity magnitudes between shell and bore channels differ because the cross section of the shell is larger than the cross section of the seven channels.

Arrows in Figures 4.2 (a.ii) to (c.ii) depict the direction of the radial velocities, and their length corresponds to the velocity magnitude (as well as the colormap). The radial velocity magnitude in the channels decreases with the flow along with the module in all seven bores and correlate appropriately to the mass balance. The noisy flow velocities seem to stabilize towards the end of the membrane. The center bore channel shows lower radial velocities compared to the outer bore channels. This behavior already appears close to the feed inlet. The arrows reveal that the flow is directed from the center to the shell side without diverting and follows the path of least resistance. The magnitude of the six outer bores differs from the center bore. Flow from the inner bore permeates through the entire circumference, through the membrane structure and towards outer lumen channels. In contrast, the water from the outer bores permeates straight in the direction of the shell. Here the flow is not distributed over the whole circumference.

The pressure is the highest in the central bore and lowest in the shell domain. Thus, a pressure difference from the central bore to the outer bore and a pressure difference from the outer bore to the shell domain exists, corresponding to the fluid's driving force. The CFD study assumes a homogeneous porous polymer matrix of the membrane domain. Therefore, the resistance from the inner bore to the shell side is higher in comparison to the resistance from the six outer bores to the shell side.

However, the FeSEM images in Figure 2.10 of the cross section of the multibore membrane reveal a gradient in porosity. The solvent exchange process during membrane fabrication influences the formation of the sep-

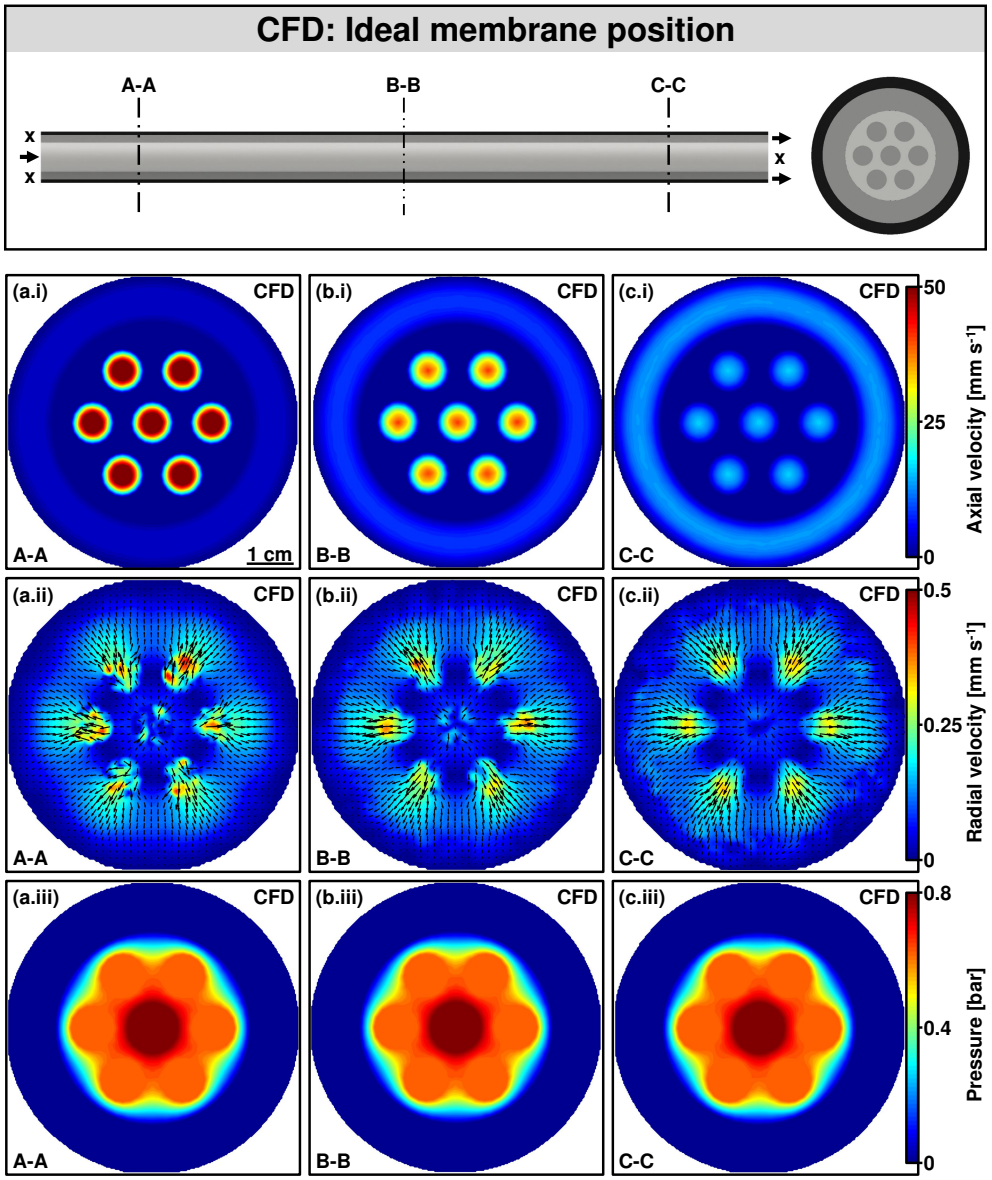

Figure 4.2: CFD simulation of ideal membrane position during inside-out permeation at three positions. Top: axial velocities, middle: radial velocities, bottom: pressure distribution. No shell-sided secondary flow field is indicated. The lumen flow is on a direct path to the shell side without diverted direction.

aration skin and micro- to macro-voids. The separation skin forms a diffusive barrier which slows down the phase inversion process beyond the skin layer creating asymmetry in the final polymeric structure. For ceramic membranes, the assumption of a homogeneous pore size holds. Only the separation skin varies in ceramic membranes. The results indicate that the porous membrane structure plays a crucial role in flow field and pressure development and demands a more detailed investigation.

4.3.2 CFD velocimetry - eccentric membrane position in the module

Next, the CFD study investigates the effects on the flow field if a membrane is positioned eccentrically, as this could easily be found in commercial modules containing a couple thousand of these multibore membranes. The results of the eccentric membrane position are displayed in Figure 4.3.

Similar effects as discussed in Section 4.3.1 can be observed. Opposite to the reference geometry, a radial flow field on the shell side is now induced. The fluid is forced from the minimum distance between the membrane and inner tube wall to the maximum distance. This effect results from a lower pressure drop of the annular gap flow with increasing gap distance. The eccentric position does not influence the lumen to shell side directed flow through the porous membrane. This can be seen by the directed outward flow inside the lumen channel.

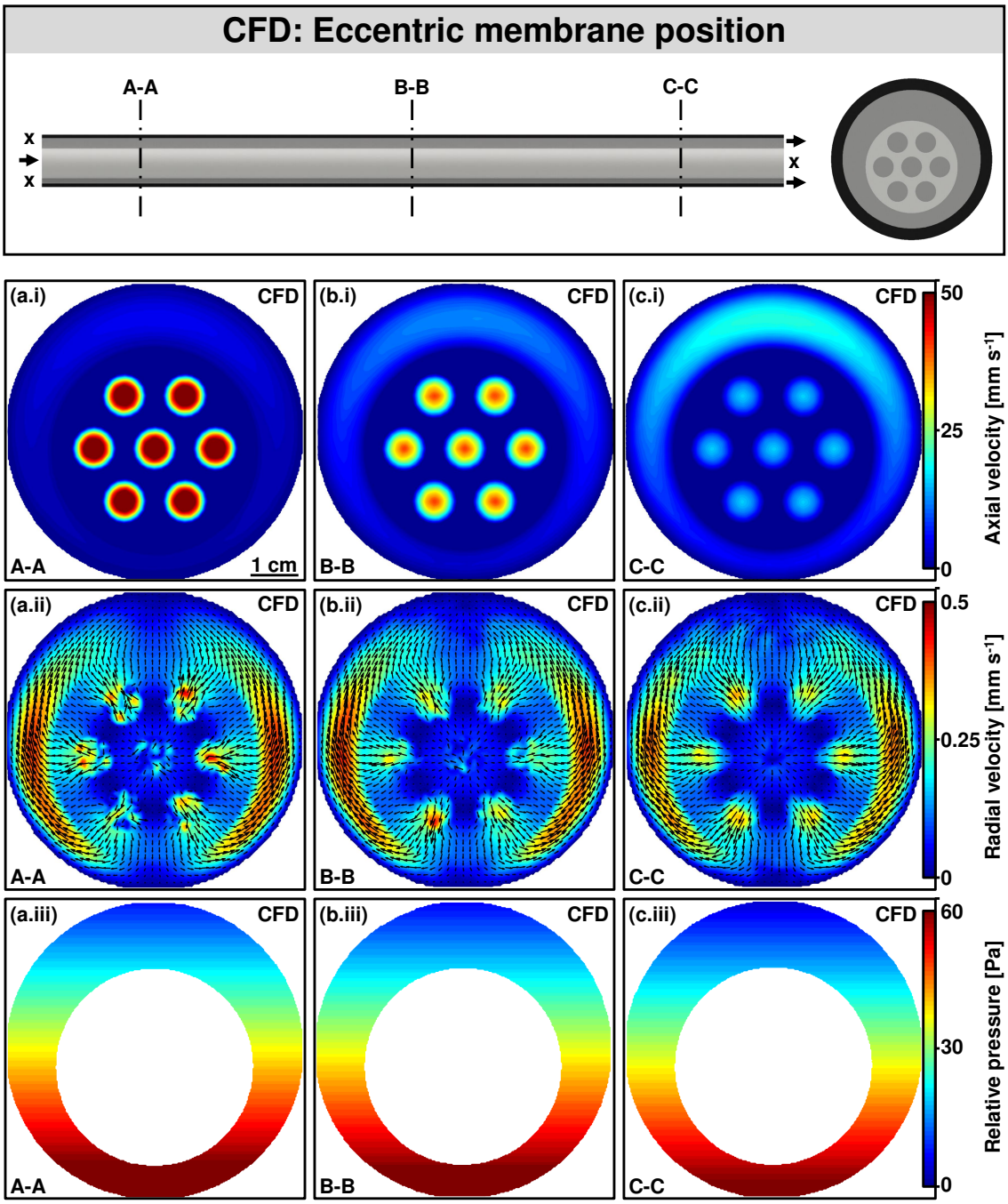

Figure 4.3: CFD simulation of an eccentric membrane position in the module during inside-out permeation at three positions. Top: axial velocities, middle: radial velocities, bottom: relative pressure distribution. The lumen flow is on a direct path to the shell side without diverted direction. A shell-sided secondary annular gap flow field is introduced due to the different distances to the tube wall.

4.3.3 CFD velocimetry - sagging membrane in the module

Hollow fibers bend during permeation because of their swelling behavior in contact with pure water. This sagging effect and its impact on the flow field is shown in Figure 4.4. At the inlet and outlet boundary, the membrane is placed concentrically. In B-B, the sagged membrane is in maximum deflection.

Sagging of the membrane introduces a secondary flow in the lumen channel [Hawt1951]. Oppositely, the radial velocity components are not only directed outwards during inside-out permeation. The sagging of the hollow fiber membrane introduces a radial directed flow towards the bending direction. The radial velocity magnitude is most strongly pronounced in two lumen channels at the outermost arc of the bending. The direction of the secondary flow is reversed after crossing the center point of the module. At C-C, the radial velocity magnitude is most strongly pronounced in the two opposite lumen channels.

Additionally, a shell-sided secondary annular gap flow field is observed corresponding to the distance of the membrane to the tube wall. The curvature of the membrane results in an increased annular gap due to the different distances to the tube wall. The fluid is forced from the minimum distance between the membrane and tube wall to the maximum distance (due to small local pressure differences) as observed in Section 4.3.2. This effect is reversed after crossing the inflection point between B-B and C-C.

The results of the sagged membrane suggest that the positioning of the membrane within the module causes a radial flow field formation. Flow conditions along and through the membrane influence the retention behavior and the resulting fouling behavior during operation. Hence, the sagging of the membrane causes the membrane to behave non-ideal. This kind of heterogeneous flow profile should be anticipated in commercial membrane filtration modules where perfect (multibore) fiber alignment typically does not exist.

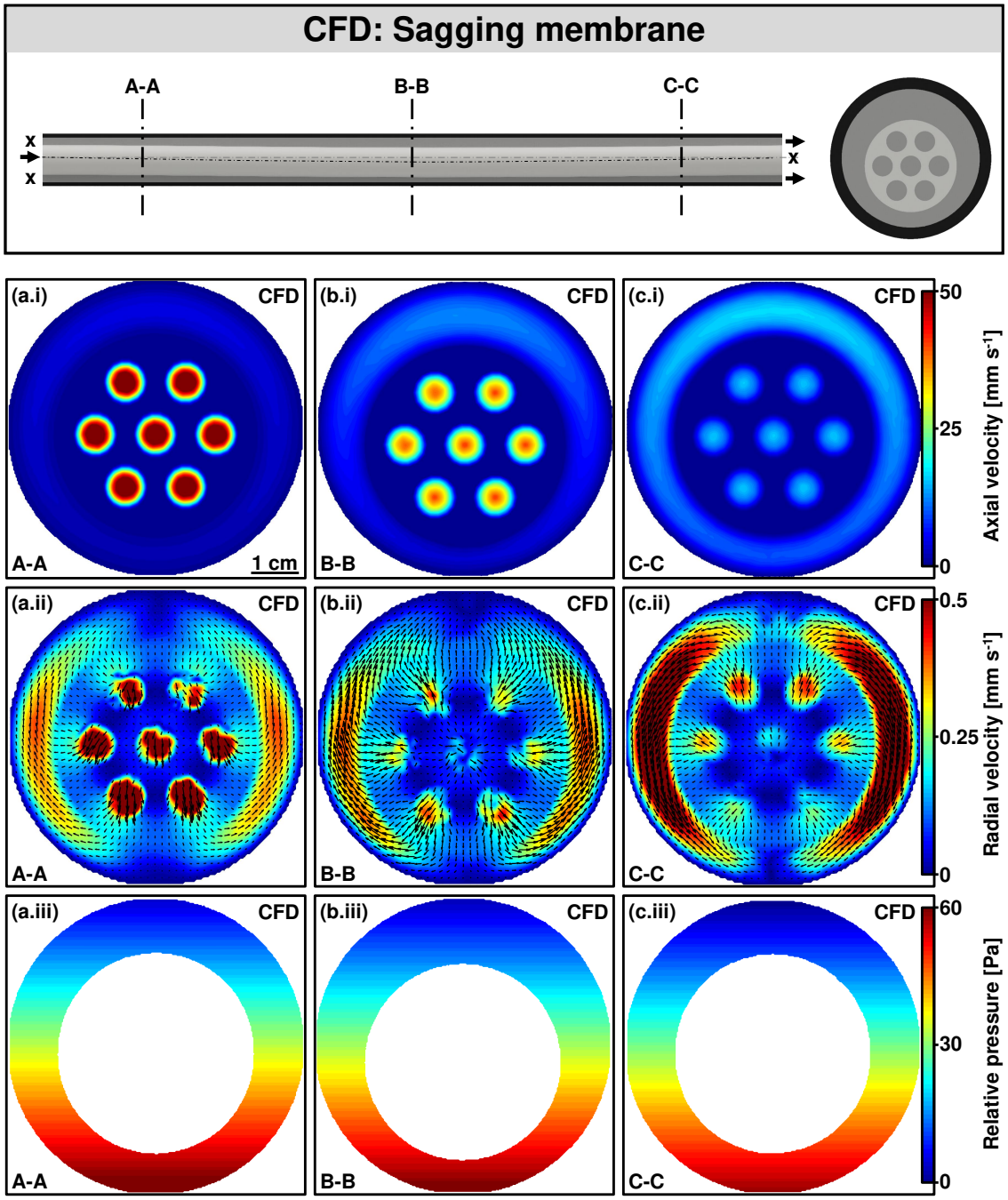

Figure 4.4: CFD simulation of a sagging membrane in the module during membrane inside-out permeation at three positions. Top: axial velocities, middle: radial velocities, bottom: relative pressure distribution. Sagging of the membrane introduces secondary flow fields in the lumen channel. A shell-sided secondary annular gap flow field is introduced due to the different distances to the tube wall.

4.3.4 CFD velocimetry - damaged separation skin membrane

Membrane spacers are predominantly used in flat sheet spiral-wound modules and stacked flat sheet modules. These spacers define the channel geometry and act as mixing devices to reduce concentration polarization by redirecting the flow field. Equipping membrane modules with spacers may cause damage to the membrane skin during module construction. Also, defects in hollow fiber membranes along the outer skin can occur during the fiber spinning process and fiber handling during manufacturing modules.

In the following, the impact of axial damages in the outside skin of the membrane is investigated. Altering the properties of porosity and permeability along the outer side of the fiber mimics this axial damage. The module is operated in dead-end inside-out filtration mode. The damaged domain can either have a higher or a lower intrinsic permeability. The results of the corresponding CFD simulation are shown in Figure 4.6 for a higher permeability and in Figure 4.5 for a lower permeability, respectively.

It seems that the damaged outer skin has no significant effect on the permeation performance of the membrane. The relative pressure illustrations depict the differences between higher and lower intrinsic permeability. A damaged outer membrane skin with higher permeability results in a higher flow from the lumen channel into the shell side. Damages that lead to a lower permeability show exactly the opposite effect. Due to the relatively high resistance of the porous membrane material, the surrounding lumen channels are not affected by a damaged outer skin. No bypass flow can be observed.

The separation layer of the multibore membrane is located at the lumen side. Therefore, damages at the membrane outside structure do not negatively influence the performance of the membranes. A benefit of inside-out hollow fiber membranes is that the skin is well protected.

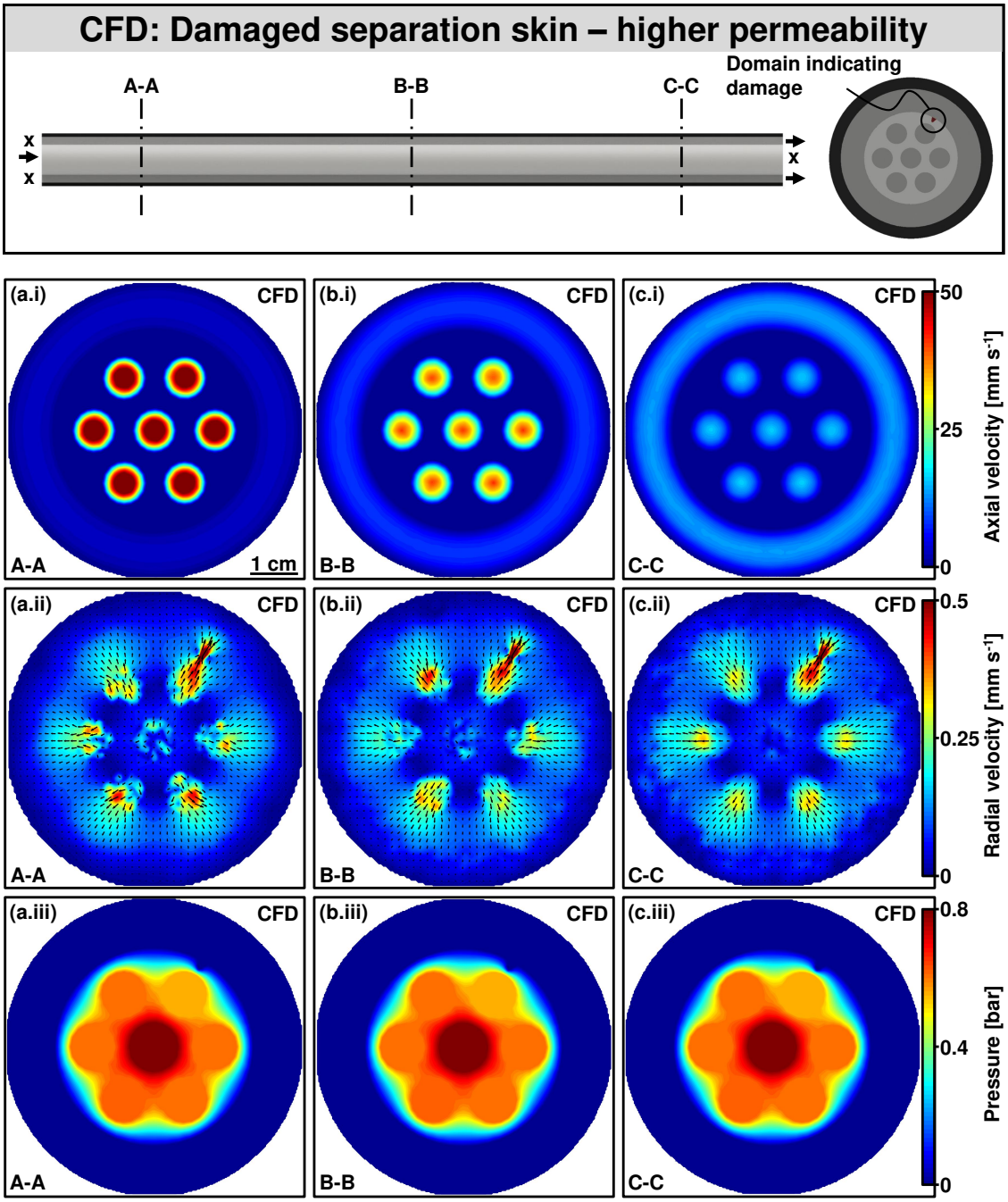

Figure 4.5: CFD simulation of a membrane with damaged separation skin (higher permeability) during membrane inside-out permeation at three positions. Top: axial velocities, middle: radial velocities, bottom: pressure distribution. Damages at the outer layer of the membrane structure do not significantly influence the flow field and consequently the membrane performance.

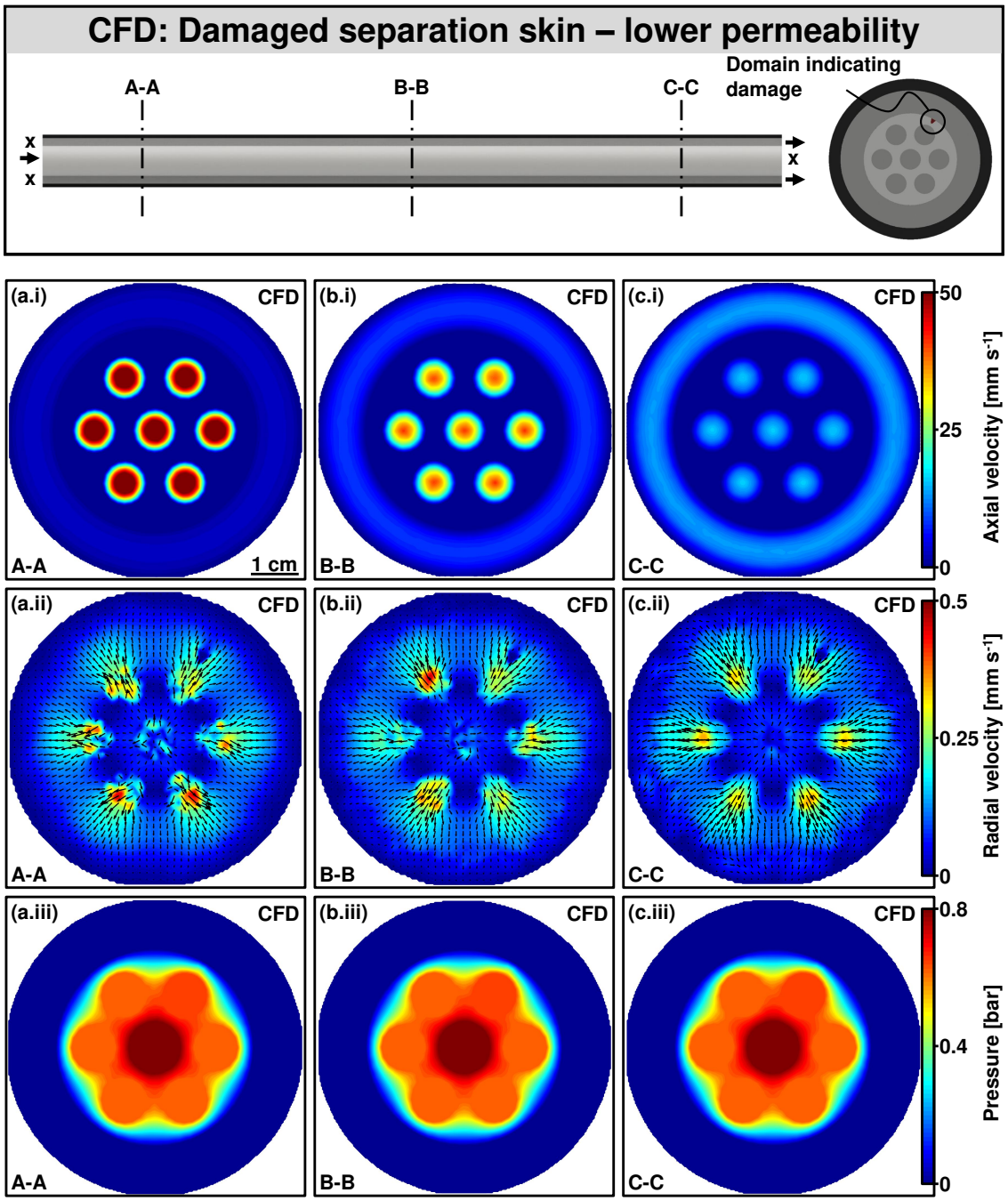

Figure 4.6: CFD simulation of a membrane with damaged separation skin (lower permeability) during membrane inside-out permeation at three positions. Top: axial velocities, middle: radial velocities, bottom: pressure distribution. Damages at the outer layer of the membrane structure do not significantly influence the flow field and consequently the membrane performance.

4.3.5 CFD velocimetry - module flow field

Up until now, a horizontal velocity outlet is assumed. In the following, a vertical outlet channel position for the shell side of the membrane module is investigated.

Module flow field - shell-sided flow The module for MRI measurements has no colinear inlet and outlet in the direction of the membrane. The connection between the shell of the module and the ambient is perpendicular to the membrane direction. This flow arrangement is shown in Figure 4.7.

The perpendicular arrangement of the outlet in inside-out dead-end filtration does not affect the fluid flow as indicated by slices A-A and B-B. The outlet channel has no significant influence on the lumen- to shell-sided permeation throughout the multibore membrane. Distinct characteristics, as shown for the reference module in Section 4.3.1 are dominant. Only in slice C-C, the flow is directed to the outlet to maintain the mass balance in the dead-end arrangement.

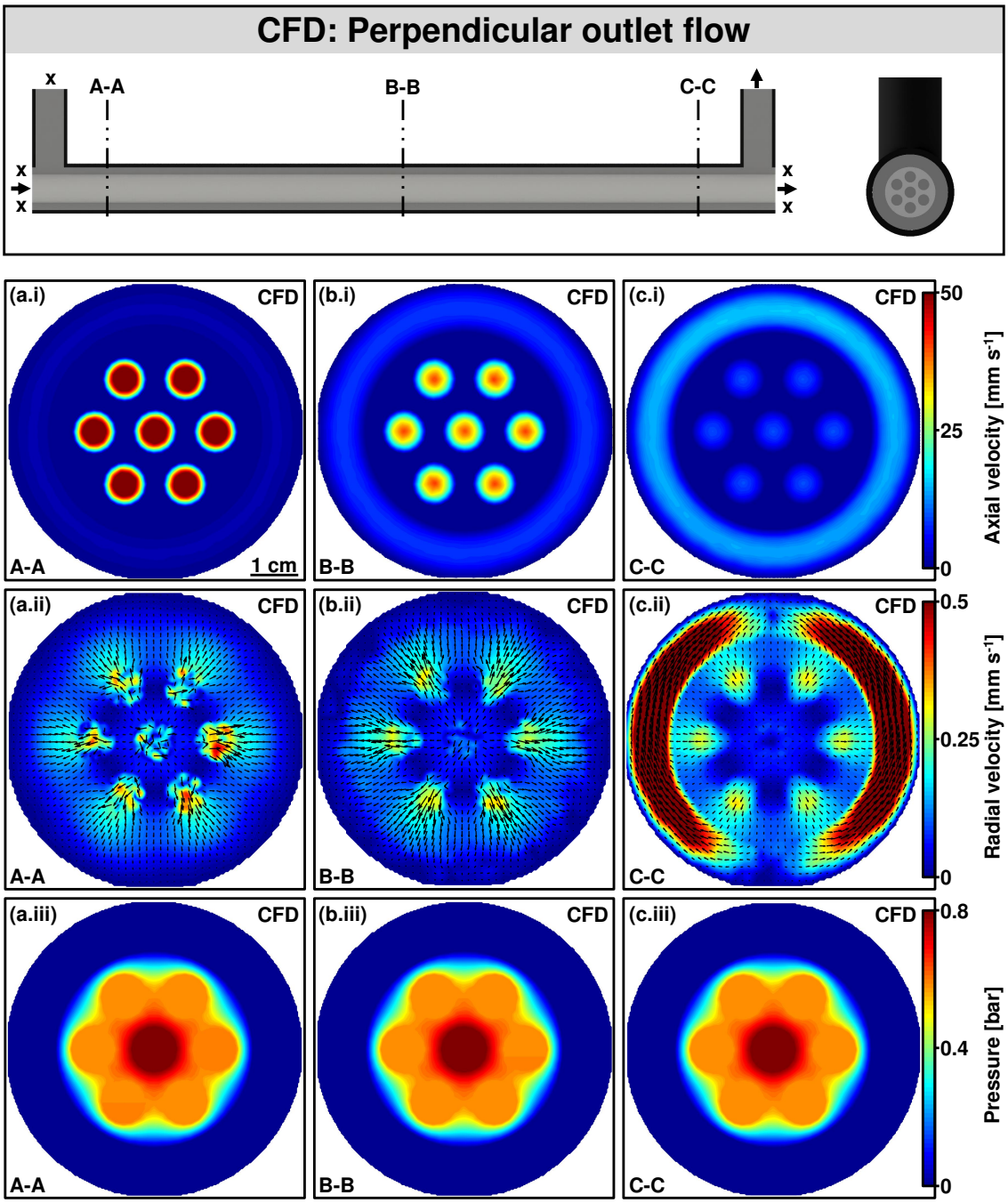

Figure 4.7: CFD simulation of the fluid flow effects on the shell side due to the perpendicular arrangement of the outlet at three positions. Top: axial velocities, middle: radial velocities, bottom: pressure distribution. The outlet channel shows no distinct influence on the lumen- to shell-sided permeation. Only in section C-C the flow is directed to the outlet.

4.4 Comparison CFD simulations and MRI measurements

As mentioned in the introduction, MRI measurements of multibore membranes conducted by Schuhmann et al. [Schu2019] and Wypysek et al. [Wypy2019] showed some unexpected flow phenomena that now can be explained by the simulation results examined in this chapter. The CFD results reveal that hydrodynamic conditions inside membrane modules highly depend on the membrane's position inside the module.

For comparison reasons, Figure 4.8 shows the axial (a) and radial (b) velocity magnitude in the multibore membrane during dead-end pure water inside-out filtration, in which arrows indicate the direction of flow obtained by Wypysek et al. [Wypy2019]. Potting of the membrane inside the module and its swelling behavior cause a bent of the membrane towards one side (here towards the left side). The results are comparable to the CFD simulation of the sagging membrane in Figure 4.4 (slice A-A).

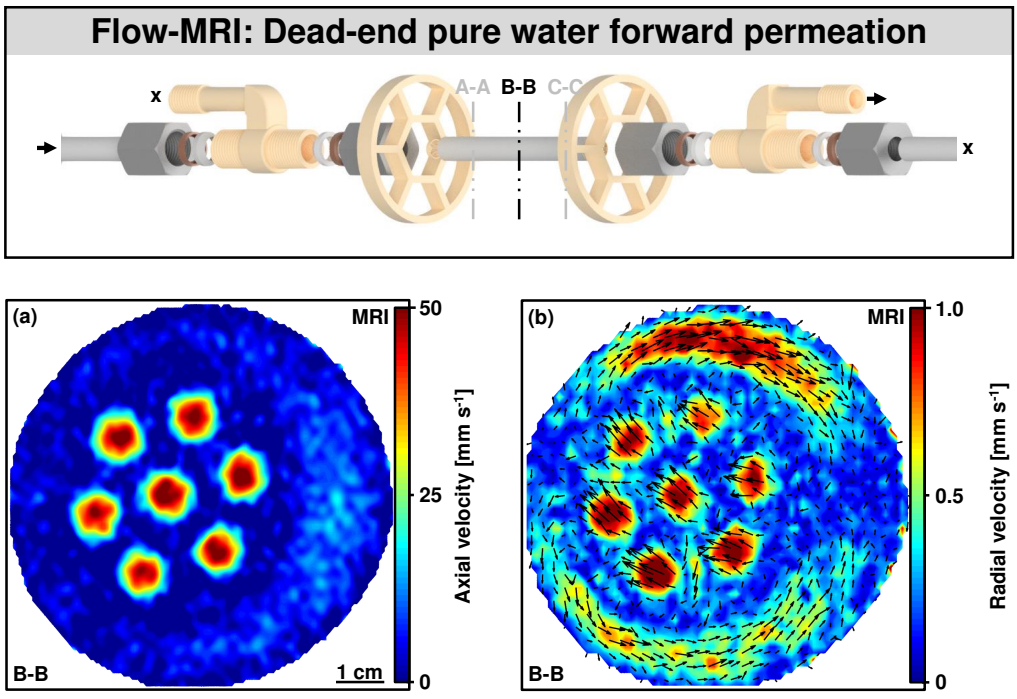

Figure 4.8: MRI velocimetry of pure water dead-end filtration. (a) Axial and (b) radial flow pattern with lumen velocities pointing in one direction and a directed annular gap flow on the shell side.

The axial velocity magnitude at the shell side is highest at the maximum distance between the membrane and inner tube wall, caused by small local pressure differences on the lumen side. This is in good agreement with the CFD results shown in Figure 4.3 and Figure 4.4.

The fluid inside the bore channels forms parabolic laminar profiles similar to all CFD results. However, contrary to the CFD simulations, the flow is distributed unevenly within the seven bores. Thus, the bores contribute unequally to the filtration process. In this experiment, the velocity magnitude of the upper bores is 8 % greater compared to the bottom ones. However, the position and magnitude of deviation vary within different experiments. One possible reason might be small differences in the shape of each channel.

The illustration of the radial velocity magnitude in Figure 4.8 (b) additionally contains arrows to depict the direction of the radial velocities. A secondary flow field forms around the membrane from the minimum distance between membrane and inner tube wall to the maximum distance. This behavior can also be observed in the CFD simulations of the eccentric membrane (Figure 4.3) and the sagging membrane (Figure 4.4). Secondary flow fields arise when the membrane is not situated concentrically within the housing due to local pressure differences.

In MRI measurements, radial velocities in all bore channels are oriented in one direction. In comparison, this effect is only observed for the CFD study of the sagged membrane (A-A, Figure 4.4), in which the middle axis of the membrane has a negative slope and not for the results of the eccentrically positioned membrane. The sagging between two fixed positions occurs due to the manual manufacturing of the module and the swelling behavior of the polymer membrane. The shown images of both measured and simulated flow fields are averaged over a thickness of 10 mm. The net velocity follows the direction of the sagging membrane that is not parallel to the measurement axis of the NMR tomograph. Therefore, averaging results in flux in one direction in every bore. However, this phenomenon also occurs in an infinitesimal slice in the CFD simulation. These directed flow velocities can also be a reason for particle deposition behavior observed

by Wypysek et al. [Wypy2019] as drag forces may force the particles to deposit on one side of the membrane.

Due to higher pressures inside each bore channel, flux that has left one bore does not re-enter another bore. Thus, contrary to the CFD simulations, water flows through the porous matrix instead of the outer bore channels, being the path of least resistance with the highest velocities in between the external bore channels. This can be explained by the skin formation around the bores and the gradual porosity of the polymeric matrix. However, the CFD simulation results show the behavior of ceramic multibore membranes with only little gradients in porosity.

4.5 Conclusion and outlook

The study in this chapter investigated the influence of hydrodynamics on shell and lumen side flow and pressure communication during membrane operation. CFD simulations were performed to analyze the pathways of filtration measured by MRI experiments inside a custom-made multibore single membrane module [Wypy2019]. This combination helps to deeper understand (a) flow phenomena inside multibore membranes in dead-end filtration, (b) the membrane's interaction with its surrounding inside the module because of a non-ideal membrane positioning, and (c) particle deposition behavior during dead-end and cross-flow filtration mode.

CFD simulations are used to mimic challenges within the production process of a membrane module. In a perfectly aligned concentric membrane module in dead-end inside-out filtration mode, the volume flow decreases in the lumen channels and increases in the shell side according to the membrane's permeation properties. The fluid flow permeates with a directed radial flow path through the whole lumen's circumference. The resulting flow field shows no secondary flow field on the shell side. This changes when the positioning of the membrane is changed.

- An eccentric position of the membrane creates a secondary flow field on the shell side due to different distances between membrane and tube wall and, thus, small local pressure differences.
- A sagging membrane due to swelling during permeation and a fixed end position result in a radial flow field formation on shell and lumen side. On the shell side, similar phenomena as in an eccentric position arise. Radial secondary flow in bore channels in the bent direction is observed.
- A permeate outlet perpendicular to the multibore membrane orientation only influences the shell side flow in the vicinity of the outlet. The flow through the membrane is not affected.
- A damaged outside skin does not have a significant negative influence on the flow field and performance of the membrane. The flow diverts insignificantly from its original path. The membrane structure protects the inner separation skin. Hence, a decrease in selectivity is unlikely.

The performed CFD simulations reveal the importance of the module geometry on the flow field during membrane permeation. Unavoidable non-idealities of membrane positioning during construction of the module influences the filtration performance, fouling behavior and backwash capabilities [Wypy2019]. Combining CFD simulations and MRI experiments pioneers the pathway to finding strategies to optimize membrane module design and operation.

However, as stated in Section 4.4, only the simulated flow distribution on the shell and lumen side resembles MRI measurements. Flow paths inside the porous structure of the multibore membrane differ from each other. The model assumptions of the multibore membrane, stated in Section 4.1, in which the geometry does not possess separation layers, and membrane skin does not resemble the membrane structure accurately. Therefore, **Chapter 5: Single Multibore Membrane with Porosity Gradients** focuses on simulating multibore membranes with gradients in porosity and permeability to examine the layers' influence on the internal flow pathways.

5

Single Multibore Membrane with Porosity Gradients

Parts of this chapter have been published as:

Denis Wypysek, Deniz Rall, Tobias Neef, Alex Jarauta, Marc Secanell, Matthias Wessling, "How does porosity heterogeneity affect the transport properties of multibore filtration membranes?", *Journal of Membrane Science* 636 (2021) 119520.

DOI: 10.1016/j.memsci.2021.119520*

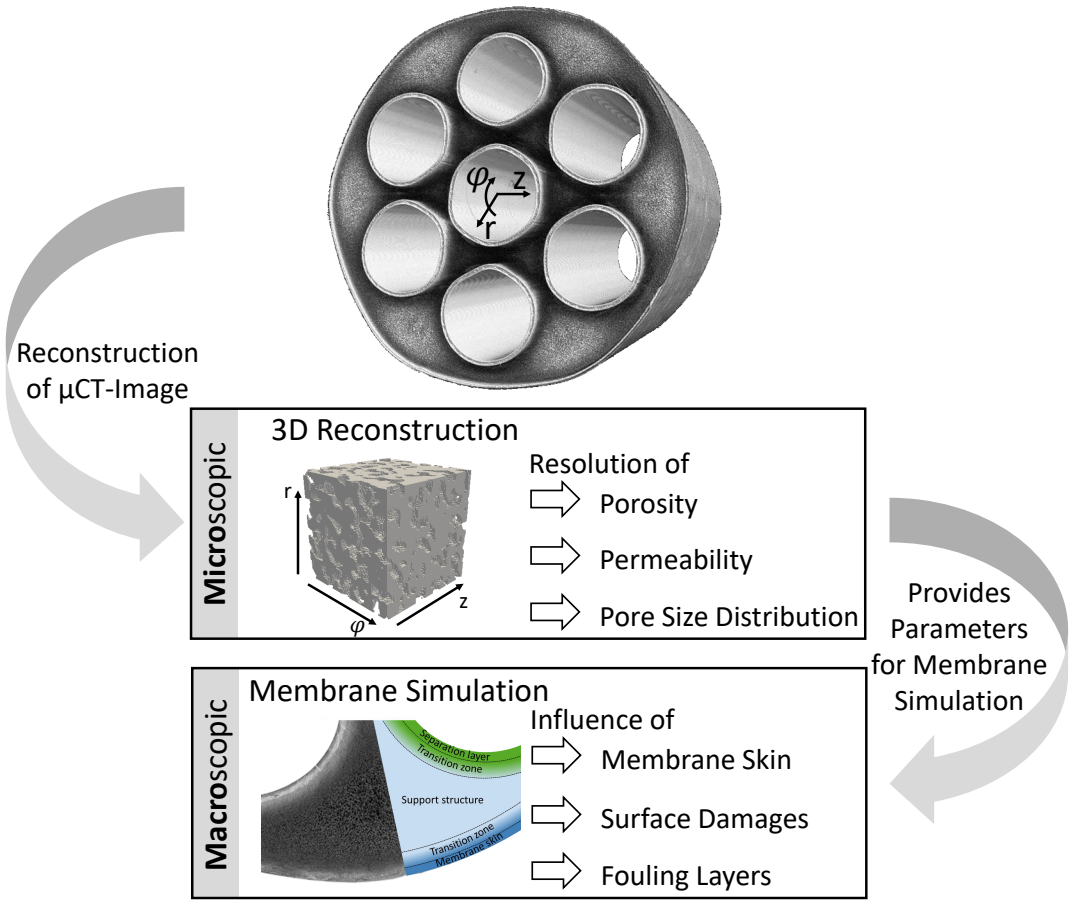

*Journal of Membrane Science Editor's Choice Article for June, 2021

5.1 Introduction

As mentioned in *Chapter 1: Introduction*, ultrafiltration membranes in the pre-treatment in water purification plants feature a porous structure with spatially varying properties depending on the material and manufacturing method [Werb2016]. While pore size distribution and porosity are regarded as homogeneous over the membrane cross section in ceramic membranes [Zhu2015a; Zhu2015b; Zhu2017; Chi2017], polymeric membranes often possess porosity gradients inside the porous structure. Especially in polymeric multibore membranes, these heterogeneities are more predominant than in tubular or fiber membranes because micro- and macrovoids form during fabrication in the precipitation step [Smol1992; Spru2013; Luel2018; Back2019]. At the heart of the inhomogeneous porosity is the polymer coagulation process which is highly non-linear in phase separation and solidification and accompanies considerable shrinkage [Bike2010].

Multibore membranes are increasingly used in industrial processes as they outperform hollow fiber membranes concerning their mechanical sturdiness [Heij2012; Wang2014b], which is particularly important during cleaning and backwashing. However, due to their heterogeneous porous structure, the hydrodynamic conditions inside the membrane's structure are still not unraveled completely. Both the formation of the porous structure during the fabrication and the permeation and filtration behavior of multibore membranes are subjected to current research. [Fred2018; Schu2019]

The performance of multibore membranes is well-studied experimentally [Gill2005; Bu-R2007; Teoh2011; Wan2017; Simk2020]. A majority of these publications focus on the overall performance of the membrane within a membrane module. However, fundamental knowledge of internal flux pathways during permeation, fouling, and backwashing is of great interest. Le Hir et al. [Le H2018], for example, used confocal laser scanning microscopy to localize the deposition of fluorescent nanoparticles after the filtration process. However, for this technique, the authors dried the membranes before the measurement, which can change the observed phenomena. In contrast, magnetic resonance imaging can analyze internal flux

and pathways and fouling phenomena of multibore membranes in-situ and noninvasively [Schu2019; Wypy2019; Mari2020]. As mentioned in previous chapters, Schuhmann et al. [Schu2019] used MRI to investigate the filtration behavior in polymeric multibore membranes. The authors visualized velocity fields in the porous structure of the membrane and gel-layer fouling in the multibore membranes using a sodium alginate solution. They showed uneven flow distribution in the lumen channels. Wypysek et al. [Wypy2019] confirmed and extended these findings by studying pure water dead-end forward filtration and backwashing MRI experiments. Additionally, silica dead-end and cross-flow fouling experiments with subsequent backwashing steps were performed.

Kagramanov et al. [Kagr2001] studied the influence of separation layer and support layer thickness on fluid flow in multibore ceramic membranes with homogeneous pore size distributions in each layer via CFD simulations. The authors found decreasing filtration efficiency from the center to the periphery depending on the layer thicknesses. Frederic et al. [Fred2018] additionally varied the permeability contrast between the support structure (macroporous region) and the separation layer (microporous region). They found a dependency between the permeability contrast and the channels' contribution to the total permeate flux. However, these distinct regions of separation layer and porous support structure with constant porosities are only valid for ceramic multibore membranes. Due to the manufacturing process of polymeric multibore membranes, these membranes have spatial asymmetries in pore size distribution and porosity. Sorci et al. [Sorc2020], for example, used SEM images to obtain the domain geometry of commercial PES membranes and performed 2D simulations of fluid and particle flow within a small representative microporous structure. In their simulations, they identify large unused regions of the internal pore structure. However, these inhomogeneous support structures with variable spatial properties with gradients are insufficiently studied for the whole membrane cross section of fibrous polymeric membranes. In general, the design of porosity, surface properties, fluid flow conditions, and their influence on permeation and retention properties remains a challenge. Still, it

becomes more and more accessible today through combinations of sophisticated experimental and simulation methodologies [Sorc2020; Loha2020].

In Chapter 4: Single Multibore Membrane Module Performance, the pure water forward filtration experiments of Wypysek et al. [Wypy2019] were combined with computational fluid dynamics (CFD). It was shown that geometric non-idealities, such as bending of the multibore membrane and the corresponding permeate channel flow patterns, influence hydrodynamic conditions inside the membrane porosity as well as the lumen channels. Furthermore, fouling patterns follow these hydrodynamic conditions. Yet, quantifying flow through spatially inhomogeneous membranes with porosity gradients at a microscopic scale remains challenging. By now, this flow analysis inside the porous membrane support structure is limited to the rigorous assumption of homogeneous distribution of porosity and permeability. This leads to a bias in the results as the real multibore membrane features porosity gradients at different locations. In this chapter, the presented research approach addresses a methodology to relieve the previous simplifying assumption of homogeneous porosity and quantify the effect of various porosity distribution features.

Therefore, this chapter aims at developing a comprehensive CFD framework to address the missing knowledge of local flow distributions in complex membrane architectures with property gradients. It elucidates hydrodynamic effects like velocity distributions and pressure gradients in a polymeric multibore membrane with heterogeneously distributed material properties during pure water permeation and backwashing mode. Figure 5.1 illustrates the proposed simulation approach. Using the example of a polymeric multibore membrane, the membrane material and its porosity at different regions and directions (radial, angular, axial) are analyzed microscopically by scanning electron microscope (SEM) and X-ray micro-computed tomography (µCT) (see Figure 5.1 top) first. The obtained images were reconstructed into small cubes for further investigation of their properties and flow pathways. This reconstruction of porous structures based on imaging techniques has recently been established in the fields of geophysics [Zhao2018], fuel cells [Sabh2018], and symmetric flat sheet

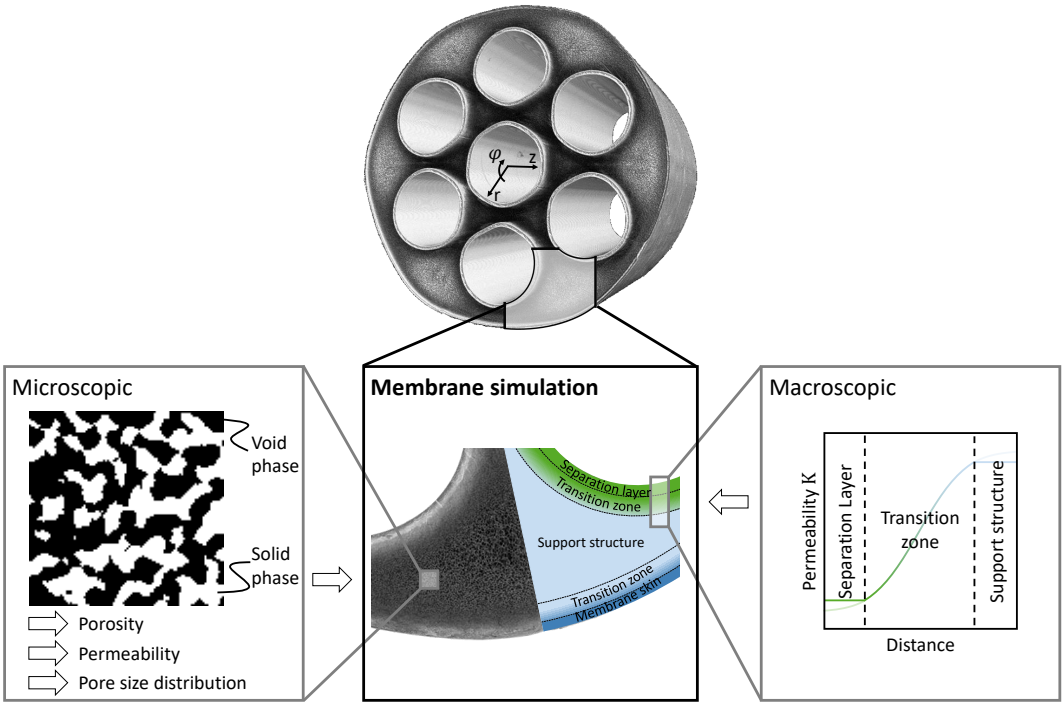

Figure 5.1: Simulation approach - µCT-scans (top) are used to reconstruct position- and direction-dependent samples to obtain microscopic membrane parameters (bottom-left). These membrane-specific properties are input parameters for macroscopic, 2D OpenFCST simulations (bottom-middle) with position-dependent properties and gradients (bottom-right).

membranes [Ley2018]; however, not for polymeric multibore membranes. These reconstructions serve as a volume to apply Stokes flow simulations to obtain values for the intrinsic permeability. Second, these reconstructions are utilized to determine membrane-specific, position- and direction-dependent structural properties like porosity and pore size distribution (see Figure 5.1 bottom-left). Third, the obtained structural properties are input parameters for a macroscopic, two-dimensional membrane simulation with the open-source software OpenFCST [Seca2014; Seca2017]. The developed OpenFCST code enables the simulation of gradients and the different zones of the multibore membrane (see Figure 5.1 bottom-right). Finally, in a case study, the OpenFCST simulation results are compared to the obtained MRI results of Wypysek et al. [Wypy2019].

5.2 Experimentals

The membrane structure of the multibore membranes (top of Figure 5.1) is analyzed and simulated in this work on two different scales: (1) the microscopic scale perspective (see Section 5.2.1) provides insights into the porous structure of the polymeric multibore membrane structure based on µCT-scans and SEM images; and (2) the macroscopic scale perspective (see Section 5.2.2) enables insight into the fluid flow through the membrane's cross section. The following methodology section presents the analysis and numerical methods used for the two different scale perspectives.

5.2.1 Micro-scale property determination

This section focuses on the analysis and reconstruction of the microscopic view of the porous support structure as visualized in Figure 5.2. Recon-

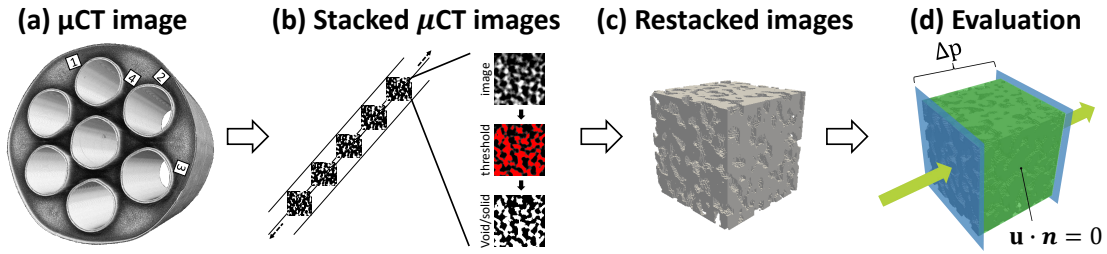

Figure 5.2: Providing insights into the porous membrane material structure through microscopic view: from (a) a µCT-scan to (b) a stack of blurred grayscale slices to a stack of black (void phase) and white (solid phase) slices to a reconstructed mesh of the void phase to (c) the restacked cuboid. (d) Boundary conditions for microscopic Stokes flow simulations for intrinsic permeability calculation.

structed µCT-scans of a hydrophilized PES Sevenbore™ fiber from SUEZ SA (Figures 5.2 (a) to (c), described in detail in Section 2.4) are used to obtain 3D voxel-based meshes of the porous structure for CFD simulations with OpenFCST. The porosity and pore size distribution of the selected slice and cuboid are determined. Stokes flow simulations with deal.II [Bang2016] evaluate the permeability of the support structure based

on the µCT-reconstruction of the polymeric matrix (Figures 5.2 (c) and (d))). As the resolution of the µCT-scans is not sufficient (here $\sim$0.9 µm side length per pixel) to reconstruct the separation layer and membrane-skin layer (pore size of the separation layer according to the manufacturer of $\sim$0.2 µm), a resistances-in-series-model was used (Equation 5.5) and experimentally obtained values by Wypysek et al. [Wypy2019] were taken to calculate the intrinsic permeability of the separation layer and the shell-side skin layer. SEM images are utilized to estimate the porosity in these regions (see Figure 2.10).

Reconstruction of µCT-scans and micro-scale mesh generation

The µCT-image, as shown in Figure 5.2 (a), is obtained by a high-resolution 3D X-ray microscopy device (SkyScan 1272, Bruker). Sample regions 1-4 used for the reconstructions are displayed in Figure 5.2 (a). Samples 1-3 are chosen to evaluate the angular influence of the permeability within the support structure. Sample 4 is chosen to evaluate the radial dependency of the permeability. Due to the limited space between the single channels, the samples are taken outside the outer channels. The chosen cuboid samples have a side length of 100 pixels, corresponding to $\sim$90 µm. The reconstructed meshes of the cuboids represent a representative elementary volume (REV) and are sufficient for the sample analysis (according to [Warg2012; Yoon2013; Garc2018]). Larger sample sizes with homogeneous properties are impracticable due to the small geometry of the multi-bore membrane. Using the µCT-software NRECON RECONSTRUCTION, the REVs are corrected by ring-artifacts reduction, beam-hardening correction, and post-alignment.

To create the 100^3 pixels REV samples, the processed µCT-scan is loaded into the open-source software Fiji [Schi2012]. The sample regions for samples 1-4 are selected and cropped out of the original stack. In the next step, the stack size is set to 100 images (Figure 5.2 (b)). The resulting REVs are then segmented into binary images to distinguish between the void phase and the solid phase of the membrane material using the Otsu

method (here, upper slice set to 75). After applying the threshold, the white color represents the porous media's solid polymer structure, and the black color represents the void phase (Figure 5.2 (b)).

Subsequently, the binary images are aggregated again to form the reconstructed cuboid. The cuboid is created by transforming the binary images from Fiji to a *vtk*-mesh. The *vtk*-mesh file consists of the spatial location of all nodes, all cells, and all material and boundary identifications (which are explained below). This file is generated with the OpenFCST python environment pyFCST. A script (writeVTK.py) generates a mesh with cells only for the porous structure's void phase. The voxel size in x-, y-, and z-direction is set to the resolution of the µCT-scans (0.9 µm in each direction). The execution of this script leads to a reconstructed REV, which can be seen in Figure 5.2 (c).

With these REVs, porosities and pore size distributions for the porous support structure can be estimated, and Stokes flow simulations with boundary conditions highlighted in Figure 5.2 (d) can be performed to evaluate intrinsic permeability.

Analysis of the porosity and the pore size distribution of the support structure

The porosity can be assessed directly from the restacked black and white µCT-images. The porosity of a single slice is calculated by dividing the number of black pixels by the total amount of pixels in one slice (10 000 in this chapter). As described by Wargo et al. [Warg2013], the use of CT imaging is more accurate for determining porosity values compared to SEM imaging.

The pore size distribution (PSD) and the mean pore size diameter are also determined with the restacked cuboids. In this chapter, the sphere fitting algorithm based on Euclidean distance transform (EDT), described and implemented by Sabharwal et al. [Sabh2016] was used (implemented in the open-source writeVTL.py script).

Governing equations and solution strategy

Fluid flow in the microscale is simulated by solving the steady-state, isothermal, incompressible, single-phase Stokes flow simulations without the influence of gravity written as:

$$\begin{aligned} \nabla \cdot \mathbf{u} &= 0 \quad \text{in} \quad \Omega \\ \nabla \cdot \left(-p\hat{\mathbf{I}} + \hat{\boldsymbol{\sigma}} \right) &= 0 \quad \text{in} \quad \Omega, \end{aligned} \tag{5.1}$$

where the shear stress $\hat{\sigma}$ is given by

$$\hat{\boldsymbol{\sigma}} = 2\mu \nabla_s \mathbf{u}, \tag{5.2}$$

and p and $\mathbf{u}$ are the fluid flow pressure and velocity, and μ the dynamic viscosity in the investigated domain Ω, respectively. The governing Stokes flow equations for mass and momentum balance are explained in more detail in Section 2.3.

The weak form of the equations above is discretized using a Taylor-Hood approximation where linear quadrilateral elements are used to approximate the pressure, and quadratic quadrilateral elements are used for the velocity. The weak form is considered as the Finite Element Method is employed, in which the derivation of the weak form is necessary. This choice stems from the fact that the method is available in OpenFCST, which is intended to solve problems with irregular grids and where several physical phenomena are involved. The resulting system of equations is solved by forming the Schur complement. The entire code for this simulation is a modified version of the open-source step-22 deal.II tutorial [Kron2016]. The code is modified to include new boundary conditions, equation parameters, and changing the flow arrangement as explained below. The equations are solved in the computational mesh obtained using pyFCST of the four vtk-meshes of the cuboid reconstructions (Figure 5.2 (c)).

Dirichlet uniform pressure boundary conditions are applied at the surface boundaries in the flow direction (Figure 5.2 (d)). The pressure inlet boundary is set to p = 1.0 Pa, while the outlet pressure is set to zero. At all

other surface boundaries, a Dirichlet boundary condition with zero normal velocity is imposed. Finally, at internal walls, a no-slip boundary condition is applied.

Permeability estimation of the support structure

The intrinsic permeability in all spatial directions is computed at post-processing by computing the volumetric flow rate at the inlet surface of the porous media. Since pore compaction in the applied pressure regimes is not expected [SUEZ], Darcy's law (Equation 5.3) is used to calculate the intrinsic permeability of the reconstructed cuboid in flow direction such that,

$$\kappa = \frac{\dot{V}\mu l}{A\Delta p}, \tag{5.3}$$

where $\dot{V}$ is the volume flow that results from the applied pressure difference, A is the cross-sectional area, l is the media's length, Δp is the applied pressure difference (set to 1.0 Pa in this study), and μ is the dynamic viscosity of the fluid (set to 0.001 Pa s in this study). Length l and cross-sectional area A are based on the cuboid side length. The volume flow is constant in every slice of the mesh along the flow direction. To calculate the volume flow (Equation 5.4), the volumetric flux is integrated over the inlet surface, i.e.,

$$\dot{V} = -\int_A \mathbf{u} \cdot \mathbf{n} \quad dA \tag{5.4}$$

where $\mathbf{n}$ is the normal to the inlet boundary, and A is the inlet Area.

Porosity and permeability estimation for separation layer and membrane-skin interface

The porosity and intrinsic permeability of the separation layer and the membrane-skin interface cannot be evaluated with the method described above for ultrafiltration membranes. Due to pore sizes below the resolution of the µCT-scans, this method is inappropriate to generate meshes.

SEM images (Figure 2.10) of the membrane have a higher resolution and can approximate the membrane-skin layer's porous structure and parts of the separation layer [Warg2013]. To obtain a smooth cross section, the multibore membrane is stored longer than 60 seconds in liquid nitrogen and fractured afterward inside the liquid nitrogen bath. The images are generated by SEM using an acceleration voltage of 5 kV (Hitachi Table Top TM3030 plus). The same cropping and threshold methods as mentioned above are used to obtain the porosity of the separation layer and the membrane-skin layer. The calculated porosity of the separation layer is overestimated with this method, as SEM images display 3D information in a 2D image. Ten samples are cropped, and the average property values and their standard deviation are computed. FIB-SEM could be used in the future for permeability estimation using the method above [Sabh2016].

To estimate the intrinsic permeabilities of the membrane-skin layer and the separation layer, the resistances-in-series model in Equation 5.5 is used (see [Sing2015]). This equation is based on the theory of asymmetric membranes, where the total membrane resistance is the sum of each layer resistance, i.e.,

$$\kappa_{\text{total}} = t_{\text{total}} \cdot \left(\frac{t_{\text{support structure}}}{\kappa_{\text{support structure}}} + \frac{t_{\text{separation layer}}}{\kappa_{\text{separation layer}}} + \frac{t_{\text{membrane-skin interface}}}{\kappa_{\text{membrane-skin interface}}} \right)^{-1}, \tag{5.5}$$

where the thickness t_i of the corresponding domain and the measured total intrinsic permeability κ_{total} is obtained from the values in the previous chapter. The membrane-skin layer's intrinsic permeability is assumed to be equal to the support structure's intrinsic permeability. This assumption is made because the mean pore radius and the porosity of the membrane-skin layer are closer to the values of the support structure than to the values of the separation layer and is necessary for solving Equation 5.5 for the unknown separation layer's intrinsic permeability $\kappa_{\text{separation layer}}$. As the separation layer is the significant domain for membrane separation, this resistance cannot be neglected.

5.2.2 Macro-scale fluid flow simulations

The macroscopic simulations provide insights into the fluid flow through the membrane's cross section. The simulation results on a membrane module scale extend the understanding of experimentally derived polymeric multibore membranes' properties.

The following section describes methods used to simulate porous multibore membranes. First, the computational domain, generated mesh (see Figure 5.3 (a)) and mesh refinement strategy (see Figure 5.3 (b)) are described. Next, the governing equations of the fluid flow in the porous media and the solution strategy are described, followed by the methodology used to implement the position-dependent properties in the porous media (see Figure 5.3 (c)). Penultimate, the simulation parameters are listed, which are the resulting porous media properties obtained with the methods described in the previous section and which are assigned as input parameters for the conducted 2D OpenFCST [Seca2014; Seca2016] simulations. Finally, the evaluation of velocities inside the separation layers is explained.

A compressible version of the used numerical model was derived and validated by Jarauta et al. [Jara2020] by first solving a lid-driven cavity flow benchmark problem and then simulating a gas permeability experimental setup and comparing experimental and numerical results. In this chapter, the OpenFCST model is supplemented by a position-dependent property method, which results are compared to MRI measurements in Section 5.3.2.

Mesh generation

A computational mesh with quadrilateral elements is generated to describe the membrane module. For this purpose, the open-source, cross-platform software SALOME 7.3.0 is used [Ribe2007]. Figure 5.3 (a) depicts the idealized cross-sectional geometry of a membrane module with a multibore membrane in its dry state. The 2D mesh consists only of the membrane domain (dark blue in Figure 5.3 (a)). The geometric values in Figure 5.3 (a) are input parameters for the mesh generation. The mesh con-

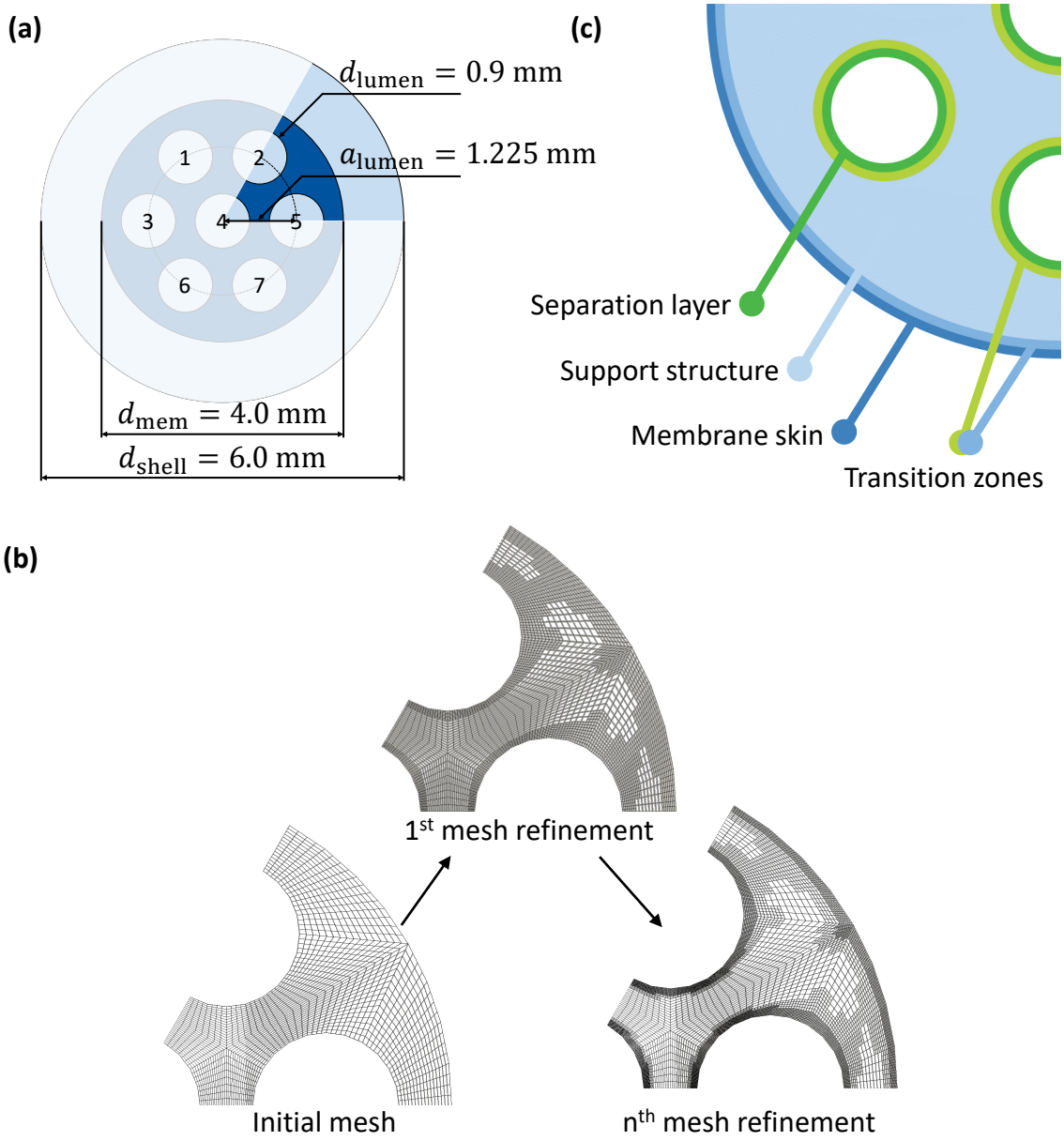

Figure 5.3: (a) Implemented geometry of a multibore membrane with parameters taken from a SevenBore™fiber provided by SUEZ, including definition of enumerated lumen channels. (b) Generation of a macroscopic mesh of the membrane geometry, including the subdivision into quadrilateral base elements and adaptive mesh refinements. (c) Abstract layer-based model of the membrane geometry with simplified constant zones for the separation layer, support structure, membrane outer skin, and transition zones guarantees continuity between constant zones and leads to property gradients.

sists of five domains: separation layer, support structure, membrane-skin, and two transition zones. Each zone is identified with a different mate-

rial identifier and will be assigned different properties. Furthermore, the mesh is adaptively refined six times in separation layer and membrane-skin zones to better approximate larger gradients in this region by dividing each quadrilateral element into four equally-sized elements at each refinement level. The final meshes with magnifications of the boundaries can be seen in Figure 5.4.

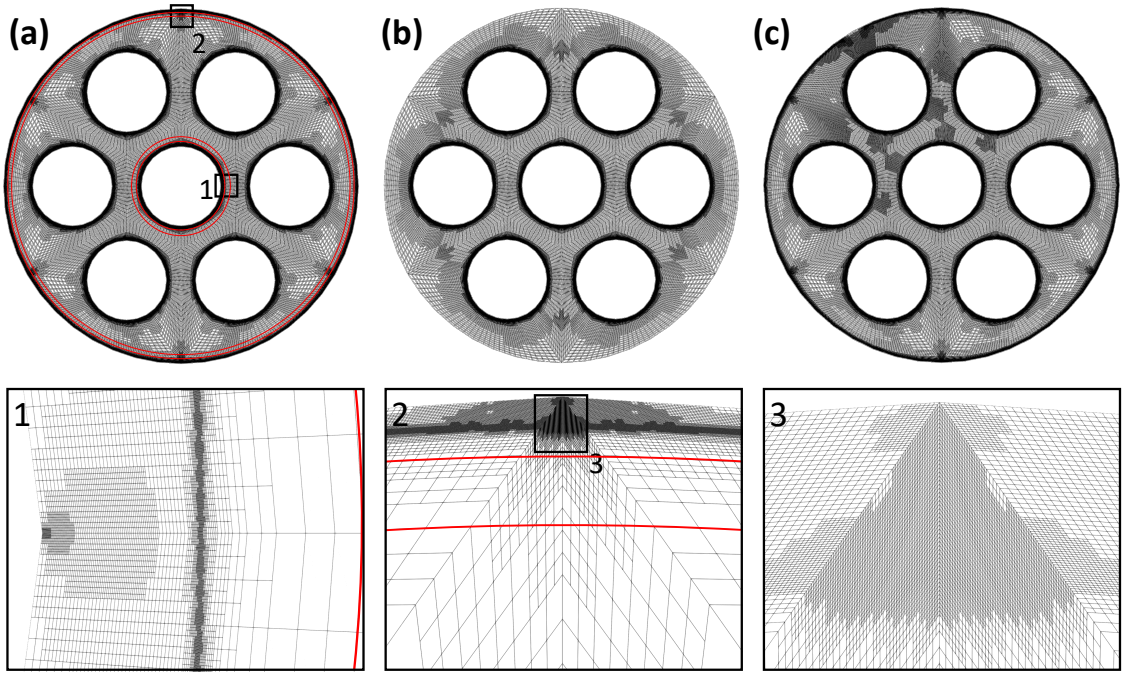

Figure 5.4: Mesh after final refinements of multibore membrane geometry (a) with skin layer, (b) without skin layer, (c) with skin layer and damaged zone and additional magnifications 1, 2, and 3. Red circles indicate position of transition zones.

Governing equations

The steady-state incompressible Navier-Stokes Equations 5.6 and 5.7 with a friction factor to account for the porous media are solved in the membrane domain, i.e,

$$\nabla \cdot \mathbf{u} = 0 \quad \text{in} \quad \Omega, \tag{5.6}$$

$$\rho\nabla\cdot\left(\frac{1}{\epsilon}\mathbf{u}\otimes\mathbf{u}\right)=\nabla\cdot\left(-p\hat{\mathbf{I}}+\hat{\boldsymbol{\sigma}}\right)+\mathbf{F}\quad\text{in}\quad\Omega, \tag{5.7}$$

where

$$\hat{\boldsymbol{\sigma}}=2\mu\nabla_s\mathbf{u}, \tag{5.8}$$

$$\mathbf{F}=\begin{cases}\mathbf{0}\quad\text{in}\quad\Omega_c,\\ -\mu\mathbf{K}^{-1}\mathbf{u}\quad\text{in}\quad\Omega_p.\end{cases} \tag{5.9}$$

ρ, p, $\mathbf{u}$ are the fluid flow density, pressure and velocity, and $\mathbf{K}$ is the permeability tensor in the investigated channel domain Ω_c and porous media domain Ω_p, respectively. A detailed derivation of the volume-averaged form of the Navier-Stokes equations, together with some analysis and validation studies, is given in [Jara2020] for the compressible form of the equations.

The Finite Element Method is used to solve the system of equations. The non-linear system of equations is solved using a Newton-Raphson algorithm where, at each iteration, the discrete, linearized weak form of the above equations is solved (see Subsection 5.2.1). The solution variables are discretized using a Taylor-Hood approximation, where linear quadrilateral elements are used to approximate the pressure, and quadratic quadrilateral elements are used for the velocity. The resulting system of equations is solved using the direct parallel solver MUMPS. The numerical solver is implemented in OpenFCST [Seca2017], which uses the parent Finite Element deal.II libraries [Kron2016]. A detailed explanation of the volume-averaging and solution strategy is provided in [Jara2020] for a compressible version of the same solver, including the solution of some classical benchmark problems such as a lid-driven cavity flow.

Position-dependent property method

Implementing a continuous position-dependent property method is infeasible with the commercial software COMSOL Multiphysics® as it can be seen in the previous chapter. OpenFCST, on the other hand, allows to implement a C++ class to impose a position-dependent porosity and intrinsic permeability. In this chapter, the porosity and intrinsic permeability are continuous position-dependent functions in the whole membrane.

The membrane's geometry is categorized into five zones to account for the different porosity and intrinsic permeability values. Figure 5.3 (c) illustrates the different zones in a sketch of a membrane section. Three zones have constant properties, i.e., the separation layer, the membrane-skin interface, the support structure, and two zones have variable properties allowing for a smooth transition between zones.

While the porosity is a single number, the intrinsic permeability is a rank two tensor. The permeability tensor $\mathbf{K}$ contains intrinsic permeabilities in a Cartesian coordinate system. The samples in Section 5.2.1 are cropped and twisted by the angle ϕ to account for the cylindrical shape of the membrane fiber. Therefore, the returned $\mathbf{K}$-tensor is the product of a base transformation matrix and the evaluated permeabilities from the Stokes flow simulations in Section 5.2.1.

The values for the constant zones are given by input parameters (summarized in Table 5.3). The transition zones guarantee a continuous transition of the property values between two neighboring constant property zones. One possibility for such a transition function is the Heaviside function. The original Heaviside function H is a step function with the function values 0 at $x < 0$ and 1 at $x \geq 0$. A modified smooth analytical approximation of the Heaviside function is used (Equation 5.10), where K_{max} and K_{min} are the property values of the neighboring constant zones, Δx is half the transition zone width, x_0 is the distance of the middle of the transition zone from the origin, and $q \in [0.5, 1]$ is the percentage of the step height $H_{max} - H_{min}$, which is obtained in the distance Δx from x_0. The distances are obtained by counting pixels in the SEM images of the membrane.

Table 5.1 summarizes input parameters for the used smooth Heaviside function. Figure 5.5 illustrates the function and its parameters. At each quadrature point in the domain, the Cartesian coordinates of the point are used to calculate its cylindrical coordinates, r and ϕ, and identify in which zone the point is located. Depending on the assigned zones, the **K**-tensors are calculated. In the three constant zones, the permeability tensor is specified based on the input parameters. In transition zones, the corresponding Heaviside function value determines the **K**-tensor.

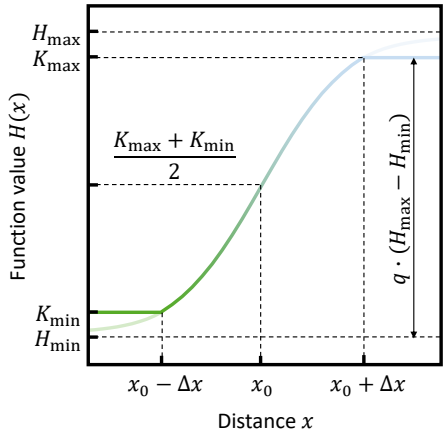

$$H(x) = H_{min} + \frac{H_{max} - H_{min}}{1 + e^{-2k(x-x_0)}}$$

$$\text{with} \quad k = \frac{ln(\sqrt{\frac{q}{1-q}})}{\Delta x}$$

$$H_{min} = \frac{K_{max}(1 + e^{-2k\Delta x}) - K_{min}(1 + e^{2k\Delta x})}{e^{-2k\Delta x} - e^{2k\Delta x}}$$

$$H_{max} = K_{min}(1 + e^{2k\Delta x}) - H_{min}e^{2k\Delta x} \tag{5.10}$$

Figure 5.5: Smooth Heaviside function used to model the transition zones with a width of $2 \cdot \Delta x$ that guarantees continuous property values between constant zones. The steepness of the transition is regulated with the parameter q.

Table 5.1: Input parameters for the smooth Heaviside function obtained from SEM images.

Parameter	Value
Separation layer thickness	55 µm
Skin layer thickness	40 µm
Separation transition zone width	55 µm
Skin transition zone width	40 µm
Transition smoothness q [-]	0.8

Input parameters and boundary conditions

Settings and input parameters used for the simulation are summarized in Table 5.2. Six adaptive refinements are used to achieve a grid-independent solution and accurate results where large changes in solution variables exist. The refinement threshold specifies the percentage of cells to be refined as only the cells with the highest estimated error are refined. Error estimation is performed using a Kelly error estimator [Kell1983].

Table 5.2: Settings and input parameters for OpenFCST simulations.

Property	Setting
Non-linear solver	NewtonLineSearch
Refinement method	AdaptiveRefinement
Cycles of refinement	6
Refinement threshold	0.4
Coarsening threshold	0.0
Equations	Volume-averaged Navier-Stokes
Simulation conditions	steady-state, incompressible, isothermal, single-phase, single-component, no gravity
Boundary condition	Outlet: Dirichlet pressure normal stress free at 0 bar Else: Dirichlet pressure at 0.6 bar
Fluid	Water at 20 °C

Dirichlet pressure boundary conditions are specified in the lumen and shell. For the filtration mode (meaning pure water forward permeation) simulations, high pressure is set in the lumen and low pressure in the shell. For backwashing mode simulations, the pressure gradient is reversed. A pressure difference of 0.6 bar is specified between lumen and shell based on the pressure results of the simulations in the previous chapter.
To analyze the influence of the membrane-skin interface and to show the possibilities of the developed simulation model, the simulations are conducted under three different conditions:

1. The properties of the membrane-skin interface are set equal to the properties of the separation layer. This configuration resembles the multibore membrane's structure best as SEM- and μCT-scans show lower porosities on the outer skin of the membrane as well as on each lumen channel's surface.

2. The properties of the membrane-skin interface are set equal to the properties of the support structure. With this setting, a membrane without an outer skin is mimicked. Due to the lack of an additional resistance, backwashing efficiency could be improved.

3. The properties of the membrane-skin interface are set equal to the properties of the separation layer. An additional damaged zone above channel 1 (top-left) is implemented, which has the same properties as the support structure. During the manufacturing process of multibore membrane modules for MRI analysis, spacers were used to hold the membrane in place, which caused damage to the membrane's outer skin. With this setting, the influence of a damage on the outer membrane skin is analyzed.

The corresponding permeability and porosity values result from the Stokes flow simulations of the cuboids. These input parameters can be found in Table 5.3.
In Section 5.3.2, OpenFCST simulations are compared to MRI measurement from Wypysek et al. [Wypy2019]. In this simulation, the pressure drop (here TMP) is changed to 50 mbar to match the MRI experiments. Setting one is chosen, in which the membrane-skin interface is set equal to the properties of the separation layer because (a) the MRI measurement shows no significant asymmetries in the membrane domain, and (b) SEM images reveal the existence of a membrane-skin layer.
In the following, backwashing experiments after fouling with silica particles are mimicked. To perform this simulation, the blocked domain permeability and porosity are reduced to $K_{\phi\phi} = K_{\mathrm{rr}} = 1.6 \times 10^{-14}\,\mathrm{cm}^2$, and $\epsilon = 0.2$. Parameters for start angle of blocking, end angle of blocking, and penetration depth of blocking (which equals a fouling thickness of 10 µm) are also

Table 5.3: Parameter configurations for three macroscale simulation settings of a polymeric multibore membrane with OpenFCST. Porosity of separation layer is averaged over 10 SEM images. Permeability of support structure taken from Stokes flow simulations results of reconstructed µCT-images.

		Settings		
		1	2	3
		Membrane-skin =	Membrane-skin =	Membrane-skin =
Zone	Variable	Separation layer	Support structure	Separation layer + defect
Membrane-skin	ε [-]	0.2	0.63	0.2
	K_{rr} [cm^2]	1.6×10^{-12}	2.0×10^{-8}	1.6×10^{-12}
	$K_{\phi\phi}$ [cm^2]	1.6×10^{-12}	1.3×10^{-8}	1.6×10^{-12}
Separation layer	ε [-]	0.2	0.2	0.2
	K_{rr} [cm^2]	1.6×10^{-12}	1.6×10^{-12}	1.6×10^{-12}
	$K_{\phi\phi}$ [cm^2]	1.6×10^{-12}	1.6×10^{-12}	1.6×10^{-12}
Support structure	ε [-]	0.63	0.63	0.63
	K_{rr} [cm^2]	2.0×10^{-8}	2.0×10^{-8}	2.0×10^{-8}
	$K_{\phi\phi}$ [cm^2]	1.3×10^{-8}	1.3×10^{-8}	1.3×10^{-8}
Above channel 1	Defect	false	false	true

specified. The fouling domain's angles are based on MRI measurements by Wypysek et al. [Wypy2019]. All other parameters are identical to the case of equal membrane-skin and support structure properties. A setting without an outer skin layer is chosen to link all observed phenomena to the influence of the separation layer resistances.

Evaluation of separation layer velocities For each simulation result, the velocity distribution inside the separation layers of each bore channel was evaluated in a depth of 25 µm from the inner lumen radius and plotted in polar plots. Thus, these plots can be directly linked to each bore channel. Figure 5.6 shows an example bore and its velocity simulation result of a multibore membrane with skin layer properties similar to the separation layer during backwashing. The magnifications show that the round bore channels are simulated as a polygon with 24 corners due to simulation robustness. This has the disadvantage of velocity hot spots in each corner of the separation layer, which results from a smaller distance towards the porous support structure.

Data points from the middle of the separation layer were chosen to represent the velocity inside this layer (see Figure 5.6 (b)). These velocity values are plotted over the respective position (defined as angle) as it can be seen in Figure 5.6 (b) (zero degrees on the top of a bore channel with increasing angles clockwise). To finally evaluate the separation layer velocities, maximum (Figure 5.6 (c.i)) and minimum (Figure 5.6 (c.ii)) velocities are plotted over the respective position in the bore channel. The polar plots help visualize better how fluid flows into a bore (for backwashing mode). As shown in Figures 5.6 (c.i) and (c.ii), the shapes of the velocity profiles are similar to each other. The sole difference is the velocity magnitude. Hence, only minimum velocities in the results section are shown, and relative velocities values are compared.

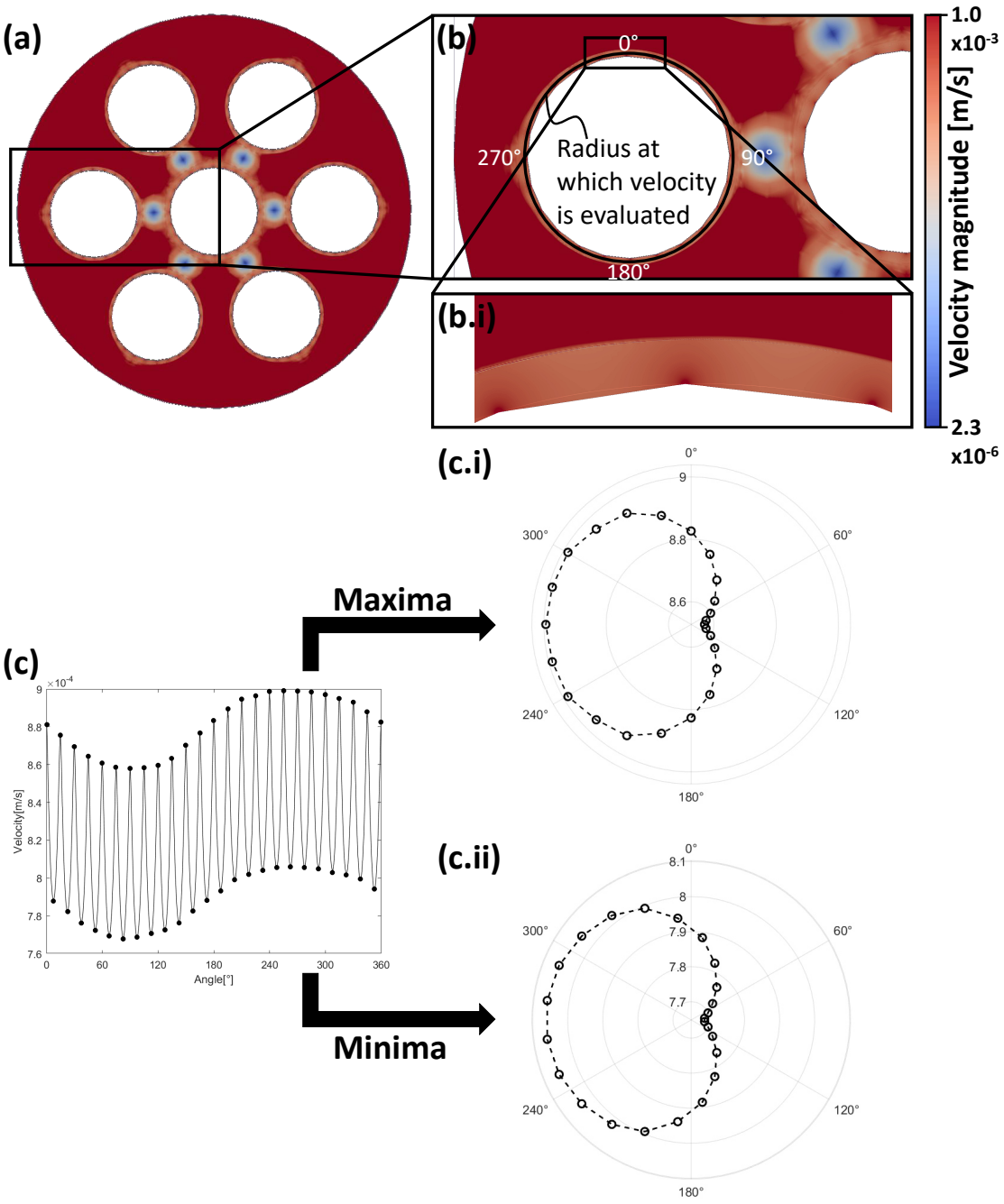

Figure 5.6: Velocity results of a multibore membrane with skin layer properties similar to the separation layer during backwashing. (a) Porous structure velocity and magnifications in (b) and (b.i). (b) Black circle illustrates position at which velocity values are evaluated; definition of angles. (c) Resulting separation layer velocities over respective angle with marked minima and maxima. Polar plots of (c.i) maximum and (c.ii) minimum velocity values.

5.3 Results and discussion

5.3.1 Micro-scale analysis of the reconstructed samples

The analysis of the four reconstructed µCT-samples provides values for the porosity, the pore size distribution (PSD), and the permeability of the membrane's support structure. First, the porosity is analyzed to ensure homogeneity of the samples in all flow directions to perform post-processing of simulations with Darcy's law. Second, the pore size distribution is analyzed to ensure comparability between the samples and determine the mean pore diameter for the support structure.

Porosity estimation for the porous support structure using µCT-scans

Table 5.4 lists all layers' average porosities for each evaluated sample and direction with its respective standard deviation. The layer porosity in all three directions fluctuates slightly (standard deviation of max. 3.3 %) around the average porosity value, and also, no gradient is recognizable from layer one to 100. As an example, Figure 5.7 shows the evaluated porosities of sample 1 plotted against their corresponding image slice.

Table 5.4: Porosity results for each direction for four evaluated µCT-samples, averaged over all layers with corresponding standard deviations.

	Support structure		
	Porosity in ϕ [-]	Porosity in r [-]	Porosity in z [-]
Sample 1	0.63 ± 0.03	0.63 ± 0.03	0.63 ± 0.02
Sample 2	0.62 ± 0.03	0.62 ± 0.04	0.62 ± 0.03
Sample 3	0.63 ± 0.03	0.63 ± 0.03	0.63 ± 0.02
Sample 4	0.63 ± 0.02	0.63 ± 0.04	0.63 ± 0.02
Total average	0.63 ± 0.03	0.63 ± 0.03	0.63 ± 0.02

All samples have a similar average porosity from 61.72 % to 63.39 % for all directions and a small standard deviation from 1.61 % to 3.29 %, indicating a homogeneous porosity and directional independence for large areas in the membrane's support structure. The smallest average porosity standard

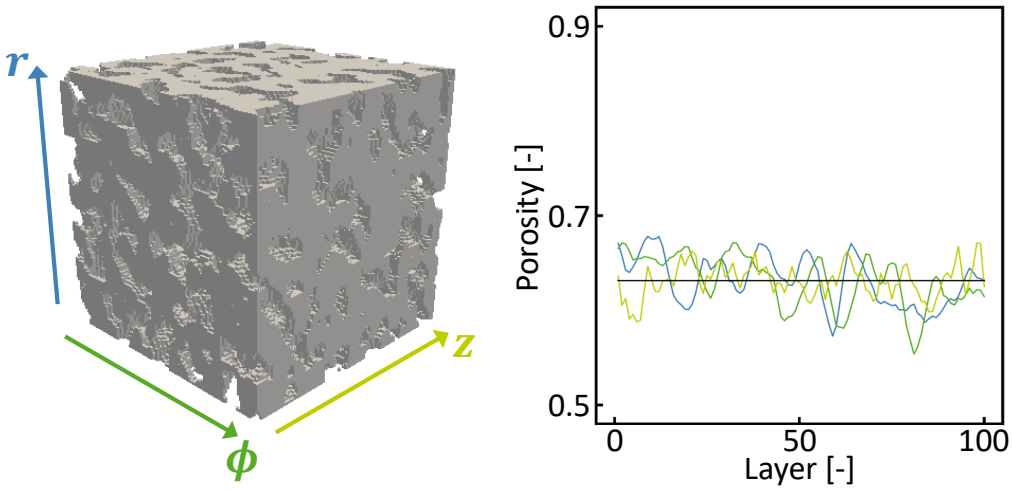

Figure 5.7: Analyzed porosity of a reconstructed mesh of the void phase within the support structure of the multibore membrane of sample 1. Additionally to the overall averaged total porosity in all 100 layers (solid black line), the porosity in all three directions for every layer is evaluated. Samples 2, 3 and 4 are not shown as the porosity analysis provided is similar.

deviation is in the extrusion direction of the membrane (z-direction), likely due to the manufacturing process, as the membrane is extruded through a nozzle. Given the similar average porosities in all directions, the investigated domain is expected a representative elementary volume. Therefore, it can be used to estimate average transport properties, such as intrinsic permeabilities.

The previous chapter used 2D field emission scanning electron microscope (FeSEM) images to obtain the membrane porosity. One disadvantage of analyzing FeSEM images is the presence of 3D information in a 2D image. That is why FeSEM images do not depict a 2D plane in the membrane correctly. Even if the SevenBore™membranes may vary from batch to batch, the porosity value of 0.82 was overestimated. This limitation is reduced by the µCT-scans in this chapter.

PSD for the porous support structure using µCT-scans

The pore size distribution behaves similarly for each sample without significant fluctuations. The mean pore radius is averaged over all mean pore

radii and results in $3.7 \pm 0.2\,\mu m$. The support structure's pore size distribution for all four samples is shown in Figure 5.8.

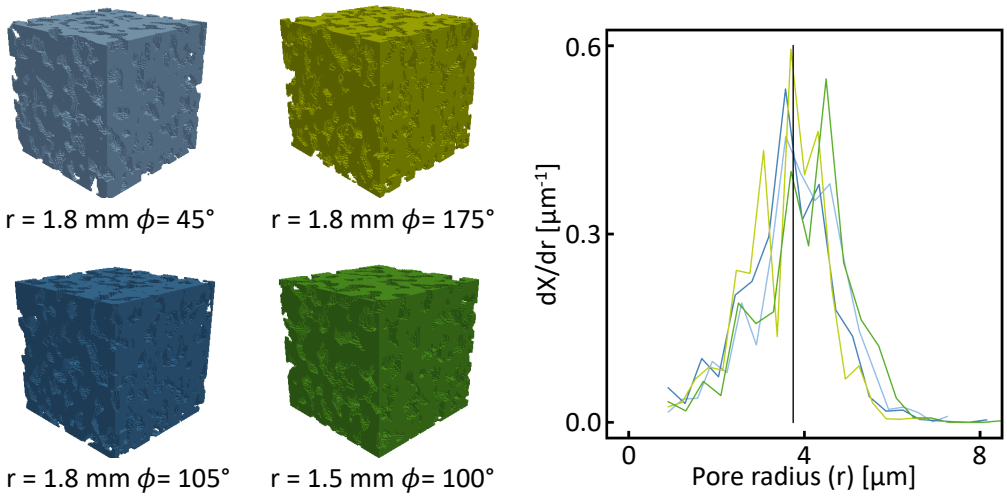

Figure 5.8: Analysis of the pore size distribution of the reconstructed samples. The overall mean pore radius (black line) is averaged over all mean pore radii.

Permeability estimation for the porous support structure using Stokes flow simulations

Intrinsic permeability values for the porous support structure with its respective standard deviations (for all analyzed samples) are obtained from Stokes flow simulations for an applied pressure gradient of 1 Pa and are summarized in Table 5.5.

The results show that the intrinsic permeability values are independent of the angle ϕ and radius r of the sample position in the support structure. However, the resulting intrinsic permeability differs depending on the flow direction and suggests an anisotropic support structure. The value in r-direction is the highest, and the one in z-direction (extrusion direction) the lowest in all samples. This is a new insight from the used multibore membrane. This variation may stem from the precipitation process of the extruded hollow fiber. For subsequent simulation steps, the averages in r- and ϕ-orientation are used as the permeability value. They describe the slice of the membrane simulated by the openFCST framework.

Table 5.5: Stokes flow simulation results for intrinsic permeability values in each flow direction for the porous support structure, averaged over four samples with corresponding standard deviations.

	Support Structure
Direction	Permeability [cm^2]
K_{rr}	$2.0 \pm 0.3 \times 10^{-8}$
$K_{\phi\phi}$	$1.3 \pm 0.2 \times 10^{-8}$
K_{zz}	$5.4 \pm 0.6 \times 10^{-9}$

The pressure distribution simulation results for the porous support structure for an applied pressure gradient of 1 Pa and the graphs with all resulting intrinsic permeabilities plotted over the four individual samples are shown in Figure 5.9.

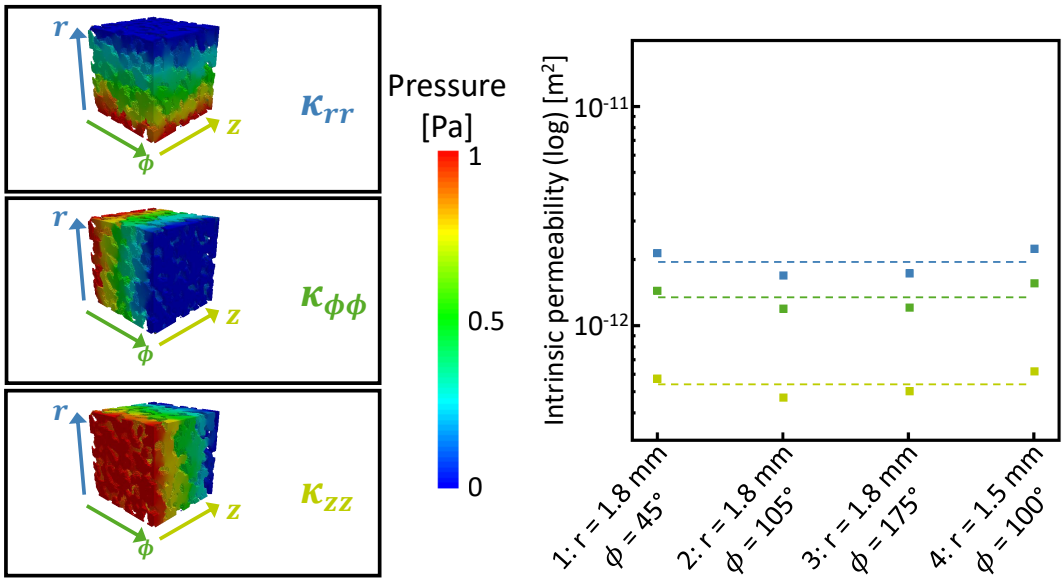

Figure 5.9: Stokes flow simulation results. Left: solution mesh with the pressure drop in radial (top), ϕ (middle) and axial (bottom) flow direction. Right: Direction dependent intrinsic permeabilities plotted over each sample (dashed line represents average value).

Porosity and permeability estimations for separation layer and membrane-skin interface

The estimated averaged mean pore radius, R_m, and the averaged porosity, ϵ, of the ten analyzed SEM images of the separation layer, and the membrane-skin interface are listed in Table 5.6. The estimated mean pore radius of the separation layer is in good agreement with the manufacturer data of 20 nm [SUEZ].

Table 5.6: Results of SEM analysis of mean pore radius and porosity of the separation layer and the membrane-skin interface with corresponding standard deviations. For comparison reasons corresponding simulated values for the support structure are added.

Parameter	Separation layer	Membrane-skin int.	Support structure
R_m [nm]	18 ± 2	960 ± 40	3700 ± 200
ϵ [-]	0.20 ± 0.04	0.54 ± 0.02	0.63 ± 0.03

To calculate the separation layer permeability K_{ii}, the measured total intrinsic permeability of $1.1 \times 10^{-15}\,m^2$ as well as and t_i values from the previous chapter are used. The permeability values of the support structure and the membrane-skin interface are assumed to be equal as the mean pore radius and the porosity of the membrane-skin interface are closer to the support structure values than to the values of the separation layer. This overestimation of the intrinsic permeability of the membrane-skin interface leads to a slightly overestimated intrinsic permeability for the separation layer. Using the resistances-in-series model in Equation 5.5, the permeability for the separation layer is calculated to: $K_{ii,\,\text{separation layer}} = 1.6 \times 10^{-12}\,cm^2$. A prediction of the different K_{ii} values in the separation layer is not possible. Therefore, only one value for all directions is used in the final membrane simulation step.

5.3.2 Macro-scale membrane simulation

Figures 5.10 to 5.13 show the predicted velocity and pressure distributions for different membrane-skin interface conditions, illustrated on top of each

figure. The top row depicts pure water forward permeation simulation results (from lumen into shell), whereas the bottom row shows backwashing results (from shell into lumen). The left figures provide velocity magnitude data in the corresponding colormap ($\sqrt{v_x^2 + v_y^2}$) with normalized arrows depicting the velocity direction. The figures in the middle show the pressure distribution within the membrane domain. The scale ranges from 0.6 bar (set pressure boundary condition) at the inlet boundaries to 0 bar at the outlet boundaries in all figures. Velocities evaluated in the middle of each separation layer are visualized in polar plots on the right in each figure.

Properties of membrane-skin interface set equal to properties of separation layer

Figure 5.10 shows simulation results of a multibore membrane with a membrane-skin interface with the properties of the separation layer. This setting mimics a membrane with a less porous layer on the outer skin and resembles the original membrane best. The scale of the velocity magnitude in this setting ranges from $0\,\mathrm{mm\,s^{-1}}$ to $5\,\mathrm{mm\,s^{-1}}$. It is noticeable that the permeation mode and the backwashing mode are interchangeable in this case. The pressure graphs' colormaps are reversed, the velocity magnitudes are identical, and the arrows for the velocity direction point in the opposite direction. Also, the velocity magnitudes inside the separation layers are equal for each bore, respectively. The behavior can be regarded as ideal and symmetric due to non-existing damage or fouling resistances. Since the results are rotationally symmetric, only one-fourth of the whole membrane cross section is presented in the flow field and pressure distribution graph.

Pressure distribution The pressure graphs depict a pressure drop in the separation layer (from 0.6 bar to approx. 0.3 bar) as well as in the membrane-skin interface (from approx. 0.3 bar to 0 bar). The pressure gradient in the support structure is negligible compared to the gradients in the separation layer and membrane-skin interface. The total pressure of

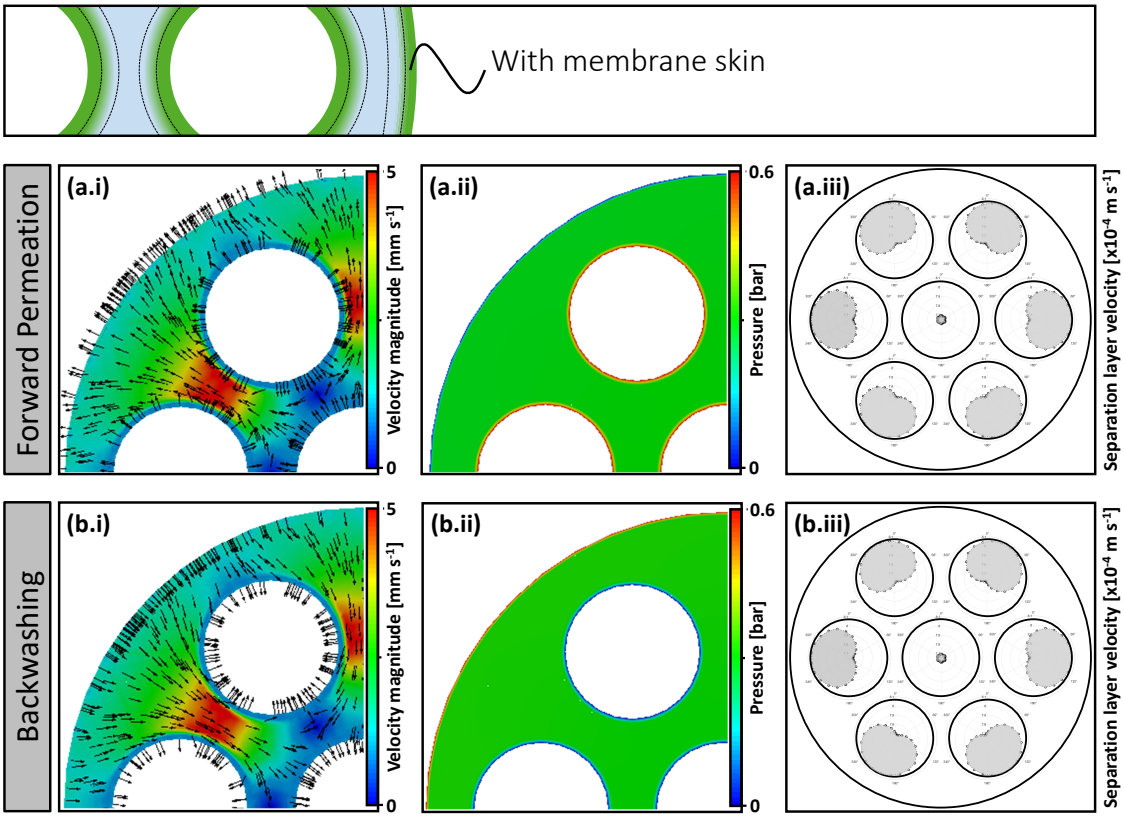

Figure 5.10: Porous structure velocity ((a.i) and (b.i)), pressure ((a.ii) and (b.ii)) and separation layer velocity ((a.iii) and (b.iii)) distribution inside a polymeric multi-bore membrane with skin layer properties similar to the separation layer during forward permeation mode (top) and backwashing mode (bottom). Due to rotationally symmetric results, only one-fourth is visualized.

approx. 0.3 bar in the support structure is the average of the set pressure boundary condition of 0.6 bar at the inlet and 0 bar at the outlet boundary. This value would change with asymmetrical thicknesses of the pressure drop zones. Fluid that enters the support structure will not reenter other bore channels through the high-pressure separation layer because the pressure potential in the support structure is too low. The separation layer and the membrane-skin represent the highest resistances in the membrane.

Velocity distribution The velocity graphs also indicate that, for permeation mode, the fluid always follows the path from the lumen into the separation layer into the support structure towards the shell. This flow path is also seen for channel 4 (central). The velocity graphs show a low velocity

magnitude in the separation layers and higher magnitudes in the support structure. This velocity distribution is expected based on the higher intrinsic permeability in the support structure. The highest velocity magnitude can be found in the support structure between the outer channels, whereas the lowest velocity magnitude is located between channel 4 (central) and outer channels. The high magnitude of the velocity in the narrow region follows the continuity equation for incompressible fluid flow.

Separation layer velocities It seems that the separation layers have hardly any velocity gradients. However, Figures 5.10 (a.iii) and (b.iii) indicate an uneven velocity distribution around each bore channel's circumference. Here, the velocity plots in the six outer channels are kidney-shaped, with the maximum velocity at the position with the shortest distance to the shell side and the minimum velocity facing towards channel 4 (central). The shorter the distance to the shell side, the lower the resistance for the fluid and thus the higher the velocity in the separation layer. Detailed flow profiles are shown in Figure 5.11. The difference between maximal and minimum values in one single outer bore channel amounts to approx. 4.7 %. The sum of velocity magnitudes in channel 4 (central) is lower than the magnitudes in the outer lumen channels, with a difference in maximum velocities of approx. 4.6 %. The lowest velocities in channel 4 (central) are located at the position closest to the outer lumen channels and are identical to the velocity of the outer lumen channel at this position. The highest velocities in channel 4 (central) can be found at the positions between two outer bore channels. However, the difference in maximum and minimum channel 4 (central) velocities amounts to only 0.11 %.

Mass flux These unequal velocity magnitudes comparing channel 4 (central) and outer lumen channels lead to different mass flux contributions. The mass flux analysis through the bore channel boundaries shows that the same mass flux exits from every outer lumen channel (14.34 % of the total mass flux). The mass flux from channel 4 (central) is marginally smaller (13.96 % of the total mass flux), i.e., less than 3 % of the mass flux through

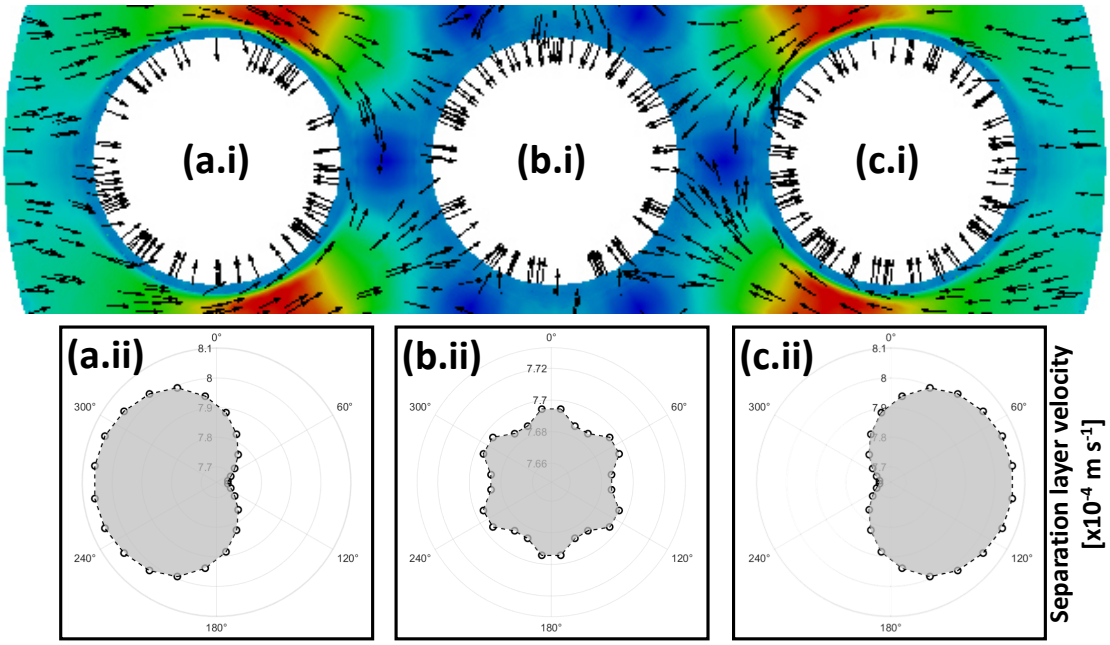

Figure 5.11: Magnification of porous structure velocity (top), and separation layer velocity (bottom) distribution inside a polymeric multibore membrane with skin layer properties similar to the separation layer during backwashing mode. Different scales for channel 4 and outer channels.

the outer lumen channel. Consequently, the multibore membrane has the same order of magnitude permeation performance in all its channels. The total mass flux was calculated to $\dot{m} = 16.89\,\mathrm{g\,s^{-1}}$.

Conclusion Even if the mass flux through all channels is nearly equal, the slightly lower flow through channel 4 (central) might negatively influence the overall filtration and backwashing performance as a smaller force is present to detach attached particles, for example.

Properties of membrane-skin interface set equal to properties of support structure

Figure 5.12 shows simulation results of a multibore membrane with a membrane-skin interface that has the properties of the support structure. This setting mimics a membrane without a denser layer on the outer skin. In this setting, the maximum velocity magnitude in the scale is approx. twice as high compared to Figure 5.10 and ranges from $0\,\mathrm{mm\,s^{-1}}$ to $10\,\mathrm{mm\,s^{-1}}$.

The graphs of the permeation and backwashing mode are again interchangeable and rotationally symmetric as well as in Figure 5.10.

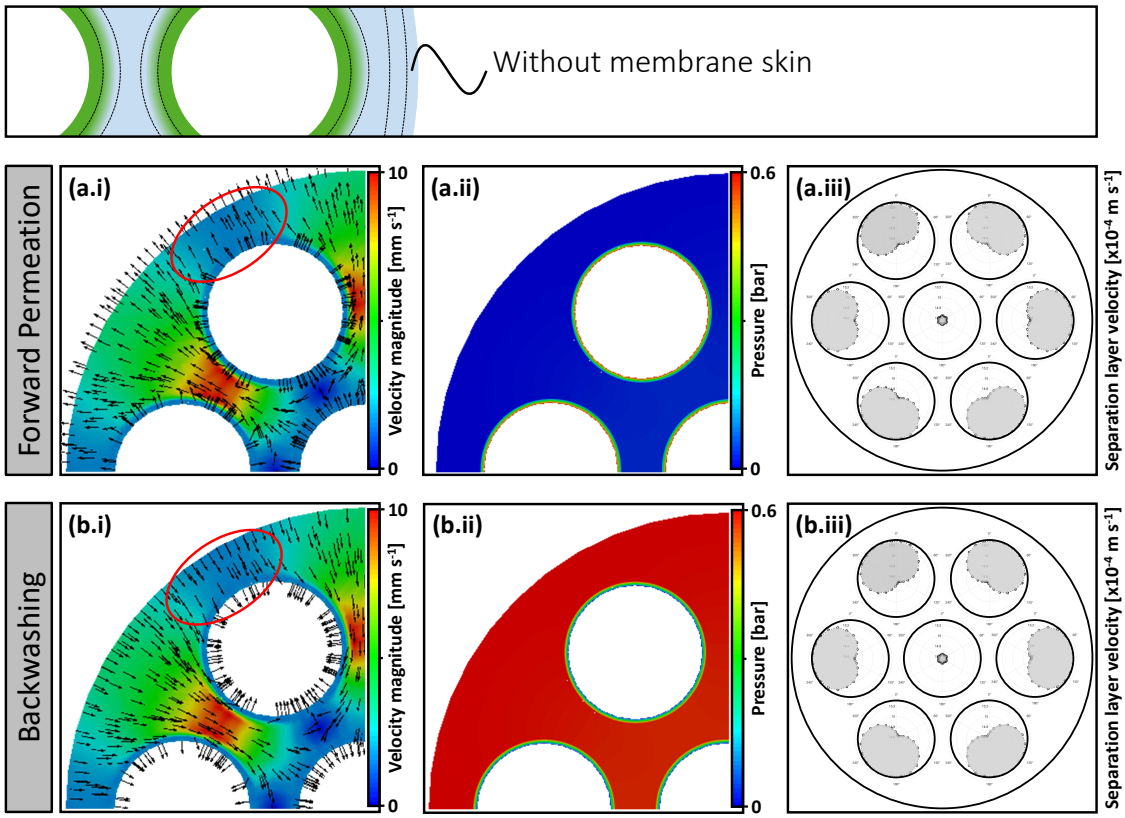

Figure 5.12: Porous structure velocity ((a.i) and (b.i)), pressure ((a.ii) and (b.ii)) and separation layer velocity ((a.iii) and (b.iii)) distribution inside a polymeric multibore membrane with skin layer properties similar to the support layer during forward permeation mode (top) and backwashing mode (bottom). Red circles mark major differences in fluid distribution to Figure 5.10. Due to rotationally symmetric results, only one-fourth is visualized.

Pressure distribution Due to the membrane-skin interface setting, this case displays two different pressure zones in the membrane: one with high porosity and intrinsic permeability and one with low porosity and intrinsic permeability. In Figures 5.12 (a.ii) and (b.ii), the main pressure gradient is located in the separation layer around the lumen channels of the membrane. The pressure gradient in the support structure is negligible compared with the pressure gradient in the separation layer. Again, due to the different pressure regimes, the fluid does not reenter other bores.

Velocity distribution In the velocity plots, similar main conclusions can be drawn as in the results with a membrane-skin in the previous section. One difference is the maximum velocity magnitude that is roughly twice as high. These higher velocities are expected since the additional resistance of the outer skin is removed. Hence, the total intrinsic permeability of this setting is higher, leading to higher velocities. Besides the higher velocity magnitudes, the velocity distribution in Figures 5.12 (a.i) and (b.i) is slightly different from those in Figures 5.10 (a.i) and (b.i). Caused by the removed membrane-skin interface, the magnitudes in the area between the outer bore channels and the membrane-skin relative to the maximal magnitude in Figures 5.12 (a.i) and (b.i) are lower (see red circles in Figures 5.12 (a.i) and (b.i)) than the corresponding relation in Figures 5.10 (a.i) and (b.i). The flow distributes more equally if the resistance is higher.

Separation layer velocities Besides the total velocity magnitudes inside the porous support structure, the separation layer velocities are also approx. twice as high compared to the case with a membrane-skin. The major difference is the slightly broader profile close to the shell side. This could be a reason for the lower velocities in the porous support structure in the region between outer bore channels and shell side (red circled area). Otherwise, the velocity profiles in the two cases look similar to each other.

Mass flux The mass flux analysis through the boundaries shows that the total mass flux is proportional to the total membrane resistance, as expected from Darcy's law. By removing a higher resistance for the membrane-skin interface, the total mass flux increases accordingly. The total mass flux in this setting was calculated to $\dot{m} = 31.57\,\mathrm{g\,s^{-1}}$ (Setting 1: $\dot{m} = 16.89\,\mathrm{g\,s^{-1}}$). The difference between mass flux through channel 4 (central) and outer lumen channels remains at 3 %.

Conclusion Due to the lack of differences between the two settings in the separation layer, which is responsible for the separation, a membrane with a removed membrane-skin interface performs better regarding the mass

flux leaving the membrane. It has a lower total resistance and, therefore, a higher flux for the same applied pressure difference. The results suggest an economically more viable option when considering inside-out filtration mode without an outer membrane-skin. Here, additional resistances are mitigated, and backwashing is performed more evenly.

Properties of membrane-skin interface set equal to properties of separation layer with damaged zone above channel 1 (top-left) which has properties of support structure

Figure 5.13 shows simulation results of a multibore membrane with a damaged membrane-skin interface. The membrane-skin interface has the properties of the separation layer, excluding the damaged zone. The damaged zone is located above channel 1 (top-left) of the membrane. It is 0.3 mm wide and has the properties of the support structure. The velocity magnitude ranges from 0 mm s^{-1} to 40 mm s^{-1}, which is higher compared to the two simulation results without a damaged zone. The high magnitudes appear in the region around the damaged zone. Hence, the damaged zone significantly changes the flow pattern and pressure distribution inside the membrane. Again, the permeation and backwashing modes are the inverse of one another. It has to be mentioned that the flow paths in Figure 5.13 result from the position and amount of the observed damages at the outer skin. Changing the position or the number of damaged zones would strongly influence the observed flow field.

Pressure distribution The pressure drop in the separation layer and in the intact membrane-skin interface is present. However, the pressure drop of the intact membrane-skin interface diminishes as the damaged zone is approached. At this position, the pressure in the damaged zone equals the pressure in the support structure. In this setting, the pressure gradient in the support structure is no longer negligible. The pressure in the support structure rises from the damaged zone towards channel 7 (bottom-right) for permeation mode (and vice versa for backwashing mode). From the

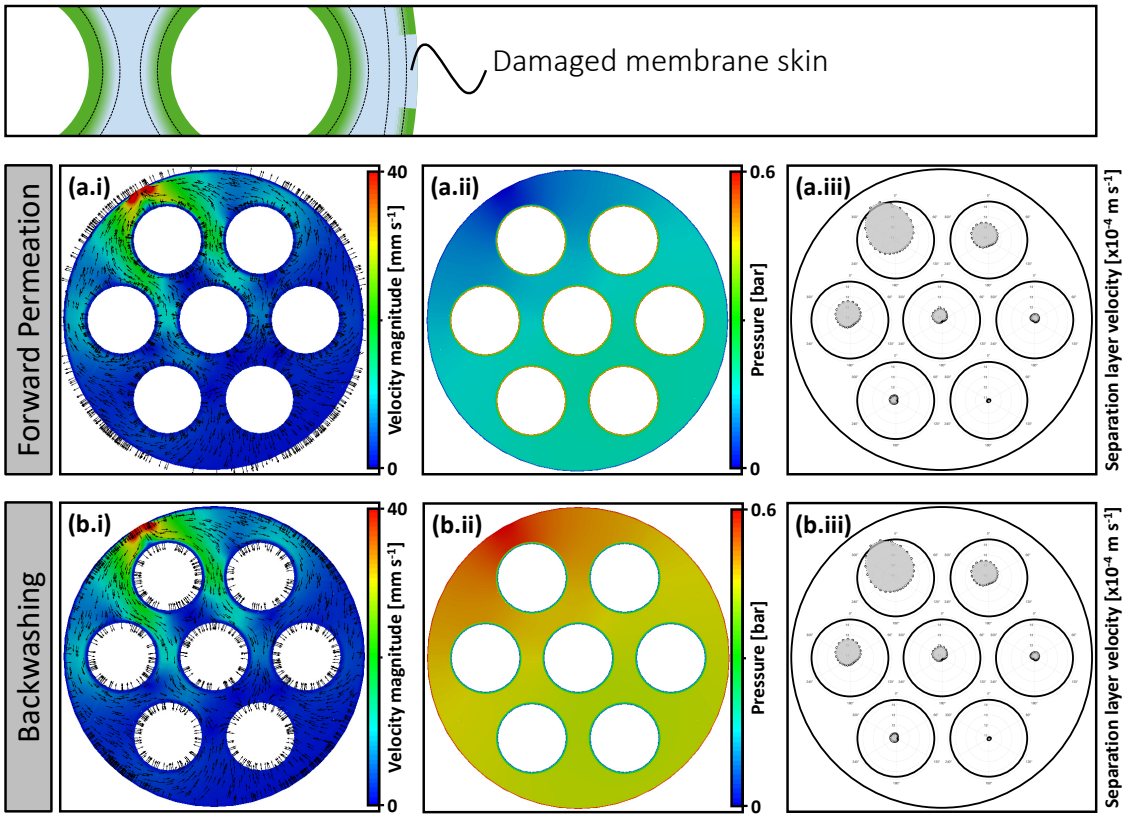

Figure 5.13: Porous structure velocity ((a.i) and (b.i)), pressure ((a.ii) and (b.ii)) and separation layer velocity ((a.iii) and (b.iii)) distribution inside a polymeric multi-bore membrane with skin layer properties similar to the separation layer but with a damaged zone above channel 1 (top-left) that has the properties of the support structure during forward permeation mode (top) and backwashing mode (bottom).

bottom-right corner towards the damaged zone, the pressure difference is approx. 0.3 bar for the permeation and backwashing mode. This pressure distribution implies the velocity flow pattern visible in the left column.

Velocity distribution The velocity pattern is not rotationally symmetric anymore, as they were in the previous settings. Compared to settings one and two, the damaged zone significantly changes the flow pattern in the whole support structure. The fluid preferably flows through the damaged zone into the shell. Thus, the flow pattern in the porous support structure is directed towards the damaged zone. Nevertheless, the fluid exits (for permeation mode) and enters (for backwashing mode) the membrane's whole circumference. The extreme case of fluid exiting/entering exclusively through the damaged zone is not observed as the pressure gradient bound-

ary condition is valid for the entire circumference. Also, the flow streamlines from the support structure through the intact membrane-skin interface are influenced by the damaged zone. The velocity magnitude is high in the narrow zones between channel 1 (top-left) and its adjacent outer channels (approx. 20 mm s^{-1}). Another local velocity hot spot is between the adjacent outer channels and the membrane-skin (10 mm s^{-1}) due to the higher radial intrinsic permeability of the support structure. This relation changes for a higher angular intrinsic permeability.

Separation layer velocities The flow profiles inside the separation layers are not symmetrical anymore and are manipulated by the damaged zone. The damaged area has a significant influence on the flow profiles as they are directed towards it. The velocities on the bore channel's circumference result from an interplay between the distance and position of the damaged zone and the lumen channel's position. With increasing distance from the damaged zone, its influence on the flow profile's shape becomes smaller; however, the velocity magnitudes decrease (max. velocity decrease by 26.7 % regarding channel 1 (top-left) and channel 7 (bottom-right)). This decreasing behavior can also be seen in the mass flux analysis.

Mass flux The mass flux analysis through the separation layers shows that with $\dot{m} = 24.69\,g\,s^{-1}$ it lies between the two previous settings (Setting 1: $\dot{m} = 16.89\,g\,s^{-1}$, Setting 2: $\dot{m} = 31.57\,g\,s^{-1}$). The contribution of the individual channels to the total volume flow through the separation layers can be obtained from Table 5.7. The individual mass fluxes through the channels depend on the distance from the damaged zone. Channel 1 (top-left) has the highest mass flux, followed by channel 2 (top-right) and channel 3 (left), channel 4 (central), channel 5 (right) and channel 6 (bottom-left), and channel 7 (bottom-right). The mass flux of channel 7 (bottom-right) is 16.3 % lower than the mass flux of channel 1 (top-left). The damaged zone does influence the mass fluxes. Ideally, each channel contributes approximately 14 % to the membrane performance. However, in this setting, channel 7 (bottom-right) contributes only 13.4 % to the total mass flux.

Table 5.7: Numerically estimated relative contribution of each individual channel to the total volume flow through the multibore membrane for setting 3 (damage). Numerical values according to simulation results in Figure 5.13.

Lumen location	Contribution [%]
Channel 1 (top-left)	16.0
Channel 2 (top-right)	14.7
Channel 3 (left)	14.7
Channel 4 (central)	13.9
Channel 5 (right)	13.7
Channel 6 (bottom-left)	13.7
Channel 7 (bottom-right)	13.4

Conclusion Summarizing, a damage in the membrane-skin interface significantly influences the flow in the whole support structure. This was not visible in the previous chapter, as the membrane was modeled with a constant and homogeneous porosity. Thus, the fluid flow inside the porous structure differs from the results in this chapter. The results suggest that a membrane with a membrane-skin layer on the outside is susceptible to damage, which harms the permeation and filtration result. This clearly illustrates that a membrane without an outer separation layer is also advantageous for inside-out filtration. Damages on the outer surface are buffered by the homogeneous porosity. They are thus mitigating the negative influence on the filtration result. As mentioned above, flow paths and velocities strongly depend on the amount and position of the observed damage. A damaged zone between two outer lumen channels would result in different flow paths compared to Figure 5.13 so that flow would be directed towards the damaged zone with higher velocities between those respective lumen channels. How the flow would spread with several positions that mimic damaged zones is left as work for future investigations.

Comparison with MRI measurement and old simulation model

Figure 5.14 (a) depicts the MRI measurement of Wypysek et al. [Wypy2019], and Figure 5.14 (c) the COMSOL simulation of the previous chapter for the forward permeation mode. Figure 5.14 (b) shows the

resulting graph of a 2D OpenFCST simulation of a multibore membrane with skin layer properties similar to the separation layer properties with a pressure gradient of 50 mbar to match the MRI experiment. This pressure difference was chosen to compare flow paths and magnitude. Additionally, in Figures 5.14 (d.1) to (d.3) and (e.1) to (e.3), flow profiles taken from MRI measurements and OpenFCST simulations are depicted to better compare experiments with simulations. The values are taken from between the outer lumen channels and between channel 4 and outer lumen channels, respectively (see Figures 5.14 (a) and (b)). Due to symmetry in the simulation results, respective velocity values between the outer lumen channels are equal to each other.

Compared to both simulation results (Figures 5.14 (b) and (c)), the MRI measurement (Figure 5.14 (a)) is noisier due to the lower spatial resolution. Nevertheless, regarding the membrane structure and the internal flow pathways, the MRI measurement and the OpenFCST simulation show the highest velocity magnitudes in the narrow zone between the outer channels. In contrast, the COMSOL simulation shows the highest velocity magnitudes at the shortest distance between bore channels and membrane skin as the resistance in this direction is the smallest. These phenomena are caused by applying a denser zone in the separation layer and the outer skin. Since in the COMSOL simulation the whole membrane is modeled with equal properties (there is no discrimination between separation layer, porous structure, and outer membrane skin), the velocity pathways differ a lot. Also, channel 4 (central) has hardly any flux in the COMSOL simulation. In contrast, the OpenFCST simulation shows only 3 % less flow through channel 4 (central) in the ideal case without fouling compared to outer channels. For a better comparison, velocity profiles along the marked lines d.1, d.2, and d.3 (see Figures 5.14 (a) and (b)) can be found in Figures 5.14 (d.1) to (d.3). For all observed positions, the course of MRI measurements resembles OpenFCST simulation results. At the shortest distance between outer lumen channels, the velocity magnitude is highest. The magnitude decreases towards the skin layer and lumen channel 4 (central), at which the velocity increases slightly at the separation layer.

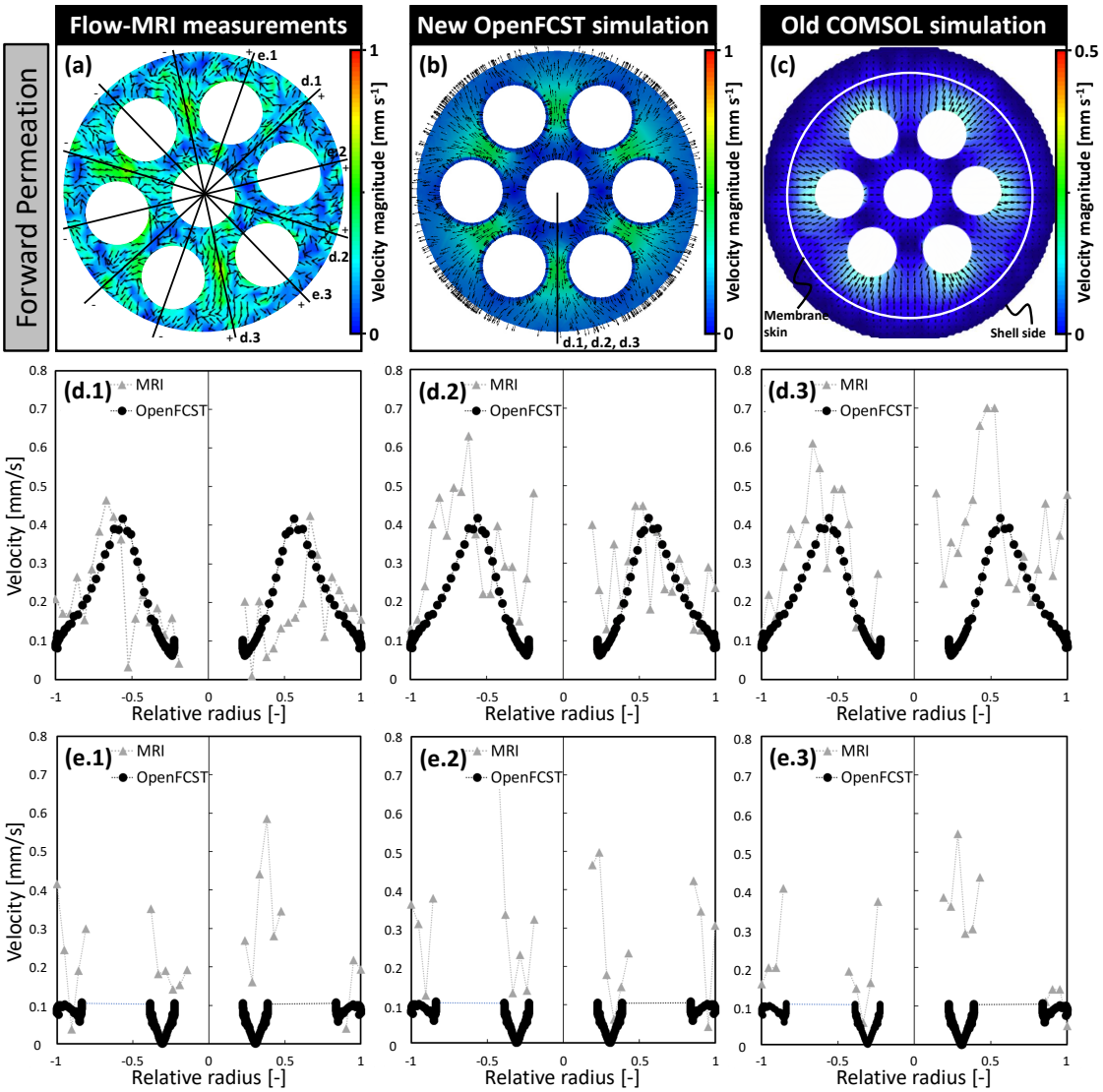

Figure 5.14: (a) Excerpt of MRI measurement from a whole module's cross section and (c) COMSOL simulation of radial velocity magnitude in a membrane module with the polymeric multibore membrane in forward permeation mode. (b) 2D OpenFCST simulation with radial velocity magnitude of a polymeric multibore membrane with skin layer properties similar to the separation layer in forward permeation mode. Velocity profiles from MRI measurements and OpenFSCT simulations taken from (d.1)-(d.3) between the outer lumen channels, and (e.1)-(e.3) between channel 4 and outer channels for better comparability. MRI adapted from Wypysek et al. (2019) [Wypy2019] with permission of Elsevier.

Depending on the position, velocity magnitude differences can be observed. Low deviations of 1.6 %, 7.5 %, and 11.2 % can be observed for maximum velocity magnitudes between channels 2 and 5, 5 and 7, and 3 and 6, respectively. However, high deviations of 46.1 %, 50.6 %, and

67.8 % can be observed for maximum velocity magnitudes between channels 1 and 2, 1 and 3, and 6 and 7, respectively. These big differences, especially between channels 6 and 7, are caused, on the one hand, by the low spatial and velocity resolution of the MRI measurements [Wypy2019], and, on the other hand, by MRI measurements of the whole membrane module (including shell side, inlets and outlets). As shown in the previous chapter, secondary flow fields develop on the membrane's shell side, causing drag forces that influence the flow field in the membrane itself. For these reasons, a comparison of velocities between channel 4 (central) and outer channels is challenging, as MRI resolution (especially velocity resolution as velocities are in the range of the noise obtained in the measurements) is too low and the limit of MRI measurements is reached. However, the course of the velocity profiles of MRI measurements is still comparable to OpenFCST simulation results (see Figures 5.14 (e.1) to (e.3)).

The same reasons apply to backwashing mode. As secondary flow fields develop on the shell side, backwashing fluid does not enter the membrane equally over the whole circumference [Wypy2019], making a comparison to the simulation model challenging in backwashing mode. Regarding the simulations with damaged skin (see Figure 4.5), the COMSOL simulations show hardly any influence on the flow field inside the membrane structure, while Figure 5.13 reveals a huge reorientation of the flow inside the membrane and separation layer towards the damaged zone for the OpenFCST simulation.

In conclusion, the qualitative comparable volume flow rates and, more importantly, similar flow paths through the porous structure in the flow-MRI experiment and the OpenFCST simulation with similar applied pressures show that the developed asymmetric membrane model in this chapter is more accurate to simulate polymeric membranes than the homogeneous model used in the previous chapter. COMSOL is only partly suitable for porous structure simulations with gradients in properties. However, the simulation of membranes with spatial equal properties, e.g., ceramic membranes, is possible. Additionally, the flow distribution inside the module (e.g., shell side) and the flow inside bore channels are in good agree-

ment with flow-MRI measurements [Wypy2019]. The previous chapter's simulation model also allows the simulations of different module configurations (eccentric membrane position, sagging membrane, different outlet positions).
The effect in lumen- and shell-sided velocity and pressure distribution in the MRI measurement and their influence on the flow inside the membrane structure is not assessable with the investigations in this chapter and is subject to future studies. The complete membrane module, including gradients in membrane properties, must be considered for the whole picture.

Example of fouling layer based on MRI experiments

Figure 5.15 (b.i) shows an exemplary pressure simulation result in backwashing mode of a multibore membrane after cross-flow filtration with silica particles. Additional parameters for the blocked domain with less permeability were implemented that mimic the deposition of particles. The position of this domain was taken from MRI measurements (Figure 5.15 (a)), and porosity and permeability values in the separation layer in this region were changed. In this simulation, the membrane-skin interface has the same properties as the porous structure (no membrane-skin layer). The magnification in Figure 5.15 (b.ii) shows that the pressure drop in the separation layer is not equal over the whole circumference when an additional resistance is present in the respective bore channel. The additional resistance results in a faster pressure drop inside the separation layer. At positions without the fouling resistance, the pressure distribution behaves similarly as in the previous simulations. Neighboring bores do not influence each other. This results in identical hydrodynamic conditions for identical separation layer properties.
This behavior can also be seen in the velocity plots in Figure 5.16. Magnetic resonance images are illustrated in the top row and the corresponding simulated velocity maps in the middle row. The bottom row depicts velocity magnitudes in the separation layers. The left column illustrates the reference state, whereas backwashing after cross-flow filtration and after

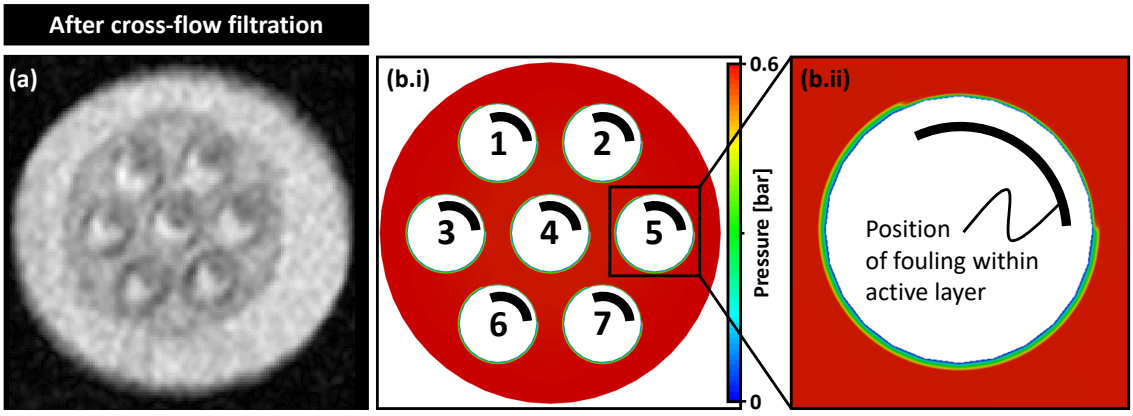

Figure 5.15: (a) Magnetic resonance image of a whole membrane module after cross-flow fouling. (b.i) Simulated pressure distribution with (b.ii) a magnification of a polymeric multibore membrane with skin layer properties similar to the support layer. Black circle sections illustrate the position of fouling in the MRI images. These sections were simulated with a 100 times lower permeability in the separation layer. The pressure difference was set to 0.6 bar. Magnetic resonance images taken from Wypysek (2019) [Wypy2019] with permission of Elsevier.

dead-end filtration can be found in the middle and right column, respectively. Velocities in the support structure range from 0 mm s^{-1} to 10 mm s^{-1} for all scenarios and up to 1.54 mm s^{-1} for separation layer velocities. It has to be mentioned that the visualized velocity fields only represent the initial backwashing flow. Since fouling layers (depending on the foulant) disappear over time, flow fields would change. This also makes a comparison to flow fields obtained by MRI impossible, as an MRI measurement took approx. 15 min and fouling layers were not visible anymore [Wypy2019].

Backwashing reference state When no additional fouling resistance is applied (see Figures 5.16 (a.i) to (a.iii)), the velocity distribution in the membrane is symmetrical. As mentioned before, high velocities are located between outer bore channels, low velocities between outer bore channels and channel 4 (central), and outer bore channels and outer shell. Every outer bore channel contributes equally with 14.34 % to the total mass flow. Channel 4 (central), however, contributes approximately 3 % less (13.96 %, see Table 5.8, left column). This lower mass flow rate can be disadvantageous for channel's 4 (central) cleaning efficiency as the force to remove particles is lowered.

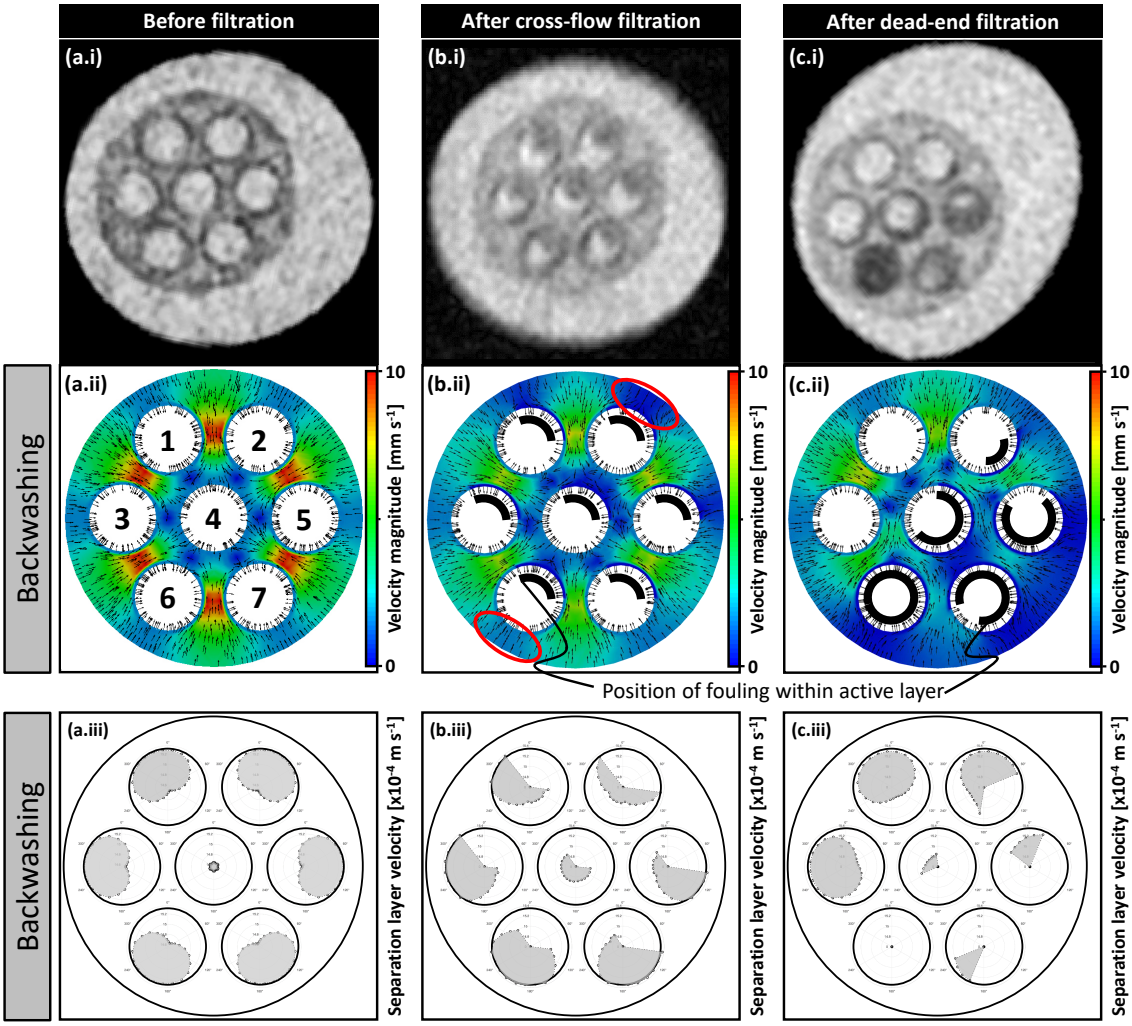

Figure 5.16: Magnetic resonance images of a whole membrane module (top), simulated porous structure velocity magnitudes with arrows for the flow direction (middle), and separation layer velocities (bottom) in backwashing mode of a polymeric multibore membrane with skin layer properties similar to the support layer in three cases: the membrane is (a) not fouled, (b) fouled during cross-flow filtration and (c) fouled during dead-end filtration. Black circle sections in (b.ii) and (c.ii) illustrate the position of fouling in the MRI images. These sections were simulated with a 100 times lower permeability in the separation layer. The pressure difference was set to 0.6 bar. Magnetic resonance images taken from Wypysek (2019) [Wypy2019] with permission of Elsevier.

Backwashing after cross-flow filtration If the fouling resistance in all seven bore channels is located at the same position (equal fouling based on fouling volume and location of the foulant after cross-flow filtration, see Figures 5.16 (b.i) to (b.iii)), the velocity distribution is nearly as symmetrical as in the reference state. However, the maximum velocities in the support

structure are approximately half for the fouled state.
Another difference is the uneven distribution in the separation layers (see Figure 5.16 (b.iii)). The velocities at the position of the increased resistance are close to 0 mm s^{-1}. The fluid needs more force to overcome the fast pressure drop in the high resistance area. It prefers to enter the bore channel through the lower resistance region in the separation layer. The velocity profiles in the separation layers develop through the combination of the bore's location in the membrane and the fouling location. The more the fouling layer is turned away from the shell side (location where liquid enters membrane), the higher the separation layer's overall velocities and vice versa. Also, the profiles are turned towards the shortest distance to the shell side if no fouling layer is present. Channel 4 (central) has the lowest velocities again.
These effects result in a slight velocity maldistribution in the porous structure, which can be seen best when comparing the areas between the outer bore channels 2 (top-right) and 6 (bottom-left) and the membrane-skin interface (red circles in Figure 5.16 (b.ii)). In channel 2 (top-right), the area with higher resistance is closer to the membrane-skin interface than to channel 4 (central). Thus, the velocities in the support structure in this region are also close to 0 mm s^{-1}. The fluid rather flows around the higher resistance area and enters the bore from the other side. In channel 6 (bottom-left), the higher fouling resistance points towards channel 4 (central). Here, the velocity in the area between bore channel and membrane-skin interface is higher (approximately 2 mm s^{-1}) compared to the velocity at channel 2 (top-right).
The mass flow contributions range from 14.24 % to 14.41 % for the outer channels and 14.09 % for channel 4 (central), which is only less than 2 % lower than the outer channels. This deviation is lower as in the reference state, which is advantageous for the cleaning process of the membrane (see Table 5.8).

Backwashing after dead-end filtration In the case of asymmetrical fouling (after dead-end filtration, see Figures 5.16 (c.i) to (c.iii)), the flow distri-

bution in the porous structure is also asymmetric. As the fouling occurs in the bottom-right part of the membrane, the backwashing velocities in this region are smaller compared to the not fouled top-left area.
The behavior of velocities in the separation layer is similar to the cross-flow case - the profiles depend on the position of the bore and the fouling layer. In the extreme case of complete pore blocking (channel 6 (bottom-left)), the separation layer's whole circumference shows a velocity that is close to zero, which drastically reduces the backwashing efficiency for this bore channel. This can also be seen in the mass flow contributions that are summarized in Table 5.8.

Table 5.8: Numerically estimated relative contribution of each individual channel to the total volume flow through the multibore membrane for backwashing in a non-fouled membrane and after fouling in dead-end and cross-flow mode. Numerical values according to simulation results in Figure 5.16.

	Total mass flow contribution		
Lumen location	Reference [%]	After cross-flow fouling [%]	After dead-end fouling [%]
Channel 1	14.34	14.28	28.19
Channel 2	14.34	14.24	19.48
Channel 3	14.34	14.36	28.24
Channel 4	13.96	14.09	9.95
Channel 5	14.34	14.27	7.94
Channel 6	14.34	14.41	0.69
Channel 7	14.34	14.36	5.52

The completely blocked channel 6 (bottom-left) contributes hardly to the total mass flux in this backwashing mode (0.69 %). Otherwise, the channels which are not blocked at all (channel 1 (top-left) and channel 3 (left), respectively) have contribution values that are approximately twice as high as in the reference state (28.10 % and 28.24 %, respectively). In general, channel 4 (central) contributes less to the total mass flux than the outer channels. Also, the more fouling resistance is added to a bore channel, the smaller the respective mass flux contribution. This uneven flow distribution

into each bore channel makes efficient cleaning challenging.
In conclusion, dead-end fouling changes the fluid flow distribution between the single bore channels during backwashing. The velocity magnitudes display why the cleaning performance and cleaning times could differ between each channel. Therefore, cross-flow is a measure to prolong the lifetime of the membrane process.

5.4 Conclusion and outlook

This comprehensive CFD simulations study elucidates the hydrodynamic effects in a multibore membrane featuring heterogeneously distributed material properties during permeation and backwashing. It uses spatial-dependent membrane porosities and intrinsic permeabilities in the separation layer, the support structure, and the membrane-skin interface. The transition zones between these layers are modeled by a smooth transition function, representing the property gradients between the zones. This chapter closes the gap of measuring macroscopic flow paths inside the membrane and membrane module and modeling flow through the membranes at a microscopic scale with spatial-dependent membrane properties.
First, the spatial-dependent membrane properties (porosity and pore size distribution) are determined using µCT-scans and SEM images of a polymeric multibore membrane. Second, Stokes flow simulations in reconstructed µCT-scan samples are executed and post-processed to obtain permeability estimates. The results of the porous structure simulations with deal.II are required as input to perform OpenFCST simulations of the membrane structure itself. Third, a property function for the multibore membrane geometry is derived and implemented considering the different zones in the membrane. Fourth, the macroscale flow is simulated in the multibore membrane to evaluate the flow pattern within the domain. Thereby, three cases are studied: (1) properties of the membrane-skin interface are set equal to the properties of the separation layer, (2) properties of the membrane-skin interface are set equal to the properties of the support structure, and (3)

properties of the membrane-skin interface are set equal to the properties of the separation layer, and an additional damaged zone above channel 1 (top-left) is implemented, which has the same properties as the support structure. Finally, this chapter's simulation results are compared to the MRI measurements of Wypysek et al. [Wypy2019] and to COMOSOl simulation from the previous chapter, and backwashing experiments after fouling with silica particles are mimicked.
The obtained results provide insights into the membrane's direction-dependent properties and the permeation and backwashing phenomena of polymeric multibore membranes. The porous structure simulations for the micro-scale property determination show that the membrane's support structure in this study is not isotropic. Its radial and angular intrinsic permeabilities are higher than the axial intrinsic permeability.
The simulations of the entire membrane without additional fouling resistances reveal

- that the main pressure drop is present in the separation layer and/or the membrane-skin interface with similar properties.
- that the highest flow velocity magnitudes in the simulations and the MRI measurement are located between the outer channels of the membrane.
- that flow patterns and pressure distribution are inversed when comparing forward permeation and backwashing mode without foulant or damaged zone.
- that the volume flow through the membrane without a membrane-skin interface is approx. twice as high as compared to with a membrane-skin interface. Hence, membrane permeation and the total flux increase when a skin layer is missing with no resistance on the shell side.
- that a damaged membrane-skin influences the flow pattern within the support structure significantly. Thus, pressure gradients within the support structure become more pronounced. The results support the

hypothesis that flow paths strongly depend on positions and the number of damaged zones, and the observed flow paths are case-specific.

- that each lumen channel contributes nearly equally to the permeation and filtration performance of the membrane. However, channel 4 (central) contributes slightly less to the overall mass flux (3 % less), influencing the cleaning performance. In no case, a lumen channel contributes less than 13 % to the total mass flux.
- that the flow distribution within the separation layer depends on the lumen position and is not equal around its circumference.

The simulations of the membrane with additional fouling resistances reveal

- that additional fouling resistances influence pressure and velocity distribution during backwashing mode. These resistances result in a higher pressure drop in the separation layer at positions where fouling occurs. It is assumed that asymmetrical fouling makes recovering each channel equally more difficult.
- that the fluid reaches each lumen channel of the membrane, and thus, backwashing is theoretically possible. However, the cleaning performance and cleaning times differ between each channel, as the mass flow contributions vary from channel to channel, and the pathways are different for the outer and the central lumen channels, respectively.
- that even a completely blocked bore channel contributes slightly (approx. 0.69 %) to the total mass flux during backwashing. However, the more a bore channel is blocked, the less it contributes to the total mass flux. Thus, the cleaning performance is different for each channel. For symmetrical fouling, the contribution to the total mass flux is nearly equal in all bore channels.

The developed methodology of image-based structure analysis and CFD simulations for asymmetric membranes is essential to understand phenomena within membranes with an asymmetric porosity or permeability distribution. The chapter's simulation results can be used as a basis and orientation for future studies with position-dependent properties in asymmetric

membranes or membranes with various numbers of lumen channels. The coherence between the measured and simulated velocity magnitudes in the membrane illustrates the applicability of the model.

The previous chapter, *Chapter 4: Single Multibore Membrane Module Performance* and this chapter, *Chapter 5: Single Multibore Membrane with Porosity Gradients*, investigated the hydrodynamic conditions of one single membrane. However, in industrial applications, the packing density of membrane modules is much higher as several hundred membranes are placed inside one module. Therefore, **Chapter 6: Hydrodynamics in Multi-Multibore Membrane Modules** focuses on the interplay of several multibore membranes inside a membrane module and evaluates the influence of packing density and the module's outlet on the flow field by MRI measurements.

6

Hydrodynamics in Multi-Multibore Membrane Modules

Parts of this chapter are in preparation for publication:

Denis Wypysek, Simon Wennemaring, Matthias Wessling, "Flow, Fouling, and Backwashing in Highly-Packed Multibore Membrane Modules", *Journal of Membrane Science*.

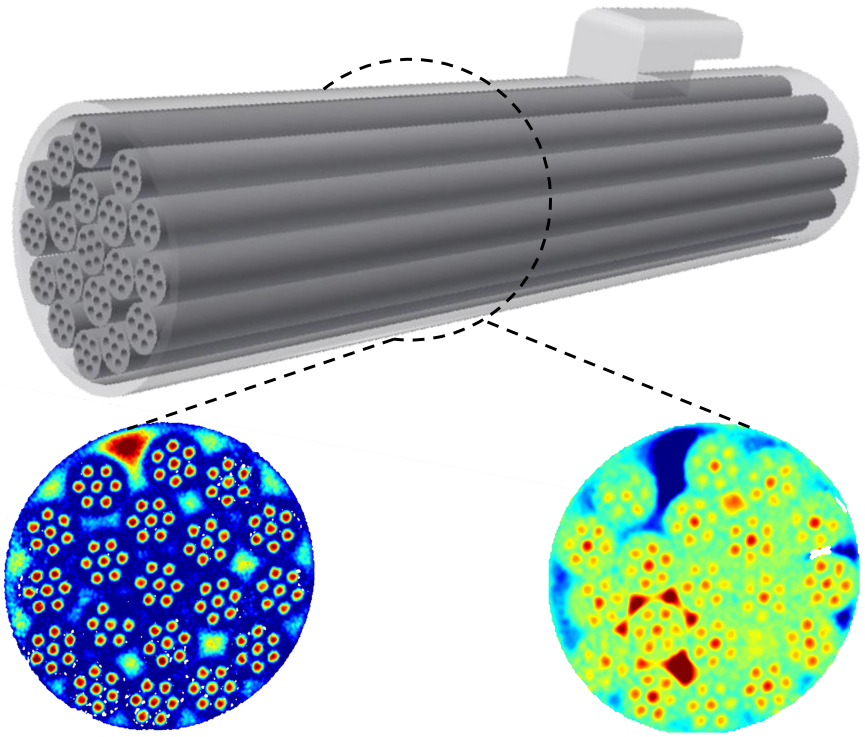

Flow magnetic resonance imaging in
forward permeation and **backwashing mode**
reveals jet streams, recirculation flows, and uneven flow distribution.

6.1 Introduction

The previous chapters, *Chapter 4: Single Multibore Membrane Module Performance* and *Chapter 5: Single Multibore Membrane with Porosity Gradients*, focused on a single multibore membrane and compared results to the MRI measurements of a multibore membrane from Schuhmann et al. [Schu2019] and Wypysek et al. [Wypy2019]. However, one membrane inside a membrane module is not feasible in industrial applications. Such modules are highly packed and often feature several hundred to some thousand membranes. The unknown interplay of several membranes and the influencing effects of membranes between each other is a question for which the answer is being searched for a long time.

In the past, simulative approaches answered questions about flow distribution in highly-packed modules regarding (a) the manifold design [Park1986], (b) the influence of packing densities on mass transfer [Cost1993; Bao2002; Günt2010], (c) the uneven particle deposition and cake growth [Günt2012], (d) and the shell-sided mass transfer performance of randomly packed hollow fiber modules [Wu2000; Bao2002]. Also, the influence of the packing density on (e) the fiber's dimension [Zhua2015] or (f) the position and distance (fiber-fiber interaction) of membranes [Ma2019] on the flux distribution was investigated simulatively. Costello et al. [Cost1993], for example, stated that on the shell side, fluid flows preferentially through parts with lower packing (higher void phase) and that simulation models have to take these non-idealities into account since an axial laminar flow assumption is insufficient on the shell side of a hollow fiber module. Bao et al. [Bao2002] also showed the dependency of higher fiber packing and lower flow at these regions, thus a more significant mass transfer. Ma et al. [Ma2019] introduced the terms *permeate competition* and *bundle resistance* that explain fiber-fiber interactions concerning fiber diameter and their distance (distance<diameter: permeate competition; distance=diameter: permeate competition disappears, bundle resistance dominates; distance>diameter: both negligible). However, defining fiber diameter in multibore membranes becomes challenging. All the men-

tioned studies focused on hollow fiber membranes. Wang et al. [Wang2019] analyzed hollow fiber zeolite membrane modules incorporating seven multi-bore membranes using CFD simulations to optimize the module's structure using axial and radial flow baffles. These low-packed modules achieved the best results regarding even flow distribution on the shell side and high separation efficiency for a module with two radial baffles and four axial baffles.

As one of the most prominent hollow fiber modules with several fibers, hemodialyzers were subject to many experimental, on the one hand, MRI studies investigating the (a) inlet and outlet flow behavior [Pang1989], (b) the flow distribution in shell and lumen side [Hamm1990] with different packing densities [Zhan1995; Hard2002], spacers between the fibers [Lauk1998; Poh2003b], and contrast agents like Gd-DTPA [Osug2004a; Weer2015; Weer2016] or heavy water [Osug2004b], and (c) the optimization of flow paths with installed flow baffles [Poh2003a]. On the other hand, other approaches like residence time studies [Enga1980] were used to study flow distribution in dialyzers. All investigations reported a maldistribution on either shell or lumen side which can influence toxin removal. Besides dialyzers, other modules were also investigated regarding the fiber-fiber interaction with PIV measurements [Zhan2018], a noninvasive ultrasonic technique [Li2014], and with MRI in randomly packed modules [Yan2021] and with differently shaped membranes and incorporated spacers [Yang2014].

Zhang et al. [Zhan1995], for example, analyzed three dialyzers with different packing densities and showed a relatively uniform flow distribution inside the lumen channels of all dialyzers. Contrarily, the shell-sided flow was not uniform and skewed to higher flow rates. No clear trend could be found regarding different packing densities. Poh et al. [Poh2003b; Poh2003a] also reported non-uniformities on the shell side and channeling occurring on the periphery. In their PIV and CFD study, Zhang et al. [Zhan2018] highlighted the importance of the outlet and inlet position. A more efficient outside-in filtration could be achieved with a non-centered fluid inlet, introducing a swirling flow. Recently, Yan et al. [Yan2021] performed flow-MRI measure-

ments in a membrane module containing over 400 hollow fiber membranes and analyzed flow distribution, fouling and backwashing phenomena. They found that only 91 % of the fibers were active in forward permeation mode. 73 % of the fibers were flown through after fouling with sodium alginate from which only 79 % recovered after chemical cleaning was applied. Not every membrane was reached by the backwashing flux, decreasing the module performance significantly.
All mentioned studies show the importance of understanding the interaction of fibers and increasing packing density in membrane modules. However, up until now, information on the flow distribution of several multibore membranes inside one membrane module does not exist. Therefore, this chapter focuses on the interplay of several multibore membranes inside a membrane module and evaluates the influence of packing density and the module's outlet on the flow field by MRI measurements. Flow-MRI measurements of three differently packed multibore modules in forward filtration and backwashing mode reveal the flow behavior on the shell and lumen side and answer the question if the backwashing flux reaches every lumen channel.

6.2 Experimentals

Membrane The investigated inside-out ultrafiltration membranes are commercially available PES SevenBore™ fibers supplied by SUEZ Water Technologies & Solutions and described in detail in Section 2.4.

Module As shown in Figures 6.1 (b) to (d), 50 cm long membrane modules with one, seven, and 19 multibore membranes were built, resulting in packing densities of approx. 5 %, 35 %, and 94 % ($\frac{A_{\text{membrane}}}{A_{\text{housing}}}$), respectively. 3D-printed spacers close to the module's ends are used to ensure constant positioning of the membrane fibers inside the single- and seven-fiber modules. The manufactured modules have an internal diameter of 18 mm. Furthermore, the membrane modules contain one connection for the feed stream and one for the permeate and retentate, respectively. Axial

and radial flow fields are measured at five different positions along with the module (see Figure 6.1 (a)). Measurement distances from the module inlet are 8.3 cm for position A-A, and every following measurement slice is also 8.3 cm away from the previous one.

Magnetic resonance imaging setup Figure 6.1 (a) illustrates the experimental setup. All MRI measurements are carried out on a Magritek low-field NMR tomography system combined with a KEA^2 low-frequency spectrometer using a 2D spin-echo pulse sequence. Details of the used tomography system and pulse sequences can be obtained from Section 2.2.3. Within the 60 mm inner diameter imaging probe, the membrane module is placed horizontally. Radial and axial velocity measurements are carried out in the x-y-plane, the cross section of the membrane module.

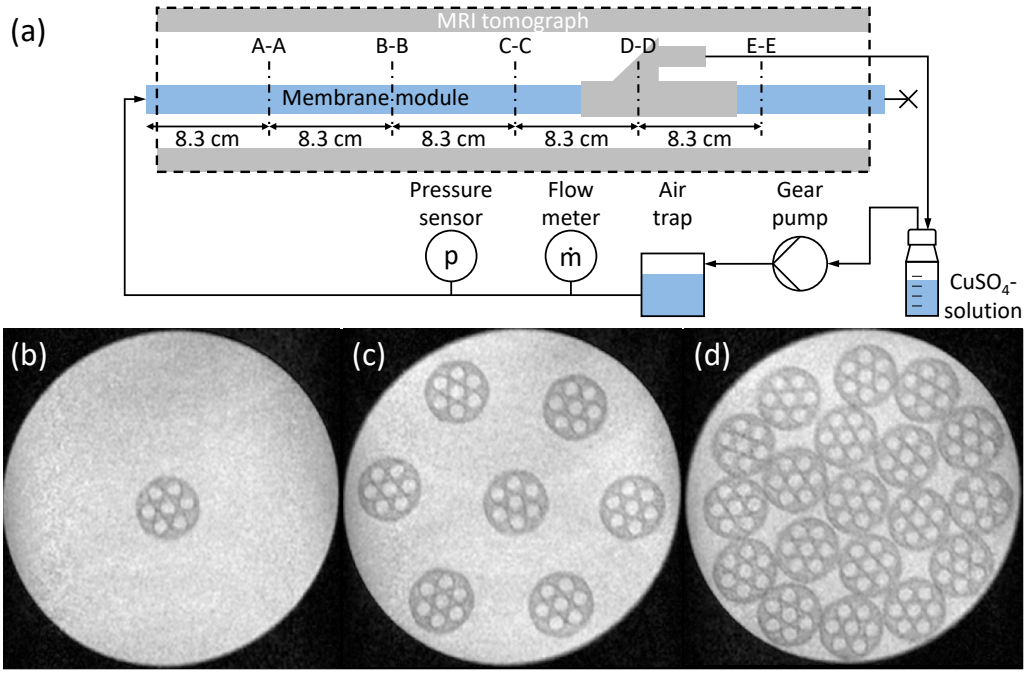

Figure 6.1: (a) Experimental setup for investigations on hydrodynamic behavior of membrane modules containing (b) one, (c) seven, and (d) 19 SevenBore™ membranes via MRI.

In all experiments, a fluid circuit is established with an ISMATEC® ISM405A gear pump. Thereby, fluxes of 100 liter per square meter membrane area and hour (LMH) and 200 LMH are applied to the membrane modules in forward permeation and backwashing mode, respectively. A copper sul-

fate solution of 1.5 g L^{-1} copper(II) sulfate pentahydrate ($CuSO_4 \cdot 5\,H_2O$, $\geq$ 99.5%, Carl Roth, Germany) in de-ionized water was used as permeating fluid. $CuSO_4$ is indispensable for MRI since the required time to capture a magnetic resonance image is significantly reduced. Mass flow rates across the membrane are checked with a mini CORI-FLOW™ M14 (Bronkhorst High-Tech B.V., Netherlands). The resulting transmembrane pressure (TMP) is recorded with a Wika pressure transmitter S-11 (Wika, Germany). MRI parameters vary to obtain a maximum spatial and temporal resolution for different conditions. The set MRI parameters are listed in Table 6.1.

Data processing with Matlab The obtained MRI raw data from Magritek's software PROSPA is post-processed using Matlab routines. The pixel by pixel stored velocity data is translated into contour and vector plots while data smoothing is applied. Maximum and minimum lumen- and shell-sided velocity values are taken from the matrices. For the calculation of the deviation (if not otherwise stated), the maximum lumen velocities in all membranes were compared. Assuming parabolic flow profiles in the lumen channels, maximum velocities are located in the middle of each channel. Equation 6.1 calculates the deviation in maximum lumen velocities:

$$\text{Deviation} = (1 - \frac{\text{Minimal maximum velocity}}{\text{Maximal maximum velocity}}) \cdot 100\% \qquad (6.1)$$

Table 6.1: MRI parameters for the investigation of hydrodynamics in multibore membrane modules with different packing densities. Field of view (FoV).

Permeation mode		Forward permeation			Backwashing	
No. of membranes		1 | 7 | 19	1 | 7 | 19	1 | 7 | 19	7 | 19	7 | 19
Slice		A-A to C-C	D-D	E-E	A-A to C-C	D-D, E-E
Parameter	Unit	Value	Value	Value		
Repetition time	[ms]	900	900 | 900 | 600	900 | 300 | 600	600	600
Echo time	[ms]	32	32 | 32 | 18	32	32 | 26	20, 32 | 26, 26
FoV Read [x]	[mm]	24	46 | 46 | 50	24 | 46 | 50	24	46 | 48
FoV Phase [y]	[mm]	24	46 | 46 | 50	24 | 46 | 50	24	46 | 48
Slice thickness [z]	[mm]	8	8	8	8	8
No. of pixels [x $\times$ y]	[-]	256 $\times$ 256	256 $\times$ 256	256 $\times$ 256	128 $\times$ 128	128 $\times$ 128
Number of scans	[-]	4	4 | 4 | 2	4 | 4 | 2	4	4
Acquisition time	[min:sec]	15:22	15:22| 15:22 | 10:14	15:22| 5:07 | 5:07	5:07	5:07

6.3 Results and discussion

Chapter 4: Single Multibore Membrane Module Performance revealed the sensitivity of flow patterns inside membranes and modules towards small geometric deviations from the ideal membrane position. Uneven flow distribution also occurs in modules with higher packing densities [Zhan1995; Lauk1998; Hira2012; Yang2014]. Therefore, in the following, the flow distribution in membrane modules is investigated in three packing densities in forward permeation and backwashing mode.

6.3.1 Pure water forward permeation - along module axis

Figure 6.2 shows axial flow velocities from $0\,\mathrm{mm\,s^{-1}}$ in dark blue to $100\,\mathrm{mm\,s^{-1}}$ in dark red at three positions before the permeate outlet. Due to the dead-end setup, the lumen channels' velocity decreases and shell-sided velocities increase towards the permeate outlet.

Axial velocities shell side With increasing packing density, inhomogeneities on the shell side increase. Also, maximum velocities on the shell side increase with higher packing density. Since the same flux is applied (here 100 LMH) for all module configurations, higher mass flow rates are applied for higher packing densities. However, less space on the shell side is present, which leads to higher velocities. For the lowest packing density in Figures 6.2 (a.i) to (a.iii), no notable shell-sided flow can be measured. This behavior changes drastically in the highly packed membrane module in Figures 6.2 (c.i) to (c.iii). High jet-like shell flows develop in the peripheral area of the membrane module between most outer twelve membranes and the membrane housing. Thereby, velocities in the upper half are higher compared to the bottom half. One explanation may be the permeate outlet location that points upwards. Another explanation may be the paths of least resistance and lower resistances for bigger gaps on the shell side [Cost1993]. Slightly lower velocities can be found between the outer twelve membranes and the neighboring six ones, and hardly any shell flow

is present around the central membrane as the membranes at this position are very close to each other.
A small void volume (higher local packing) leads to lower flow rates and higher residence times. Thus, mass transfer would be higher in high packing domains. However, in a randomly packed module, regions of lower packing (higher flow rates) dominate the whole module performance leading to a decreasing mass transfer. [Bao2002]
For the seven-membrane module in Figure 6.2 (b.iii), it seems that the shell-sided flow is distributed homogeneously. However, when looking at Figure 6.3 (membranes are hidden with white circles), in which the velocity gradient was set to lower velocities during the measurement, a maldistribution becomes visible when setting the scale from 0 mm s^{-1} in dark blue to 15 mm s^{-1} in dark red. All seven membranes are shifted slightly towards the bottom of the module. Therefore, the gaps between the membranes are bigger in the top part of the module leading to higher velocities at these regions [Hamm1990; Yao1995a]. Another hypothesis is that higher velocities develop at the top area in the module due to the permeate outlet position. These higher velocities then force the membranes to move away from the permeate outlet [Zhan2018]. All in all, as learned from *Chapter 4: Single Multibore Membrane Module Performance*, for small geometric deviations from the ideal membrane positions, small local pressure differences built up affecting flow and probably filtration performance, also in each lumen channel of the respective membranes.

Axial velocities lumen side As mentioned before, the velocities inside the lumen channels decrease along the module axis due to the dead-end configuration. However, the flow distribution in all seven lumen channels in one membrane as well as among different membranes is non-uniform. To better visualize these phenomena, Figure 6.4 shows magnifications of the flow fields in Figure 6.2 at slice C-C with different maximum velocities on the scale of 64, 80, and 86 mm s^{-1}, respectively.
It seems that no trend can be recognized regarding the flow distribution inside one multibore membrane. For the lowest packed module in Fig-

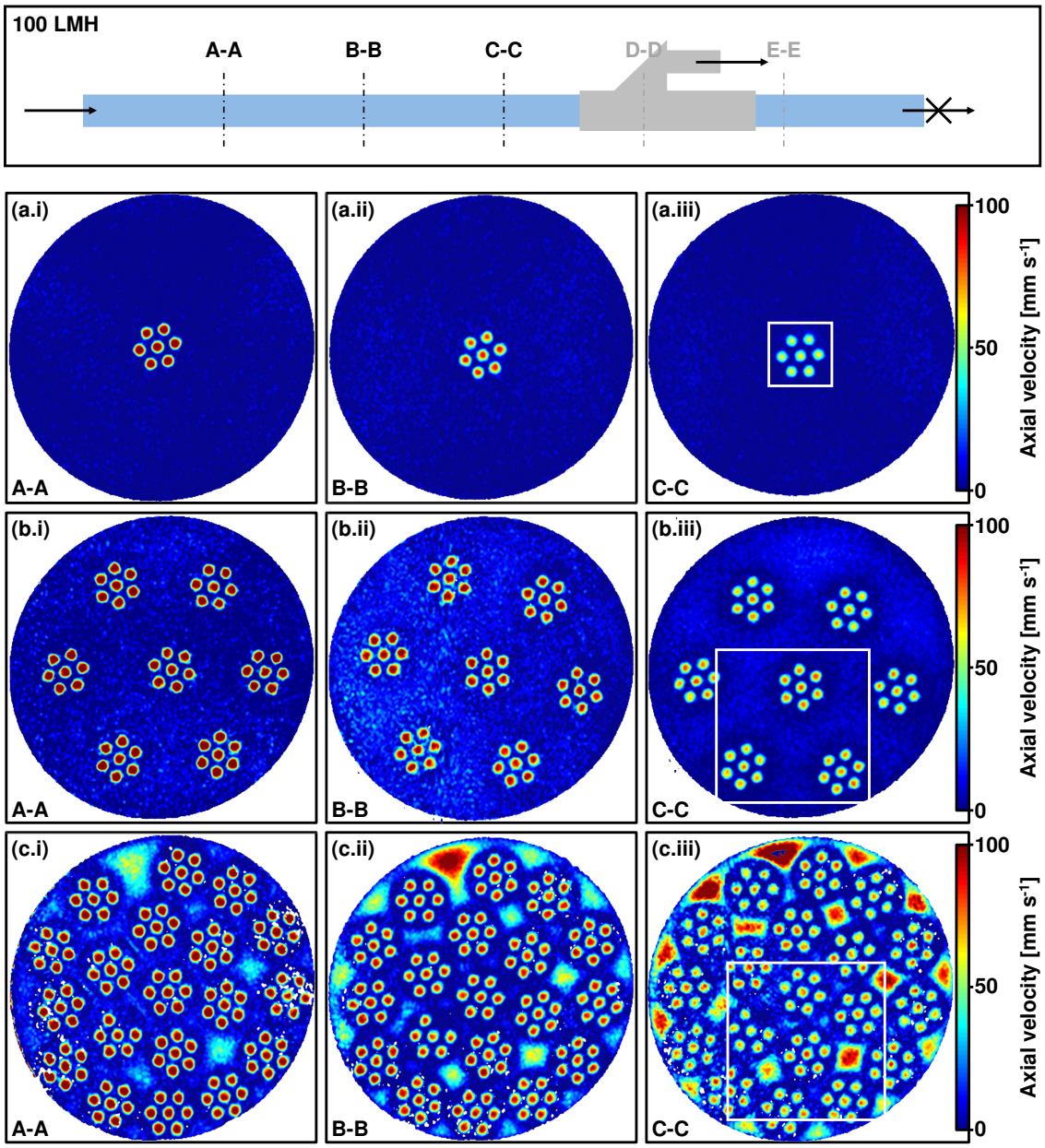

Figure 6.2: Axial flow-MRI measurements of multibore membrane modules in forward permeation mode containing (a) one, (b) seven, and (c) 19 SevenBore™ membranes at three different positions before the permeate outlet. White squares in (.iii) indicate zoomed position shown in Figure 6.4.

ure 6.4 (a), the highest velocities can be found in the central, right and bottom right lumen channel. In the magnification of the seven-membrane module in Figure 6.4 (b), the top membrane (central membrane in the whole module) has higher velocities compared to the two other ones; the bottom left membrane has the highest velocities in the central lumen channel; the

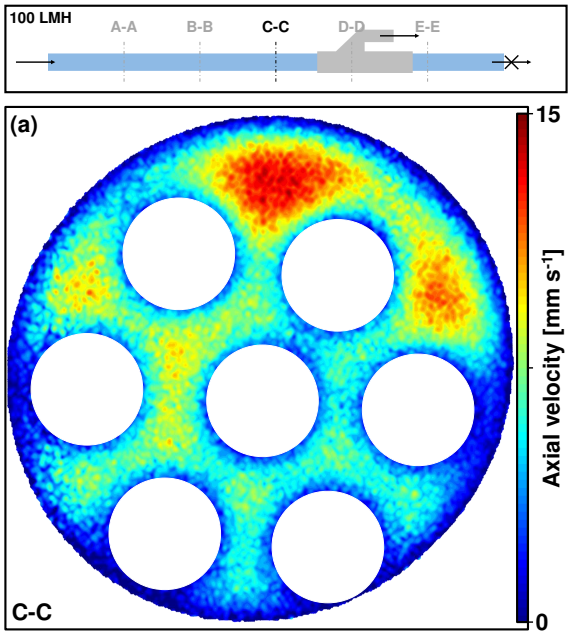

Figure 6.3: Axial flow-MRI measurements of a multibore membrane module in forward permeation mode with seven SevenBore™ membranes at position C-C. Only the uneven flow distribution on the shell side is visualized.

bottom right membrane has higher flows in the right lumen channels. One lumen channel even possesses negative velocities in the highly-packed module (see Figure 6.4 (c)). This phenomenon probably occurs as this channel is blocked at a position closer to the feet inlet (before slice A-A). Looking at the several contributions of individual lumen channels shows that, on the one hand, the difference in maximum lumen velocity increases with higher packing densities. On the other hand, the maldistribution becomes more pronounced along the module axis. For example, the flow in the one-membrane module is relatively evenly distributed with a deviation in maximum lumen velocities of 8.5 % close to the feed inlet (A-A) and increases to 9.4 % close to the permeate outlet (C-C) (an increase of 0.9 %). This heterogeneity increases for the seven-membrane module to 17.7 % at slice A-A and 21.2 % at slice C-C (an increase of 3.4 %), and even more for the 19-membrane module to 27.9 % at slice A-A and 35 % at slice C-C (an increase of 7.1 %). In conclusion, the higher the packing density, the more complex the flow field and heterogeneities become more likely. Nevertheless, if lumen channels are not clogged, they are flown through, and

the liquid leaves the porous structure.

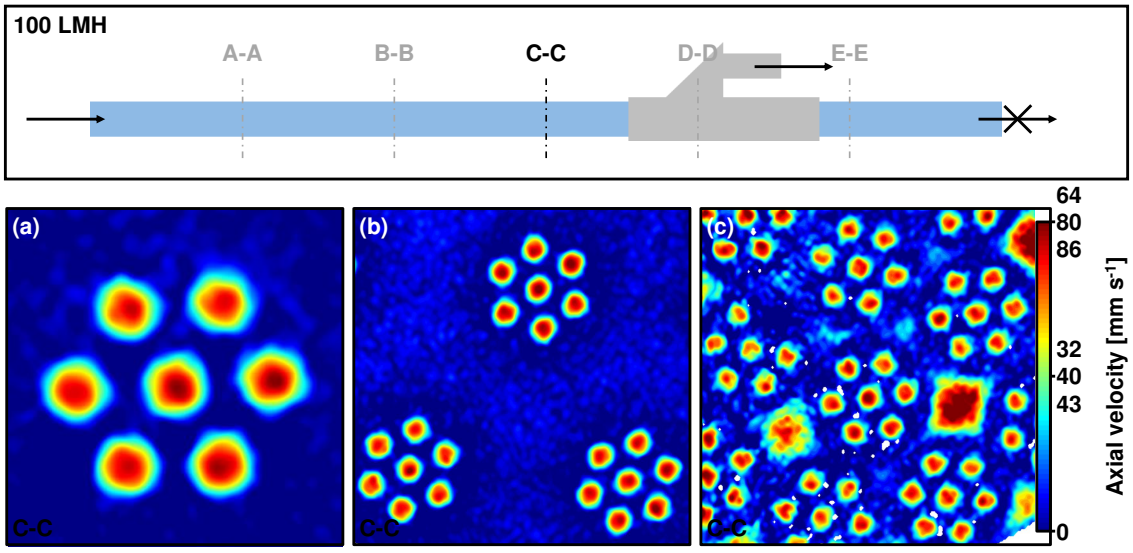

Figure 6.4: Zoom in flow-MRIs from Figure 6.2. Velocity scales differ in each magnification to highlight uneven flow distribution in membranes. Max. values of 64 mm s^{-1} for (a), 80 mm s^{-1} for (b), and 86 mm s^{-1} for (c).

Radial velocities The resulting radial flow velocities for the highly-packed membrane module can be obtained from Figure 6.5. The flow magnitude is represented by colors from 0 mm s^{-1} in dark blue to 3 mm s^{-1} in dark red, arrows depict the flow direction. Depending on the measured position, the liquid flows on the shell side between the membranes and distributes, following the path of least resistance. No trend can be detected as the fluid seems to flow randomly (according to the position of the membranes) through the module. As stated by Costello et al. [Cost1993], the fluid flows continuously and looks for areas with lower packing densities. Since the resolution is too low, flow profiles in the lumen channels could not be measured. Also, no flow paths form for the seven-membrane and one-membrane modules due to too much void space for the liquid on the shell side.

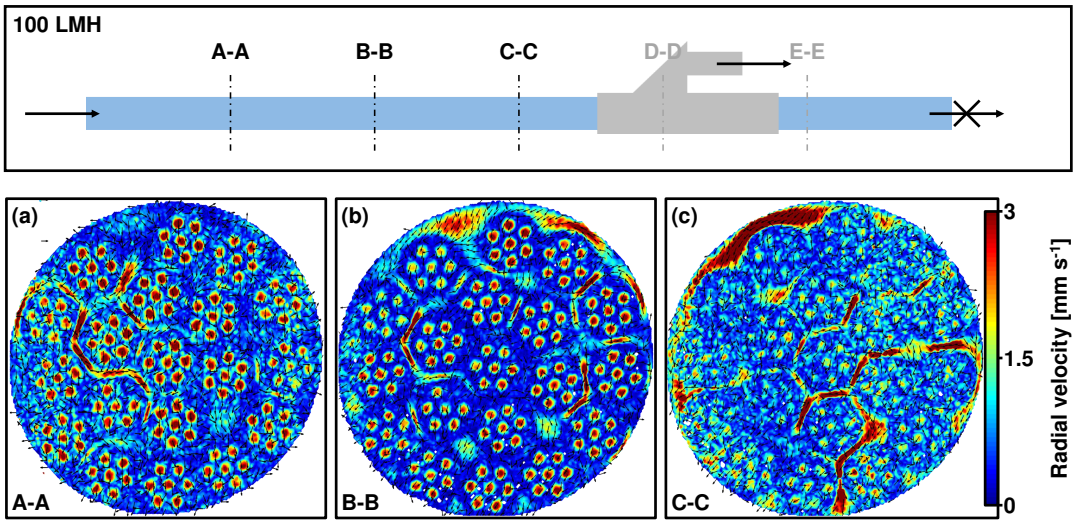

Figure 6.5: Radial flow-MRI measurements of a multibore membrane module in forward permeation mode containing 19 SevenBore™ membranes at three different positions before the permeate outlet.

6.3.2 Pure water forward permeation - the role of the outlet position

More interesting than the flow fields in front of the permeate outlet position are the positions directly at the outlet, especially behind the permeate outlet. Figure 6.6 depicts axial flow fields at (.i) and behind (.ii) the outlet position for a membrane module with one (a), seven (b) and nineteen (c) multibore membranes at 100 LMH with different scales.

Shell side In the lowest packed module (Figure 6.6 (a)), axial flow velocities on the shell side are close to zero as the volume flow rate is too low to generate significant flows at the shell side.
For the seven-membrane module in Figure 6.6 (b.i), permeate outlet flows in two directions were measured. Since the module does not end at this position, fluid from both sides accumulates and flows through the permeate outlet. Thereby, negative velocities from behind the permeate outlet are present on the right side and positive velocities from before the permeate outlet on the left side. It can be seen that the middle membrane is slightly shifted to the right. Thus, as mentioned before, this small deviation from the ideal position leads to a maldistribution and slightly higher velocities left

from the central membrane. This phenomenon can also be seen behind the outlet position (see Figure 6.6 (b.ii)) with velocities of about –5 mm s^{-1}.

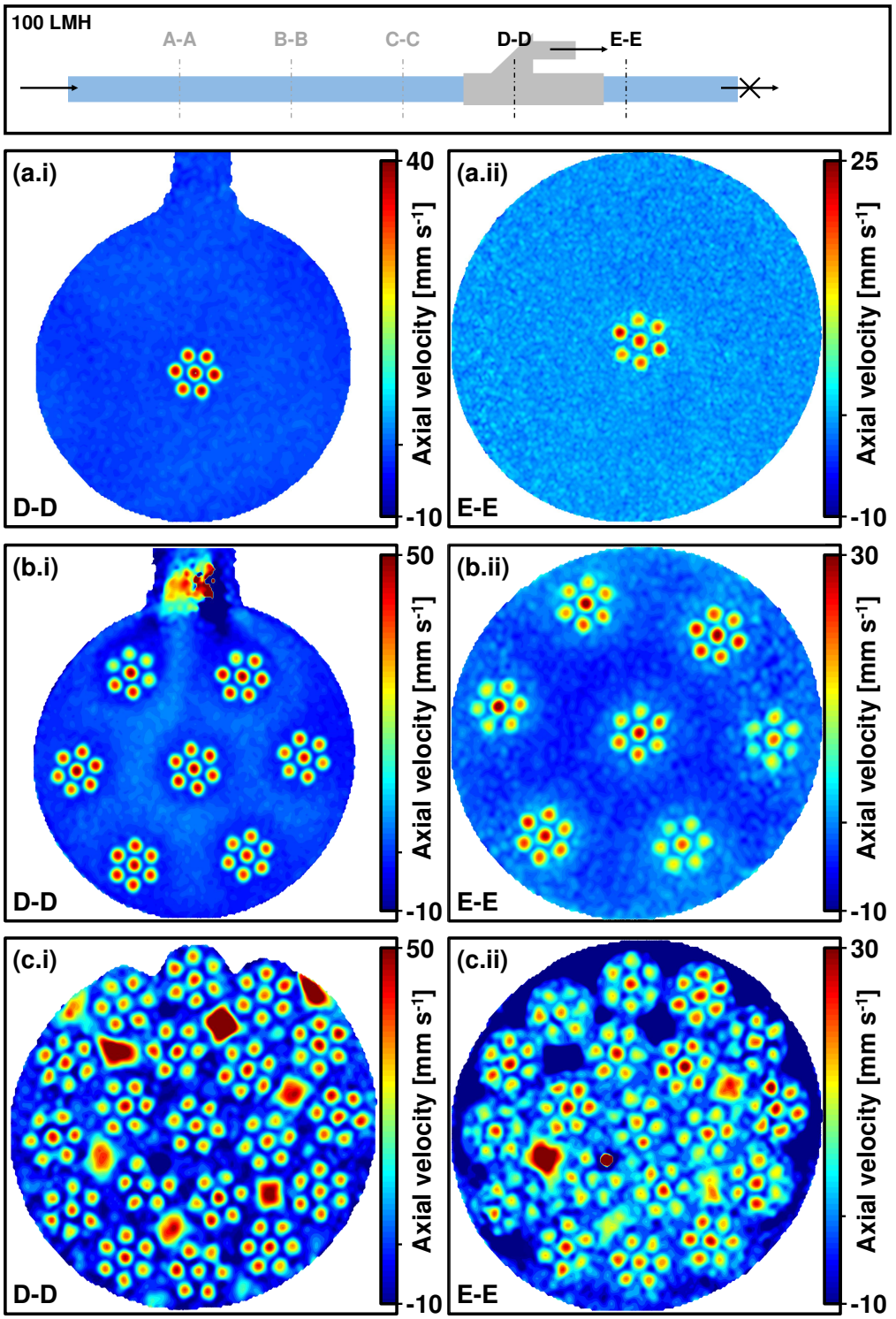

Figure 6.6: Axial flow-MRI measurements of multibore membrane modules in forward permeation mode containing (a) one, (b) seven, and (c) 19 SevenBore™ membranes at the permeate outlet and 8.3 cm behind.

In the highly-packed membrane module in Figure 6.6 (c.i), no outlet flows can be measured as the volume flow is too high to capture any velocities at this position. As mentioned in the previous section, jet streams build up between the membranes with higher velocities in the upper half of the module. Still, hardly any velocity can be measured next to the central membrane. Curiously, one can find spots with negative flow velocities of –26 mm s^{-1} on the shell side next to the jet streams of about 114 mm s^{-1}. This phenomenon is more pronounced at position E-E (see Figure 6.6 (c.ii)). Negative flows are expected behind the permeate outlet as the fluid on the shell side has to leave the membrane module via the outlet. On the top part of the module, these negative velocities of maximum –85 mm s^{-1} can be found. However, especially when the membranes are close to each other, positive velocities of 40 mm s^{-1} are present as well. In the module, a recirculating flow on the shell side exists that may affect the fluid flow distribution in the several lumen channels due to local pressure differences.

Lumen side As mentioned in the previous section, the non-uniform flow distribution along the membrane axis further increases towards to module's end. Especially at position E-E the deviation in maximum lumen velocities increases drastically, and the flow distribution in the lumen channels is highly uneven. In the one-membrane module, this deviation is 13.8 % for the slice at the permeate outlet (D-D), rising to 34.6 % at slice E-E (an increase of 20.8 %).

Lumen flow velocities in Figure 6.6 (b.i) reveal that the permeate outlet influences the membranes' hydrodynamic behavior. The lumen channels closest to the permeate outlet possess the lowest velocities leading to high deviations of 52.4 %. It seems that the high shell-sided velocities at the outlet induce drag forces and suck the fluid out of the respective lumen channels. These high deviations further increase to 69.7 % towards the module's end (slice E-E, Figure 6.6 (b.ii)). Here, the highest velocities in all membranes can always be found in the central lumen channel. This means that the central channel contributes less to the filtration performance, which is in accordance with separation layer velocity simulations in *Chapter 5*.

The phenomenon of drag forces at the permeate outlet can also be seen in the highly-packed module (see Figure 6.6 (c.i)), even if the effect is not as strong as in the seven-membrane module. Still, at these two positions, the deviations are increasing to 42.3 % at slice (D-D) and to 58.3 % at the module's end (slice E-E), with mostly the highest velocities in the central lumen channels. Moreover, the velocities inside the lumen channel with negative flow velocities further increase (Figure 6.6 (c.ii) shows a measuring artifact).

6.3.3 Pure water backwashing

For backwashing experiments, the direction of the fluid flow is reversed to outside-in mode, and the flow rate is increased to 200 LMH. Figure 6.7 shows axial flow distributions at three different positions (A-A, C-C, and E-E). Each graph has another scale bar to better highlight flow phenomena.

Shell side In the seven-membrane module, velocities decrease from $-11\,\mathrm{mm\,s^{-1}}$ at A-A to $-25\,\mathrm{mm\,s^{-1}}$ at C-C and increases to $10\,\mathrm{mm\,s^{-1}}$ at E-E. This increase is reasonable as the backwashing fluid has to reach the end of the module. It is assumed that the shell side flow decreases to $0\,\mathrm{mm\,s^{-1}}$ at the module's end at both sides.

More interesting are the shell-sided velocities for the 19-membrane module. The backwashing fluid enters the module from the top and moves along the module until slice A-A (and E-E) is reached (see Figures 6.7 (b.i) and (b.ii)). Thereby, maximum negative velocities of $-315\,\mathrm{mm\,s^{-1}}$ at C-C and $-176\,\mathrm{mm\,s^{-1}}$ at A-A are reached. It seems that the backwashing fluid at A-A in Figure 6.7 (b.i) pushes the membranes to the bottom side of the module. Thus, a close packing of seven membranes forms (bottom-left), leading to the formation of jet streams in a positive flow direction of up to $165\,\mathrm{mm\,s^{-1}}$. These recirculating flows diminish closer to the backwashing inlet (at slice C-C) and build up again behind the backwashing inlet at E-E (see Figure 6.7 (b.iii)). Thereby, velocities range from $-149\,\mathrm{mm\,s^{-1}}$ to over $300\,\mathrm{mm\,s^{-1}}$ leading to a highly non-uniform shell-sided flow distribution.

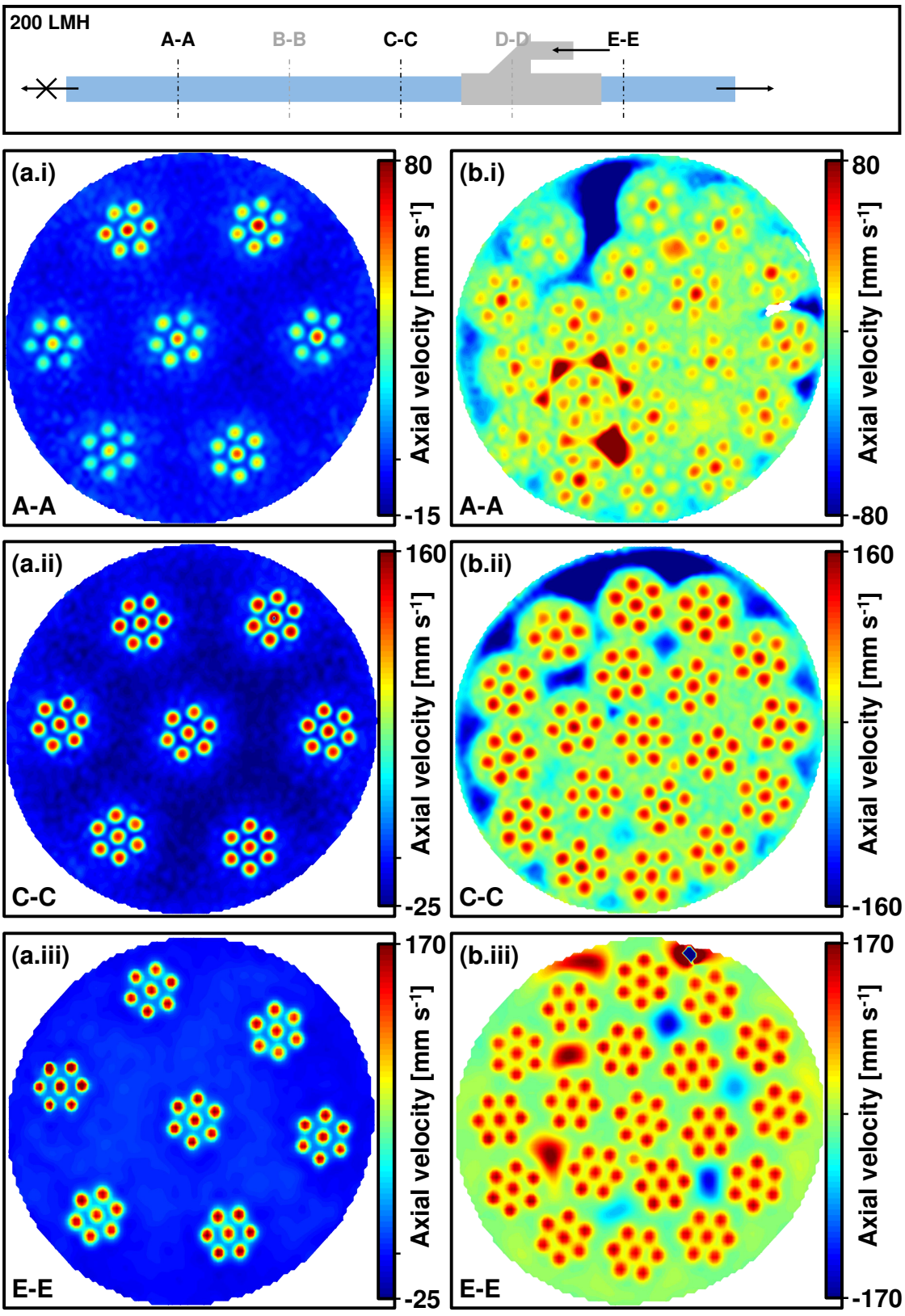

Figure 6.7: Axial flow-MRI measurements of multibore membrane modules in backwashing mode containing (a) seven and (b) 19 SevenBore™ membranes at three different positions - two before the backwashing inlet and one behind the backwashing inlet.

Lumen side Every lumen channel is reached at slice A-A (furthest away from the backwashing inlet), and a velocity can be measured. This behavior was not expected as the (former retentate) outlet is closer to the backwashing inlet. That means that backwashing is potentially successful. However, Figures 6.7 (a.i) and (b.i) show that not every lumen channel is reached equally. In each membrane, the central lumen channel possesses the highest velocity value. The deviation in maximum lumen velocities in the seven-membrane module at slice A-A amounts to 63.6 %. In the highly-packed module, several lumen channels have hardly any flow at slice A-A, resulting in a deviation of more than 90 %. These inequalities even out along the module axis. For example, in the 19-membrane module, deviations decrease to 43.4 % at slice C-C and to 28.4 % at slice E-E. The lumen channel analysis gives reason to believe that effective backwashing is challenging as not every lumen channel is flushed equally.

6.4 Conclusion and outlook

In this chapter, a comprehensive magnetic resonance imaging study reveals the hydrodynamic effects in multibore membrane modules with three different packing densities in forward permeation and backwashing mode. This study helps to understand the interaction of membranes with their surroundings and shows challenging flow phenomena on shell and lumen side as well as an influence of the outlet position.

In detail, in front of the outlet position, the forward permeation mode shows that the shell-sided flow is more and more heterogeneous for higher packing densities, and jet streams evolve in the highest-packed module. Also, the deviation in maximum velocities increases along the module axis and the uneven flow distribution is higher for higher packing densities. These non-uniformities become extremely pronounced behind the outlet position, showing that the outlet's position can majorly influence the permeation (and especially the backwashing) behavior. Additionally, streams with positive and negative velocities recirculate at the end of the membrane module leading to local pressure differences, which again counteract a homoge-

neous flow distribution.

In the backwashing experiments, all lumen channels are reached even at the furthest position from the backwashing inlet. However, the flow inside one membrane is unevenly distributed with the highest velocities in the central lumen channel. Even if this maldistribution evens out along the module axis, it can lead to an inefficient backwashing process.

All chapters in the thesis up until now (*Chapter 4: Single Multibore Membrane Module Performance*, *Chapter 5: Single Multibore Membrane with Porosity Gradients*, and *Chapter 6: Hydrodynamics in Multi-Multibore Membrane Modules*) focused on multibore membranes and membrane modules after reaching a steady state. However, this is only the case after a first filtration cycle in which pre-wetting and pore-stabilizing agents are removed. But how does this first filtration cycle look like? **Chapter 7: Initial Wetting Patterns in Multibore Membrane Modules** investigates the initial dynamic wetting progress in multibore membrane modules in which the membranes are filled with different pre-wetting agents.

7

Initial Wetting Patterns in Multibore Membrane Modules

Parts of this chapter have been published as:

Denis Wypysek, Anna Maria Kalde, Florian Pradellok, Matthias Wessling,

"In-situ investigation of wetting patterns in polymeric multibore membranes via magnetic resonance imaging", *Journal of Membrane Science* 622 (2021) 119026.

DOI: 10.1016/j.memsci.2020.119026

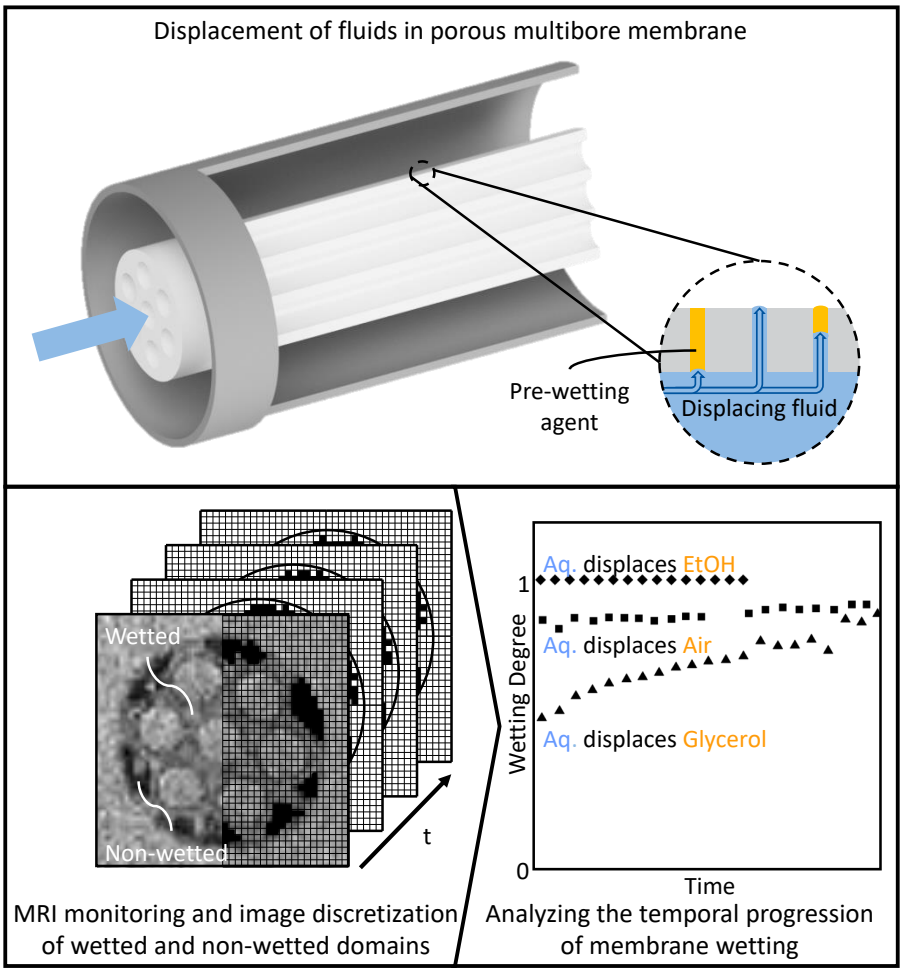

7.1 Introduction

As analyzed in *Chapter 5: Single Multibore Membrane with Porosity Gradients*, especially multibore membranes possess a porous nature that allows them to separate particular matter from a liquid system. Multibore membranes are monolithic and house several bore channels within one porous polymer matrix with porosity gradients. Especially the flow distribution across a multibore membrane has been proven to be very sensitive to non-idealities such as bending, skin damages, or eccentric positioning. In turn, this altered flow distribution causes distinct changes in flow patterns across the whole module (see Chapter 4: Single Multibore Membrane Module Performance).

A versatile method for analyzing fluid flow distribution and the online and in-situ characterization of membrane filtration is magnetic resonance imaging (MRI) and flow-MRI. MRI is a noninvasive tool to monitor fluid velocities and particle depositions. Studies using MRI and flow-MRI for characterization of membrane filtration with liquid-liquid [Yao1995a; Pope1996] as well as liquid-solid systems [Aire1998; Buet2011; Çulf2011] have been presented in literature. Thereby, there is no need for large superconducting magnet MRI systems for the measurement of membrane modules to gain valuable information, as low-field benchtop hardware can be used for this purpose [Yang2014; Wies2018b].

As the MRI technology also allows the measurement of liquid content present in the membrane, wetted and non-wetted areas inside the porous structure can be distinguished. Incomplete wetting of membranes can influence the permeation and performance of the filtration process significantly [Peña1993; Wang2005; Boho2005]. Hence, quantifying the degree of wetting and wetting times is important to judge the extent of permeable porosity. The majority of studies must assume that permeation experiments access a completely solvent-wetted membrane porosity. Comprehensive studies presented in the literature perform washing and wetting experiments prior to the final transport studies without further investigation of the achieved wetting degree. Hence, most investigations in the literature

focus on membrane performance in steady-state or after several usage cycles. However, this initial sub-optimal membrane performance might significantly impact later non-uniform flow distributions and fouling events. As early sub-optimal membrane performance has yet hardly been evaluated, investigating this loss in membrane performance at an early stage of usage is the main aim of this chapter.
Here, MRI inspection studies on the degree of wetting are reported and correlated with permeation experiments. The wetting behavior of commercial polyethersulfone (PES) multibore membranes (SevenBore™) inside custom-made membrane modules is investigated. The effect of packing density inside the module on membrane wetting is analyzed in detail. Direct wetting of membranes in delivery conditions is compared to pre-wetted membranes. Wetting degrees and wetting times are measured. This chapter aims at providing a more detailed understanding of initial permeation conditions. It suggests process conditions allowing a complete wetting of the membranes, leading to overall homogenized transport properties. Analyzing wetting and flow patterns at first membrane usage helps to understand and quantify the mechanisms causing sub-optimal membrane usage.

7.2 Background on wetting

Membrane wetting is mainly addressed for membrane contactors [Ibra2018], membrane distillation [Peña1993; Reza2018; Yao2020], microsieves [Giro2005], and monoliths [Mari2020]. However, literature affirms that the membrane's wetting state significantly influences microfiltration and ultrafiltration membrane performance [Roud2000; Koch2009; Argy2015; Argy2017]. Conventionally, commercially available ultrafiltration membranes are pre-filled with a pore stabilizer such as glycerol [He2004]. This fluid needs to be replaced by the feed solution before the filled pore can contribute to the filtration performance.
The results presented in literature indicate that even at advanced stages of filtration, the membranes remain partially non-wetted with water, especially for hydrophobic membranes in microporous parts of the struc-

ture [Koch2009; Argy2015]. This incomplete wetting is caused by the non-uniform pore size distribution in polymer networks produced via phase separation. Non-uniform pores that are connected and simultaneously wetted by a fluid form communicating networks. This network communication leads to non-uniform wetting [Das2005] and effects like fluid droplet trapping and bypassing flows [Pind2008]. In those cases, the necessary hydrodynamic pressure to wet the pores cannot be reached with the macroscopically applied transmembrane pressure (TMP). Hence, macroscopically non-uniformly wetted structures arise.

On a pore-scale level, the necessary pressure for pore wetting Δp_B depends on the surface tension γ, the macroscopic contact angle θ, and the local pore diameter d_{Pore} of the specific membrane and liquid system. It can be derived from the Young-Laplace equation (see Equation 7.1). The Young-Laplace equation is valid for large pore diameters, as additional effects such as van der Waals and electrostatic double-layer forces can have a dominating impact on the fluid-membrane interface for small pores of only some nanometers [Butt2003]. The membranes investigated are ultrafiltration membranes with a nominal pore size of 40 nm. Equation 7.1 is valid for the system used in this chapter.

$$\Delta p_B = \frac{4 \cdot \gamma \cdot cos\theta}{d_{Pore}} \tag{7.1}$$

7

At the membrane surface, where the retention of particular matter takes place, liquid only penetrates the membrane through wetted pores. Hence, the total liquid transport can be calculated by the sum of all flows through single pores. The volume flow $\dot{V}$ through a single pore can be calculated using the law of Hagen-Poisseuille as described in Equation 7.2. Here, the flow depends on the pore radius r, the local pressure gradient Δp, the liquid viscosity η, and the pore length L.

$$\dot{V} = \frac{\pi r^4}{8 \cdot \eta} \frac{\Delta p}{L} \tag{7.2}$$

A non-uniformly wetted membrane decreases the flux across the membrane in two ways. First, the number of pores contributing to the flux is reduced. Thus, the overall flux linearly decreases with an increasing number of non-water-wetted pores. Second, a non-uniformly wetted membrane only allows distinct flow paths for the liquid to pass through the membrane. Hence, flow patterns inside the membrane change, which causes unfavorable pathways limiting the liquid mass transport by increased pressure drop.

7.3 Experimentals

7.3.1 Experimental setup

Membrane The investigated inside-out ultrafiltration membranes are commercially available PES SevenBore™ fibers supplied by SUEZ Water Technologies & Solutions and described in detail in Section 2.4. Figure 7.1 (a) depicts the unique pore structure of the investigated membrane fibers. While blue framed areas mark the active membrane layer with smaller pore sizes, white framed areas depict the areas with bigger pore sizes representing the membrane's support structure. Domains with bigger pore sizes provide mechanical stability of the membrane fiber and do not contribute to particular matter separation.

Module For the examination of wetting morphologies inside the pore structure, individual fibers must be incorporated into modules. Thereby, three packing densities are investigated, which contain either one, seven, or 16 membrane fibers accounting for packing densities of 5 %, 35 %, and 79 %, respectively. Due to different batches, membranes used in this chapter are slightly bigger than in the previous chapter, and only 16 fibers fit in the module. The corresponding membrane arrangements are presented in Figure 7.1 (b). 3D-printed spacers are used to ensure constant positioning of the membrane fibers inside the single- and seven-fiber modules. The manufactured modules are similar to those from the previous chapter

and are 50 cm in length and have an internal diameter of 18 mm, containing connections for the feed stream and the permeate and retentate, respectively. The wetting behavior is monitored at three positions along the module length (see Figure 7.1 (c)). Measurement distances from the module inlet are 8.3 cm for position A-A, 16.6 cm for position B-B and 25 cm for position C-C.

Magnetic resonance imaging setup Figure 7.1 (c) represents the developed experimental setup which is similar to the setup in the previous chapter. All MRI measurements are carried out on a Magritek low-field NMR tomography system using a 2D spin-echo pulse sequence. Details of the used tomography system and pulse sequences can be obtained from Section 2.2.3. Within the 60 mm inner diameter imaging probe, the membrane module is placed horizontally. Measurements in the tomograph are carried out in the x-y-plane, being the cross section of the membrane module.
In all experiments, a fluid circuit is established with an ISMATEC® ISM405A gear pump. Thereby, fluxes of 50 liter per square meter membrane area and hour (LMH), 100 LMH, and 200 LMH are applied to the membrane modules. For wetting experiments, a copper sulfate solution of 3.12 g L^{-1} copper(II) sulfate pentahydrate ($CuSO_4 \cdot 5\,H_2O$, $\geq$ 99.5%, Carl Roth, Germany) in de-ionized water was used as aqueous phase, hereafter termed aqueous solution. This concentration is equivalent to 0.05 M ionic strength. The use of a $CuSO_4$-solution has a potential influence on the wetting progress as it might shift the contact angle of the used material system. However, $CuSO_4$ reduces measuring times significantly. Corresponding mass flow rates across the membrane are monitored with a mini CORI-FLOW™ M14 (Bronkhorst High-Tech B.V., Netherlands). The resulting TMP is recorded with a Wika pressure transmitter S-11 (Wika, Germany). An individual module with new membranes was fabricated for each experiment to ensure comparability between experiments on the impact of flux and packing density.
Depending on the material system, the MRI parameters vary to obtain a maximum spatial and temporal resolution. Thus, imaging times varied from

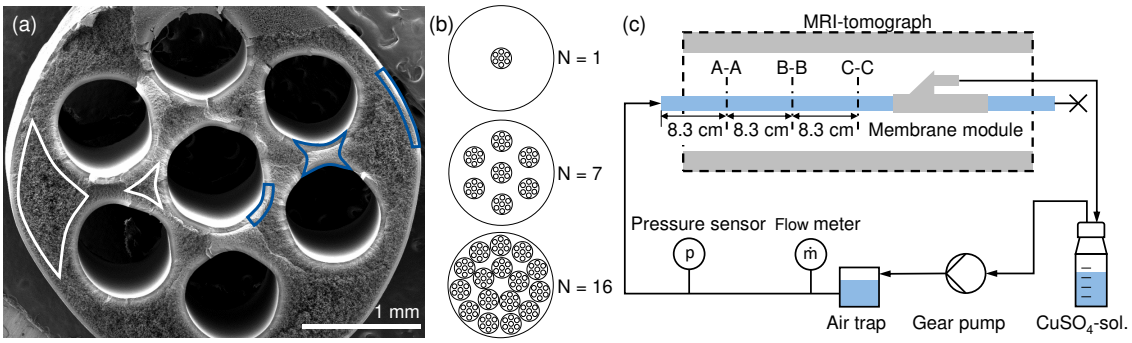

Figure 7.1: Presentation of (a) a FESEM image of the cross section of the investigated SevenBore™™ membrane fibers, (b) three considered membrane packing densities and the correlating membrane arrangements in the membrane module, (c) the experimental setup for the investigation on the wetting behavior of SevenBore™ membranes via MRI.

4:47 min for delivery-state, as well as for washed and dried membranes to 6:50 min for ethanol-filled membranes leading to time-averaged magnetic resonance images. MRI parameters for all three material systems are listed in Table 7.1.

Table 7.1: MRI parameters for the investigation of wetting morphologies in delivery-state, washed & dried (wd), and ethanol-filled membrane fibers with copper sulfate solution ($CuSO_4$). Filed of view (FoV).

Wetting fluid in pores		Glycerol	Air (wd)	Ethanol
Displacing fluid		$CuSO_4$	$CuSO_4$	$CuSO_4$
Parameter	Unit	Value	Value	Value
Repetition time	[ms]	280	280	400
Echo time	[ms]	48	48	32
FoV Read [x]	[mm]	24	24	45
FoV Phase [y]	[mm]	24	24	40
Slice thickness [z]	[mm]	10	10	10
No. of pixels [x × y]	[-]	256 × 256	256 × 256	256 × 256
Resolution [x × y]	[µm/px]	94 × 94	94 × 94	176 × 156
Number of scans	[-]	4	4	4
Acquisition time	[min:sec]	4:47	4:47	6:50

7.3.2 Wetting procedures

Proof of concept - weight loss after washing Typically, ultrafiltration membranes are factory-filled with a pore stabilizer, as the pore network in the selective layer tends to collapse when dried. According to the manufacturer, glycerol is used as a pre-wetting agent, which is known to be a prominent choice for pore network stabilization [SUEZ]. Glycerol as a pre-wetting agent can be removed by washing with ethanol. To investigate the amount of contained pre-wetting agent, as well as to evaluate the approach of ethanol-washing, single membrane fiber samples are immersed in EtOH for two hours and were dried in an exsiccator for 30 min. The sample masses were compared to delivery-state membranes, also dried in an exsiccator for the same time. The weight loss of 5 cm membrane samples can be seen in Table 7.2 and confirms that the pre-filling agent is washed out successfully.

Table 7.2: Weight of 5 cm membrane samples for delivery-state membranes, dried membranes, and washed and dried membranes and the corresponding weight loss after treatment.

Configuration	Mass [mg/cm]	Weight loss [mg/cm]	Weight loss [%]
Delivery-state	35.54 $\pm$ 1.7	-	-
Dried	33.04	2.50	7.03
Washed & dried	16.94	18.60	52.34

Proof of concept - initial wetting conditions and porous structure signal To correlate the MRI data obtained from membrane investigation to the observed changes in mass due to drying, MRI reference measurements were used. The signal strengths of pure fluids, as well as different fluid systems inside a membrane structure, were compared to the reference time steps (t = 0) of delivery state and ethanol-washed and dried (air-filled) membranes to show the suitability of MRI measurements to distinguish wetting states inside the membrane. These reference experiments are shown in Figure 7.2. Averaging over multiple pixels is indicated by the straight white lines.

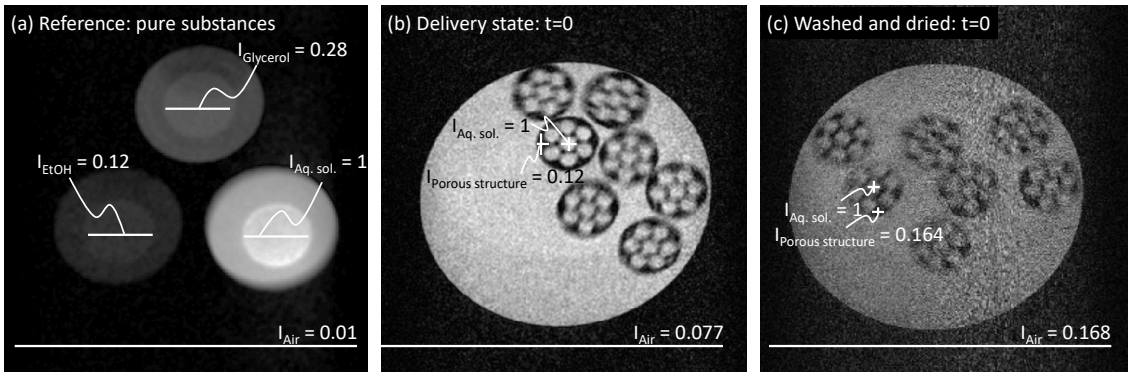

Figure 7.2: Fluid signal intensity comparison for ethanol, glycerol, and copper sulfate solution, normalized for the signal strength of the aqueous solution. (a) Pure fluids measured for reference. Reference time step images at the beginning of the permeation experiment for a module containing seven (b) delivery-state membrane fibers and (c) ethanol-washed and subsequently dried membrane fibers.

Figure 7.2 (a) shows the relative signal strengths of ethanol (bottom left), glycerol (top), and aqueous solution (bottom right) used for the wetting experiments in this chapter. The MRI signals are normalized to the signal of the aqueous solution. Figures 7.2 (b) and (c) show the reference time steps of the wetting experiments for a seven-fiber module in delivery state (b) and ethanol-washed and dried membranes (c). The reference time step is defined as the time step when the shell side is carefully flooded with the aqueous solution, and the lumen channels are initially flooded without pressure build-up. Hence, the signal in the module's shell side and inside the lumen channels arises from the pure aqueous phase. The signal strength inside the membrane's porous structure arises from an average of the polymer and the contained fluid system. The polymer can be assumed to lead to no or very low signal. The MRI signals inside the membrane structure are uniform within one MRI measurement.

The signal in the polymer matrix region is significantly higher than the module-surrounding air signal for the delivery-state fibers shown in Figure 7.2 (b). However, for the washed and dried fibers displayed in Figure 7.2 (c), the signal is nearly the same as the surrounding air. Hence, it is concluded that the membranes' porous structure is at least partially or even completely filled with a pore-stabilizing agent in the delivery state. This pore-stabilizing agent that is assumed to be glycerol can entirely be

removed by membrane washing in ethanol. The drying procedure applied in this study is sufficient for complete solvent removal as the membranes appear to be fully air-filled after the drying procedure.
This data implies that main parts of the membrane are factory-filled with a pore-stabilizing agent that can be removed with ethanol-washing. It is concluded that at least the selective layer of the investigated membranes is fully pre-filled with a pore-stabilizing agent. Also, a clear trend regarding the initial wetting state of the more macroporous support structure is present.

Wetting experiments Based on the findings of sample masses and MRI references, three sets of experiments were carried out to investigate the impact of the wetting fluid on the wetting morphologies inside the pore structure via MRI. Each wetting experiment was conducted in dead-end mode for approximately 6 hours.
First, the pre-wetting agent in the pore structure of commercially available membrane fibers is displaced with the aqueous solution. The pre-wetting agent is assumed to be present at least in all pores of the selective layer and to some extent in the mechanical support domains.
Second, the pre-wetting and stabilizing agent is removed by ethanol washing. Throughout ethanol washing, seven membrane fibers are immersed in approximately 150 mL ethanol (EtOH, $\geq$ 96 %, Carl Roth, Germany) for 24 hours. Afterward, the washed fibers are dried by placing them in a fume hood for at least 24 hours at room temperature and ambient pressure. Washed and dried membrane fibers are incorporated into modules containing seven fibers and are wetted with the aqueous solution.
Third, membranes are washed with ethanol directly inside the module to replace the prevalent glycerol in the pores entirely. Without any drying step, the ethanol is displaced by aqueous solution. For ethanol wetting, an ethanol flux of 100 LMH is applied to a membrane module containing seven SevenBore™ fibers. Thereby, the progress of ethanol wetting is monitored via MRI. With the fibers thoroughly wetted with ethanol, the fluid is switched to aqueous solution at a flux of either 50 LMH or 100 LMH.
All applied experimental setup conditions are summarized in Table 7.3.

Table 7.3: Figures with corresponding setup configurations. ds=delivery state; wd = washed and dried. $CuSO_4$ = copper sulfate solution.

	Wetting fluid in pores	Displacing fluid	Res. [x × y] in µm/pixel	No. of membranes	Slice	Flux in LMH
Figure 7.4	Glycerol (ds)	$CuSO_4$	94 × 94	1	A-A	200
Figure 7.5	Glycerol (ds)	$CuSO_4$	94 × 94	1, 7, 16	C-C	100, 200
Figure 7.6	Glycerol (ds)	$CuSO_4$	-	1, 7, 16	C-C	100, 200
Figure 7.7	Glycerol (ds)	$CuSO_4$	94 × 94	16	A-A, B-B, C-C	200
Figure 7.8	Air (wd)	$CuSO_4$	94 × 94	7	C-C	100, 200
Figure 7.9	Ethanol	$CuSO_4$	176 × 156	7	C-C	50, 100
Figure 7.10	Glycerol (ds)	$CuSO_4$	-	7	C-C	100
	Air (wd)	$CuSO_4$	-	7	C-C	100
	Ethanol	$CuSO_4$	-	7	C-C	100
	Glycerol (ds)	Ethanol	-	7	C-C	100
Figure. 7.11	Air (wd)	$CuSO_4$	-	7	C-C	100, 200
Figure. 7.12	Glycerol (ds)	Ethanol	94 × 94	7	C-C	100
Figure. 7.13	Air (wd)	$CuSO_4$	-	7	C-C	100, 200
Figure. 7.14	Glycerol (ds)	$CuSO_4$	-	7	C-C	100, 200
Figure. 7.15	Glycerol (ds)	$CuSO_4$	94 × 94	7	C-C	50, 100, 200

7.3.3 Data processing for wetting quantification

Data processing with Matlab The obtained MRI raw data consist of 512x512 pixel images (due to zero filling) that depict a normalized signal strength assigned to the corresponding pixel. Figure 7.3 (a) shows an exemplary raw imaged during the wetting procedure of a single-fiber module. The light outer domain represents the shell side of the module filled with aqueous solution, while the middle darker structure depicts the SevenBore™ membrane. Figure 7.3 (b) shows a magnification of the membrane area. Different values on the grayscale can be distinguished. The seven light circles depict the seven lumen channels of the membrane. However, also inside the polymer structure, different signal strengths are observed. This difference in signal strength results from a combination of aqueous solution wetted (brighter) or non-wetted (darker) sections inside the membrane.

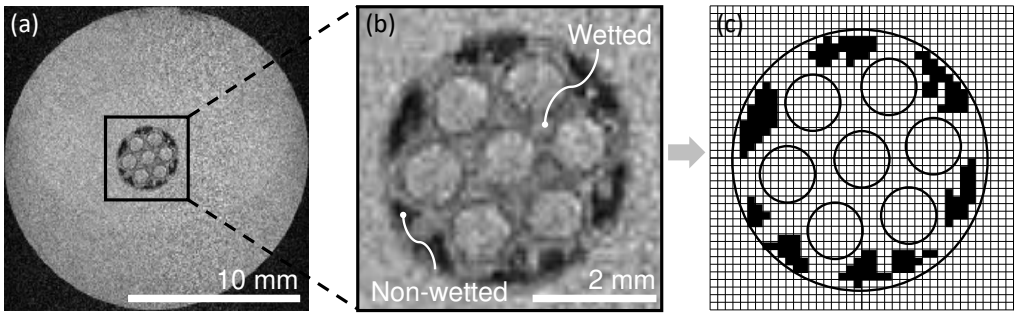

Figure 7.3: Representation of the functionality of the developed Matlab tool for the determination of the membrane's wetting degree. (a) Magnetic resonance image of a single-fiber module during the wetting process. (b) Magnified image of the membrane fiber with wetted (grayish) and non-wetted (blackish) areas in the membrane cross section. (c) Discretization performed by the developed Matlab tool in wetted and non-wetted pixels.

The membranes' wetting degree (WD) can only be compared qualitatively with the obtained raw data. Image processing with a developed Matlab code enables a quantitative analysis. The membrane area was defined automatically. Within this area, setting a threshold (obtained from the sensitivity analysis, see below) for single pixels' signal strength lead to a binary image. Light pixels were attributed as wetted membrane area, black pixels as non-wetted membrane area. Figure 7.3 (c) shows an exemplary binary

image. The wetting degree was determined by the ratio of wetted area to the total membrane area (see Equation 7.3).

$$\text{Wetting degree WD} = \frac{\sum \text{Wetted pixels}}{\sum \text{Wetted pixels} + \sum \text{Non-wetted pixels}} \tag{7.3}$$

Sensitivity analysis of wetting degree towards variations of the threshold To identify a reasonable threshold, a membrane was fully wetted with aqueous solution, and the MRI signal strength within the wetted membrane matrix was measured. A signal strength of 0.8 was then set as the threshold for distinguishing wetted and non-wetted membrane areas. The wetting degree appears to be robust to variations in the threshold. By changing the threshold by $\pm$10 % of its original value, the obtained wetting degrees differ by only two to six percent, which can be seen in Table 7.4.

Table 7.4: Wetting degree evaluation of MRIs from Figure 7.5 of single-, seven- and 16-fiber modules at different applied thresholds to consider a pixel as wetted. These evaluations were done to evaluate the sensitivity of wetting degree towards variations of the threshold.

		Wetting degree		
Minimum signal strength		0.8 - 10%	0.8	0.8 + 10%
100 LMH	Single-fiber module	0.75	0.72	0.68
	Seven-fiber module	0.79	0.77	0.75
	16-fiber module	0.76	0.75	0.69
200 LMH	Single-fiber module	0.84	0.81	0.78
	Seven-fiber module	0.76	0.73	0.70
	16-fiber module	0.91	0.89	0.87

7.4 Results and discussion

7.4.1 Reproducibility of wetting experiments

Although only one experiment per configuration is presented in the following, it is assumed that the observed results are representative as clear trends between several experiments can be seen. A high number of manual steps is needed for module assembly, which in itself causes slight variations in the setup. This is why some variations in the observed wetting degrees between single experiments are expected. Still, the characteristics of the applied hydrodynamic stresses remain the same. Tables 7.5 and 7.6 present wetting degrees of all single fibers inside a single-fiber module, a seven-fiber module, and a 16-fiber module obtained from the MRIs in Figure 7.5 for 100 and 200 LMH, respectively. Here, all phenomenological wetting patterns observed in the membrane fibers are similar within one experiment. This is coherent with the wetting degrees calculated for the single fibers. These wetting degrees differ by only three to five percent. Hence, this observation indicates that the formed wetting pathways are reproducible for similar applied hydrodynamic stresses.

Table 7.5: Evaluation of the wetting degree (WD) for each single fiber in a module containing one, seven, and 16 fibers (fib.) at 100 LMH.

1 fib.	WD	7 fib.	WD	16 fib.	WD	16 fib.	WD
1	0.72	1	0.81	1	0.74	9	0.68
		2	0.75	2	0.69	10	0.68
		3	0.82	3	0.67	11	0.69
		4	0.81	4	0.71	12	0.72
		5	0.77	5	0.73	13	0.74
		6	0.72	6	0.81	14	0.69
		7	0.72	7	0.73	15	0.76
				8	0.70	16	0.70
100 LMH		Average	0.77 $\pm$0.04	Average	0.71 $\pm$0.04		

Table 7.6: Evaluation of the wetting degree (WD) for each single fiber in a module containing one, seven, and 16 fibers (fib.) at 200 LMH.

1 fib.	WD	7 fib.	WD	16 fib.	WD	16 fib.	WD
1	0.81	1	0.72	1	0.86	9	0.82
		2	0.77	2	0.86	10	0.88
		3	0.70	3	0.90	11	0.85
		4	0.71	4	0.88	12	0.91
		5	0.76	5	0.91	13	0.91
		6	0.75	6	0.86	14	0.92
		7	0.72	7	0.84	15	0.92
				8	0.87	16	0.94
200 LMH		Average	0.73 $\pm$0.03	Average	0.88 $\pm$0.03		

7.4.2 Aqueous solution wetting delivery-state membranes

Single fiber wetting Figure 7.4 shows MRIs of the progression of membrane wetting over time for a single-fiber module at an inside-out flux of 200 LMH. The signals were detected close to the feed inlet of the module (position A-A).

The image depicted in Figure 7.4 (a) is taken directly after filling the module with the aqueous solution and starting the permeation experiment. The membrane area appears to be non-wetted with aqueous solution. The membrane is surrounded by the electrolyte but not positioned centrally. Compared to images taken later during the wetting progress, the membrane is initially found in a different position in the module cross section. This shift in position is induced by swelling of the polymer material that causes strains and bending of the membrane [Wypy2019]. The lumen channels cannot be seen as circular light structures but show crescent-shaped light areas. One reason is the membrane's movement that causes artifacts in the MRI measurements and thereby the same position of the

light areas inside the lumen channels.

Throughout the permeation experiment presented in Figure 7.4, a brightening of the membrane area is detected, which expands from the lumen channels outwards. This brightening depicts the wetting areas inside the membrane polymer structure. Thereby, domains associated with smaller pore sizes, as demonstrated in 7.1 (a), tend to be wetted earlier during the permeation process than domains with larger pore sizes. This is unexpected as the Young-Laplace equation predicts earlier wetting of bigger pore sizes. Additional to the wetting of smaller pores, flow paths through domains associated with larger pore sizes have formed after two hours.

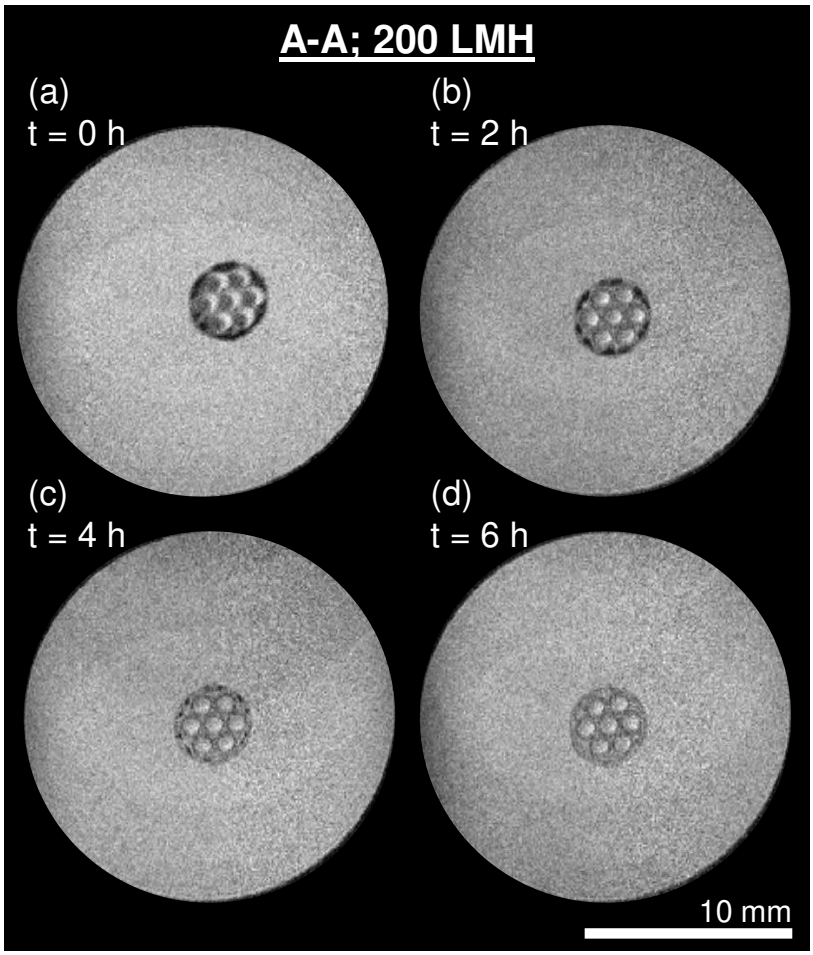

Figure 7.4: Magnetic resonance images of a delivery-state single-fiber module during the wetting process at 200 LMH at position A-A (a) at the beginning of the experiment, after (b) two hours, (c) four hours, and (d) six hours of permeation.

However, even after four hours of permeation, macroscopic non-wetted areas can still be detected, as shown in Figure 7.4 (c). Only after approxi-

mately six hours, no distinct non-wetted areas remain. This period is in the same range as filtration cycles in commercial applications of SevenBore™ fibers. Hence, the initial effect of membrane wetting might significantly impact the processes' filtration performance and potentially exacerbate fouling and inhomogeneous backwashing phenomena in industrial-scale applications.

A hypothesis for the unexpected chronology of pore wetting is the used setup control and the series connection of multiple pore sizes along the fluid pathway. In the setup, the applied pressure is adjusted to achieve a constant flux across the membrane. Thereby, the pressure distribution inside the membrane fibers varies over the cross section, as shown in *Chapter 5: Single Multibore Membrane with Porosity Gradients*. High pressure gradients are observed at the membrane interfaces, while a low pressure drop within the support structure is monitored. However, no study has been presented so far on the dynamic pressure distribution during initial membrane wetting.

To form a wetted pathway from the lumen to the shell side, a series of pores with different pore sizes needs to be wetted subsequently. First, the pores of the active layer at the lumen interface need to be wetted. Second, the larger pores of the support regions need to be traversed. Third, the pores at the shell side interface are flown through. In this last region, narrow pores are predominant due to the phase inversion process used for membrane fabrication. Besides surface energies, viscous forces to displace the higher viscous glycerol need to be overcome. These viscous resistances decline during the displacement process. This is why, initially, a higher pressure needs to be applied to obtain the desired flux. Once the pores of the active layer on the lumen side are wetted with aqueous solution, a lower number of pores in the support domain wetted is necessary to obtain the desired flux as stated by Equation 7.2. In contrast, numerous pores in the membrane shell need to contribute to fluid transport. Presumably, the pressure distribution during the dynamic membrane wetting also causes steeper gradients at the layers with smaller pore sizes. Hence, a lower driving force for fluid displacement is expected in the support structure, causing the un-

expected succession of pore wetting. Longer-term wetting of the support domain is then probably driven by incidental interface instabilities and dissolving effects.

Packing density The previous chapters showed the sensitivity of flow patterns inside membranes and modules towards small pressure disturbances. Pressure disturbances increase with non-uniformity in the flow, which can be induced by changing packing density (see *Chapter 6: Hydrodynamics in Multi-Multibore Membrane Modules*). Therefore, the influence of membrane packing density on the initial membrane wetting behavior was investigated. Magnetic resonance images for one-, seven-, and 16-fiber modules containing membranes in delivery state are displayed in Figure 7.5. Experiments were conducted for 100 LMH and 200 LMH, respectively. The signals were obtained close to the permeate outlet at the C-C plane defined in Figure 7.1 (c). As initial wetting state and entirely wetted membranes have the same appearance in MRI for all packing densities, the wetting pathways at their maximum divergence are compared, which is at approximately three hours of permeation.

Considering the wetting progression of multiple packing densities at 100 LMH, it can be noted that with increasing packing density, air entrapment between the fibers on the shell side becomes more prominent (no residual air in Figure 7.5 (a.i), air at the top of the module in Figure 7.5 (b.i), air entrapment between fibers in Figure 7.5 (c.i)). This air might accumulate due to incomplete module flooding, or it might be displaced air from the lumen channels, pores that are not wetted with the pre-wetting agent, or temperature enhanced degassing effects, respectively. The latter two phenomena might especially arise if the porous network structure is not fully filled by the pre-wetting agent in delivery state. In this case, most probably, air is contained in the larger pores of the mechanical support domains. This might induce additional resistances for displacement and have significant effects on the evolving flow patterns.

However, it also can be noted that the wetted pattern inside the membranes looks the same for one, seven, and 16 membranes at 100 LMH. The area

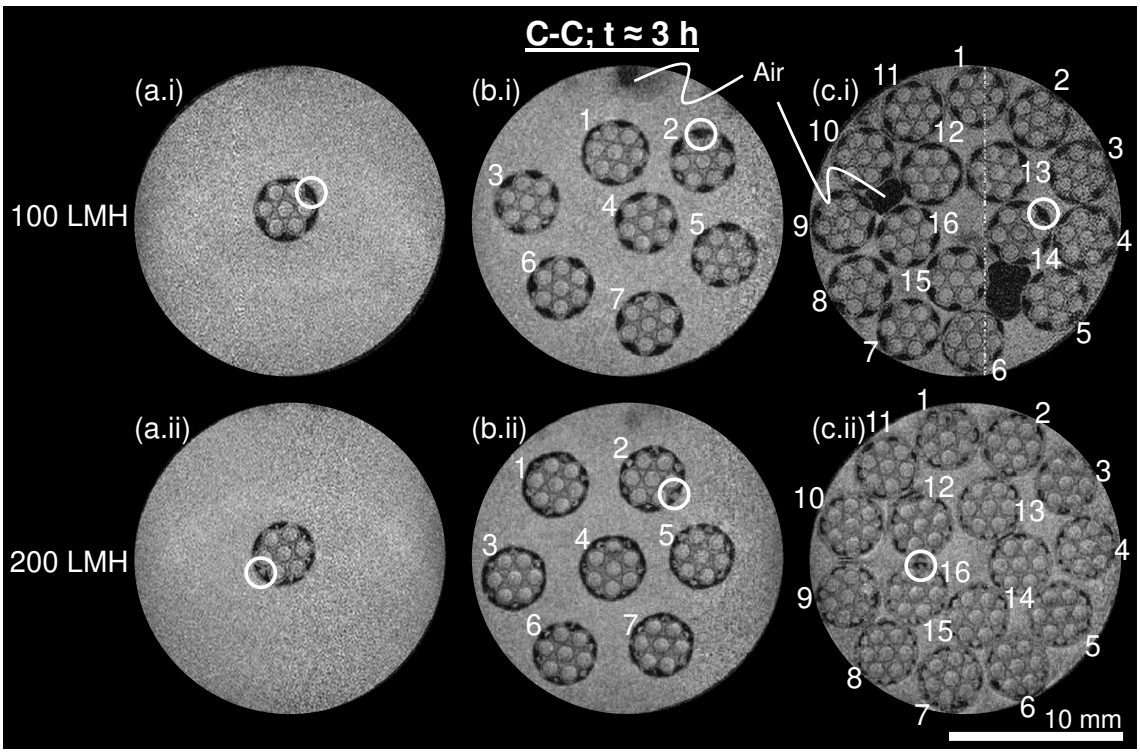

Figure 7.5: Magnetic resonance images of (a.i-ii) single-fiber modules, (b.i-ii) seven-fiber modules, and (c.i-ii) 16-fiber modules containing delivery-state membranes at position C-C taken after approximately 3 hours during the wetting process at 100 LMH (top) and 200 LMH (bottom) with flow rate dependent differences in the wetting behavior highlighted by white-circled areas. These images were taken to evaluate the reproducibility, see Table 7.5 and Table 7.6

surrounding the middle lumen channel in each membrane is fully wetted. In contrast, the outer regions of the fibers' support structure and a large part of the area close to the outer membrane skin remain non-wetted. The white circles in Figure 7.5 (top) indicate these non-wetted areas. Areas that are wetted with aqueous solution can be found where the outer lumen channels are closest to the outer membrane skin. Since the aqueous phase can only pass the membrane through wetted areas, it is assumed that the total feed flux across the membrane is transported through these small wetted parts of the membrane. When comparing this to the results by Schuhmann et al. [Schu2019], a loss in membrane performance, as well as an inhomogeneous flow distribution due to incomplete wetting, can be assumed, as all parts of the membrane significantly contribute to the overall mass transport when in a fully wetted steady state.

Applying a flux of 200 LMH to the same number of membranes in the same module geometry has a significant effect on the evolving wetting patterns, as can be seen in Figures 7.5 (a.ii), (b.ii) and (c.ii). In general, a trend of a higher wetting degree with increasing packing density is observed. While the area surrounding the inner lumen channel is fully wetted for all packing densities, especially for the module containing 16 fibers displayed in Figure 7.5 (c.ii), the increase in wetting degree is very prominent. This increasing wetting degree can be reasoned with the effect of changed shell side flow conditions in the module and a generally higher TMP level for higher packing densities. Although maintaining a constant flow per membrane area, the permeate flow per shell side volume drastically increases. In turn, this leads to higher flow velocities at the shell side. Combined with an increased feed pressure level to supply a sufficiently high mass flow to the lumen channels, this leads to a variation of pressure conditions with changes in the packing density. However, the prevalent pressure conditions mainly determine the local wetting behavior, as described in Equation 7.1. Hence, the breakthrough pressure is exceeded in more pores for higher packing densities at sufficiently high overall flow rates.

A distinct difference can be seen for all packing densities when comparing the wetting patterns of the permeation experiments conducted at 100 LMH and 200 LMH. The fibers' support structure's outer regions are wetted when applying a flux of 200 LMH, whereas those domains were non-wetted for a lower flux of 100 LMH. Again, these domains are highlighted by white circles in the bottom row of Figure 7.5. The wetting of these domains majorly contributes to the enhanced wetting degree for the high packing density module at 200 LMH. As described above, an elevated pressure level, also at the pore scale, seems most likely to cause this effect. However, no wetted areas of the fibers' outer skin can be detected for the seven-fiber module at 200 LMH flux, whereas wetted areas next to the outer lumen channels for a lower flux are present. One potential reason for this unexpected wetting pattern is that the displacement of the glycerol probably occurs in a radial direction. Therefore, the glycerol formerly trapped in the polymer structure is displaced towards the outer membrane skin.

As the data presented in Figure 7.5 only displays a temporal snapshot during the wetting process, no conclusion can be drawn from this data regarding the exact evolution of these wetting patterns. To investigate the temporal progress of the membrane fiber wetting, the full data sets of the experiments displayed in Figure 7.5 were processed with the methods discussed above. This processed data is displayed in Figure 7.6. Permeation experiments were performed over six hours each. The initial wetting degree is higher than zero due to spontaneous wetting during the module's shell-sided flooding and temporal resolution limitations. Although there is no concrete physical motivation for a linear correlation between wetting degree and time, linear trend lines are added to allow an easier comparison of trends.

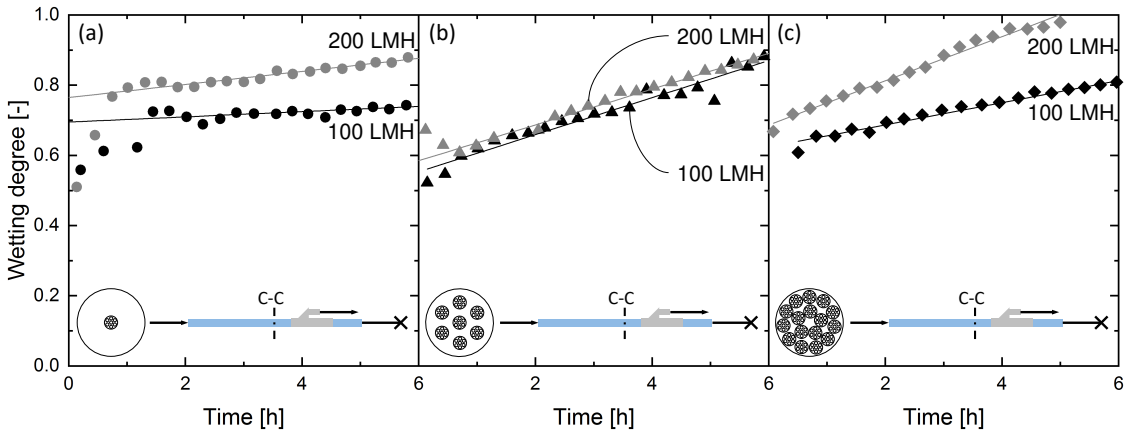

Figure 7.6: Evaluation of the wetting degree over time at 100 LMH and 200 LMH at position C-C of (a) single-fiber modules, (b) seven-fiber modules, and (c) 16-fiber modules containing delivery-state membranes including linear curves fitted to the progress of the wetting degree.

For the single-fiber (Figure 7.6 (a)) and the 16-fiber module (Figure 7.6 (c)), a significantly higher wetting degree throughout the permeation experiments is observed for higher flow rates. However, no such difference can be detected for a seven-fiber module (Figure 7.6 (b)). The wetting degrees calculated for the single-fiber module and the seven-fiber module show deviating progress at the beginning of the experiments compared to higher packing densities. One potential reason is the initial movement of the membrane due to swelling and bending. This movement causes indistinct MRI signals,

which leads to an inaccurate evaluation of the wetting degree. These effects of membrane movement are less pronounced for higher packing densities than for single fibers due to spatial limitations. Nevertheless, the very similar data obtained for seven-fiber modules at different fluxes cannot yet be fully explained.
Figure 7.6 (c) displays the wetting degree over time for a 16-fiber module. Here, the different slopes of the trend lines for 100 LMH and 200 LMH are prominent. As discussed above, this might be reasoned with the overall higher pressure level used for 200 LMH permeation. In general, it should be noted that the highest possible packing density of 16 fibers in the module at 200 LMH is the only configuration that reached a fully wetted state within the six hours of transport study.

Wetting progression along the module length The dominating transport direction inside the porous structure is in a radial direction. However, due to axial flows of feed and permeate streams as well as inhomogeneities in the module like eccentric fiber positioning, the flow conditions change along the module length (see *Chapter 4: Single Multibore Membrane Module Performance*). Therefore, the wetting state of a 16-fiber module at the three positions A-A, B-B, and C-C as defined in Figure 7.1 (c) is investigated. During one permeation experiment, the MRI signals at all three positions were measured alternatingly, starting at position C-C and moving towards the feed inlet. As one MRI measurement takes approximately five minutes, one data point was taken every 15 minutes at every position. The results of this experiment are displayed in Figure 7.7.
Figures 7.7 (a.i), (b.i), and (c.i) show MRIs of the three positions after approximately three hours of permeation at 200 LMH flux. Wetting degrees at this point in permeation time are indicated in the upper right corner. At position A-A, displayed in Figure 7.7 (a.i), the polymer matrix of the membrane fibers appears fully wetted. Only two lumen channels are filled with air, which can be caused by an unintentional intake of single air bubbles via the feed flow. At position B-B, displayed in Figure 7.7 (b.i), some domains in the region of the outer membrane skin remained non-wetted. As observed

before in Figure 7.5, these areas tend to be between two lumen channels at the outer membrane skin, whereas the outer membrane skin appears to be wetted with aqueous solution at domains in the proximity of lumen channels. At position C-C, displayed in Figure 7.7 (c.i), the non-wetted domains already seen in Figure 7.7 (b.i) are more pronounced. Hence, the fiber wetting is less progressed with increasing distance from the feed inlet.

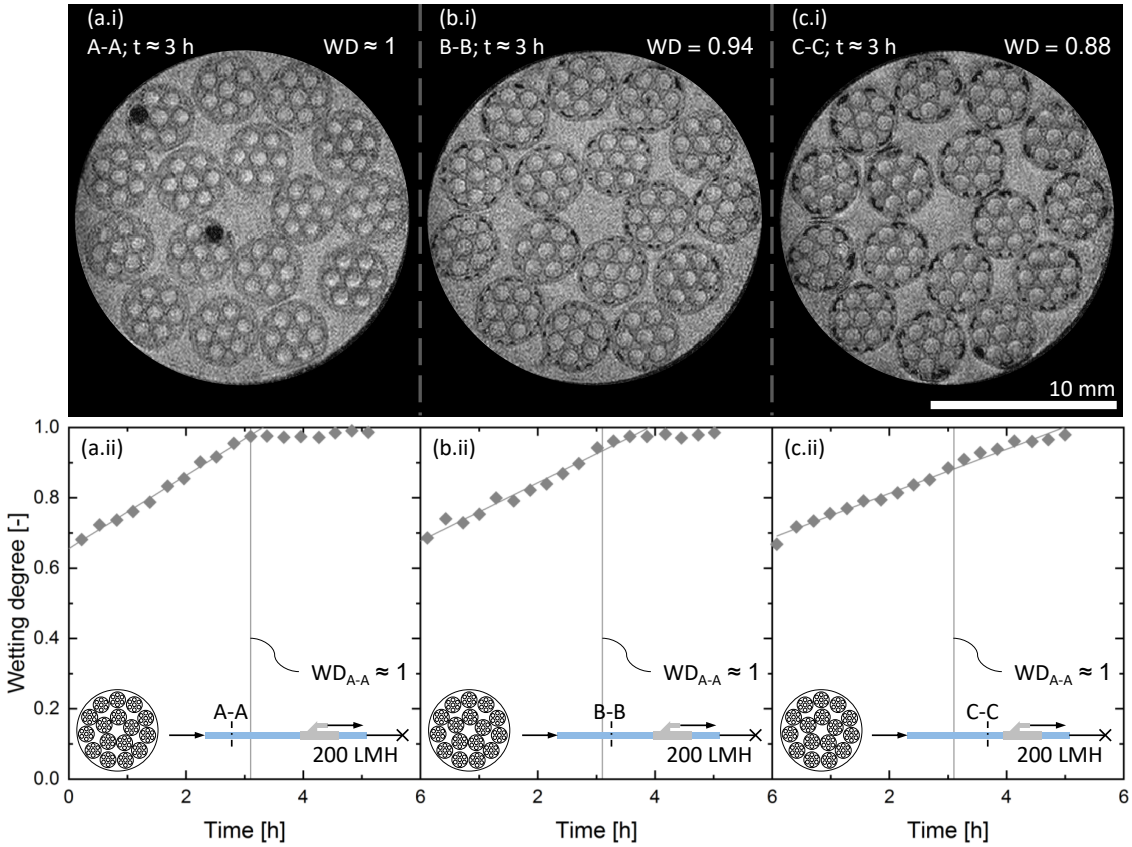

Figure 7.7: Presentation of (top) magnetic resonance images of a 16-fiber module containing delivery-state membranes as complete wetting was obtained at 200 LMH after approximately 3 hours at position A-A (a.i) and (bottom) the corresponding evaluation of the wetting degree (dots) and the fitted linear function (line) at position A-A (a.ii). No complete wetting was achieved at position B-B (b.i) and C-C (c.i) at this point in time. The slope of the fitted linear functions decreases from position A-A (a.ii) to C-C (c.ii).

This trend of decreased wetting degree with increasing distance from the feed inlet can also be seen in the temporal resolution of the observed wetting degree at the three monitored positions in the module, shown in Fig-

ures 7.7 (a.ii), (b.ii), and (c.ii). At all three positions, the initial wetting degree at the beginning of the permeation experiment is almost identical. As discussed above, the initial wetting degree is significantly higher than zero due to initial wetting during the module flooding by capillary effects and small pressure fluctuations. Also, the effects taking place in the first contact with the liquid system cannot be resolved in MRI measurements due to the measuring time of approximately five minutes and the signal averaging over the entire measuring time.

Linear trends of the wetting degrees over time are indicated. It can be noted that the slope of these trends decreases with increasing distance from the feed inlet. At position A-A, complete wetting is obtained after approximately three hours. For reference, this point in permeation time is indicated with a vertical line in all three graphs showing the wetting degree over time. At positions B-B and C-C, the fibers are not fully wetted after three hours. While a complete wetting was obtained shortly after at position B-B, a wetting degree close to one at position C-C could only be obtained after more than five hours of permeation.

The difference in wetting kinetics along the module length is puzzling at first sight. Since the experiments are conducted in dead-end mode, little pressure drop along the lumen length is expected. Also, the membrane fibers are expected to be uniform in the module length direction. Additionally, the membrane packing density prevents strong membrane bending and movement inside the module. Therefore, uniform flow distribution and, hence, uniform wetting is expected over the module length. However, two phenomena can be hypothesized that lead to this wetting gradient over the module length.

First, pressure drops occur both at the shell and the lumen side. The pressure drop inside the lumen channels is expected to be higher due to their smaller flow diameter and, more importantly, the used dead-end permeation mode. This means that the applied TMP as the driving force for membrane wetting is non-uniform over the membrane length, which is well in line with the observation of a decrease in lumen side velocity over the filtration length of the membrane fiber in dead-end mode (see *Chapter 4: Single*

Multibore Membrane Module Performance). This would explain an earlier wetting at the inlet of the membrane module. As a hypothesis, the axial wetting progression is caused by stochastic events that locally exceed the breakthrough pressures of the neighboring pores (see Equation 7.1). Additionally, the flow entering the membrane matrix possesses impulse in the axial direction, increasing the local kinetic pressure in axial direction.
Second, there might be an axial transport of the aqueous phase inside the polymer matrix of the membrane fibers. On the one hand, this might be induced due to shear flows at the membrane lumen and shell side. On the other hand, part of the feed flow might enter the membrane at the feed side through the open polymer matrix cross section. Although the pressure drop across the membrane in the axial direction is very high, local mixing effects and miscibility of feed solution with the pore-stabilizing glycerol might lead to a more preferential wetting in the first part of the module.
As commercial membrane modules mostly possess a module length significantly higher than the module investigated here, it seems likely that this effect is even more pronounced in commercial membrane modules. In industrial applications, filtration cycles may lie in the same order of magnitude as the wetting processes observed in the scope of this study. Hence, the findings regarding the wetting progress revealed in this chapter can significantly affect the membrane performance in industrial membrane processes. However, the gradient in the wetting degree over the module length needs further investigation in future studies to understand the axial progression of membrane wetting fully.

7.4.3 Aqueous solution wetting ethanol-washed and dried (air-filled) membranes

The wetting behavior of the membrane pores depends on the invading fluid's properties, as well as the defending fluid that is displaced during the wetting procedure. After investigating influence parameters on the invading fluid, namely flux and packing density, this study also aimed to examine effects arising from the defending fluid properties. Therefore, the factory-

filled glycerol inside the pores was removed by washing the membranes with ethanol. The air inside the polymer matrix was displaced with the same experimental parameters described in Section 7.3.2. As indicated in literature [Koch2009], the material system is stable in ethanol. In Figure 7.8, results are displayed for permeation experiments at 100 LMH (top) and 200 LMH flux (bottom) in the initial state (left), as well as after three hours of permeation (right). The temporal evolution can be seen in the Appendix Figure 7.11.

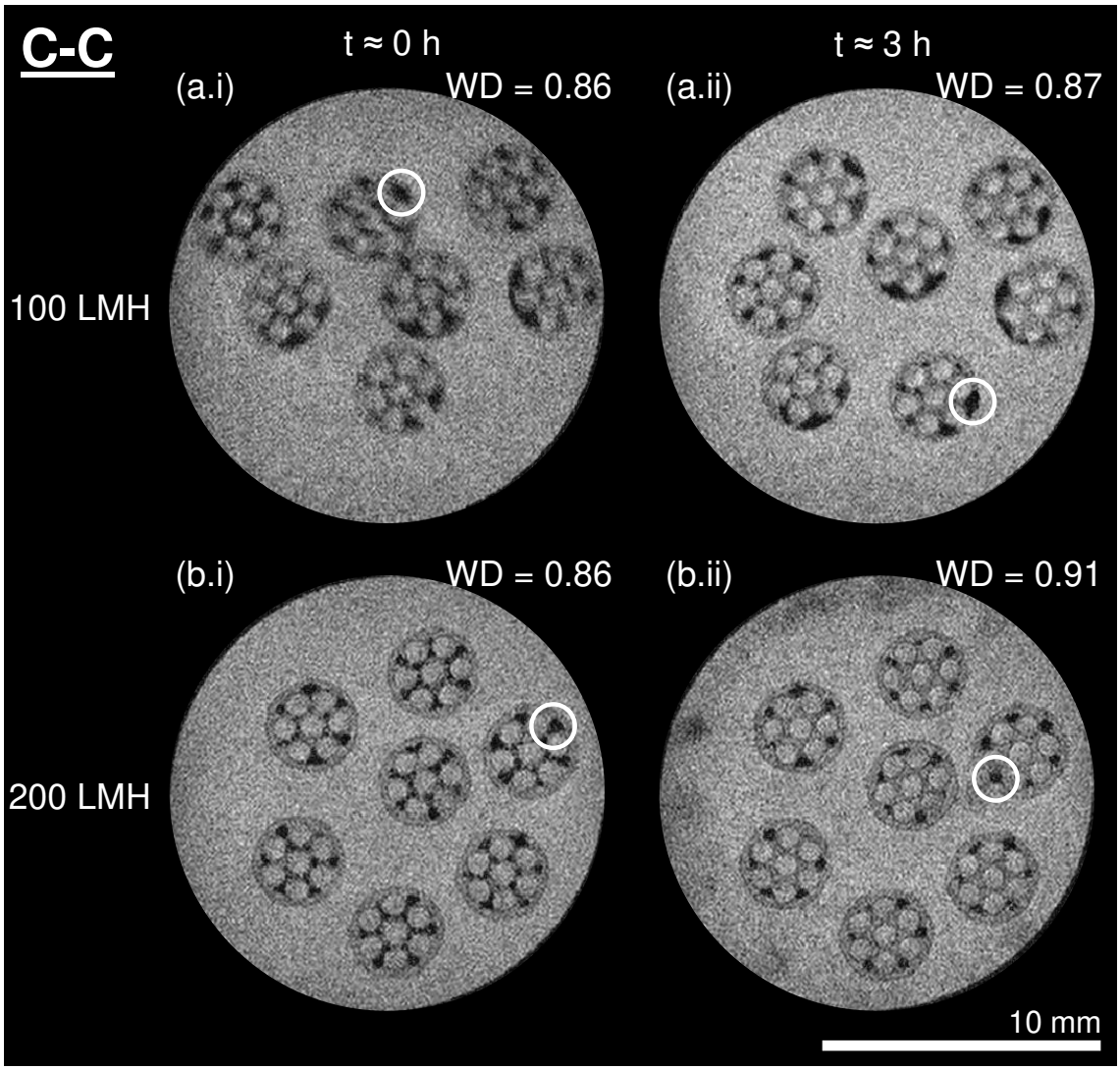

Figure 7.8: Magnetic resonance images of seven-fiber modules containing ethanol washed and dried membranes operated at 100 LMH (top) and 200 LMH (bottom) in the initial stage of the experiment (left) and after approximately three hours (right). White-circled areas highlight the different wetting behavior compared to untreated membranes (see Figure 7.5).

Initially, the membranes swell during the first contact with aqueous solution. This swelling causes significant bending of the fibers, which results in blurred visualization from MRI measurements, as shown in Figure 7.8 (a.i). The initial wetting pattern distinctly differs from the behavior observed with delivery-state fibers. Here, the circular region next to the outer membrane skin is immediately wetted with aqueous solution, independent of the applied flux. The rest of the polymer matrix remains non-wetted.

After three hours of permeation, non-wetted domains remain in the membrane fibers for both applied fluxes, as shown in Figures 7.8 (a.ii) and (b.ii). For a flux of 100 LMH, the remaining non-wetted domains are unevenly distributed. This asymmetry is in contrast to the reference experiments with delivery-state fibers. One potential reason for these non-uniform wetting patterns is a partial collapse of the active skin pore system throughout the washing procedure. As glycerol is assumed to be factory-filled as a pore stabilizer, the drying step after glycerol removal might have led to a mechanical change of the polymer matrix. A change in some parts of the polymer matrix can lead to non-uniform transport resistances in the membrane. These non-uniformities would cause uneven flow distributions and, hence, non-uniform wetting patterns. A potential second cause is the more distinct membrane movement observed at the beginning of the experiment with 100 LMH flux. However, the wetting pattern observed after three hours of permeation with a flux of 200 LMH is symmetric. Like before, the outer membrane skin is entirely wetted. Similar to the experiments discussed before, this leads to fully wetted areas between the outer lumen channel and the outer membrane skin. In contrast to the reference experiments with delivery-state fibers (see Section 7.4.2), the polymer matrix domains with larger pore sizes remain non-wetted. For reference, these specific domains, again, are highlighted by white circles in Figure 7.8.

Especially the observation of non-wetted domains with large pore sizes even for high fluxes is unexpected. With PES being a hydrophobic material, it would be more intuitive to wet larger pores more easily than narrow pores, where the necessary local pressure gradient needs to be higher. It is concluded that the feed flow bypasses the polymer matrix domains with

larger pore sizes that are mainly contributing to the mechanical stability of the fiber to a large extent. This way, the local fluid pressure acting on the air-filled pores does not reach the breakthrough pressure. Also, the difference in wetting patterns might be explained if the feed flow enters the membrane fibers in the axial direction through the open cross section of the polymer matrix at the feed inlet. For the glycerol pre-wetted fibers, aqueous feed solution and glycerol's miscibility might lead to a steady axial wetting of the membrane fiber in the axial direction. As air macroscopically is not miscible with the feed solution, this mixing effect cannot contribute to the overall fiber wetting. However, the exact flow conditions during wetting in radial and axial direction need further investigation in future studies. Setting a corresponding CFD model would be useful to estimate temporal pressure and flow distributions, and thus, draw conclusions on the wetting behavior.

7.4.4 Aqueous solution wetting ethanol-filled membranes

In the section above, the membrane pore system might have been altered due to the drying procedure. To observe the feed wetting progression without any distortion by pore system altering, the wetting behavior with aqueous solution in ethanol-filled membranes was investigated.

An ethanol flux of 100 LMH was applied to the membrane module. This washing step represents a displacement procedure of glycerol by another fluid. However, the attempt to investigate the wetting kinetics and wetting patterns for this displacement procedure failed. Monitoring this displacement in MRI lead to results that are not suitable for image processing analysis (see Appendix Figure 7.12). Three reasons explain this reduction in image quality for ethanol displacing glycerol. First, the measuring time needs to be increased to approximately 40 min per image as the MRI signal of ethanol is only about a tenth of the water signal. Second, wetting kinetics are faster for ethanol displacing glycerol than for aqueous solution displacing glycerol. Hence, the temporal resolution is not sufficient for monitoring this wetting process. Third, the membranes bend significantly when flushed with ethanol due to swelling effects. This induces membrane move-

ment during the MRI measurement, which leads to further signal noise in the obtained data.

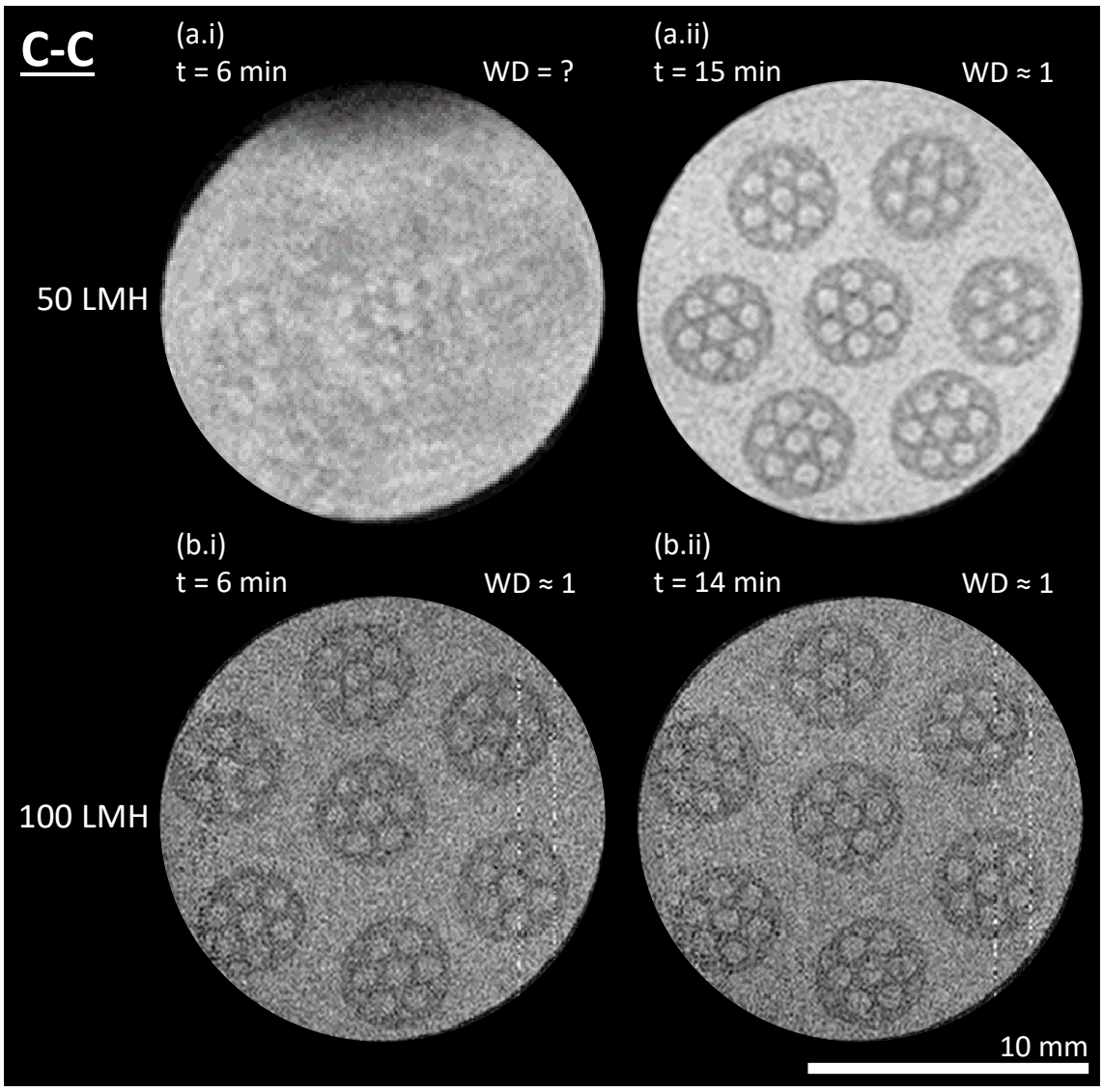

Figure 7.9: Magnetic resonance images of seven-fiber modules containing ethanol filled membranes taken during the initial stage of the displacement process of ethanol with aqueous solution at 50 LMH (top) and 100 LMH (bottom) at position C-C.

After full wetting of the membrane fibers with ethanol, aqueous solution was used for ethanol displacement with 50 and 100 LMH, respectively. In Figures 7.9 (a.i) and (a.ii), results are shown for aqueous solution displacing ethanol with a reduced flux of 50 LMH. At the first contact with the aqueous solution, the membranes start to move significantly due to swelling effects. This movement causes the blurry image shown in Figure 7.9 (a.i).

After approximately ten minutes, the movement of the fibers has ceased. The subsequent measurement shows an evenly strong signal throughout the whole cross-sectional area of the SevenBore™ fibers. With a flux of 100 LMH, even the initial MRI measurement after shell-sided module flooding revealed thoroughly wetted polymer structures.
Two reasons were identified for this tremendously faster wetting with aqueous solution compared to differently pre-treated membranes. First, ethanol has a significantly lower viscosity than glycerol, a lower surface tension, and a lower contact angle on PES surfaces [Koch2009]. This lower surface tension reduces the necessary breakthrough pressure for pore wetting. Second, the polymer matrix itself mechanically reacts to the immersion in ethanol by swelling. The swelling leads to more free volume inside the polymer matrix and increases the permeability for a water-rich phase by diffusion. This increase, in turn, causes faster transport of aqueous solution throughout the membrane and, hence, faster wetting kinetics. However, a remaining membrane swelling causes a transport resistance for the convective aqueous flux and might lead to lower fluxes compared to differently pre-wetted membranes.

7.4.5 Temporal evolution of obtained flux, transmembrane pressure, wetting degree, and membrane resistance

Besides the phenomenological observation of local membrane wetting patterns, the macroscopic quantities flux and TMP of the permeation were also observed. Figure 7.10 shows the course of flux (Figure 7.10 (a)), TMP (Figure 7.10 (b)), calculated membrane resistance (Figure 7.10 (c)), and wetting degree obtained from MRI data (Figure 7.10 (d)) over time for a seven-fiber module with a target flux of 100 LMH for the investigated material systems. Inside the polymer matrix, glycerol is displaced by the aqueous solution (△), air is displaced by the aqueous solution (□), and ethanol displaced by the aqueous solution (◇). For reference, the measured data during the initial displacement of glycerol by ethanol is dispayed (●). For

a higher flux, the graphs' characteristics remain the same, although the absolute values change (see Appendix Figure 7.13 and Figure 7.14).

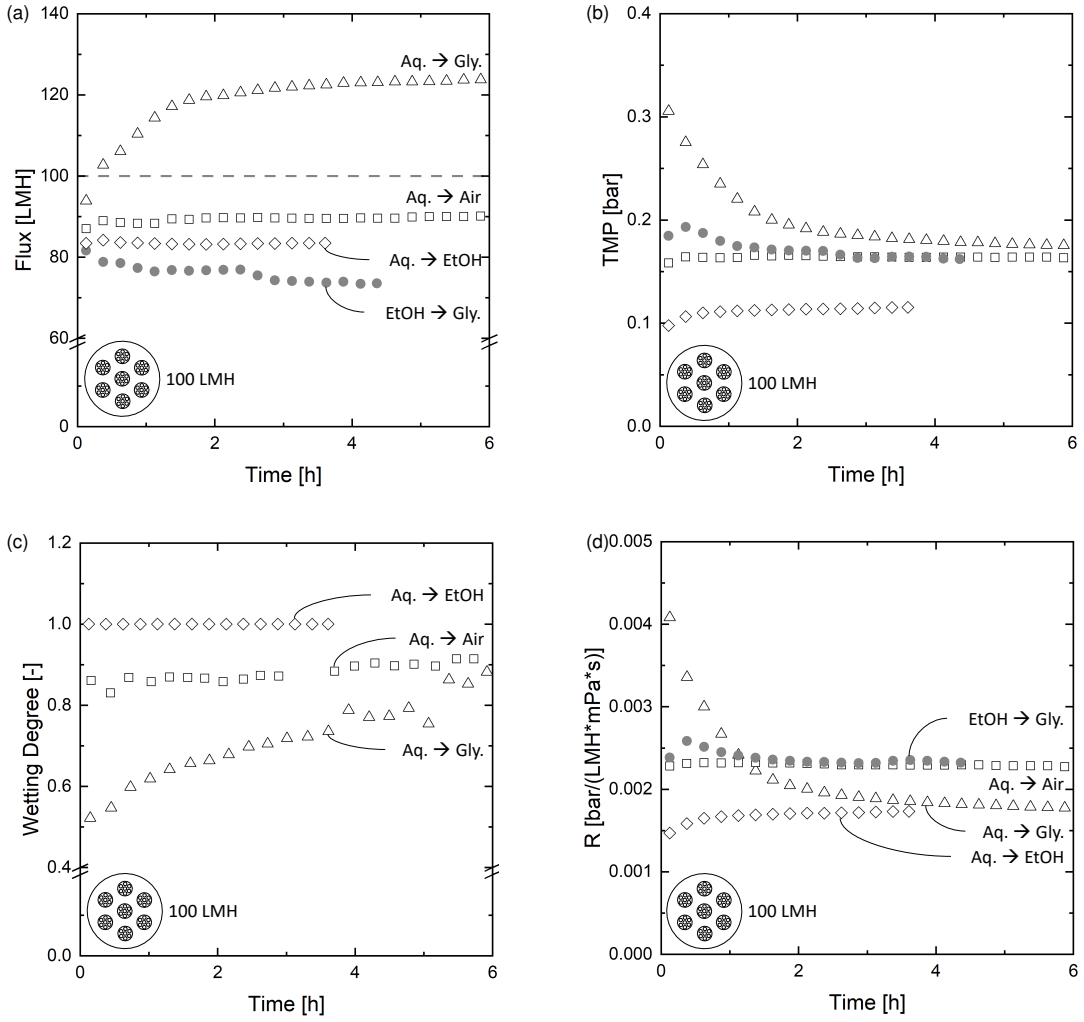

Figure 7.10: Temporal evolution of (a) the measured flux, (b) the measured correlating TMP, (c) the monitored wetting degree in C-C, and (d) the calculated membrane resistance during the wetting of seven-fiber modules at 100 LMH with an initial value of 85 LMH. Investigated material systems are delivery-state membrane fibers wetted with aqueous solution (△), washed and dried (air-filled) membrane fibers wetted with aqueous solution (□), untreated membrane fibers wetted with ethanol (◉), and ethanol-filled membrane fibers wetted with aqueous solution (◇).

Since a gear pump was used for all experiments conducted in this study without any other control loop, neither an ideal constant flux nor an ideal constant pressure mode was realized. The initial flux at the beginning of the experiment was set to 85 LMH. During the experiments, wetting of the membranes led to changes in flux as well as in TMP. However, the behavior

of flux and TMP over time can still be used for qualitative wetting characterization. From this data, the membrane resistance R can be calculated as described in Equation 7.4 as a function of the applied TMP, the measured flux J, and the viscosity of the invading fluid η.

$$R = \frac{\text{TMP}}{J \cdot \eta} \tag{7.4}$$

Figure 7.10 (a) shows the flux over time for the three investigated material systems with a target flux of 100 LMH. Also, the progression of flux during the displacement of glycerol by ethanol is displayed for reference. The flux remains mostly constant over time for aqueous solution perfusing washed and dried membranes (□, air-filled) and ethanol-filled membranes (◇). In contrast, flux increases significantly for the delivery-state membranes permeated with the aqueous solution (△). In general, this is in good agreement with the optical analysis discussed above since the air-filled and the ethanol-filled membranes show mostly wetted membrane skins from the beginning of the experiments. Hence, the active membrane area does not increase over time, resulting in stable membrane performance. During the permeation with ethanol (●), the flux constantly decreases, which can be accounted for polymer swelling.

Concerning the course of the applied TMP displayed in Figure 7.10 (b) for the ethanol permeation (●), only the drop in flux between two and three hours of permeation time can be reasoned. At the beginning of the experiment, the TMP slightly increases before returning to the initial value, as does the membrane resistance. It is concluded that flux and TMP courses are mainly dominated by swelling and altering phenomena of the polymer matrix immersed in ethanol. After four hours of permeation, a steady state is reached in all experiments displayed in Figure 7.10. Here, the permeation with ethanol through delivery-state membranes (●) shows the lowest flux at a similar applied TMP. The transport resistance is highest as displayed in Figure 7.10 (d), which is caused by an altered pore size distribution caused by swelling effects. In contrast, no change in flux and TMP over time was observed for the aqueous solution displacing ethanol (◇). In

combination with the MRI results presented in Figure 7.10 (c), this hints at a fast and complete wetting progression due to good miscibility and low viscosity.

No significant change in either flux or TMP was observed for the ethanol-washed, dried, and subsequently perfused membranes (□, air-filled membranes). Although the optical evaluation via MRI revealed large parts of the membrane domains with larger pore sizes as non-wetted (see Figure 7.8), these appear to be no limiting factor for the mass transport in the absence of a particular matter. However, drying the membrane without a pore-stabilizing agent might have altered the active membrane skin morphology. Potentially, the pore network system in the active layer has collapsed, leading to larger pore diameters. This collapse would reduce the necessary breakthrough pressure (see Equation 7.1) and explains the low membrane resistance (see Figure 7.10 (d)) at the beginning of the permeation experiments compared to other fluid systems. Towards the end of the permeation experiments, the resistance of the air-filled fiber (□) remains the same, whereas the resistance of the delivery-state fiber (△) has dropped. The higher resistance level might be caused by the non-wetted areas that locally require higher flow rates inducing an additional transport resistance. Also, the reduced flux of the air-filled compared to delivery-state membranes at steady-state of permeation might be reasoned with a reduced number of pores in a collapsed pore network system. However, this reasoning requires spatial resolution of flow patterns and in-depth active layer investigation, which need to be addressed in future studies.

The increase in flux for the delivery-state membranes (△) at the beginning of permeation with aqueous solution complies with a decrease in TMP. As well as in the evaluation of the wetting degree over time (see Figure 7.10 (c)), a flattening of the curve displayed in Figure 7.10 (a) can be observed after approximately two hours. At this point in the permeation experiment, the optical evaluation via MRI shows the first macroscopic connection of wetted domains between the lumen channels and the shell side of the module (see Appendix Figure 7.15, wetting degree as a function of time and applied flux for delivery-state membrane fibers wetted with aqueous solution).

From this point onward, the further increase in flux can be reasoned with a broadening of the existing wetted fluid flow pathways in radial and axial directions.

7.5 Conclusion and outlook

In this chapter, MRI was used as an in-situ characterization of macroscopic wetting patterns inside polymeric hollow fiber multibore membranes. The effects of packing density, applied flux, lateral position, and membrane pre-treatment are elaborated. For quantitative analysis, an image processing tool is developed to calculate the membranes' wetting degree. This study helps to understand (a) complex wetting phenomena inside multibore membranes in dead-end permeation, (b) the membranes' interaction with their surroundings due to neighboring membranes, and (c) the effect of the used fluid system for displacement on the resulting wetting patterns.

It is highlighted that the wetting procedure of these commercial membranes takes several hours when conventionally flushed with aqueous solution, even with high fluxes of 200 LMH. The membrane performance is tremendously decreased, as not all theoretically possible active area is available for mass transport for the duration of this displacement procedure.

In general terms, the wetting progresses inside-out while building wetted short-cut pathways between the outer lumen channels and the membranes' outer skin. Wetting patterns change drastically by changing the flux from 100 LMH to 200 LMH, and the wetting kinetics increase with increasing packing density. This increase in wetting kinetics can be reasoned with higher flow rates at the shell side, inducing different pressure gradients across the membrane.

In addition to a successive wetting in the radial direction, an axial wetting direction is revealed by comparing the wetting patterns at different lateral positions inside the module. This axial wetting, again, can be reasoned with changing shell-sided flow conditions along the module length. This phenomenon needs further in-depth investigation and will be subject to future studies.

To compare wetting patterns and kinetics, the wetting behavior of ethanol-washed, dried, and subsequently filtrated membranes are investigated. The arising wetting patterns differ in two striking ways. First, the resulting wetting patterns have a less symmetric shape. Second, the membranes' outer area was immediately wetted, while some inner parts of the membrane remained air-filled. In contrast, the complete membrane cross section is almost immediately wetted when displacing ethanol inside the polymer matrix by aqueous solution. However, the initial immersion in ethanol causes significant polymer swelling that displays an additional transport resistance.

This chapter reveals the importance of flow conditions during the first cycle of membrane filtration on membrane wetting efficiency. The resilient patterns of non-wetted membrane domains hint towards an optimization potential for current industrial modes of operation. Hence, this work pioneers finding strategies for membrane performance optimization by more active wetting control.

7.6 Appendix

7.6.1 Wetting progression in air-filled membranes

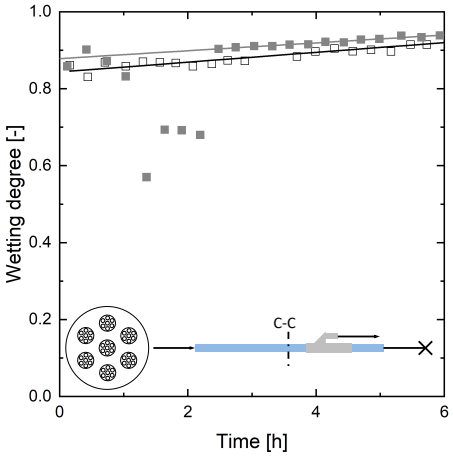

Figure 7.11: Illustration of the wetting degree over time at the module center (position C-C) in modules containing seven washed and dried (air-filled) membranes at 100 LMH (□) and 200 LMH (■). The four data points not following the trend lines are were excluded from the trend line calculation because of temporal malfunctions of the MRI device during the experiment.

7.6.2 Magnetic resonance imaging of ethanol displacing glycerol

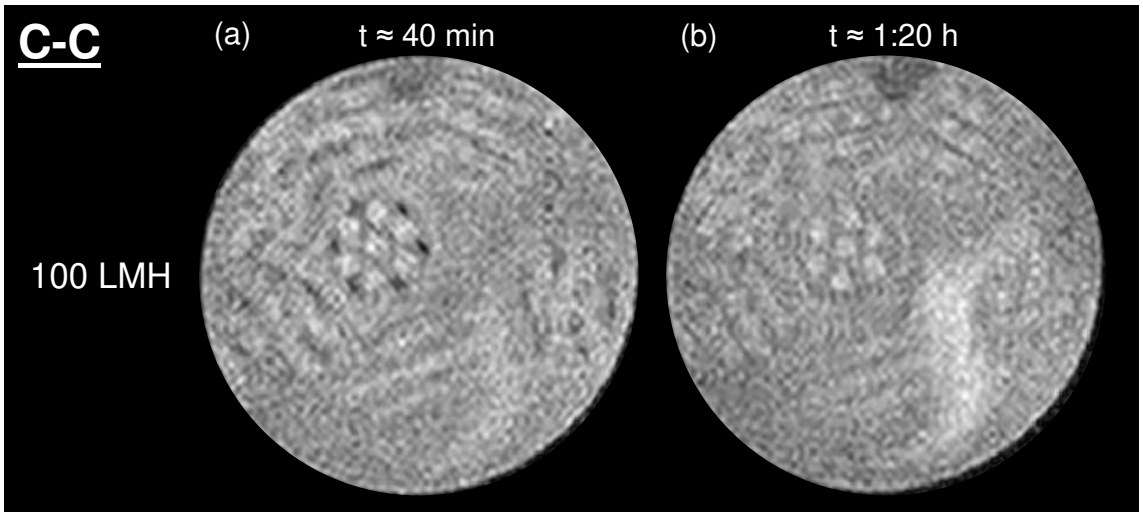

Figure 7.12: Magnetic resonance images of a seven-fiber module during the wetting process at 100 LMH with ethanol at position A-A (a) after approximately 40 minutes, and (b) after approximately 1:20 hours of filtration.

7.6.3 Flux and TMP behavior at higher applied fluxes

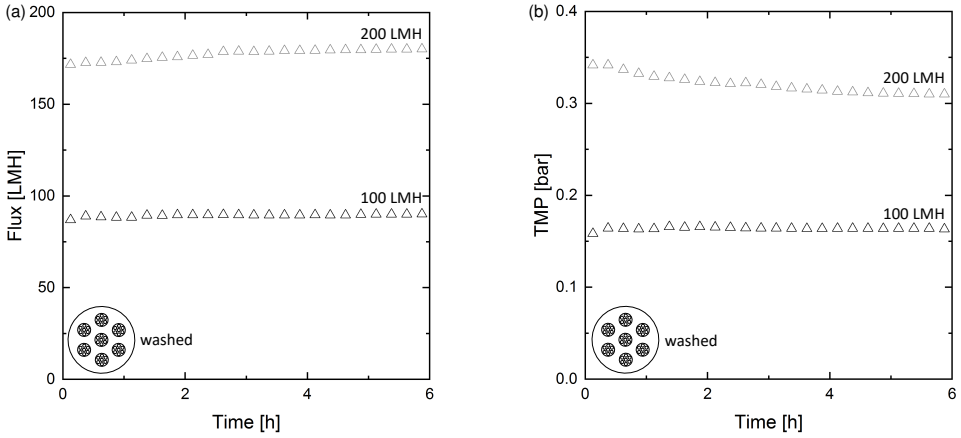

Figure 7.13: Illustration of (a) the measured flux during aqueous solution perfusing washed and dried (air-filled) membranes in seven-fiber modules at 100 LMH and 200 LMH, and (b) the measured trans membrane pressure correlating to the volume flow rate applied to the membrane modules.

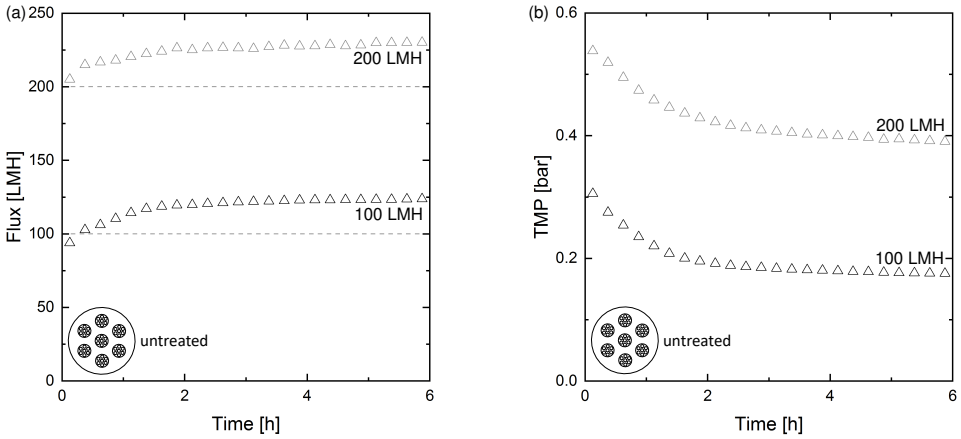

Figure 7.14: Illustration of (a) the measured flux during aqueous solution perfusing glycerol filled membranes in seven-fiber modules at 100 LMH and 200 LMH, and (b) the measured trans membrane pressure correlating to the measured flux.

7.6.4 Wetting degree as a function of time and applied flux

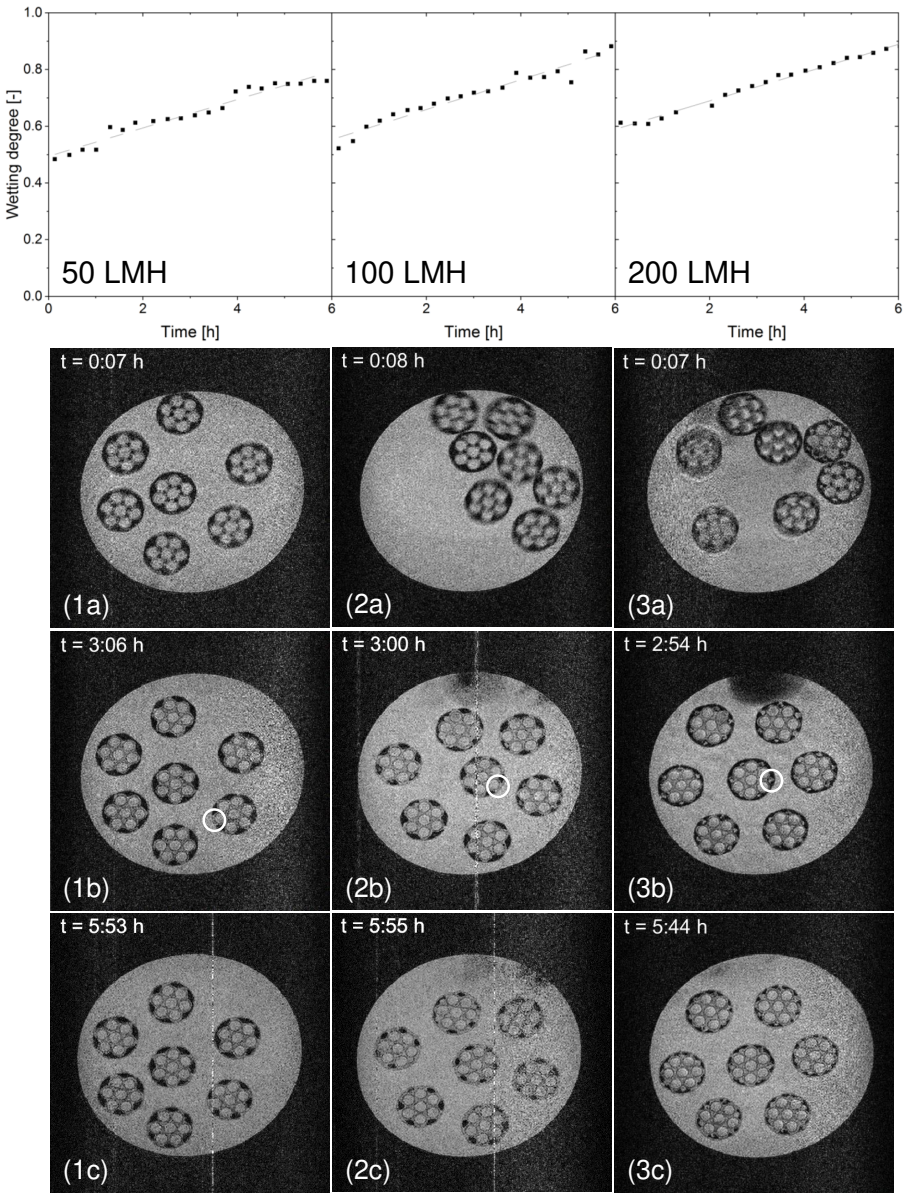

Figure 7.15: Wetting degree and magnetic resonance images of the module center (position C-C) of seven-fiber modules during investigations with a flux of: 1a-c) 50 LMH, 2a-c) 100 LMH, 3a-c) 200 LMH.

8

Conclusion and Future Perspectives

Parts of this chapter have been published as:
Denis Wypysek, Matthias Wessling, "MRI in membrane filtration processes" in "Magnetic Resonance Microscopy: Instrumentation and Applications in Engineering, Life Science and Energy Research", *John Wiley & Sons, Ltd* (2022). ISBN: 978-3-527-82725-1

To reach the United Nations sustainable development goal of 'ensure[d] access to water and sanitation for all', membrane processes have proven as versatile techniques to achieve this target. One approach to analyze membrane processes is MRI. MRI can spatially resolve flow velocity distributions and, at least partially, porosities and permeabilities in any selected plane. Furthermore, its noninvasiveness allows elucidating structures and different components in opaque systems in-situ. This information is of highest interest as it uncovers how fouling can be controlled and minimized and how backwashing and cleaning processes should be designed.
In recent years, multibore membranes have emerged as promising candidates for drinking water production, although their flow behavior is not understood in full detail. This thesis aimed to reveal hydrodynamic conditions in multibore membranes and membrane modules by comprehensive CFD simulations and MRI measurements and answer questions raised in *Section 1.1: Open Research questions and thesis goals*.
Single multibore membranes with homogeneous properties in the membrane's cross section were investigated inside a module with 3D Comsol simulations. In these kinds of modules (also applicable for higher-packed

modules), shell-sided axial flow inhomogeneities arise as the fluid flows continuously through the module and always seeks the areas with lower packing, which present the path of least resistance due to small local pressures differences. These pressure differences are also the reason for a radial secondary flow development on the shell side in modules where the membrane is not aligned concentrically. A bent membrane that results from swelling phenomena in self-made membrane modules shows radial velocities in all lumen channels that point in one direction. The reason for this is the negative or positive slope of the membrane's middle axis that results in drag forces on the lumen channel's inner side. This Comsol analysis gives first assumptions that flow phenomena change close to the permeate outlet position.

2D OpenFCST simulations provided insights into fluid flow and pressure distribution in multibore membranes with gradients in porosity and permeability. Flow fields obtained by OpenFCST better resemble the obtained MRI results by Wypysek et al. [Wypy2019] than Comsol simulations. The contribution of each lumen channel to the overall mass transport varies, and the central lumen channel contributes the least. Also, the flow through the separation layer is unequal over its circumference leading to drag forces that can influence particle deposition on the inner lumen side. However, even in the simulations that mimicks fouling, the backwashing flux reached every lumen channel, showing that backwashing can be effective.

The behavior of backwashing flow that reaches all lumen channels also applies to membrane modules with more than one membrane. Therefore, the interaction of membranes with their surrounding (membranes as well as the membrane housing) was studied via MRI measurements. Even though challenging flow phenomena on the shell and lumen side are observed (jet stream or recirculating flows), the hypothesis of an effective backwashing process is still valid since the backwashing flow reaches all lumen channels. This study also highlights the role of the permeate outlet position as flow phenomena at and behind the outlet change drastically. From that point on, non-uniformities on the shell and lumen side increase, affecting particle filtration performance of the whole membrane module.

The mentioned results were obtained after the multibore membranes reached steady-state. However, the first filtration cycle is a dynamic process in which the pre-wetting fluid is removed. Therefore, the initial wetting evolution until the membranes reached this steady-state was investigated. Preferential flow paths at the radial direction and wetting along the module axis were elucidated. Thereby, long wetting times of over 6 hours show that the first filtration cycle is a crucial step towards a continuous steady-state membrane filtration process and that fluxes, pre-wetting agents, and invading fluids have to be known to optimize the process.
This thesis answered many open questions regarding multibore membranes, the interplay between each membrane in a membrane module and module design aspects. Although multibore membranes and modules are better understood now, new findings always raise further questions:

- While polymeric membranes are soft and possess porosity gradients, **ceramic multibore membranes with homogeneously distributed porosity** (not presented here) show a different flow distribution. As these membranes are stiff, they will not bend, and therefore other flow phenomena regarding the positioning of membranes like an eccentric position could be investigated. A recirculating flow inside the lumen channels was observed in such membranes, just like on the shell side of the highly-packed polymeric multibore membrane modules. **Could these recirculating flows in ceramic as well as in highly packed membrane modules be utilized** somehow as the fluid passes the membrane several times with increasing internal residence times?

- Since the OpenFCST simulations resemble the MRI measurements better than Comsol simulations, an **OpenFCST 3D model of a whole membrane module** should be pursued. Modeling the membrane in combination with the housing is essential, as it was shown that flow fields develop due to the membrane's position in the module. Thereby, **other membrane properties such as the distribution of functional groups**, for example, can be investigated in future studies in equivalence to the porosity and permeability studies. Furthermore, **mem-**

branes with several damaged zones at various locations should be simulated to better understand the interplay between such zones. Also, **a model for particle transport** can gain new insights and a better understanding of fouling physics in hollow fibers and multibore membranes. At last, **modeling a membrane module with several membranes** would lead to the complete picture and leave space for optimizing membrane modules.

- As shown by Wypysek et al. [Wypy2019], a multibore membrane module with one membrane could not be entirely recovered during the backwashing process. Also, Yan et al. [Yan2021] analyzed a 400-membrane module via MRI and stated that not every membrane was recovered after backwashing was performed. That is why future studies should focus on **particle filtration and subsequent backwashing experiments in highly packed multibore membrane modules** to qualitatively and quantitatively analyze the efficiency of backwashing processes.

- This thesis indicated that module design is a crucial parameter in the performance of membrane modules. On the one hand, inlet flow conditions like too small inlets may influence membrane module performance negatively. On the other hand, the permeate outlet seems to play an essential role in module design. Future work should focus on the **permeate outlet amount and position**, and **inlet flow design**. Especially concerning backwashing efficiencies, it could be favorable if the permeate outlet is located in the middle of the module or two outlets are installed. Two outlets are beneficial for the backwashing process as one half of the module is cleaned with each fluid entrance. Measuring flow distribution with MRI will unravel unknown flow phenomena in such modules.

As this work has demonstrated, the combination of MRI measurements and CFD simulations is a powerful tool for fluid flow analysis. Due to its flexible methodologies, especially MRI is beneficial for many different purposes in chemical engineering, such as characterizing material or rheo-

logical properties of fluids, investigating dynamic systems and reactions, analyzing electrochemical systems, and measuring porous media and flow in membranes and membrane modules. [Bend2019]

This thesis highlights the strengths of MRI for studying membrane processes. However, as effects on the membrane surface can occur very fast and on a smaller scale, MRI suffers from its spatial resolution of some microns and its time resolution in the range of up to several minutes. In addition, the use of metallic/magnetic parts inside an MRI tomograph is challenging due to high magnetic fields. Still, the development of faster and more robust pulse sequences to increase temporal and spatial resolution does not stop. [Bend2019]

For investigations where MRI comes to its limit, other techniques may be deployed, including the experimental microfluidic observation of fouling layer behavior [Link2016; Link2019] or CFD-DEM simulations of fouling and backwashing mechanisms [Loha2018; Loha2020]. These studies give insights into the spatio-temporal behavior of filter cake deposits in relevant hydrodynamic conditions. Additionally, computed tomography for in-situ measurements of concentration distributions [Fran2000], or light deflection, radioisotope labeling, electron diode array microscopy, and direct pressure measurement for in-situ monitoring of concentration polarization layers can be used [Chen2004a]. In-situ monitoring of cake formation and membrane fouling can be realized via direct observation methods using microscopy approaches, laser triangulometry, optical laser measurements, ultrasonic time-domain reflectometry, and electrical impedance spectroscopy [Chen2004a]. Small-angle neutron and X-ray scattering may reveal pore blockage and cake structures [Chen2004a].

Bibliography

[Aire1998] D. Airey, S. Yao, J. Wu, V. Chen, A. Fane, and J. Pope. “An investigation of concentration polarization phenomena in membrane filtration of colloidal silica suspensions by NMR micro-imaging”. *Journal of Membrane Science* 145.2 (1998) 145–158. DOI: 10.1016/S0376-7388(98)00051-9 (cit. on pp. 40–42, 158).

[Amar2010] A. Amar, B. Blümich, and F. Casanova. “Rapid Multiphase Flow Dynamics Mapped by Single-Shot MRI Velocimetry”. *ChemPhysChem* 11.12 (2010) 2630–2638. DOI: 10.1002/cphc.201000062 (cit. on p. 54).

[Argy2015] I. S. Argyle, A. Pihlajamäki, and M. R. Bird. “Black tea liquor ultrafiltration: Effect of ethanol pre-treatment upon fouling and cleaning characteristics”. *Food and Bioproducts Processing* 93 (2015) 289–297. DOI: 10.1016/j.fbp.2014.10.010 (cit. on pp. 159, 160).

[Argy2017] I. S. Argyle, C. J. Wright, and M. R. Bird. “The effect of ethanol pretreatment upon the mechanical, structural and surface modification of ultrafiltration membranes”. *Separation Science and Technology* 52.12 (2017) 2040–2048. DOI: 10.1080/01496395.2017.1310234 (cit. on p. 159).

[Arnd2016] F. Arndt, U. Roth, H. Nirschl, S. Schütz, and G. Guthausen. “New insights into sodium alginate fouling of ceramic hollow fiber membranes by NMR imaging”. *AIChE Journal* 62.7 (2016) 2459–2467. DOI: 10.1002/aic.15226 (cit. on pp. 46, 47).

[Arnd2017] F. Arndt, S. Schuhmann, G. Guthausen, S. Schütz, and H. Nirschl. “In situ MRI of alginate fouling and flow in ceramic hollow fiber membranes”. *Journal of Membrane Science* 524 (2017) 691–699. DOI: 10.1016/j.memsci.2016.11.079 (cit. on pp. 46, 47).

[Atec2019] Atech innovations GmbH. *Ceramic membranes for process stability*. http://www.atech-innovations.com/en/products/membranes.html. Accessed 10 September 2021. 2019 (cit. on p. 2).

[Back2019] J. O. Back, R. Brandstätter, M. Spruck, M. Koch, S. Penner, and M. Rupprich. “Parameter Screening of PVDF/PVP Multi-Channel Capillary Membranes”. *Polymers* 11.3 (2019) DOI: 10.3390/polym11030463 (cit. on pp. 2, 88).

[Bait2021] K. Baitalow, D. Wypysek, M. Leuthold, S. Weisshaar, J. Lölsberg, and M. Wessling. “A mini-module with built-in spacers for high-throughput ultrafiltration”. *Journal of Membrane Science* 637 (2021) 119602. DOI: 10.1016/j.memsci.2021.119602 (cit. on pp. 62, 63).

[Bake2012] R. W. Baker. *Membrane Technology and Applications*. 3rd edition. John Wiley & Sons, 2012. DOI: 10.1002/0470020393 (cit. on pp. 1, 2, 11–15, 64).

[Bang2016] W. Bangerth, D. Davydov, T. Heister, L. Heltai, G. Kanschat, M. Kronbichler, M. Maier, B. Turcksin, and D. Wells. “The deal.II Library, Version 8.4”. *Journal of Numerical Mathematics* 24.3 (2016) 135–141. DOI: 10.1515/jnma-2016-1045 (cit. on p. 92).

[Bao2002] L. Bao and G. Glenn Lipscomb. “Mass transfer in axial flows through randomly packed fiber bundles with constant wall concentration”. *Journal of Membrane Science* 204.1 (2002) 207–220. DOI: 10.1016/S0376-7388(02)00043-1 (cit. on pp. 138, 145).

[Batc2010] G. K. Batchelor. *An introduction to fluid dynamics*. 1st edition. Cambridge: Cambridge Univ. Press, 2010. DOI: 10.1017/CBO9780511800955 (cit. on p. 32).

[Bend2019] S. Benders and B. Blümich. “Applications of magnetic resonance imaging in chemical engineering”. *Physical Sciences Reviews* 4.10 (2019) 20180177. DOI: 10.1515/psr-2018-0177 (cit. on p. 199).

[Bigg2015] E. M. Biggs, E. Bruce, B. Boruff, J. M. Duncan, J. Horsley, N. Pauli, K. McNeill, A. Neef, F. van Ogtrop, J. Curnow, B. Haworth, S. Duce, and Y. Imanari. “Sustainable development and the water–energy–food nexus: A perspective on livelihoods”. *Environmental Science & Policy* 54 (2015) 389–397. DOI: 10.1016/j.envsci.2015.08.002 (cit. on p. 1).

[Bike2010] M. Bikel, I. G. Pünt, R. G. Lammertink, and M. Wessling. “Shrinkage effects during polymer phase separation on microfabricated molds”. *Journal of Membrane Science* 347.1-2 (2010) 141–149. DOI: 10.1016/j.memsci.2009.10.015 (cit. on p. 88).

[Bill1982] M. Billeter, W. Braun, and K. Wüthrich. “Sequential resonance assignments in protein ^{1}H nuclear magnetic resonance spectra: Computation of sterically allowed proton-proton distances and statistical analysis of proton-proton distances in single crystal protein conformations”. *Journal of Molecular Biology* 155.3 (1982) 321–346. DOI: 10.1016/0022-2836(82)90008-0 (cit. on p. 36).

[Binn2013] J. Binney and D. Skinner. *The Physics of Quantum Mechanics*. OUP Oxford, 2013 (cit. on p. 17).

[Bloc1946a] F. Bloch. “Nuclear Induction”. *Phys. Rev.* 70 (7-8 1946) 460–474. DOI: 10.1103/PhysRev.70.460 (cit. on p. 35).

[Bloc1946b] F. Bloch, W. W. Hansen, and M. Packard. “The Nuclear Induction Experiment”. *Phys. Rev.* 70 (7-8 1946) 474–485. DOI: 10.1103/PhysRev.70.474 (cit. on p. 35).

[Boho2005] D. M. Bohonak and A. L. Zydney. “Compaction and permeability effects with virus filtration membranes”. *Journal of Membrane Science* 254.1-2 (2005) 71–79. DOI: 10.1016/j.memsci.2004.12.035 (cit. on p. 158).

[Bony2012] S. Bonyadi and M. Mackley. “The development of novel microcapillary film membranes”. *Journal of Membrane Science* 389 (2012) 137–147. DOI: 10.1016/j.memsci.2011.10.023 (cit. on p. 3).

[Bris2020] N. Bristow, S. Vogt, K. O’Neill, J. Vrouwenvelder, M. Johns, and E. Fridjonsson. “Flow field in fouling spiral wound reverse osmosis membrane modules using MRI velocimetry”. *Desalination* 491 (2020) 114508. DOI: 10.1016/j.desal.2020.114508 (cit. on pp. 64, 65).

[Bris2021] N. W. Bristow, S. J. Vogt, S. S. Bucs, J. S. Vrouwenvelder, M. L. Johns, and E. O. Fridjonsson. “Novel Magnetic Resonance Measurements of Fouling in Operating Spiral Wound Reverse Osmosis

Membrane Modules". *Water Research* 196 (2021) 117006. DOI: 10.1016/j.watres.2021.117006 (cit. on p. 66).

[Brit2017] M. M. Britton. "MRI of chemical reactions and processes". *Progress in Nuclear Magnetic Resonance Spectroscopy* 101 (2017) 51–70. DOI: 10.1016/j.pnmrs.2017.03.001 (cit. on p. 27).

[Bu-R2007] K. A. Bu-Rashid and W. Czolkoss. "Pilot Tests of Multibore UF Membrane at Addur SWRO Desalination Plant, Bahrain". *Desalination* 203.1-3 (2007) 229–242. DOI: 10.1016/j.desal.2006.04.010 (cit. on pp. 2, 3, 88).

[Buet2011] S. Buetehorn, L. Utiu, M. Küppers, B. Blümich, T. Wintgens, M. Wessling, and T. Melin. "NMR imaging of local cumulative permeate flux and local cake growth in submerged microfiltration processes". *Journal of Membrane Science* 371.1 (2011) 52–64. DOI: 10.1016/j.memsci.2011.01.018 (cit. on pp. 42, 43, 158).

[Butt2003] H.-J. Butt, K. Graf, and M. Kappl. *Physics and chemistry of interfaces*. Weinheim: Wiley-VCH and Chichester : John Wiley, 2003. DOI: 10.1002/3527602313 (cit. on p. 160).

[Chen2004a] J. Chen, Q. Li, and M. Elimelech. "In situ monitoring techniques for concentration polarization and fouling phenomena in membrane filtration". *Advances in Colloid and Interface Science* 107.2 (2004) 83–108. DOI: 10.1016/j.cis.2003.10.018 (cit. on pp. 36, 199).

[Chen2004b] V. Chen, H. Li, and A. Fane. "Non-invasive observation of synthetic membrane processes – a review of methods". *Journal of Membrane Science* 241.1 (2004) 23–44. DOI: 10.1016/j.memsci.2004.04.029 (cit. on p. 36).

[Chi2017] Y. Chi, T. Li, B. Wang, Z. Wu, and K. Li. "Morphology, performance and stability of multi-bore capillary $La_{0.6}Sr_{0.4}Co_{0.2}Fe_{0.8}O_{3-\delta}$ oxygen transport membranes". *Journal of Membrane Science* 529 (2017) 224–233. DOI: 10.1016/j.memsci.2017.02.010 (cit. on pp. 2, 88).

[COMS2021] COMSOL, Inc. *COMSOL Multiphysics ®*. https://www.comsol.com. Accessed 10 September 2021. 2021 (cit. on p. 70).

[Cost1993] M. Costello, A. Fane, P. Hogan, and R. Schofield. “The effect of shell side hydrodynamics on the performance of axial flow hollow fibre modules”. *Journal of Membrane Science* 80.1 (1993) 1–11. DOI: 10.1016/0376-7388(93)85127-I (cit. on pp. 138, 144, 148).

[Creb2010] S. Creber, J. Vrouwenvelder, M. van Loosdrecht, and M. Johns. “Chemical cleaning of biofouling in reverse osmosis membranes evaluated using magnetic resonance imaging”. *Journal of Membrane Science* 362.1 (2010) 202–210. DOI: 10.1016/j.memsci.2010.06.052 (cit. on pp. 64, 65).

[Çulf2010] P. Z. Çulfaz, E. Rolevink, C. van Rijn, R. Lammertink, and M. Wessling. “Microstructured hollow fibers for ultrafiltration”. *Journal of Membrane Science* 347.1 (2010) 32–41. DOI: 10.1016/j.memsci.2009.10.003 (cit. on p. 43).

[Çulf2011] P. Z. Çulfaz, S. Buetehorn, L. Utiu, M. Kueppers, B. Bluemich, T. Melin, M. Wessling, and R. G. H. Lammertink. “Fouling Behavior of Microstructured Hollow Fiber Membranes in Dead-End Filtrations: Critical Flux Determination and NMR Imaging of Particle Deposition”. *Langmuir* 27.5 (2011) 1643–1652. DOI: 10.1021/la1037734 (cit. on pp. 14, 43, 44, 158).

[Dale2015] B. M. Dale, M. A. Brown, and R. C. Semelka. *MRI - Basic Principles and Applications*. New York: John Wiley & Sons, 2015. DOI: 10.1002/9781119013068 (cit. on pp. 21, 26).

[Das2005] D. B. Das and S. M. Hassanizadeh. *Upscaling Multiphase Flow in Porous Media: From Pore to Core and Beyond*. Dordrecht: Springer, 2005. DOI: 10.1007/1-4020-3604-3 (cit. on p. 160).

[Diop2002] S. Diop, R. Johnstone, D. Lisbjerg, and P. M’mayi. *Vital Water Graphics: An Overview of the State of the World’s Fresh and Marine Waters*. Nairobi, Kenya: United Nations Environment Programme, 2002 (cit. on p. 1).

[Dono1992] C. Donoghue, M. Brideau, P. Newcomer, B. Pangrle, D. DiBiasio, E. Walsh, and S. Moore. “Use of magnetic resonance imaging to analyze the performance of hollow-fiber bioreactors”. *Annals of the New York Academy of Sciences* 665 (1992) 285–300. DOI: 10.1111/j.1749-6632.1992.tb42592.x (cit. on p. 58).

[Drio2007] E. Drioli and E. Curcio. “Membrane engineering for process intensification: a perspective”. *Journal of Chemical Technology & Biotechnology* 82.3 (2007) 223–227. DOI: 10.1002/jctb.1650 (cit. on p. 2).

[Enga1980] J. Engasser, J. Caumon, and A. Marc. “Hollow fiber enzyme reactors for maltose and starch hydrolysis”. *Chemical Engineering Science* 35.1 (1980) 99–105. DOI: 10.1016/0009-2509(80)80075-3 (cit. on p. 139).

[Erns1966] R. R. Ernst and W. A. Anderson. “Application of Fourier Transform Spectroscopy to Magnetic Resonance”. *Review of Scientific Instruments* 37.1 (1966) 93–102. DOI: 10.1063/1.1719961 (cit. on p. 35).

[Fran2000] A. Frank, G. Lipscomb, and M. Dennis. “Visualization of concentration fields in hemodialyzers by computed tomography”. *Journal of Membrane Science* 175.2 (2000) 239–251. DOI: 10.1016/S0376-7388(00)00421-X (cit. on p. 199).

[Fred2018] E. Frederic, C. Guigui, M. Jacob, C. Machinal, A. Krifi, A. Line, and P. Schmitz. “Modelling of fluid flow distribution in multichannel ceramic membrane: Application to the filtration of produced water”. *Journal of Membrane Science* 567 (2018) 290–302. DOI: 10.1016/j.memsci.2018.09.021 (cit. on pp. 3, 68, 88, 89).

[Frid2015] E. Fridjonsson, S. Vogt, J. Vrouwenvelder, and M. Johns. “Early non-destructive biofouling detection in spiral wound RO membranes using a mobile earth’s field NMR”. *Journal of Membrane Science* 489 (2015) 227–236. DOI: 10.1016/j.memsci.2015.03.088 (cit. on pp. 64, 65).

[Garc2018] P. A. García-Salaberri, I. V. Zenyuk, A. D. Shum, G. Hwang, M. Vera, A. Z. Weber, and J. T. Gostick. “Analysis of representative elementary volume and through-plane regional characteristics of carbon-fiber papers: diffusivity, permeability and electrical/thermal conductivity”. *International Journal of Heat and Mass Transfer* 127 (2018) 687–703. DOI: 10.1016/j.ijheatmasstransfer.2018.07.030 (cit. on p. 93).

[Geis2010] G. M. Geise, H.-S. Lee, D. J. Miller, B. D. Freeman, J. E. McGrath, and D. R. Paul. “Water purification by membranes: The role of polymer science”. *Journal of Polymer Science Part B: Polymer Physics* 48.15 (2010) 1685–1718. DOI: 10.1002/polb.22037 (cit. on pp. 1, 2).

[Gill2005] D. Gille and W. Czolkoss. “Ultrafiltration with multi-bore membranes as seawater pre-treatment”. *Desalination* 182.1-3 (2005) 301–307. DOI: 10.1016/j.desal.2005.03.020 (cit. on pp. 2, 3, 88).

[Giro2005] M. Gironès, Z. Borneman, R. G. Lammertink, and M. Wessling. “The role of wetting on the water flux performance of microsieve membranes”. *Journal of Membrane Science* 259.1-2 (2005) 55–64. DOI: 10.1016/j.memsci.2005.03.006 (cit. on p. 159).

[Glad1999] L. F. Gladden. “Applications of in situ magnetic resonance techniques in chemical reaction engineering”. *Topics in Catalysis* 3 (1999) 87–95. DOI: 10.1023/A:1019180220757 (cit. on pp. 27, 36).

[Glad2003] L. F. Gladden. “Magnetic resonance: ongoing and future role in chemical engineering research”. *American Institute of Chemical Engineers. AIChE Journal* 49.1 (2003) 2. DOI: 10.1002/aic.690490102 (cit. on pp. 27, 36).

[Glad2017] L. F. Gladden and A. J. Sederman. “Magnetic Resonance Imaging and Velocity Mapping in Chemical Engineering Applications”. *Annual Review of Chemical and Biomolecular Engineering* 8.1 (2017) 227–247. DOI: 10.1146/annurev-chembioeng-061114-123222 (cit. on pp. 27, 36).

[Graf2008] D. Graf von der Schulenburg, J. Vrouwenvelder, S. Creber, M. van Loosdrecht, and M. Johns. “Nuclear magnetic resonance microscopy studies of membrane biofouling”. *Journal of Membrane Science* 323.1 (2008) 37–44. DOI: 10.1016/j.memsci.2008.06.012 (cit. on p. 64).

[Günt2010] J. Günther, P. Schmitz, C. Albasi, and C. Lafforgue. “A numerical approach to study the impact of packing density on fluid flow distribution in hollow fiber module”. *Journal of Membrane Science*

348.1 (2010) 277–286. DOI: 10.1016/j.memsci.2009.11.011 (cit. on p. 138).

[Günt2012] J. Günther, D. Hobbs, C. Albasi, C. Lafforgue, A. Cockx, and P. Schmitz. “Modeling the effect of packing density on filtration performances in hollow fiber microfiltration module: A spatial study of cake growth”. *Journal of Membrane Science* 389 (2012) 126–136. DOI: 10.1016/j.memsci.2011.10.055 (cit. on p. 138).

[Hamm1990] B. E. Hammer, C. A. Heath, S. D. Mirer, and G. Belfort. “Quantitative Flow Measurements in Bioreactors by Nuclear Magnetic Resonance Imaging”. *Nature Biotechnology* 8 (4 1990) 327–330. DOI: 10.1038/nbt0490-327 (cit. on pp. 40, 139, 145).

[Hard2002] P. Hardy, C. Poh, Z. Liao, W. Clark, and D. Gao. “The use of magnetic resonance imaging to measure the local ultrafiltration rate in hemodialyzers”. *Journal of Membrane Science* 204.1 (2002) 195–205. DOI: 10.1016/S0376-7388(02)00038-8 (cit. on pp. 59, 139).

[Hawt1951] W. R. Hawthorne. “Secondary circulation in fluid flow”. *Proceedings of the Royal Society of London. Series A. Mathematical and Physical Sciences* 206.1086 (1951) 374–387. DOI: 10.1098/rspa.1951.0076 (cit. on pp. 68, 76).

[He2004] T. He and I. Blume. *A process for drying a wet porous membrane structure and the porous membrane structure obtained from said process*. https://patents.google.com/patent/EP1466659A1/en. EP1466659A1. Oct. 2004 (cit. on p. 159).

[Heat1990] C. A. Heath, G. Belfort, B. E. Hammer, S. D. Mirer, and J. M. Pimbley. “Magnetic resonance imaging and modeling of flow in hollow-fiber bioreactors”. *AIChE Journal* 36.4 (1990) 547–558. DOI: 10.1002/aic.690360406 (cit. on p. 40).

[Heib2003] A. K. Heibel, F. J. Vergeldt, H. van As, F. Kapteijn, J. Moulijn, and T. Boger. “Gas and liquid distribution in the monolith film flow reactor”. *AIChE Journal* 49.12 (2003) 3007–3017. DOI: 10.1002/aic.690491203 (cit. on p. 3).

[Heij2012] M. Heijnen, R. Winkler, and P. Berg. “Optimisation of the geometry of a polymeric Multibore® ultrafiltration membrane and its operational advantages over standard single bore fibres”. *Desalina-*

tion and Water Treatment 42.1-3 (2012) 24–29. DOI: 10.1080/19443994.2012.682968 (cit. on pp. 3, 88).

[Hira2012] A. Hirano, S. Kida, K. Yamamoto, and K. Sakai. "Experimental evaluation of flow and dialysis performance of hollow-fiber dialyzers with different packing densities". *Journal of Artificial Organs* 15 (2012) 168–175. DOI: 10.1007/s10047-011-0620-6 (cit. on p. 144).

[Hore2015] P. Hore. *Nuclear Magnetic Resonance*. Oxford Chemistry Primers. Oxford University Press, 2015 (cit. on pp. 20, 22).

[Horo2012] A. L. Horowitz. *MRI Physics for Radiologists - A Visual Approach*. Berlin Heidelberg: Springer Science & Business Media, 2012. DOI: 10.1007/978-1-4612-0785-6 (cit. on p. 23).

[Ibra2018] M. H. Ibrahim, M. H. El-Naas, Z. Zhang, and B. van der Bruggen. "CO_2 Capture Using Hollow Fiber Membranes: A Review of Membrane Wetting". *Energy & Fuels* 32.2 (2018) 963–978. DOI: 10.1021/acs.energyfuels.7b03493 (cit. on p. 159).

[Inst2005] Institute of Medicine. *Dietary Reference Intakes for Water, Potassium, Sodium, Chloride, and Sulfate*. Washington, DC: The National Academies Press, 2005. DOI: 10.17226/10925 (cit. on p. 1).

[Jaff2012] M. Y. Jaffrin. "Hydrodynamic Techniques to Enhance Membrane Filtration". *Annual Review of Fluid Mechanics* 44.1 (2012) 77–96. DOI: 10.1146/annurev-fluid-120710-101112 (cit. on p. 15).

[Jara2020] A. Jarauta, V. Zingan, P. Minev, and M. Secanell. "A Compressible Fluid Flow Model Coupling Channel and Porous Media Flows and Its Application to Fuel Cell Materials". *Transport in Porous Media* 134 (2020) 351–386. DOI: 10.1007/s11242-020-01449-2 (cit. on pp. 98, 101).

[Kagr2001] G. G. Kagramanov, Y. I. Dytnerskii, and P. G. Il'in. "A Model Simulation of the Filtering Process in Multichannel Ceramic Membranes". *Refractories and Industrial Ceramics* 42.3 (2001) 139–145. DOI: 10.1023/A:1011332113153 (cit. on pp. 3, 68, 89).

[Kell1983] D. W. Kelly, J. P. De S. R. Gago, O. C. Zienkiewicz, and I. Babuska. “A posteriori error analysis and adaptive processes in the finite element method: Part I—error analysis”. *International Journal for Numerical Methods in Engineering* 19.11 (1983) 1593–1619. DOI: 10.1002/nme.1620191103 (cit. on p. 104).

[Koch2009] J. Kochan, T. Wintgens, R. Hochstrat, and T. Melin. “Impact of wetting agents on the filtration performance of polymeric ultrafiltration membranes”. *Desalination* 241.1-3 (2009) 34–42. DOI: 10.1016/j.desal.2008.01.056 (cit. on pp. 159, 160, 182, 186).

[Kron2016] M. Kronbichler and W. Bangerth. *The deal.II Library: The step-22 tutorial program*. https://www.dealii.org/8.4.1/doxygen/deal.II/step_22.html. Accessed 10 September 2021. 2016 (cit. on pp. 95, 101).

[Lauk1998] S. Laukemper-Ostendorf, H. Lemke, P. Blümler, and B. Blümich. “NMR imaging of flow in hollow fiber hemodialyzers”. *Journal of Membrane Science* 138.2 (1998) 287–295. DOI: 10.1016/S0376-7388(97)00241-X (cit. on pp. 59, 139, 144).

[Laut1973] P. C. Lauterbur. “Image Formation by Induced Local Interactions: Examples Employing Nuclear Magnetic Resonance”. *Nature* 242 (1973) 190–191. DOI: 10.1038/242190a0 (cit. on p. 36).

[Le H2018] M. Le Hir, Y. Wyart, G. Georges, L. Siozade Lamoine, P. Sauvade, and P. Moulin. “Effect of salinity and nanoparticle polydispersity on UF membrane retention fouling”. *Journal of Membrane Science* 563 (2018) 405–418. DOI: 10.1016/j.memsci.2018.05.077 (cit. on pp. 3, 88).

[Levi2009] M. H. Levitt. *Spin dynamics: Basics of nuclear magnetic resonance*. Second edition, reprinted with corrections. Chichester, Hoboken, NJ, and San Francisco, CA: John Wiley & Sons Ltd, 2009 (cit. on pp. 16, 17, 19, 21–25).

[Ley2018] A. Ley, P. Altschuh, V. Thom, M. Selzer, B. Nestler, and P. Vana. “Characterization of a macro porous polymer membrane at micron-scale by Confocal-Laser-Scanning Microscopy and 3D image analysis”. *Journal of Membrane Science* 564 (2018) 543–551. DOI: 10.1016/j.memsci.2018.07.062 (cit. on p. 91).

[Li2008] H. Li, Y. Tang, Z. Wang, Z. Shi, S. Wu, D. Song, J. Zhang, K. Fatih, J. Zhang, H. Wang, Z. Liu, R. Abouatallah, and A. Mazza. “A review of water flooding issues in the proton exchange membrane fuel cell”. *Journal of Power Sources* 178.1 (2008) 103–117. DOI: 10.1016/j.jpowsour.2007.12.068 (cit. on p. 1).

[Li2014] X. Li, J. Li, J. Wang, H. Wang, B. He, H. Zhang, W. Guo, and H. H. Ngo. “Experimental investigation of local flux distribution and fouling behavior in double-end and dead-end submerged hollow fiber membrane modules”. *Journal of Membrane Science* 453 (2014) 18–26. DOI: 10.1016/j.memsci.2013.10.052 (cit. on p. 139).

[Li2017] X. Li, Y. Mo, J. Li, W. Guo, and H. H. Ngo. “In-situ monitoring techniques for membrane fouling and local filtration characteristics in hollow fiber membrane processes: A critical review”. *Journal of Membrane Science* 528 (2017) 187–200. DOI: 10.1016/j.memsci.2017.01.030 (cit. on p. 36).

[Link2016] J. Linkhorst, T. Beckmann, D. Go, A. Kuehne, and M. Wessling. “Microfluidic colloid filtration”. *Scientific Reports* 6.22376 (2016) DOI: 10.1038/srep22376 (cit. on p. 199).

[Link2019] J. Linkhorst, J. Rabe, L. Hirschwald, A. Kuehne, and M. Wessling. “Direct Observation of Deformation in Microgel Filtration”. *Scientific Reports* 9.18998 (2019) DOI: 10.1038/s41598-019-55516-w (cit. on p. 199).

[Loha2018] J. Lohaus, Y. Perez, and M. Wessling. “What are the microscopic events of colloidal membrane fouling?” *Journal of Membrane Science* 553 (2018) 90–98. DOI: 10.1016/j.memsci.2018.02.023 (cit. on p. 199).

[Loha2020] J. Lohaus, F. Stockmeier, P. Surray, J. Lölsberg, and M. Wessling. “What are the microscopic events during membrane backwashing?” *Journal of Membrane Science* 602 (2020) 117886. DOI: 10.1016/j.memsci.2020.117886 (cit. on pp. 90, 199).

[Lu2016] K.-J. Lu, J. Zuo, and T.-S. Chung. “Tri-bore PVDF hollow fibers with a super-hydrophobic coating for membrane distillation”. *Journal of Membrane Science* 514 (2016) 165–175. DOI: 10.1016/j.memsci.2016.04.058 (cit. on pp. 2, 3).

[Lu2018] K. J. Lu, J. Zuo, J. Chang, H. N. Kuan, and T.-S. Chung. “Omniphobic Hollow-Fiber Membranes for Vacuum Membrane Distillation”. *Environmental Science & Technology* 52.7 (2018) 4472–4480. DOI: 10.1021/acs.est.8b00766 (cit. on p. 69).

[Luel2018] T. Luelf, D. Rall, D. Wypysek, M. Wiese, T. Femmer, C. Bremer, J. U. Michaelis, and M. Wessling. “3D-printed rotating spinnerets create membranes with a twist”. *Journal of Membrane Science* 555 (2018) 7–19. DOI: 10.1016/j.memsci.2018.03.026 (cit. on pp. 2, 3, 30, 55, 68, 71, 88).

[Luo2014] L. Luo, P. Wang, S. Zhang, G. Han, and T.-S. Chung. “Novel thin-film composite tri-bore hollow fiber membrane fabrication for forward osmosis”. *Journal of Membrane Science* 461 (2014) 28–38. DOI: 10.1016/j.memsci.2014.03.007 (cit. on p. 3).

[Luo2015] L. Luo, G. Han, T.-S. Chung, M. Weber, C. Staudt, and C. Maletzko. “Oil/water separation via ultrafiltration by novel triangle-shape tri-bore hollow fiber membranes from sulfonated polyphenylenesulfone”. *Journal of Membrane Science* 476 (2015) 162–170. DOI: 10.1016/j.memsci.2014.11.035 (cit. on p. 3).

[Ma2019] C. Ma, Y. Liu, F. Li, C. Shen, M. Huang, Z. Wang, C. Cao, Q. Zhou, Y. Sheng, and W. Sand. “CFD simulations of fiber-fiber interaction in a hollow fiber membrane bundle: Fiber distance and position matters”. *Separation and Purification Technology* 209 (2019) 707–713. DOI: 10.1016/j.seppur.2018.09.029 (cit. on p. 138).

[Mans1973a] P. Mansfield and P. K. Grannell. “NMR ’diffraction’ in solids?” *Journal of Physics C: Solid State Physics* 6.22 (1973) L422–L426. DOI: 10.1088/0022-3719/6/22/007 (cit. on p. 35).

[Mans1973b] P. Mansfield, M. J. Orchard, D. C. Stalker, and K. H. B. Richards. “Symmetrized Multipulse Nuclear-Magnetic-Resonance Experiments in Solids: Measurement of the Chemical-Shift Shielding Tensor in Some Compounds”. *Phys. Rev. B* 7 (1 1973) 90–105. DOI: 10.1103/PhysRevB.7.90 (cit. on p. 35).

[Mari2020] J. M. Marinkovic, S. Benders, E. J. Garcia-Suarez, A. Weiß, C. Gundlach, M. Haumann, M. Küppers, B. Blümich, R. Fehrmann, and A. Riisager. “Elucidating the ionic liquid distribution in monolithic SILP hydroformylation catalysts by magnetic resonance

imaging". *RSC Advances* 10 (31 2020) 18487–18495. DOI: 10.1039/C9RA09515B (cit. on pp. 89, 159).

[Mark2005] M. Markl. "Velocity encoding and flow imaging". *ISMRM Eductational Sessions - Annual Meeting, University Hospital Freiburg, Dept of Diagnostic Radiology, Germany* (2005) (cit. on p. 28).

[McRo2017] D. W. McRobbie, E. A. Moore, and M. J. Graves. *MRI from picture to proton*. Cambridge medicine. Cambridge: Cambridge University Press, 2017 (cit. on pp. 21, 22).

[Muld2000] M. Mulder. *Basic principles of membrane technology*. 2nd edition., reprint. Dordrecht: Kluwer, 2000. DOI: 10.1007/978-94-009-1766-8 (cit. on p. 1).

[Nish1996] D. Nishimura. *Principles of Magnetic Resonance Imaging*. Stanford University, 1996 (cit. on p. 20).

[Nybo2018] E. Nybo, J. E. Maneval, S. L. Codd, M. A. Ryder, G. A. James, J. Woodbury, and J. D. Seymour. "Flow velocity maps measured by nuclear magnetic resonance in medical intravenous catheter needleless connectors". *Journal of Pharmaceutical and Biomedical Analysis* 152 (2018) 1–11. DOI: 10.1016/j.jpba.2018.01.037 (cit. on p. 63).

[Osug2004a] T. Osuga, T. Obata, and H. Ikehira. "Detection of small degree of nonuniformity in dialysate flow in hollow-fiber dialyzer using proton magnetic resonance imaging". *Magnetic Resonance Imaging* 22.3 (2004) 417–420. DOI: 10.1016/j.mri.2003.08.008 (cit. on pp. 60, 139).

[Osug2004b] T. Osuga, T. Obata, and H. Ikehira. "Proton magnetic resonance imaging of flow motion of heavy water injected into a hollow fiber dialyzer filled with saline". *Magnetic Resonance Imaging* 22.3 (2004) 413–416. DOI: 10.1016/j.mri.2003.07.003 (cit. on pp. 60, 61, 139).

[Pang1989] B. J. Pangrle, E. G. Walsh, S. Moore, and D. DiBiasio. "Investigation of fluid flow patterns in a hollow fiber module using magnetic resonance velocity imaging". *Biotechnology Techniques* 3 (1989) 67–72. DOI: 10.1007/BF01876224 (cit. on pp. 58, 139).

[Pang1992] B. Pangrle, E. Walsh, S. Moore, and D. DiBiasio. “Magnetic resonance imaging of laminar flow in porous tube and shell systems”. *Chemical Engineering Science* 47.3 (1992) 517–526. DOI: 10.1016/0009-2509(92)80001-S (cit. on p. 40).

[Park1986] J. K. Park and H. N. Chang. “Flow distribution in the fiber lumen side of a hollow-fiber module”. *AIChE Journal* 32.12 (1986) 1937–1947. DOI: 10.1002/aic.690321202 (cit. on p. 138).

[Park2017] H. B. Park, J. Kamcev, L. M. Robeson, M. Elimelech, and B. D. Freeman. “Maximizing the right stuff: The trade-off between membrane permeability and selectivity”. *Science (New York, N.Y.)* 356.6343 (2017) DOI: 10.1126/science.aab0530 (cit. on p. 1).

[Peña1993] L. Peña, de Zárate, José M. Ortiz, and J. I. Mengual. “Steady states in membrane distillation: Influence of membrane wetting”. *J. Chem. Soc., Faraday Trans.* 89.24 (1993) 4333–4338. DOI: 10.1039/FT9938904333 (cit. on pp. 158, 159).

[Peng2011] N. Peng, M. M. Teoh, T.-S. Chung, and L. L. Koo. “Novel rectangular membranes with multiple hollow holes for ultrafiltration”. *Journal of Membrane Science* 372.1-2 (2011) 20–28. DOI: 10.1016/j.memsci.2011.01.022 (cit. on p. 3).

[Peng2012] N. Peng, N. Widjojo, P. Sukitpaneenit, M. M. Teoh, G. G. Lipscomb, T.-S. Chung, and J.-Y. Lai. “Evolution of polymeric hollow fibers as sustainable technologies: Past, present, and future”. *Progress in Polymer Science* 37.10 (2012) 1401–1424. DOI: 10.1016/j.progpolymsci.2012.01.001 (cit. on p. 2).

[Perl2015] J. Perlo, E. V. Silletta, E. Danieli, G. Cattaneo, R. H. Acosta, B. Blümich, and F. Casanova. “Desktop MRI as a promising tool for mapping intra-aneurismal flow”. *Magnetic Resonance Imaging* 33.3 (2015) 328–335. DOI: 10.1016/j.mri.2014.12.005 (cit. on p. 30).

[Pind2008] G. F. Pinder and W. G. Gray. *Essentials of multiphase flow and transport in porous media*. Hoboken, NJ: Wiley-Interscience, 2008. DOI: 10.1002/9780470380802 (cit. on p. 160).

[Poh2003a] C. Poh, P. Hardy, Z. Liao, Z. Huang, W. Clark, and D. Gao. “Effect of Flow Baffles on the Dialysate Flow Distribution of Hollow-Fiber Hemodialyzers: A Nonintrusive Experimental Study Using MRI”. *Journal of Biomechanical Engineering* 125 (2003) 481–489. DOI: 10.1115/1.1590355 (cit. on pp. 59, 139).

[Poh2003b] C. Poh, P. Hardy, Z. Liao, Z. Huang, W. Clark, and D. Gao. “Effect of spacer yarns on the dialysate flow distribution of hemodialyzers: a magnetic resonance imaging study”. *ASAIO Journal* 49.4 (2003) 440–448. DOI: 10.1097/01.MAT.0000073966.24950.28 (cit. on pp. 59, 139).

[Pope1996] J. Pope, S. Yao, and A. Fane. “Quantitative measurements of the concentration polarisation layer thickness in membrane filtration of oil-water emulsions using NMR micro-imaging”. *Journal of Membrane Science* 118.2 (1996) 247–257. DOI: 10.1016/0376-7388(96)00107-X (cit. on pp. 40, 158).

[Purc1946] E. M. Purcell, H. C. Torrey, and R. V. Pound. “Resonance Absorption by Nuclear Magnetic Moments in a Solid”. *Phys. Rev.* 69 (1-2 1946) 37–38. DOI: 10.1103/PhysRev.69.37 (cit. on p. 35).

[Rabi1938] I. I. Rabi, J. R. Zacharias, S. Millman, and P. Kusch. “A New Method of Measuring Nuclear Magnetic Moment”. *Phys. Rev.* 53 (4 1938) 318–318. DOI: 10.1103/PhysRev.53.318 (cit. on p. 35).

[Reza2018] M. Rezaei, D. M. Warsinger, J. H. Lienhard V, M. C. Duke, T. Matsuura, and W. M. Samhaber. “Wetting phenomena in membrane distillation: Mechanisms, reversal, and prevention”. *Water research* 139 (2018) 329–352. DOI: 10.1016/j.watres.2018.03.058 (cit. on p. 159).

[Ribe2007] A. Ribes and C. Caremoli. “Salomé platform component model for numerical simulation”. In*31st Annual International Computer Software and Applications Conference (COMPSAC 2007)*. Vol. 2. IEEE, 2007, 553–564. DOI: 10.1109/COMPSAC.2007.185 (cit. on p. 98).

[Roud2000] A. R. Roudman and F. A. DiGiano. “Surface energy of experimental and commercial nanofiltration membranes: Effects of wetting and natural organic matter fouling”. *Journal of Membrane Science*

175.1 (2000) 61–73. DOI: 10.1016/S0376-7388(00)00409-9 (cit. on p. 159).

[Sabh2016] M. Sabharwal, L. M. Pant, A. Putz, D. Susac, J. Jankovic, and M. Secanell. “Analysis of Catalyst Layer Microstructures: From Imaging to Performance”. *Fuel Cells* 16.6 (2016) 734–753. DOI: 10.1002/fuce.201600008 (cit. on pp. 94, 97).

[Sabh2018] M. Sabharwal, J. T. Gostick, and M. Secanell. “Virtual Liquid Water Intrusion in Fuel Cell Gas Diffusion Media”. *Journal of The Electrochemical Society* 165.7 (2018) F553–F563. DOI: 10.1149/2.0921807jes (cit. on p. 90).

[Schi2012] J. Schindelin, I. Arganda-Carreras, E. Frise, V. Kaynig, M. Longair, T. Pietzsch, S. Preibisch, C. Rueden, S. Saalfeld, B. Schmid, J.-Y. Tinevez, D. J. White, V. Hartenstein, K. Eliceiri, P. Tomancak, and A. Cardona. “Fiji: an open-source platform for biological-image analysis”. *Nature methods* 9 (2012) 676–682. DOI: 10.1038/nmeth.2019 (cit. on p. 93).

[Scho2018] N. Schork, S. Schuhmann, F. Arndt, S. Schütz, G. Guthausen, and H. Nirschl. “MRI investigations of filtration: Fouling and cleaning processes”. *Microporous and Mesoporous Materials* 269 (2018) 60–64. DOI: 10.1016/j.micromeso.2017.05.042 (cit. on pp. 46, 48).

[Scho2019] N. Schork, S. Schuhmann, H. Nirschl, and G. Guthausen. “In situ measurement of deposit layer formation during skim milk filtration by MRI”. *Magnetic Resonance in Chemistry* 57.9 (2019) 738–748. DOI: 10.1002/mrc.4826 (cit. on p. 46).

[Scho2020] R. Schopf, N. Schork, E. Amling, H. Nirschl, G. Guthausen, and U. Kulozik. “Structural Characterisation of Deposit Layer during Milk Protein Microfiltration by Means of In-Situ MRI and Compositional Analysis”. *Membranes* 10.4 (2020) 59. DOI: 10.3390/membranes10040059 (cit. on p. 46).

[Scho2021] N. Schork, S. Schuhmann, H. Nirschl, and G. Guthausen. “Compressed sensing MRI to characterize sodium alginate deposits during cross-flow filtration in membranes with a helical ridge”. *Journal of Membrane Science* 626 (2021) 119170. DOI: 10.1016/j.memsci.2021.119170 (cit. on p. 57).

[Schu2018] S. Schuhmann, N. Schork, K. Beller, H. Nirschl, T. Oerther, and G. Guthausen. “In-situ characterization of deposits in ceramic hollow fiber membranes by compressed sensing RARE-MRI”. *AIChE Journal* 64.11 (2018) 4039–4046. DOI: 10.1002/aic.16201 (cit. on pp. 46, 49).

[Schu2019] S. Schuhmann, J. W. Simkins, N. Schork, S. L. Codd, J. D. Seymour, M. Heijnen, F. Saravia, H. Horn, H. Nirschl, and G. Guthausen. “Characterization and quantification of structure and flow in multichannel polymer membranes by MRI”. *Journal of Membrane Science* 570-571 (2019) 472–480. DOI: 10.1016/j.memsci.2018.10.072 (cit. on pp. 3, 50, 51, 68, 83, 88, 89, 138, 175).

[Scot2013] K. Scott. *Industrial Membrane Separation Technology*. The Netherlands: Springer, 2013. DOI: 10.1007/978-94-011-0627-6 (cit. on pp. 1, 14).

[Seca2014] M. Secanell, A. Putz, P. Wardlaw, V. Zingan, M. Bhaiya, M. Moore, J. Zhou, C. Balen, and K. Domican. “OpenFCST: An Open-Source Mathematical Modelling Software for Polymer Electrolyte Fuel Cells”. *ECS Transactions* 64.3 (2014) 655–680. DOI: 10.1149/06403.0655ecst (cit. on pp. 91, 98).

[Seca2016] M. Secanell. *OpenFCST - Open Source Fuel Cell Simulation Toolbox*. https://github.com/OpenFCST/OpenFCSTv03. Accessed 10 September 2021. 2016 (cit. on p. 98).

[Seca2017] M. Secanell, A. Jarauta, A. Kosakian, M. Sabharwal, and J. Zhou. “PEM Fuel Cells, Modeling”. In *Encyclopedia of Sustainability Science and Technology*. Ed. by R. A. Meyers. Vol. 138. New York: Springer, 2017. 1–61. (Cit. on pp. 91, 101).

[Shan2008] M. A. Shannon, P. W. Bohn, M. Elimelech, J. G. Georgiadis, B. J. Marinas, and A. M. Mayes. “Science and technology for water purification in the coming decades”. *Nature* 452 (2008) 301–310. DOI: 10.1038/nature06599 (cit. on pp. 1, 2).

[Siem2003] Siemens Medical Solutions. *Magnete, Spins und Resonanzen: Eine Einführung in die Grundlagen der Magnetresonanztomographie*. Ed. by Siemens AG. Erlangen, 2003 (cit. on pp. 18, 19).

[Simk2020] J. W. Simkins, S. Schuhmann, G. Guthausen, M. Heijnen, S. L. Codd, and J. D. Seymour. “Characterization of biofilm distribution in hollow fiber membranes using Compressed Sensing Magnetic Resonance Imaging”. *Journal of Membrane Science* 594 (2020) 117437. DOI: j.memsci.2019.117437 (cit. on pp. 3, 88).

[Sing2015] R. Singh. *Membrane technology and engineering for water purification: Application, systems design and operation*. Second edition. Oxford, UK: Butterworth-Heinemann, 2015 (cit. on pp. 1, 2, 97).

[Smol1992] C. A. Smolders, A. J. Reuvers, R. M. Boom, and I. M. Wienk. “Microstructures in phase-inversion membranes. Part 1. Formation of macrovoids”. *Journal of Membrane Science* 73.2 (1992) 259–275. DOI: 10.1016/0376-7388(92)80134-6 (cit. on p. 88).

[Song1998] L. Song. “Flux decline in crossflow microfiltration and ultrafiltration: mechanisms and modeling of membrane fouling”. *Magnetic Resonance Imaging* 139.2 (1998) 183–200. DOI: 10.1016/S0376-7388(97)00263-9 (cit. on p. 13).

[Sorc2020] M. Sorci, C. C. Woodcock, D. J. Andersen, A. R. Behzad, S. Nunes, J. Plawsky, and G. Belfort. “Linking microstructure of membranes and performance”. *Journal of Membrane Science* 594 (2020) 117419. DOI: 10.1016/j.memsci.2019.117419 (cit. on pp. 89, 90).

[Spru2013] M. Spruck, G. Hoefer, G. Fili, D. Gleinser, A. Ruech, M. Schmidt-Baldassari, and M. Rupprich. “Preparation and characterization of composite multichannel capillary membranes on the way to nanofiltration”. *Desalination* 314 (2013) 28–33. DOI: 10.1016/j.desal.2013.01.002 (cit. on pp. 2, 88).

[Stap2006] S. Stapf and S.-I. Han, eds. *NMR imaging in chemical engineering*. Weinheim: Wiley-VCH, 2006. DOI: 10.1002/3527607560 (cit. on pp. 19–21, 24–28).

[Stro2002] A. D. Stroock, S. K. W. Dertinger, A. Ajdari, I. Mezić, H. A. Stone, and G. M. Whitesides. “Chaotic Mixer for Microchannels”. *Science* 295.5555 (2002) 647–651. DOI: 10.1126/science.1066238 (cit. on p. 54).

[SUEZ] SUEZ Water Technologies & Solutions. *ZW700B using SevenBore fiber technology*. https://www.suezwatertechnologies.com/products/ultrafiltration/zeeweed-700b-membrane. Accessed 10 September 2021 (cit. on pp. 34, 69, 96, 113, 164).

[Sury1951] G. Suryan. “Nuclear resonance in flowing liquids”. *Proceedings of the Indian Academy of Sciences - Section A* 33 (2 1951) 107. DOI: 10.1007/BF03172192 (cit. on p. 35).

[Teoh2011] M. M. Teoh, N. Peng, T.-S. Chung, and L. L. Koo. “Development of Novel Multichannel Rectangular Membranes with Grooved Outer Selective Surface for Membrane Distillation”. *Industrial & Engineering Chemistry Research* 50.24 (2011) 14046–14054. DOI: 10.1021/ie201292j (cit. on pp. 2, 3, 88).

[Ujih2018] R. Ujihara, E. Fridjonsson, N. Bristow, S. Vogt, S. Bucs, J. Vrouwenvelder, and M. Johns. “Earth’s field MRI for the non-invasive detection of fouling in spiral-wound membrane modules in pressure vessels during operation”. *Desalination and Water Treatment: science and engineering* 135 (2018) 16–24. DOI: 10.5004/dwt.2018.23156 (cit. on pp. 64, 65).

[UNIC2018] UNICEF. *Weltwassertag 2018: Wie viel Wasser braucht eine Familie zum Leben?* https://www.unicef.de/informieren/aktuelles/blog/weltwassertag-wasserverbrauch-familien-weltweit/161970. Accessed 10 September 2021. 2018 (cit. on p. 1).

[UNIC2021] UNICEF. *Water, Sanitation and Hygiene*. https://www.unicef.org/wash/. Accessed 10 September 2021. 2021 (cit. on p. 1).

[Unit2021] United Nations. *Water and Sanitation*. https://www.un.org/sustainabledevelopment/water-and-sanitation/. Accessed 10 September 2021. 2021 (cit. on p. 1).

[Wagn1982] G. Wagner and K. Wüthrich. “Sequential resonance assignments in protein ^{1}H nuclear magnetic resonance spectra: Basic pancreatic trypsin inhibitor”. *Journal of Molecular Biology* 155.3 (1982) 347–366. DOI: 10.1016/0022-2836(82)90009-2 (cit. on p. 36).

[Wan2017] P. Wan, J. Yin, and B. Deng. “Seven-bore hollow fiber membrane (HFM) for ultrafiltration (UF)”. *Chemical Engineering Research and Design* 128 (2017) 240–247. DOI: 10.1016/j.cherd.2017.09.019 (cit. on pp. 3, 88).

[Wang2005] R. Wang, H. Zhang, P. Feron, and D. Liang. “Influence of membrane wetting on CO_2 capture in microporous hollow fiber membrane contactors”. *Separation and Purification Technology* 46.1 (2005) 33–40. DOI: 10.1016/j.seppur.2005.04.007 (cit. on p. 158).

[Wang2012] P. Wang and T.-S. Chung. “Design and fabrication of lotus-root-like multi-bore hollow fiber membrane for direct contact membrane distillation”. *Journal of Membrane Science* 421-422 (2012) 361–374. DOI: 10.1016/j.memsci.2012.08.003 (cit. on pp. 2, 3).

[Wang2013] P. Wang and T.-S. Chung. “A new-generation asymmetric multi-bore hollow fiber membrane for sustainable water production via vacuum membrane distillation”. *Environmental science & technology* 47.12 (2013) 6272–6278. DOI: 10.1021/es400356z (cit. on pp. 2, 3).

[Wang2014a] P. Wang and T.-S. Chung. “Exploring the spinning and operations of multibore hollow fiber membranes for vacuum membrane distillation”. *AIChE Journal* 60.3 (2014) 1078–1090. DOI: 10.1002/aic.14323 (cit. on pp. 2, 3).

[Wang2014b] P. Wang, L. Luo, and T.-S. Chung. “Tri-bore ultra-filtration hollow fiber membranes with a novel triangle-shape outer geometry”. *Journal of Membrane Science* 452 (2014) 212–218. DOI: 10.1016/j.memsci.2013.10.033 (cit. on pp. 2, 3, 88).

[Wang2019] J. Wang, X. Gao, G. Ji, and X. Gu. “CFD simulation of hollow fiber supported NaA zeolite membrane modules”. *Separation and Purification Technology* 213 (2019) 1–10. DOI: 10.1016/j.seppur.2018.12.017 (cit. on p. 139).

[Warg2012] E. A. Wargo, A. C. Hanna, A. Çeçen, S. R. Kalidindi, and E. C. Kumbur. “Selection of representative volume elements for pore-scale analysis of transport in fuel cell materials”. *Journal of Power Sources* 197 (2012) 168–179. DOI: 10.1016/j.jpowsour.2011.09.035 (cit. on p. 93).

[Warg2013] E. Wargo, T. Kotaka, Y. Tabuchi, and E. Kumbur. “Comparison of focused ion beam versus nano-scale X-ray computed tomography for resolving 3-D microstructures of porous fuel cell materials”. *Journal of Power Sources* 241 (2013) 608–618. DOI: 10.1016/j.jpowsour.2013.04.153 (cit. on pp. 94, 97).

[Weer2015] B. Weerakoon and T. Osuga. “The Applicability of Gd-DTPA Magnetic Resonance Imaging Contrast Agent for the Evaluation of Blood Compartment Flow Distribution in Hollow Fiber Hemodialyzers”. *Journal of Biomedical Science and Engineering* 08.11 (2015) 789–796. DOI: 10.4236/jbise.2015.811075 (cit. on pp. 61, 139).

[Weer2016] B. Weerakoon and T. Osuga. “Characterization of Flow Distribution in the Blood Compartment of Hollow Fiber Hemodialyzers with Contrast-Enhanced Spin Echo Magnetic Resonance Imaging”. *Applied Magnetic Resonance* 47.4 (2016) 453–469. DOI: 10.1007/s00723-016-0766-8 (cit. on pp. 61, 139).

[Werb2016] J. R. Werber, C. O. Osuji, and M. Elimelech. “Materials for next-generation desalination and water purification membranes”. *Nature Reviews Materials* 1 (2016) 16018. DOI: 10.1038/natrevmats.2016.18 (cit. on pp. 1, 2, 88).

[Wide1982] G. Wider, K. H. Lee, and K. Wüthrich. “Sequential resonance assignments in protein ^{1}H nuclear magnetic resonance spectra: Glucagon bound to perdeuterated dodecylphosphocholine micelles”. *Journal of Molecular Biology* 155.3 (1982) 367–388. DOI: 10.1016/0022-2836(82)90010-9 (cit. on p. 36).

[Wies2018a] M. Wiese, S. Benders, B. Blümich, and M. Wessling. “3D MRI velocimetry of non-transparent 3D-printed staggered herringbone mixers”. *Chemical Engineering Journal* 343 (2018) 54–60. DOI: 10.1016/j.cej.2018.02.096 (cit. on pp. 30, 54, 55, 71).

[Wies2018b] M. Wiese, C. Malkomes, B. Krause, and M. Wessling. “Flow and filtration imaging of single use sterile membrane filters”. *Journal of Membrane Science* 552 (2018) 274–285. DOI: 10.1016/j.memsci.2018.02.002 (cit. on pp. 30, 61, 62, 158).

[Wies2019] M. Wiese, O. Nir, D. Wypysek, L. Pokern, and M. Wessling. “Fouling minimization at membranes having a 3D surface topology with microgels as soft model colloids”. *Journal of Membrane Science* 569 (2019) 7–16. DOI: 10.1016/j.memsci.2018.09.058 (cit. on pp. 16, 30, 55, 56).

[Wu2000] J. Wu and V. Chen. “Shell-side mass transfer performance of randomly packed hollow fiber modules”. *Journal of Membrane Science* 172.1 (2000) 59–74. DOI: 10.1016/S0376-7388(00)00318-5 (cit. on p. 138).

[Wüth1982] K. Wüthrich, G. Wider, G. Wagner, and W. Braun. “Sequential resonance assignments as a basis for determination of spatial protein structures by high resolution proton nuclear magnetic resonance”. *Journal of Molecular Biology* 155.3 (1982) 311–319. DOI: 10.1016/0022-2836(82)90007-9 (cit. on p. 36).

[Wypy2019] D. Wypysek, D. Rall, M. Wiese, T. Neef, G.-H. Koops, and M. Wessling. “Shell and lumen side flow and pressure communication during permeation and filtration in a multibore polymer membrane module”. *Journal of Membrane Science* 584.8 (2019) 254–267. DOI: 10.1016/j.memsci.2019.04.070 (cit. on pp. 3, 8, 16, 50, 51, 68, 83, 85, 86, 89–91, 93, 105, 107, 123, 125–129, 133, 138, 171, 196, 198).

[Wypy2021a] D. Wypysek, A. M. Kalde, F. Pradellok, and M. Wessling. “In-situ investigation of wetting patterns in polymeric multibore membranes via magnetic resonance imaging”. *Journal of Membrane Science* 622 (2021) 119026. DOI: 10.1016/j.memsci.2020.119026 (cit. on p. 8).

[Wypy2021b] D. Wypysek, D. Rall, T. Neef, A. Jarauta, M. Secanell, and M. Wessling. “How does porosity heterogeneity affect the transport properties of multibore filtration membranes?” *Journal of Membrane Science* 636 (2021) 119520. DOI: 10.1016/j.memsci.2021.119520 (cit. on p. 8).

[Yan2021] B. Yan, N. W. Bristow, S. J. Vogt, J. S. Vrouwenvelder, M. L. Johns, and E. O. Fridjonsson. “Monitoring of hollow fiber module velocity field and fouling inside individual fibers using benchtop MRI”. *Jour-*

nal of Membrane Science 629 (2021) 119238. DOI: 10.1016/j.memsci.2021.119238 (cit. on pp. 44, 45, 139, 198).

[Yang2014] X. Yang, E. Fridjonsson, M. Johns, R. Wang, and A. Fane. "A non-invasive study of flow dynamics in membrane distillation hollow fiber modules using low-field nuclear magnetic resonance imaging (MRI)". *Journal of Membrane Science* 451 (2014) 46–54. DOI: 10.1016/j.memsci.2013.09.015 (cit. on pp. 57, 139, 144, 158).

[Yao1995a] S. Yao, M. Costello, A. Fane, and J. Pope. "Non-invasive observation of flow profiles and polarisation layers in hollow fibre membrane filtration modules using NMR micro-imaging". *Journal of Membrane Science* 99.3 (1995) 207–216. DOI: 10.1016/0376-7388(94)00219-O (cit. on pp. 16, 40, 41, 145, 158).

[Yao1995b] S. Yao, J. Pope, and A. Fane. "Chemical Shift Selective Flow Imaging: Applications in Membrane Filtration of Oil-water Emulsions". *Bulletin of Magnetic Resonance* 17.1-4 (1995) 220–221. (Cit. on pp. 40, 42).

[Yao1997] S. Yao, A. Fane, and J. Pope. "An investigation of the fluidity of concentration polarisation layers in crossflow membrane filtration of an oil-water emulsion using chemical shift selective flow imaging". *Magnetic Resonance Imaging* 15.2 (1997) 235–242. DOI: 10.1016/S0730-725X(96)00325-6 (cit. on pp. 40, 42).

[Yao2020] M. Yao, L. D. Tijing, G. Naidu, S.-H. Kim, H. Matsuyama, A. G. Fane, and H. K. Shon. "A review of membrane wettability for the treatment of saline water deploying membrane distillation". *Desalination* 479 (2020) 114312. DOI: 10.1016/j.desal.2020.114312 (cit. on p. 159).

[Yoon2013] H. Yoon and T. A. Dewers. "Nanopore structures, statistically representative elementary volumes, and transport properties of chalk". *Geophysical Research Letters* 40.16 (2013) 4294–4298. DOI: 10.1002/grl.50803 (cit. on p. 93).

[Zarg2020] M. Zargar, R. Ujihara, S. Vogt, J. Vrouwenvelder, E. Fridjonsson, and M. Johns. "Imaging of membrane concentration polarization by NaCl using ^{23}Na nuclear magnetic resonance". *Journal of Membrane Science* 600 (2020) 117868. DOI: 10.1016/j.memsci.2020.117868 (cit. on pp. 64, 66).

[Zhan1995] J. Zhang, D. Parker, and J. Leypoldt. “Flow distributions in hollow fiber hemodialyzers using magnetic resonance Fourier velocity imaging”. *Asaio Journal* 41.3 (1995) M678–82. DOI: 10.1097/00002480-199507000-00097 (cit. on pp. 58, 139, 144).

[Zhan2018] T. Zhang, K. Guo, C. Li, Y. Li, and C. Liu. “Investigation on Drag Reduction Characteristics and Shell-Side Hydrodynamics in Hollow Fiber Membrane Modules”. *Advanced Theory and Simulations* 1.10 (2018) 1800074. DOI: 10.1002/adts.201800074 (cit. on pp. 68, 139, 145).

[Zhao2018] Y. Zhao, G. Zhu, C. Zhang, S. Liu, D. Elsworth, and T. Zhang. “Pore–Scale Reconstruction and Simulation of Non–Darcy Flow in Synthetic Porous Rocks”. *Journal of Geophysical Research: Solid Earth* 123.4 (2018) 2770–2786. DOI: 10.1002/2017JB015296 (cit. on p. 90).

[Zhu2015a] J. Zhu, S. Guo, Z. Zhang, X. Jiang, Z. Liu, and W. Jin. “CO_2-tolerant mixed-conducting multichannel hollow fiber membrane for efficient oxygen separation”. *Journal of Membrane Science* 485 (2015) 79–86. DOI: 10.1016/j.memsci.2015.02.034 (cit. on pp. 2, 88).

[Zhu2015b] J. Zhu, Z. Liu, S. Guo, and W. Jin. “Influence of permeation modes on oxygen permeability of the multichannel mixed-conducting hollow fibre membrane”. *Chemical Engineering Science* 122 (2015) 614–621. DOI: 10.1016/j.ces.2014.10.014 (cit. on pp. 2, 88).

[Zhu2017] J. Zhu, T. Wang, Z. Song, Z. Liu, G. Zhang, and W. Jin. “Enhancing oxygen permeation via multiple types of oxygen transport paths in hepta-bore perovskite hollow fibers”. *AIChE Journal* 63.10 (2017) 4273–4277. DOI: 10.1002/aic.15849 (cit. on pp. 2, 3, 88).

[Zhua2015] L. Zhuang, H. Guo, P. Wang, and G. Dai. “Study on the flux distribution in a dead-end outside-in hollow fiber membrane module”. *Journal of Membrane Science* 495 (2015) 372–383. DOI: 10.1016/j.memsci.2015.07.060 (cit. on p. 138).